Searching for New High Mass Resonances in the Dielectron Channel, using the ATLAS Detector at CERN

Daniel Hayden

Department of Physics
Royal Holloway, University of London

A thesis submitted to the University of London for the
Degree of Doctor of Philosophy

May 17, 2012

DECLARATION

I confirm that the work presented in this thesis is my own. Where information has been derived from other sources, I confirm that this has been indicated in the document.

Daniel Hayden

Abstract

A search is conducted in the dielectron channel for beyond the Standard Model high mass neutral resonances, such as E_6 motivated Z' states and the Randall-Sundrum Graviton. The data in this thesis was recorded by the ATLAS detector during proton-proton collisions in 2011 at $\sqrt{s} = 7$ TeV, provided by the Large Hadron Collider at CERN in Geneva, Switzerland. The dataset used constitutes a total integrated luminosity of 2.12 fb^{-1} after data quality checks. The dielectron channel result is presented and combined with the equivalent 1.21 fb^{-1} dimuon channel result for the Z'. Additionally these results are combined with the 2.12 fb^{-1} diphoton channel result for the RS Graviton. The greatest excess in the dielectron channel is observed at 580 GeV with a significance of 1.34 σ. Therefore as no significant excess is observed in data above the Standard Model expectation, exclusion limits are set at 95% confidence level on the cross section times branching ratio for various signal scenarios as a function of resonance mass. A combined lower mass limit of 1.96 TeV is set on the Z'_{SSM}, and 1.95 TeV for a Randall-Sundrum Graviton with $\mathrm{k}/\overline{M}_{Pl} = 0.10$. These limits represent the world's highest observed mass exclusion for the models considered, at the time of writing this thesis.

Acknowledgements

I would like to start by thanking my wonderful supervisor Dr Tracey Berry, who has supported me throughout my PhD, and always thought about my future.

I would also like to thank the Science and Technology Facilities Council (STFC) for their financial support during my PhD, as well as Royal Holloway, and the Institute of Physics (IOP) for providing funding for several important conferences that I attended to present my work.

Acknowledgements must also go to Dr Pedro Teixeira Dias, Prof Glen Cowan, Dr Veronique Boisvert, Dr Stephen West, and Dr Simon George, for their continual help and presence, as well as honest and direct advice. At CERN I would like to thank my electron buddy Sarah Heim for those long nights we spent debugging code and understanding our analysis, and Dr Ricardo Goncalo for being a superb surrogate supervisor for the time I was based in Geneva. At Royal Holloway, I would to thank Dr Sudan Paramesvaran for his early support and friendship, as well as Dr Fabrizio Salvatore, Dr Neil Cooper-Smith, Dr Tina Potter, and Dr Matthew Tamsett, for being there to answer all of the silly questions a new PhD student has. Lastly, I would like to thank my fellow PhD students, James Robinson, Thomas Aumeyr, Matthew Rose, and Richard D’Arcy, for the working, drinking, and fun that was had on our journey.

For my Parents, John and Anita Hayden.

All these moments will be lost in time, like tears in rain.

- Blade runner

Contents

Preface

At the end of March 2010, the LHC entered the history books by colliding protons at a centre of mass energy equal to 7 TeV, more than any human made experiment before it. This signalled the start of a long journey into the unknown for particle physics, where discovery or exclusion of new physical phenomena will be brought into sharp clarity for the next $+20$ years. The elusive Higgs boson for which the LHC was arguably built, will be a flagship analysis not just for a final test of the Standard Model of particle physics, but also for pointing theorists and experimentalists alike, in the direction of what comes next, physics beyond the Standard Model.

As precise as the Standard Model is at describing three of the four known forces of nature, a GUT scale theory, and a theory that incorporates Gravity into our understanding of the Universe, are still missing. This thesis presents a search for possible new physics beyond the Standard Model, which could be a signature of such theories, via the discovery of new heavy neutral resonances, which would be evident in the invariant mass spectrum measured by the ATLAS detector.

This thesis is organised in the following way:

- Chapter 1 starts by briefly summarising the Standard Model of particle physics, including electroweak symmetry breaking and the Higgs boson. It then proceeds to set out the theory and motivation for new physics beyond the Standard Model which could be present at the TeV scale, and thus observable at the LHC. The chapter closes by considering the experimental signature high mass resonances would leave in LHC experiments such as the ATLAS detector, and the search strategy that will be used in this thesis. Current exclusion limits on the models considered are provided from recent experiments, as well as theoretical constraints.
- Chapter 2 details the LHC performance and infrastructure, focusing on the ATLAS

detector, with attention given to the subsystems that are most important to the search of this thesis.

- Chapter 3 provides the relevant information for production and use of Monte Carlo simulations in this thesis, paying particular attention to the reconstruction and identification of electrons, due to their importance in the search analysis. A study of the ATLAS detector's electron energy resolution, and dielectron invariant mass resolution, using signal Monte Carlo, is also presented for its relevance in a narrow width resonance search.

- Chapter 4 takes the study of electrons in this thesis a step further by considering high E_T electron outliers in early data. This study attempts to understand the cause of, and rectify where possible, the rare anomalous calculation of electron energies, between different stages of the ATLAS trigger system.

- Chapter 5 details the event selection applied to data to search for new high mass neutral resonances in the dielectron channel, using the ATLAS detector. The selection criteria are motivated, and translated where needed into the equivalent criteria for Monte Carlo simulation, to ensure a precise comparison with data is achieved. A study of varying electron identification selection criteria is also provided.

- Chapter 6 explains how the Standard Model background estimate is obtained using Monte Carlo simulation, and data-driven methods where possible. This is of vital importance, as any comparison between data and Monte Carlo requires a high level of precision to be able to claim a discovery should an excess be observed in the data.

- Chapter 7 presents the results of the high mass resonance search in the dielectron channel, using an integrated luminosity of 2.12 fb^{-1}. This dataset was recorded during proton-proton collisions in 2011 at $\sqrt{s} = 7$ TeV. Data is compared to the Standard Model background estimate through a number of kinematic distributions. The dielectron invariant mass spectrum is used as the search distribution, in which new physics should become evident through a deviation from the Standard Model prediction.

- Chapter 8 accounts for the systematic uncertainties present in the analysis, providing studies for each based on signal and/or background contributions. These studies are summarised, and then used in the statistical treatment of the results.

- Chapter 9 interprets the search results using both Frequentist and Bayesian statistical techniques. The dielectron invariant mass spectrum is used to quantify the level of agreement between observed data, and the Standard Model prediction. In the absence of a significant excess, 95% confidence level exclusion limits are set on the cross section times branching ratio of the signal process decaying to two electrons. The dielectron channel search result is also interpreted in combination with the latest available dimuon and diphoton channel search results, looking for the same new physics phenomena with the ATLAS detector.

- Chapter 10 draws conclusions from the presented search analysis, and looks to the future prospects of new physics searches at the LHC.

Chapters 1, 2 and 3 are a description of the theoretical and experimental aspects relevant for the topic of this thesis, and were written based on a review of the relevant literature (theoretical and experimental papers, and technical reports). Section 3.5 contains a study of the electron energy resolution, and dielectron invariant mass resolution (and its impact on the search for narrow width resonances), which was devised and carried out by the author.

The author's original work is reported in Chapters 4, 5, 6, 7, and 9. The work in Chapter 4 was carried out by the author in the context of the ATLAS Trigger electron/photon performance working group, and was included in the Trigger Egamma 2009 Collision Studies internal note [1]. Chapters 5, 6, 7, and 9, describe the author's work on Exotic searches, carried out using methods and procedures which were devised in collaboration with colleagues in the ATLAS Exotics working group, and included in the journal papers [2, 3, 4].

Chapter 8 presents results that were obtained as part of the author's collaboration with members of the ATLAS Exotic physics groups, but were not conducted by the author personally; thus only a summary is given, with further details provided in the Appendix.

All plots and tables in this thesis were produced by the author, unless otherwise stated.

Chapter 1

Theory and Motivation

Particle physics is currently experiencing a golden age, with the start of the Large Hadron Collider (LHC) program and its suite of experiments, the search for a fundamental understanding of the Universe at the TeV scale is finally beginning to become a reality. The current Standard Model (SM) of particle physics has stood the test of time and experiment remarkably well for over 35 years, but now faces a crossroads. The search for the Higgs boson, one of the last missing pieces of the SM, will make or break the model as we know it in the next few years. Even if the Higgs boson is found however, there are still questions which the SM can not answer. These questions are left to theories Beyond the Standard Model (BSM), many of which should have observable consequences visible at the LHC.

1.1 The Standard Model of Particle Physics

The SM [5, 6] describes the forces and interactions between the elementary particles of nature. Developed throughout the mid-20th century, it reached its current form in the mid-1970's and has been very successful in its predictions, leading engineers and physicists to build ever more impressive experiments to test the theory and make precision measurements. In its current state, the SM incorporates the known elementary particles generally separated into two distinct groups called fermions (spin-$\frac{1}{2}$) and bosons (spin-1), as well as their interactions via the electromagnetic, weak, and strong, forces (gravity is yet to be included successfully). The SM fermions are described in Table 1.1, with the force propagating bosons described in Table 1.2.

For fermions, each matter particle has an antimatter counterpart. The 6 leptons are

Family	Charge	Generations		
	q	I	II	III
Quark	$\frac{2}{3}$	$m_u = 2.4$ MeV u Up Quark	$m_c = 1.29$ GeV c Charm Quark	$m_t = 172.9$ GeV t Top Quark
	-$\frac{1}{3}$	$m_d = 4.9$ MeV d Down Quark	$m_s = 100$ MeV s Strange Quark	$m_b = 4.19$ GeV b Bottom Quark
Lepton	-1	$m_e = 0.511$ MeV e Electron	$m_\mu = 105.66$ MeV μ Muon	$m_\tau = 1776.82$ MeV τ Tau
	0	$m_{\nu_e} < 2$ eV ν_e Electron Neutrino	$m_{\nu_\mu} < 0.19$ MeV ν_μ Muon Neutrino	$m_{\nu_\tau} < 18.2$ MeV ν_τ Tau Neutrino

Table 1.1: Main properties of the SM spin-$\frac{1}{2}$ fermions [7].

Force	Gauge Boson	Charge	Mass
Electromagnetism	γ Photon	0	0
Weak	$W^\pm$ W Boson	± 1	80.4 GeV
	Z Z Boson	0	91.2 GeV
Strong	g Gluon	0	0

Table 1.2: The SM forces and main properties of their corresponding spin-1 propagator bosons [7].

therefore accompanied by 6 antileptons, with opposite charge, which all interact via the electromagnetic and weak force. Alongside this, the 6 quarks are reflected in type by 6 antiquarks, which all feel the electromagnetic, weak, and strong force. Quarks are commonly denoted so that the u quark for example, is mirrored by the equivalent antiquark, $\overline{u}$, and so on. Additionally, quarks have a property called "colour", which can take three values: red, green, or blue. The colour of quarks becomes important when attempting to understand the way in which quarks interact and bind together through the strong force, to form the composite particles seen in nature. Quark composite particles fall into two categories: Mesons, which are composed of a quark-antiquark pair, and Baryons, which consist of three quarks (or antiquarks). The most commonly known quark composite particles are the proton and neutron, which are baryons of the form (uud), and (ddu) respectively. Without the inclusion of colour, it would seem that the existence of baryon states with three same type quarks was forbidden by application of Pauli's Exclusion Principle (which states that no two fermions can exist in the same space with identical quantum states). This is because though the spin projections of two of the quarks could be different i.e. $+\frac{1}{2}$, $-\frac{1}{2}$ respectively, the third quark would have to match one of the other two quarks' quantum numbers. With the inclusion of colour however, each of the three quarks in a baryon has a different colour and thus do not violate Pauli's exclusion principle. The only requirement then is that all composite particles are "colourless" as this property is not directly observed in nature. Therefore, mesons are made of a quark-antiquark pair with respective colour-anticolour making it colourless (e.g. red and antired), and baryons are made of three coloured quarks (or antiquarks) so that red, green, and blue (or their anticolour equivalent) together are deemed colourless. When in 1962 the Ω^- (sss) was observed at Fermilab, this was proof that indeed colour was a necessary part of the SM.

Each force in the SM has one or more associated mediator boson particles. For electromagnetism this is the photon, for the weak force there is the neutral current-exchanging Z^0 boson, and the charged current-exchanging $W^\pm$ bosons, and the strong force is mediated via colour-charge exchanging gluons (each gluon holds two colour charges). If gravity turns out to be a force of the same ilk as the other three known forces of nature (and not for instance just an effect of space-time geometry) then it too should have an associated mediator particle, called the Graviton. These force propagating particles all have integer spin, and being bosons (obeying Bose-Einstein statistics) are not subject to

Pauli's exclusion principle as was described for fermions (which obey Fermi-Dirac statistics). It should be noted at this point that composite particles such as mesons, which are made up of an even number of fermions and thereby have integer spin, are technically bosons (baryons are not composed of an even number of fermions, and are therefore still fermions). Bosons like fermions, have antiparticle counterparts, however, certain bosons such as the photon, and Z^0 boson, have the interesting characteristic of being identical and indistinguishable from their antiparticle.

Counting the number of elementary particles discussed so far, there are the 12 leptons, and 12 quarks, that make up the fermionic particles. In addition, there is also 1 photon from electromagnetism, 3 particles from the weak interaction (Z^0, W^+, W^-), and 8 gluons from the strong interaction (taking colour-charge permutations into account), for the bosonic particles. These 36 elementary particles of the SM are theoretically joined by at least one Higgs boson as will be discussed in Section 1.1.3. Additional particles beyond this are not within the scope of the SM, and are thus predicted by BSM theories. Such particles might arise from BSM theories that predict as yet unknown symmetries, like the Z', which will be discussed in Section 1.2.1, or a new understanding of gravity, via the Graviton, which will be discussed in Section 1.2.2.

1.1.1 The Lagrangian and Gauge Invariance

The information contained within the SM can be summarised using Lagrangian mechanics, and Hamilton's principle of stationary action which states that physical systems evolve such that the Action, $\mathcal{S}$, defined in Equation (1.1), is minimised ($\delta\mathcal{S} = 0$). The Lagrangian, L, is defined as the kinetic energy of a system, T, minus its potential energy, V, and depends on time, t, as well as the generalised spatial coordinate, q_i (where i = 1,2,3,...,n dimensions) and its time derivative, $\dot{q}_i$. These conditions make it possible to obtain a system's equations of motion using the Euler-Lagrange Equation (1.2).

$$\mathcal{S}(q_i) = \int L(q_i, \dot{q}_i, t)\, dt \tag{1.1}$$

$$\frac{d}{dt}\left(\frac{\delta L}{\delta \dot{q}_i}\right) = \frac{\delta L}{\delta q_i} \tag{1.2}$$

These equations are used to describe particles in a localised way, depending on position in space and time. However, in particle physics the SM is described using Quantum Field Theory (QFT), which uses field variables (ϕ_i) that are a function of the former coordinates giving, $\phi_i(x^\mu)$ (for a scalar field), where x^μ is a space-time 4-vector (μ: 0 = ct, and 1,2,3...,n spatial dimensions). This transforms the Lagrangian into the Lagrangian Density (also usually called Lagrangian for simplicity) as shown in Equation (1.3) and implies an integration over all space-time to obtain the corresponding Action in Equation (1.4), leading to a generalised form of the Euler-Lagrange Equation (1.5) [8].

$$L(q_i,\dot{q}_i,t) \rightarrow \mathcal{L}(x^\mu,\phi_i,\delta_\mu\phi_i) \tag{1.3}$$

$$\mathcal{S}(\phi_i) = \int \mathcal{L}(x^\mu,\phi_i,\delta_\mu\phi_i)\; d^4x \tag{1.4}$$

$$\delta_\mu\left(\frac{\delta\mathcal{L}}{\delta(\delta_\mu\phi_i)}\right) = \frac{\delta\mathcal{L}}{\delta\phi_i} \tag{1.5}$$

It is possible to describe the entire SM with one Lagrangian which is presented in Equation (1.6) using Yang-Mills theory. This powerful equation can be separated into the specific constituent components of the SM described in the proceeding sections of this chapter. The $G^a_{\mu\nu}G^{\mu\nu a}$ term describes the field strength of the strong force, while the terms $W^a_{\mu\nu}W^{\mu\nu a}$ and $B_{\mu\nu}B^{\mu\nu}$, correspond to the weak and electromagnetic force field strength respectively (see Section 1.1.2 for more details on forces). Other terms in the Lagrangian denote the gauge covariant derivative, D_μ, and complex Higgs scalar field, ϕ, where the term $|D_\mu\phi|^2$ then describes the Higgs kinetic terms (Section 1.1.3), and $\overline{\psi}D_\mu\psi$ describes the electromagnetic kinetic terms. Finally, $V(\phi)$ adds the Higgs potential to the SM and $\lambda\overline{\psi}\psi\phi$ incorporates the mass term for quarks and leptons.

$$\mathcal{L}_{SM} = -\frac{1}{4}G^a_{\mu\nu}G^{\mu\nu a} - \frac{1}{4}W^a_{\mu\nu}W^{\mu\nu a} - \frac{1}{4}B_{\mu\nu}B^{\mu\nu} + |D_\mu\phi|^2 + \overline{\psi}D_\mu\psi - V(\phi) + \lambda\overline{\psi}\psi\phi \tag{1.6}$$

A requirement imposed on the SM Lagrangian is that it be gauge invariant under global and local transformations. To describe the gauge invariance of $\mathcal{L}_{SM}$, group theory can be used to form symmetry groups (a Lie group) resulting in Equation (1.7). This describes the gauge transformations under which the strong ($SU(3)_c$), weak ($SU(2)_L$),

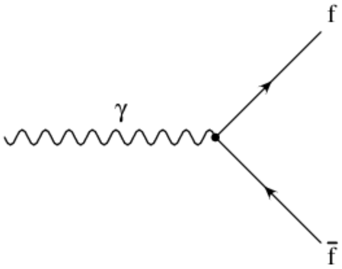

Figure 1.1: Fundamental QED interaction vertex between photons and fermions.

and electromagnetic ($U(1)_Q$) forces are invariant, where $U(n)$ is a unitary matrix with n^2 unitary matrices (generators), and $SU(n)$ are special unitary groups with determinant equal to unity and n^2-1 generators.

$$SU(3)_c \times SU(2)_L \times U(1)_Q \tag{1.7}$$

1.1.2 Forces

Quantum Electrodynamics

Quantum Electrodynamics (QED) is the gauge theory of electromagnetism, and describes the interactions between charged fermions and the massless spin-0 field associated with the photon. The photon arises from the conservation of electric charge under local gauge transformations of fermions described by the $U(1)_Q$ symmetry group, which leads to the exchange of a massless gauge boson. As QED is an abelian[1] theory with the photon having no charge, there are no self interaction terms. The fundamental vertex interaction between photons and fermions is displayed in Figure 1.1 using a Feynman diagram[2]. Electromagnetism has an infinite interaction range via the photon propagator. However the coupling strength, $\alpha(r)$, decreases with distance from a charge according to Coulomb's law which goes as $1/r^2$, meaning there is effectively a limited interaction range for large distances.

---

[1] Abelian theories are commutative, that is to say, the result is not dependent on the order in which operations are applied between two elements.

[2] All Feynman diagrams in this thesis use the convention for direction of time from left to right.

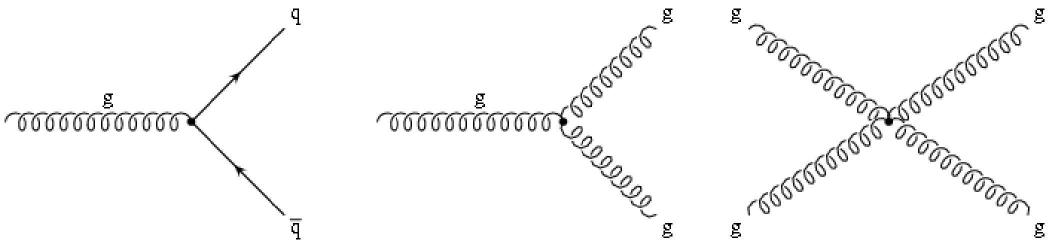

Figure 1.2: Fundamental vertex for QCD interactions. The gluon interaction with quarks (left), self-coupling triple gauge (middle), and self-coupling quadruple gauge (right), are all displayed.

Quantum Chromodynamics

Quantum Chromodynamics (QCD) is the gauge theory associated with the strong nuclear force, describing colour interactions between quarks and gluons. The $SU(3)_c$ symmetry group with $n^2 - 1$ generators, gives rise to 8 massless gluons which conserve colour symmetry under local gauge transformations. This non-abelian theory includes self interaction terms of the field due to gluons each carrying (2×) colour charge. As the gluon is self-interacting, three fundamental vertex interactions exist involving the gluon: two self-interacting, and one between gluons and quarks (Figure 1.2). The strong coupling, $\alpha_S(r)$, describes the strength of the strong interaction, which varies greatly with distance from a colour charge. With decreasing distance the interaction strength between quarks decreases, approaching asymptotic freedom. With increasing distance however, the strength of the interaction grows steeply, becoming constant at distances larger than the size of a hadron. This is called colour confinement, and implies that it is not possible to observe free quarks, which can be explained by understanding that the force between two quarks at large distances is enough to create $q\overline{q}$ pairs. The range of the strong force can therefore be estimated using the mass of the force's pseudo-mediator, the pion (because it is the lightest meson), and Heisenberg's uncertainty principle, to give a range of ~1 fm.

The Weak Force and Electroweak Unification

The weak force is the third interaction incorporated into the SM. It is responsible for most types of radioactive decay, and has the unique properties of being able to change quark flavour, as well as violate Charge Parity (CP) symmetry. The $SU(2)_L$ symmetry associated with the weak force conserves weak isospin, I_3, for fermions under local gauge transformations (lepton number is also conserved). The gauge bosons arising from this symmetry are the neutral current interaction Z^0 boson, and the charged current interaction

$W^{\pm}$ bosons (fundamental vertices for weak interactions involving leptons (Figure 1.3), and quarks (Figure 1.4) are displayed). The $W^{\pm}$ bosons are what make quark Flavour Changing Charge Current (FCCC) interactions possible, coupling to the physical states of the u, c, and t quarks, but importantly the rotated eigenstates d', s', and b'. The Cabibbo Kobayashi Maskawa (CKM) matrix [9, 10] (Equation (1.8) for latest values from [7]) then relates these "weak interactions states" to the d, s, and b quark physical states, and describes their relative coupling, controlling the 9 possible flavour changing transformations. For example, the $|V_{ud}|$ term takes part in neutron beta decay: $n \rightarrow p + e^{-} + \overline{\nu_e}$, where a down quark from the neutron decays into an up quark, yielding a proton with the emission of a W^{-} boson, which subsequently decays into e^{-} and $\overline{\nu_e}$. CP violation can be incorporated into the SM by including a complex phase in the CKM matrix. So called Flavour Changing Neutral Current (FCNC) interactions however, are not observed experimentally and forbidden in the SM.

$$V_{CKM} = \begin{pmatrix} V_{ud} & V_{us} & V_{ub} \\ V_{cd} & V_{cs} & V_{cb} \\ V_{td} & V_{ts} & V_{tb} \end{pmatrix} = \begin{pmatrix} 0.97428 \pm 0.00015 & 0.2253 \pm 0.0007 & 0.00347^{+0.00016}_{-0.00012} \\ 0.2252 \pm 0.0007 & 0.97345^{+0.00015}_{-0.00016} & 0.0410^{+0.0011}_{-0.0007} \\ 0.00862^{+0.00026}_{-0.00020} & 0.0403^{+0.0011}_{-0.0007} & 0.999152^{+0.000030}_{-0.000045} \end{pmatrix} \tag{1.8}$$

The difference with the mediating particles of the weak force, as opposed to the photon in QED, and gluons of QCD, is that the associated gauge bosons are massive. These masses have been precisely measured (Table 1.2), with latest mass estimates for the Z^0 boson of 91.2 GeV, and 80.4 GeV for the $W^{\pm}$ bosons. Due to the massive nature of these gauge bosons, the weak force has an extremely short interaction range, with the weak coupling constant, α_W, decreasing as $(1/r)e^{-m_{W,Z}r}$, limiting the effective range of the force to less than 0.1% of the diamater of a proton (much less than even the strong force). Being a non-abelian theory like QCD, and unlike QED, the weak force gauge bosons also have self-interaction terms as shown in Figure 1.5.

In 1979, Glashow [11], Weinberg [12], and Salam [13], won the Nobel prize in physics for their work on the unification of the weak and electromagnetic interactions under one theory called the electroweak interaction. At low energy the $SU(2)_L$ and $U(1)_Q$ symmetries of the weak and electromagnetic forces are effective theories, however they can be considered as one force above the electroweak unification energy of ~246 GeV. This

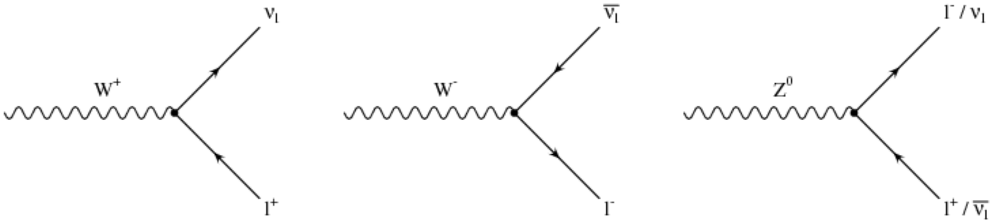

Figure 1.3: Fundamental vertices for weak interactions involving leptons.

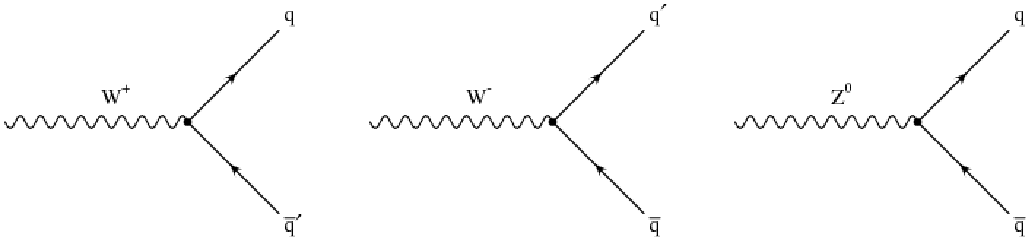

Figure 1.4: Fundamental vertices for weak interactions involving quarks.

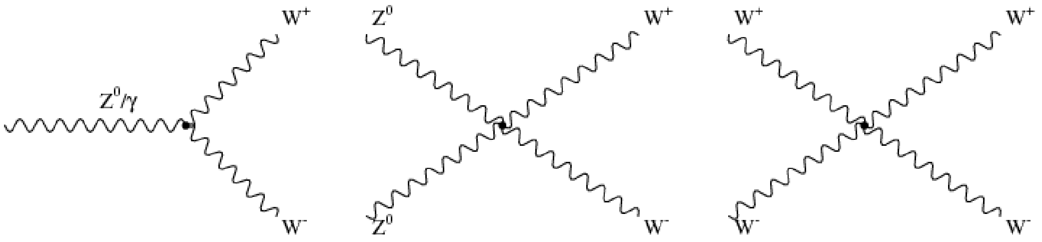

Figure 1.5: Fundamental vertices for electroweak gauge boson self interactions.

interaction has the symmetry $SU(2)_L \times U(1)_Y$, with $SU(2)_L$ conserving I_3, and $U(1)_Y$ conserving weak hypercharge, Y, under local gauge transformations. These quantities are then related to a particle's charge given Equation (1.9), which is thereby indirectly conserved. Under electroweak theory, left handed fermions interact via $SU(2)_L \times U(1)_Y$, whereas right handed fermions only interact through $U(1)_Y$.

$$Q = I_3 + Y \tag{1.9}$$

The conserved symmetries of electroweak theory give rise to four gauge bosons, namely: W^0, W^1, W^2 from $SU(2)_L$, and B^0 from $U(1)_Y$. The $W^{\pm}$ bosons then arise from the mixing of W^1 and W^2 as shown in Equation (1.10). The photon and Z^0 boson are generated from the mixing of B^0 and W^0 as shown in Equation (1.11) and (1.12) respectively, where θ_w is the weak mixing angle. This angle is an electroweak parameter depending on the ratio of m_W and m_Z as shown in Equation (1.13).

The problem with electroweak theory is that the four gauge bosons associated with the conserved symmetry, should be massless. This does not reflect experimental observations as the weak gauge bosons are known to be massive. Therefore to generate their mass, electroweak symmetry must be broken.

$$W^{\pm} = \frac{W^1 \pm iW^2}{\sqrt{2}} \tag{1.10}$$

$$\gamma = \sin\theta_w W^3 + \cos\theta_w B^0 \tag{1.11}$$

$$Z^0 = \cos\theta_w W^3 - \sin\theta_w B^0 \tag{1.12}$$

$$\cos\theta_w = \frac{m_W}{m_Z} \tag{1.13}$$

1.1.3 Electroweak Symmetry Breaking and the Higgs Mechanism

The gauge bosons arising from the symmetries of the SM are required to have zero mass. This is not a problem for the photon in QED, or the gluons of QCD, which are indeed massless. However, the weak gauge bosons are experimentally observed to have mass, which implies that electroweak symmetry must be broken. One possible explanation put forward by Peter Higgs in 1964 [14], predicts the existence of a new complex doublet of scalar fields with the form shown in Equation (1.14), called the Higgs field.

$$\phi = \begin{pmatrix} \phi^+ \\ \phi^0 \end{pmatrix} \quad , \text{ where } \quad \begin{array}{c} \phi^+ = \phi_1^+ + i\phi_2^+ \\ \phi^0 = \phi_3^0 + i\phi_4^0 \end{array} \tag{1.14}$$

Unlike other fields mentioned so far, the Higgs field has a non-zero vacuum expectation value (vev), evident by the form of the Higgs potential, $V(\phi)$, in Equation (1.15) and graphically displayed in Figure 1.6. In the early Universe before the energy scale at which electroweak symmetry is broken, all gauge bosons are massless and $SU(2)_L \times U(1)_Y$ holds. This is because the Higgs field can be in many possible states with an average value of zero ($\phi = 0$). As the local potential decreased over time with the expansion of the Universe and subsequent cooling temperatures, the shape of the Higgs potential means that it can no longer have an average value of zero. When the local potential meets the Higgs potential at $\phi = 0$ (see Figure 1.6), the Higgs field must choose a direction away from $\phi = 0$ to reach its non-zero vev at $\phi = v$, the local potential minimum[3]. This spontaneously breaks electroweak symmetry as local gauge transformations are no longer invariant in the plane of the direction away from $\phi = 0$. This represents a breaking of $SU(2)_L \times U(1)_Y$ to $U(1)_Q$ (as there is still a symmetry at the vev about the potential axis). The subsequent fields and their interactions lead to the massive weak gauge bosons, massless photon, and massive scalar Higgs boson, which are able to be understood by counting the available Degrees Of Freedom (DOF) before and after spontaneous Electroweak Symmetry Breaking (EWSB) as presented in Table 1.3.

$$V(\phi) = -\mu^2\phi^2 + \lambda\phi^4 \tag{1.15}$$

To give all quarks and leptons their masses, terms of the type $\lambda\overline{\psi}\psi\phi$ are added to $\mathcal{L}_{SM}$, so that the fermion field, ψ, interacts with the Higgs field through a Yukawa coupling with an unknown coupling strength, λ. Each fermion has an associated coupling to the Higgs field which determines the individual particle mass.

Unfortunately the Higgs boson has not yet been observed, and as the exact mass, m_H, is not predicted by the theory, it will have to be determined experimentally. Constraints

---

[3] The position of the vev is determined by the parameters μ and λ through, $<\phi>= \sqrt{\frac{-\mu^2}{\lambda}} = v$.

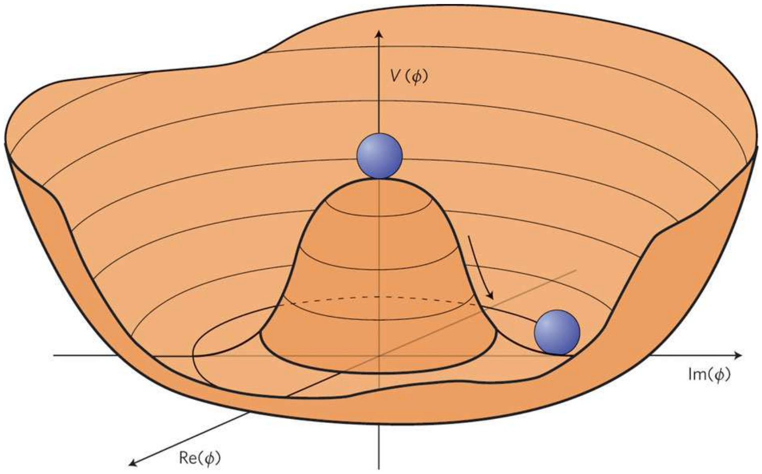

Figure 1.6: Graph displaying the form of the Higgs potential (Equation (1.15)) for $\mu^2 < 0$, $\lambda > 0$. Electroweak symmetry is spontaneously broken when the Higgs field must move away from its non-zero vev to reach a minima [15].

Key	
Type	DOF
Massive	3
Massless	2
Scalar	1

Before EWSB			
Field	Boson	Type	DOF
$W^{1,2}$	W^+, W^-	Massless	4
W^0, B^0	Z^0, γ	Massless	4
$\phi^+_{1,2}$	$\phi^+_{1,2}$	Scalar	2
$\phi^0_{3,4}$	$\phi^0_{3,4}$	Scalar	2
Total			12

After EWSB			
Field	Boson	Type	DOF
$W^{1,2}$, $\phi^+_{1,2}$	W^+, W^-	Massive	6
W^0, ϕ^0_3	Z^0	Massive	3
B^0	γ	Massless	2
ϕ^0_4	H^0	Scalar	1
Total			12

Table 1.3: Counting degrees of freedom before and after electroweak symmetry breaking. Before EWSB, all gauge bosons are required to be massless which does not reflect experimental results. After EWSB, the weak gauge bosons have “eaten” degrees of freedom from the Higgs field, generating their mass and leaving a single scalar particle, H^0, which is associated with the Higgs boson.

can be placed on m_H both by using observed data from experiment, and theory constraints on unitarity from $W^+W^- \to W^+W^-$ longitudinal scattering, which sets an upper limit of $m_H \simeq 1$ TeV [16, 17]. The latest official constraints on the Higgs boson mass at time of writing this thesis, come from the LHC which has an ATLAS combined channel result using 4.9 fb^{-1} of integrated luminosity [18]. This search excludes most Higgs boson masses at 95% confidence level, leaving only small windows open from 115.5 GeV to 131 GeV, and 237 GeV to 251 GeV. Furthermore, tantalising hints have been seen by both the ATLAS and CMS experiments at ∼126 GeV, which within one year could lead to the discovery of the Higgs boson, if it indeed exists at that mass.

If the Higgs boson is found, as well as completing the SM it will help BSM searches. The mass of the Higgs boson can be an indicator for the scale at which new physics is needed. Considering a purely SM Higgs boson at the current most likely mass of 126 GeV in Figure 1.7, and extrapolating conservatively, new physics is expected to manifest itself at or before the energy scale, $\Lambda = 10{,}000$ TeV. This does mean that new physics might not be visible at the LHC (which has a maximum $\sqrt{s} = 14$ TeV) given a SM Higgs boson at this mass, but certainly does not indicate the so called "desert" scenario for new physics which a Higgs boson mass around ∼160 GeV would predict. Higgs boson or no Higgs boson, this is an exciting time in particle physics, and the next section will deal with the theory and motivation for possible new physics BSM.

1.2 Neutral Resonances Beyond the Standard Model

Many BSM theories predict new neutrally charged resonances at the TeV scale as a consequence. Various Grand Unified Theories (GUT), as well as most supersymmetric models, and some varieties of string theory, all contain a new spin-1 particle often called the Z' [20]. The source and implications of such a particle will be discussed in Section 1.2.1. Other BSM theories seeking to answer questions such as the so called "hierarchy problem", through supersymmetry or extra spatial dimensions, involve the addition of a new spin-2 tensor boson attributed to the Graviton (G^*). The topic of Extra Dimensional Models (EDM), with specific focus on the Randall-Sundrum (RS) model will be dealt with in Section 1.2.2. Both of these new physical phenomena would appear as high mass neutral resonances in the invariant mass spectrum measured by the ATLAS detector at the LHC,

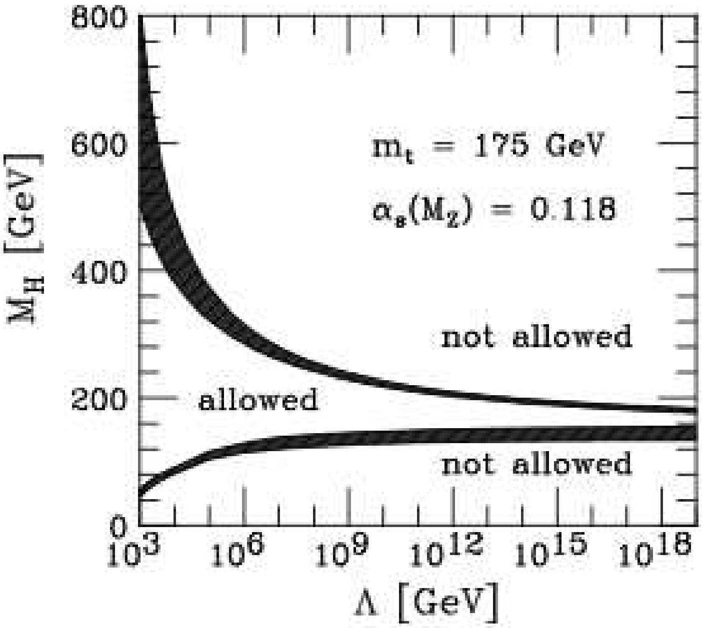

Figure 1.7: SM Higgs boson mass versus new physics energy scale, Λ. The upper limit comes from upper theoretical constraints on λ, and the lower limit describes the vacuum stability condition, requiring $\lambda > 0$. Dark bands show the impact of various uncertainties [19].

possibly ushering in a new era of discovery for particle physics, and a deeper understanding of the Universe.

1.2.1 Heavy Gauge Bosons

One of the best motivated extensions to the SM is the addition of a $U(1)'$ symmetry, with an associated Z' gauge boson. This is because it appears as a useful consequence (or extension in the case of supersymmetry) of many other theories, such as the breaking of non-abelian factors in an extended gauge group GUT, extra dimensional propagation of the SM Z^0, or a balancing of the supersymmetric Higgs boson mass in some models. An initial problem is that there is no a priori reason to suggest that the Z' mass should be at the TeV scale, and thus visible at the LHC. However, in the context of string theory, supersymmetry, and GUTs, the breaking of this extra $U(1)'$ symmetry is often linked to the electroweak or soft supersymmetry breaking scale, which would imply that the Z' could indeed have a mass around the TeV scale. Furthermore, in the motivation of this search, the implications of a Z' gauge boson go far beyond the discovery of a new $U(1)'$ symmetry. It would predict an extended Higgs sector as the SM Higgs boson does not couple to Z', possibly an extended neutrino sector in symmetric models, new exotic fermions for anomaly cancellations, possible FCNC interactions in string derived models with non-universal family charge, not to mention being perfect to study for its decay properties in the search for other heavy exotic or supersymmetric particles.

Extending the neutral current sector would imply mass and kinetic mixings between the SM Z^0 and BSM Z', due to on mass shell renormalisation and the extra abelian $\mathcal{L}$ terms [21]. Equation (1.16) shows the relation between mass eigenstates Z_1, Z_2, and associated gauge bosons. The gauge boson masses, and through association the weak mixing angle θ_W, are then related to the gauge boson mixing angle θ_M through Equation (1.17). With large datasets of $O(100\text{ fb}^{-1})$, deviations from the SM predicted M_{Z^0}, and θ_W, would then be indicative of a Z'. For Z' models considered in this thesis, the limit $M_{Z'} \gg M_{Z^0}$ is used so that Z^0-Z' mixing is suppressed, implying $M_1^2 \sim M_{Z^0}^2$ and $M_2^2 \sim M_{Z'}^2$. Interference terms between γ-Z^0-Z' would also arise from the cross terms of process amplitudes, but are deemed negligible in an early search such as this.

$$\begin{pmatrix} Z_1 \\ Z_2 \end{pmatrix} = \begin{pmatrix} \cos\theta_M & \sin\theta_M \\ -\sin\theta_M & \cos\theta_M \end{pmatrix} \begin{pmatrix} Z^0 \\ Z' \end{pmatrix} \tag{1.16}$$

$$\tan^2\theta_M = \frac{M_{Z^0}^2 - M_1^2}{M_2^2 - M_{Z^0}^2} \tag{1.17}$$

The Sequential Standard Model (SSM) [20] is used as a benchmark model for the Z' and has the main feature of predicting the same coupling to SM fermions as the Z^0. In this model the SM gauge group: $SU(3)_c$ x $SU(2)_L$ x $U(1)_Y$, is extended by arbitrarily adding an extra $U(1)'$ gauge symmetry, the breaking of which results in the Z'. However, in this simplified model there are many problems which would prevent the Z' from being a part of nature, unless it had different couplings to exotic fermions, or was the extra dimensional excitation of the SM Z^0. Nevertheless, as an entry point model the Z'_{SSM} is often used as a benchmark for comparison between experiments, and will therefore be included in the search of this thesis.

One of the simplest well motivated models involving a Z' is the Left-Right Symmetric Model (LRM) [20], where a right-handed gauge group is added to the electroweak sector of the SM, restoring parity at high energy by replacing $SU(2)_L$ with $SU(2)_L$ x $SU(2)_R$, and $U(1)_Y$ with $U(1)_{B-L}$. This model comes from the decomposition of the $SO(10)$ GUT such that: $SO(10) \rightarrow SU(3)_c$ x $SU(2)_L$ x $SU(2)_R$ x $U(1)_{B-L}$, where $SU(2)_L$ is the SM, and $SU(2)_R$ x $U(1)_{B-L}$ gives rise to the W'^{+}, W'^{-}, and Z', additional gauge bosons[4].

In a similar way, alternative LRMs can arise naturally as a subgroup of E_6 GUT models [20, 22, 23, 24] which involve two extra $U(1)'$ that occur through the decomposition $E_6 \rightarrow SO(10) \times U(1)_\psi \rightarrow SU(5) \times U(1)_\chi \times U(1)_\psi$ (where $SU(5)$ is the gauge group containing the SM suggested by Georgi and Glashow in 1974 [25]). The mixing of these extra $U(1)'$ symmetries lead to the Z' as shown in Equation (1.18), where the mixing angle θ determines the coupling to fermions and results in various possible models with specific Z' states (see Table 1.4). These E_6 motivated states, namely: Z'_ψ, Z'_N, Z'_η, Z'_I, Z'_S and Z'_χ, are included in the search of this thesis.

$$Z'(\theta) = Z'_\psi cos\theta + Z'_\chi sin\theta \tag{1.18}$$

State	Z'_ψ	Z'_N	Z'_η	Z'_I	Z'_S	Z'_χ
θ (°)	0	75.5	127.8	37.8	23.3	90

Table 1.4: Various E_6 motivated Z' models where the coupling to SM fermions depends on mixing angle θ. The models from left to right read: ψ model, neutral model, η model, inert model, secluded sector model, and χ model.

The Z' cross section is inversely proportional to its width, therefore if exotic decay modes are kinematically possible as well as the SM decay channels, the Z' width will become larger, and more significantly, the branching ratios to conventional fermions smaller. This fact would be less important at an e^+e^- or ep collider where the process would proceed via virtual Z' particles, however at the LHC this becomes important as the signal relies on Drell-Yan production of real Z' particles. The theoretical dependence on the cross section, σ, times branching ratio, B, for $\sigma(pp \rightarrow Z') \cdot B(Z' \rightarrow e^+e^-)$ as a function of Z' mass at the LHC is shown in Figure 1.8, for all Z' models considered in this thesis. Bear in mind that in reality the lepton (e, μ, τ) branching ratio fraction, $B \equiv \Gamma(Z' \rightarrow l^+l^-)/\Gamma_{tot}$, is model dependent and as previously noted will depend on the contribution of exotic fermions and supersymmetric partners to the Z' width. In general the Z' coupling to SM fermions is assumed to be generation independent, and triple gauge couplings often not quoted as they strongly depend on both the model and degree of gauge mixing.

Previous direct searches for the Z' include those done by CDF and D0 at the Tevatron,

---

[4] $U(1)_{B-L}$ has Baryon minus Lepton number conservation. This is related to hypercharge via: $Y = T_{BL} + T_{3R}$, where T_{3R} occurs in LRM models and symmetry breaking to $U(1)_Y$ occurs at a scale $m_{Z'} \gg m_{Z^0}$.

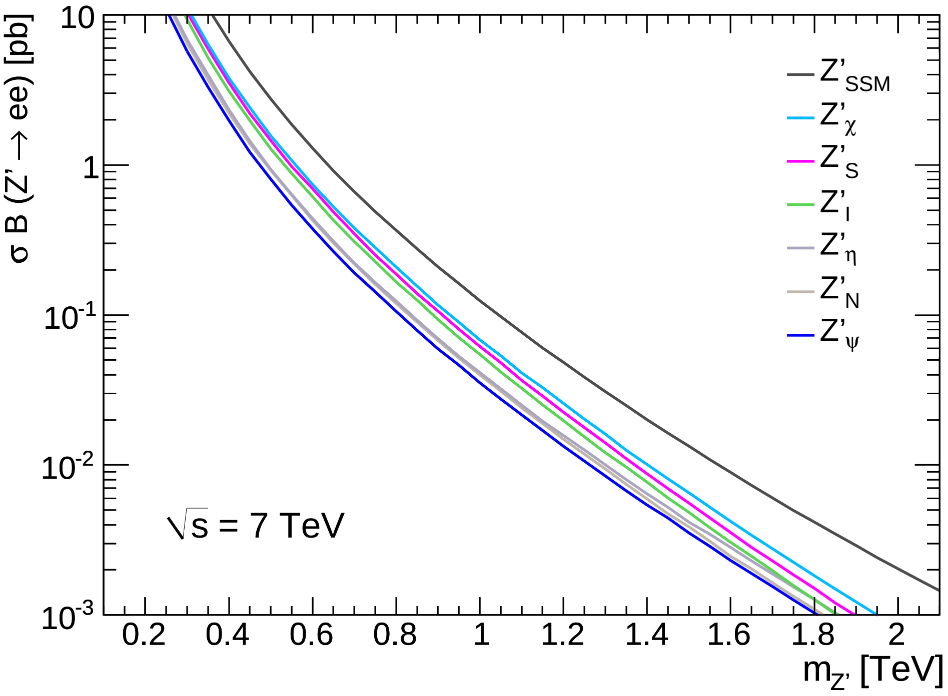

Figure 1.8: The expected cross section times branching ratio (σB) to e^+e^-, as a function of Z' mass, for the $Z'_{\rm SSM}$ and various E_6 motivated Z' states at the LHC ($\sqrt{s}$ = 7 TeV). Cross sections were calculated using PYTHIA, with 10,000 events per mass point per Z' model.

and more recently dominated by the ATLAS and CMS experiments at the LHC. The current lower mass limits on various Z' models from these experiments can be found in Table 1.5.

1.2.2 Extra Dimensional Models

It is only within perhaps the last 10 years that theories BSM involving extra dimensions have started to be taken seriously. The pioneering work done by Arkani, Dimopoulos, and Dvali (ADD) [30] showed that the inclusion of extra dimensions in a Universe which we currently understand to only have 1 time and 3 spatial dimensions, can beautifully resolve some of the outstanding problems in particle physics today not answered by the SM. This sparked many others to start using extra dimensions in their models, often with surprising and exciting results. A few selected examples [31] of the implications that extra spatial dimensions could have on our understanding of physics are: resolution of the hierarchy problem [30, 32], EWSB without a Higgs boson [33], an understanding of the SM fermion mass hierarchy [34], a TeV scale GUT that also suppresses proton decay [35], new dark matter candidates [36], and possible black hole production at TeV scale experiments [37].

Model	Observed Exclusion Limit (TeV)									
	ATLAS		CMS		CDF		D0		Highest	
	ee	ee+$\mu\mu$	ee	ee+$\mu\mu$	ee	ee+$\mu\mu$	ee	ee+$\mu\mu$	ee	ee+$\mu\mu$
Z'_{SSM}	1.70	1.83	1.73	1.94	0.96	0.97	1.02	-	CMS	CMS
Z'_{ψ}	-	1.49	1.44	1.62	0.85	0.85	0.89	-	CMS	CMS
Z'_{N}	-	1.52	-	-	0.84	0.84	0.87	-	D0	ATLAS
Z'_{η}	-	1.54	-	-	0.88	0.93	0.92	-	D0	ATLAS
Z'_{I}	-	1.56	-	-	0.74	0.74	0.77	-	D0	ATLAS
Z'_{S}	-	1.60	-	-	0.79	0.80	0.82	-	D0	ATLAS
Z'_{χ}	-	1.64	-	-	0.86	0.84	0.90	-	D0	ATLAS

Table 1.5: Observed lower mass exclusion limits for a Z' resonance, published by recent experiments. Limits are set at 95% confidence level for the models considered in this thesis. Results are the latest available at time of writing from: ATLAS [3], CMS [26], CDF [27, 28], and D0 [29].

The models concentrated on in this thesis are those that seek to address the so called hierarchy problem, introducing the ADD model and proceeding to search for high mass resonances in the RS model context. The hierarchy problem originates from the fact that the two known fundamental scales of nature are so different, namely the electroweak scale, $m_{EW} \sim 10^3$ GeV, and the (reduced[5]) Planck scale, $\overline{M}_{Pl} \sim 10^{18}$ GeV. This apparent $\mathcal{O}(15)$ scale difference seems “unnatural”, how so much of physics can involve interactions up to the TeV scale, with no other interesting phenomena up until the Planck scale where the coupling strength of gravity is theoretically unified with the other forces (and the GUT scale is somewhere in between). One mechanism that can help explain this apparent hierarchy however, are models which involve the presence of extra dimensions.

To understand the concept of extra dimensions, the 4D metric tensor that is currently used to describe our Universe, can be arbitrarily extended to 5D (see Equation(1.19)) while still requiring the invariant interval, $ds^2 = -\Delta t^2 + \Delta x^2 = g_{AB}dx^A dx^B$, where A and B are summed over all dimensions. The sign of this added dimension in the 5D metric tensor determines whether it is time-like (-), or space-like (+). Though both time-like and space-like extra dimensions are equally valid, for the want of avoiding causality complications due to negative mass particles (Tachyons), the extra dimension(s) is usually restricted to being space-like, and will therefore be considered as such for all models hence forth.

---

[5] Reduced Planck mass is often used as it simplifies a lot of equations in general relativity: $\overline{M}_{Pl} = M_{Pl}/\sqrt{8\pi}$.

$$g_{AB} = \begin{pmatrix} -1 & 0 & 0 & 0 & 0 \\ 0 & +1 & 0 & 0 & 0 \\ 0 & 0 & +1 & 0 & 0 \\ 0 & 0 & 0 & +1 & 0 \\ 0 & 0 & 0 & 0 & \pm 1 \end{pmatrix} \tag{1.19}$$

One can then instead consider a real massless scalar field in a flat 5D space, which is a solution of the 5D Klein-Gordon equation: $(\delta_A \delta^A)\Phi = (\delta_\mu \delta^\mu - \delta_y^2)\Phi(x,y) = 0$ (where y represents the extra dimension). The result is a seemingly infinite set of equations for a distinct collection of 4D scalar fields, ϕ_n, with masses, m_n, called a Kaluza-Klein (KK) tower (see Figure 1.9 for an example from the RS model). These towers can be understood as the quantised 4D excitations of a 5th dimensional particle's momentum, with $n = 0$ being a massless mode (the general relativity G^*), while $n > 0$ are massive G^* states, obtaining their mass in a manner similar to the Higgs-Goldstone mechanism. In most working models the extra dimension is "compact", i.e. of finite size (which is considered for all cases here) so that $0 \leq y \leq \pi L$, and the wavefunctions have boundary conditions pertaining to the size of the extra dimension which in turn space the KK tower masses as $m_n = n/L$. It turns out that there are no such solutions as described above for flat extra dimensions, however there do exist solutions for curled up extra dimensions with radius, R, so that there would now be periodic boundary conditions of the form: $0 \leq y \leq \pi R$, where $y = 0$, and $y = \pi R$, are the same points on a circle, and the KK masses are simply given by $m_n = n/R$ instead. This geometry is most simply described by a S^1/Z_2 orbifold.

The ADD model describes exactly this situation, with n extra compact spatial dimensions of radius, $R(n)$. In their model, they set the $4+n$ dimensional Planck scale, $M_{Pl(4+n)}$, to be the m_{EW} scale, enforcing this by requiring that: $\overline{M}_{Pl}^2 \sim M_{Pl(4+n)}^{2+n} R^n$, which fixes the size of the extra dimensions. It then follows that for two test masses within a distance $r \ll R$, the gravitational potential experienced follows Gauss's law in $4+n$ dimensions (Equation (1.20)), whereas the same test masses at $r \gg R$, no longer have gravitational flux lines penetrating into the extra dimensions, and so the potential is returned to the expected $1/r$ relation (Equation (1.21)).

$$V(r) \sim \frac{m_1 m_2}{M_{Pl(4+n)}^{n+2}} \frac{1}{r^{n+1}} \ , \ (r \ll R) \tag{1.20}$$

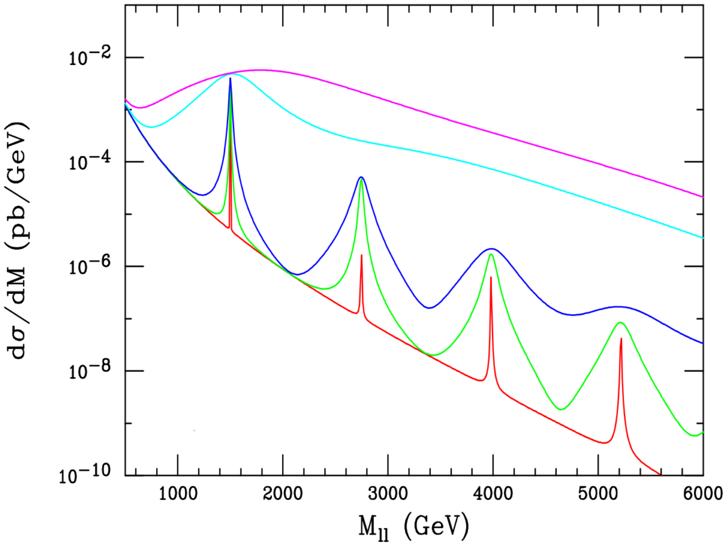

Figure 1.9: Differential cross section for a 1.5 TeV KK G^* and its subsequent tower states in the RS model context, decaying to leptons at the LHC. From upper to lower, the curves show the effect of increasing extra dimensional size on the width and distribution of tower states [38].

$$V(r) \sim \frac{m_1 m_2}{M_{Pl(4+n)}^{n+2} R^n} \frac{1}{r}\ ,\ (r \gg R) \tag{1.21}$$

Considering the cases of $n = 1$, 2, and 3, extra dimensional sizes of $R \simeq 10^{11}$ m, 10^{-3} m, and 10^{-9}m, are obtained respectively. $n = 1$ is therefore already excluded as it predicts deviations from general relativity on large scale distances which are not observed in experiment. $n = 2$ is on the scale at which experiments have recently started to probe with some considerable precision [39], setting exclusion limits close to ruling out $n = 2$ as a possibility. For $n > 2$, the size of the extra dimensions shrink to such small scales that they are currently impossible to directly probe. However, experiments at the LHC are continually setting constraints on ADD model parameters, looking for G^* emissions which would show up in the missing E_T spectrum, as the strength of the coupling to SM fermions in this model are suppressed by a $1/\overline{M}_{Pl}$ scale factor (Equation(1.22)). One problem with the ADD model is that it does not, in fact, truly solve the hierarchy problem, as much as it replaces it with another, i.e. $RM_{Pl(4+n)} \sim (\overline{M}_{Pl}^2/M_{Pl(4+n)}^2)^{1/n}$, which for small values of n, gives very large values. A model that boasts an attempt to truly solve the hierarchy problem, the RS model, will next be explored.

$$\mathcal{L} = -\frac{1}{\overline{M}_{Pl}} \sum_n G_n^{\mu\nu} T_{\mu\nu} \tag{1.22}$$

The RS model starts with the invocation of only one extra spatial dimension, compactified on a S^1/Z_2 orbifold like the ADD model. In this setup there are two 4D branes at each of the end points of the orbifold, one at $y = 0$ (called the Planck brane), and one at $y = \pi R$ (called the TeV brane), with SM processes restricted to the TeV brane, whilst gravity is free to propagate in the bulk. The main feature of this model is a change to the higher dimensional invariant interval metric that was described for the ADD model, so that there is now an exponential factor which warps the known 4D space-time along the extra spatial dimension (Equation (1.23)), depending on an initially unknown parameter $\sigma(y)$. This is vastly different from the ADD scenario, as even the 4D subspace of the overall 5D metric is y dependent because of the parameter σ. Other features of the model include a cosmological constant in the 5D bulk, and distinct tensions for both branes, which along with the parameter σ, provide a unique solution to the 5D Einstein equations. It is found from this solution that $\sigma = k|y|$, where k is a dimensional parameter arising from the calculation of the Ricci curvature invariant for the 5D space ($|R_5| = -20k^2$) that describes the constant curvature of the extra dimension[6]. As naturalness dictates that there should be no hierarchies present, the quantities: k, $\overline{M}_{Pl}$, and 5D Planck scale (M_*), should all be of comparable magnitude[7]. Taking the Action using the solutions of the 5D Einstein equations and integrating over y, yields the relation described in Equation (1.24).

$$ds^2 = e^{-2\sigma(y)} g_{\mu\nu} dx^\mu dx^\nu - dy^2 \tag{1.23}$$

$$\overline{M}_{Pl}^2 = \frac{M_*^3}{k}(1 - e^{-2\pi kR}) \tag{1.24}$$

From this it is evident that if the curvature parameter, k, becomes too large, i.e. greater than M_* so that through the relation $k \sim 1/R$, the radius of curvature becomes very small, then quantum gravity effects can dominate and the whole RS scenario breaks down (because it is considered in the classical context). Imposing $|R_5| < M_*^2$, avoids this situation and implies a rough bound on k/$\overline{M}_{Pl} \leq 0.1$, where the ratio k/$\overline{M}_{Pl}$ is known as the G^* coupling constant, and is of order one. The beauty of the RS model is that due to the exponentially warped nature of the extra dimension, mass scales are also warped depending

---

[6] The sign in this relation indicates that the curvature is negative, meaning the space is described as an Anti-de-Sitter space (AdS_5).

[7] In the ADD context there was $M_{Pl(4+n)}$, however now $n = 1$ is specified, this becomes $M_{Pl(5)}$ = M_*.

on their position in y. This is a powerful feature as it explains the ratio between m_{EW} and $\overline{M}_{Pl}$ with no fine tuning, allowing a mass of order 10^{18} GeV on the Planck brane to appear at the TeV scale on our SM brane. To get this rescaling factor, the only hierarchy is $kR \simeq$ 11-12, which is vastly more natural than the original $O(15)$ disparity. Furthermore, it has been shown by Goldberger and Wise [40, 41] that $kR \simeq$ 11-12 is a physical possibility, hence the RS model provides a true possible solution to the hierarchy problem.

To determine the coupling of the KK G^* masses to SM fermions in the RS context, examination of the Lagrangian term (Equation (1.25)) shows how the massless zero mode G^* couples to the SM fermions in the same way as the ADD model, whereas all higher KK modes have exponentially larger couplings due to the warp factor. This means that the G^* on the SM brane should appear with weak/TeV scale mass and couplings, able to be produced as a spin-2 resonance at collider experiments. Experimentally, due to the spacing of the KK states, the first non-zero mode G^* is generally searched for, with the width of the resonance depending on the mass and growing as $\sim (\mathrm{k}/\overline{M}_{Pl})^2$. Figure 1.10 shows the expected σB at the LHC for an RS G^* decaying to two electrons for various possible values of $\mathrm{k}/\overline{M}_{Pl}$. This thesis will search for (or set exclusion limits on) both the mass and $\mathrm{k}/\overline{M}_{Pl}$ parameters of interest in the RS model.

$$\mathcal{L} = -\left(\frac{G_0^{\mu\nu}}{\overline{M}_{Pl}} + \sum_{n>0} \frac{G_n^{\mu\nu}}{\Lambda_\pi}\right) T_{\mu\nu}\ , \text{ where } \ \Lambda_\pi = \overline{M}_{Pl} e^{-\pi kR} \sim 1 \text{ TeV} \qquad (1.25)$$

Theoretical constraints on the RS model come from the requirements that $|R_5| < M_*^2$ (limiting $\mathrm{k}/\overline{M}_{Pl} \leq 0.10$), and $\Lambda_\pi = \overline{M}_{Pl} e^{-\pi kR} \sim 1$ TeV, where Λ_π is the new physics energy scale (so that approximately $\Lambda_\pi \leq 10$ TeV, essentially limits $\mathrm{k}/\overline{M}_{Pl} \geq 0.01$). These theoretical constraints along with oblique parameter constraints from electroweak precision data are displayed in Figure 1.11. The current observed experimental exclusion limits from direct searches for an RS model G^*, are presented in Table 1.6 from recent experiments.

1.2.3 Search Strategy at the Large Hadron Collider

To determine if there are new physical phenomena such as high mass resonances at the TeV scale, seen via their decay into dielectrons within the ATLAS detector, one has to know to a very high accuracy both the response of the detector, and the expected number

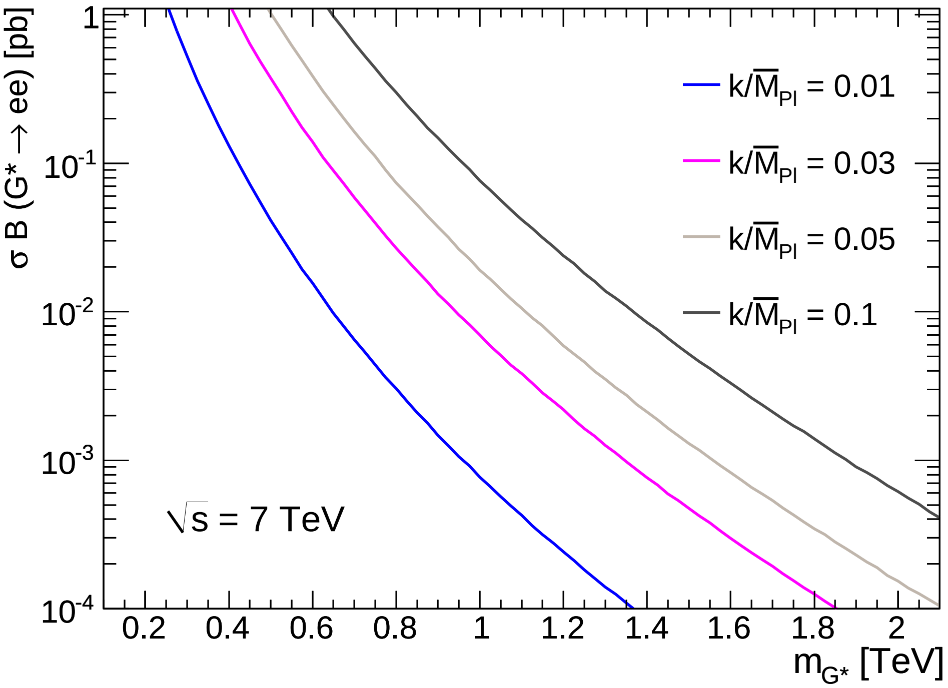

Figure 1.10: The expected cross section times branching ratio (σB) for an RS G^* decaying to two electrons at the LHC ($\sqrt{s}$ = 7 TeV). Various possible values of G^* coupling constant, k/$\overline{M}_{Pl}$, are displayed.

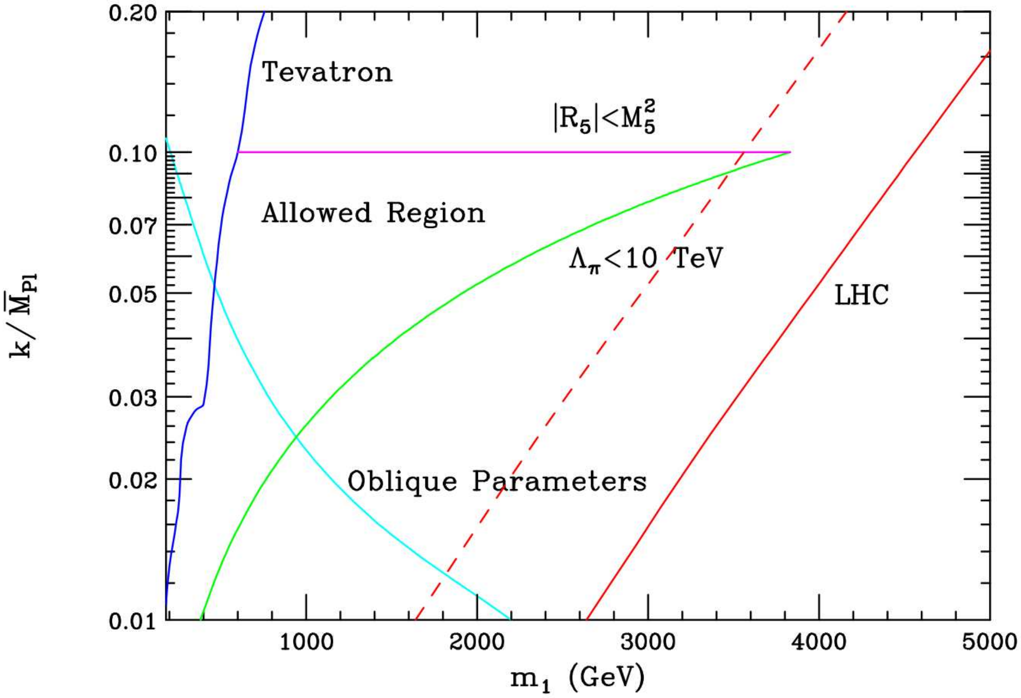

Figure 1.11: Allowed region for the RS model in theoretical parameter space as described in the text. The dashed (solid) red line shows the expected reach of the LHC with an integrated luminosity of 10 (100) fb^{-1} at $\sqrt{s}$ = 14 TeV [31, 38].

$k/\overline{M}_{Pl}$	RS Model Observed Exclusion Limit (TeV)									
	ATLAS		CMS		CDF		D0		Highest	
	ee	ee+$\mu\mu$+$\gamma\gamma$	ee	ee+$\mu\mu$	ee	ee+$\gamma\gamma$	ee	ee+$\gamma\gamma$	ee	ee+$\mu\mu$+$\gamma\gamma$
0.01	0.71	0.76	-	-	0.36	0.61	-	0.56	ATLAS	ATLAS
0.03	1.03	1.32	-	-	0.63	0.82	-	0.80	ATLAS	ATLAS
0.05	1.33	1.47	1.30	1.45	0.69	0.94	-	0.94	ATLAS	ATLAS
0.10	1.63	1.90	1.59	1.78	0.85	1.06	-	1.05	ATLAS	ATLAS

Table 1.6: Observed lower mass exclusion limits for a RS G^* resonance, published by recent experiments. Limits are set at 95% confidence level for various values of $k/\overline{M}_{Pl}$. Results are the latest available at time of writing from: ATLAS [3, 4], CMS [26, 42], CDF [27, 43], and D0 [44].

of events along with their distribution compared to the SM expectation. The response of the ATLAS detector to particles relevant to this search will be discussed in Chapter 2, with simulation of SM and BSM processes detailed in Chapter 3. The new physical phenomena being searched for can decay in a variety of ways as predicted by the theory (see branching fractions to SM particles in Figure 1.12). Leptons are by far the cleanest channel for a resonance search, dealing with well defined objects and low levels of SM background, which compensates for the relatively low branching fraction. For the RS Graviton, advantage can also be taken by using the possibility of diphoton decay, which has twice the branching fraction compared to dileptons due to spin factors. In this thesis the “Signal” process is defined as the decay of a Z' or G^* to two electrons (Figure 1.13). Physical phenomena from the SM, not deemed of interest to this search, but which are able to decay to, or mimic, the same signature of the signal process, are known as “Background” processes. The background processes considered for this BSM dielectron resonance search are presented at Leading Order (LO) in Figure 1.14, along with the QCD dijet background which will be described in Chapter 6.

Some of these background phenomena are reducible, that is, through different types of analysis can be reduced to almost negligible levels by looking at variables which easily separate the nature of the background phenomena from the signal. However, certain backgrounds are at some level irreducible to a search, meaning that in every respect the background looks like the signal process. The only way then to distinguish the two, is in the number of events seen, with the observation of more events than the SM predicts being determined as an excess, which needs to be quantified to be able to reject the SM hypothesis in favour of a given new physics hypothesis. The dominant irreducible background for a dielectron resonance search is the Drell-Yan process (see (a) in Figure 1.14)

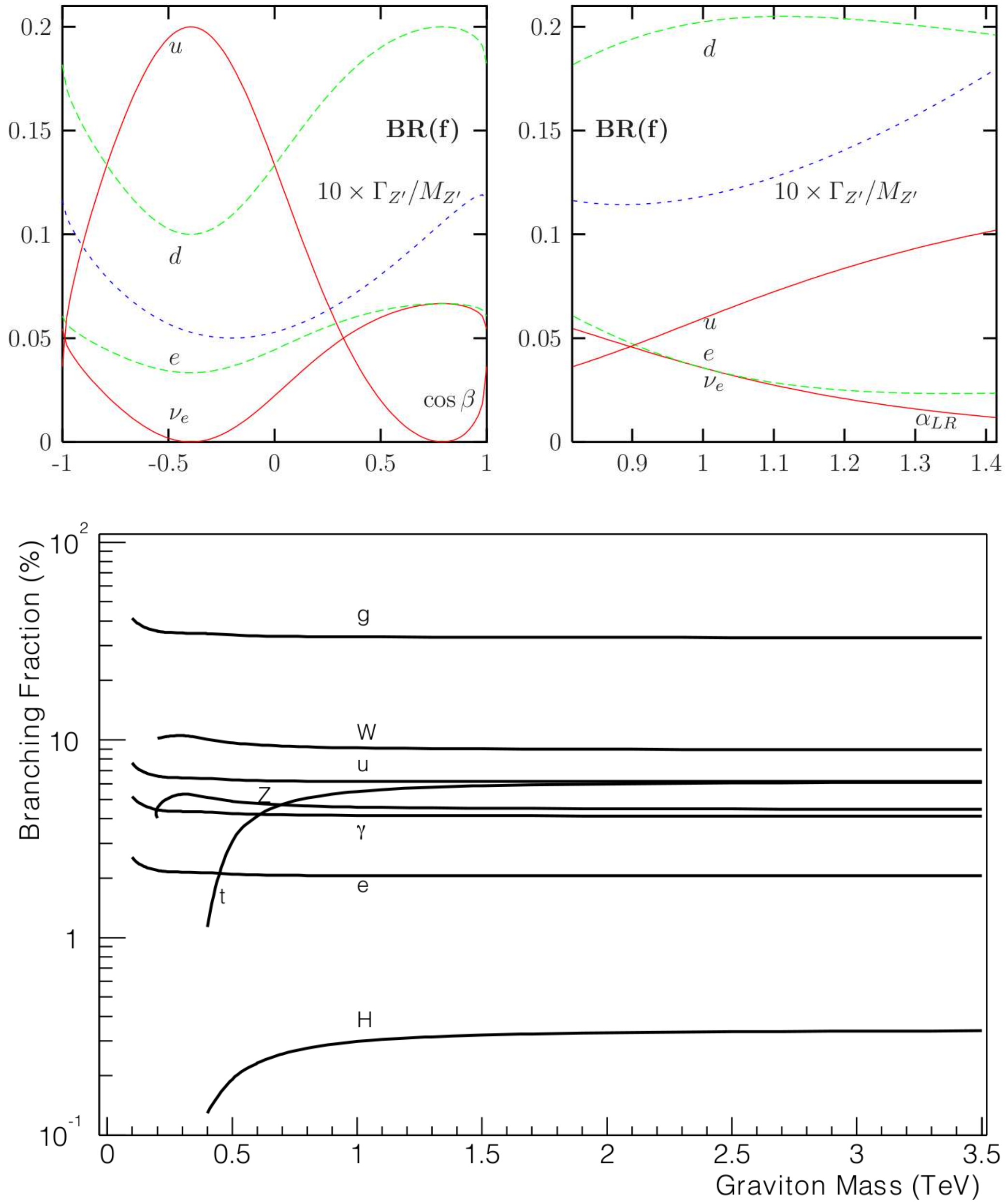

Figure 1.12: Z'/G^* decay branching fractions into SM particles. E_6 (upper left) and LRM (upper right) motivated Z' models as a function of the Z'_χ-Z'_ψ mixing parameter cosθ, and LRM parameter α, respectively, from [45]. Also shown (lower) is the RS model G^* for narrow width resonances as a function of G^* mass, from [46].

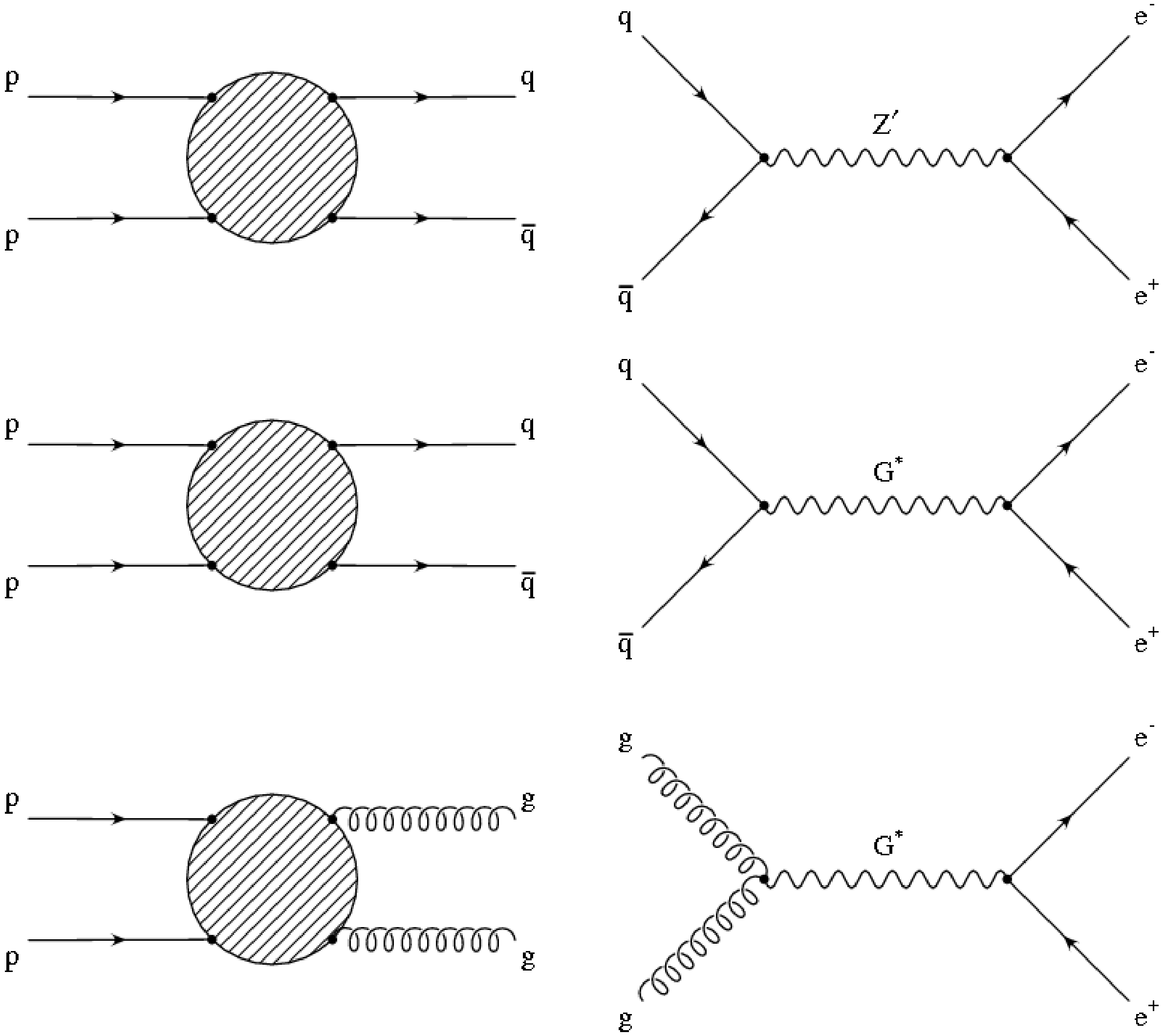

Figure 1.13: Feynman diagrams showing (left) the LHC production process of interest (without proton remnants) for (right) the leading order BSM processes: (upper) $q\bar{q}$ production, and e^+e^- decay, of a Z' gauge boson, and (middle) $q\bar{q}$ production, (lower) gg production, and associated e^+e^- decay, for the RS G^*.

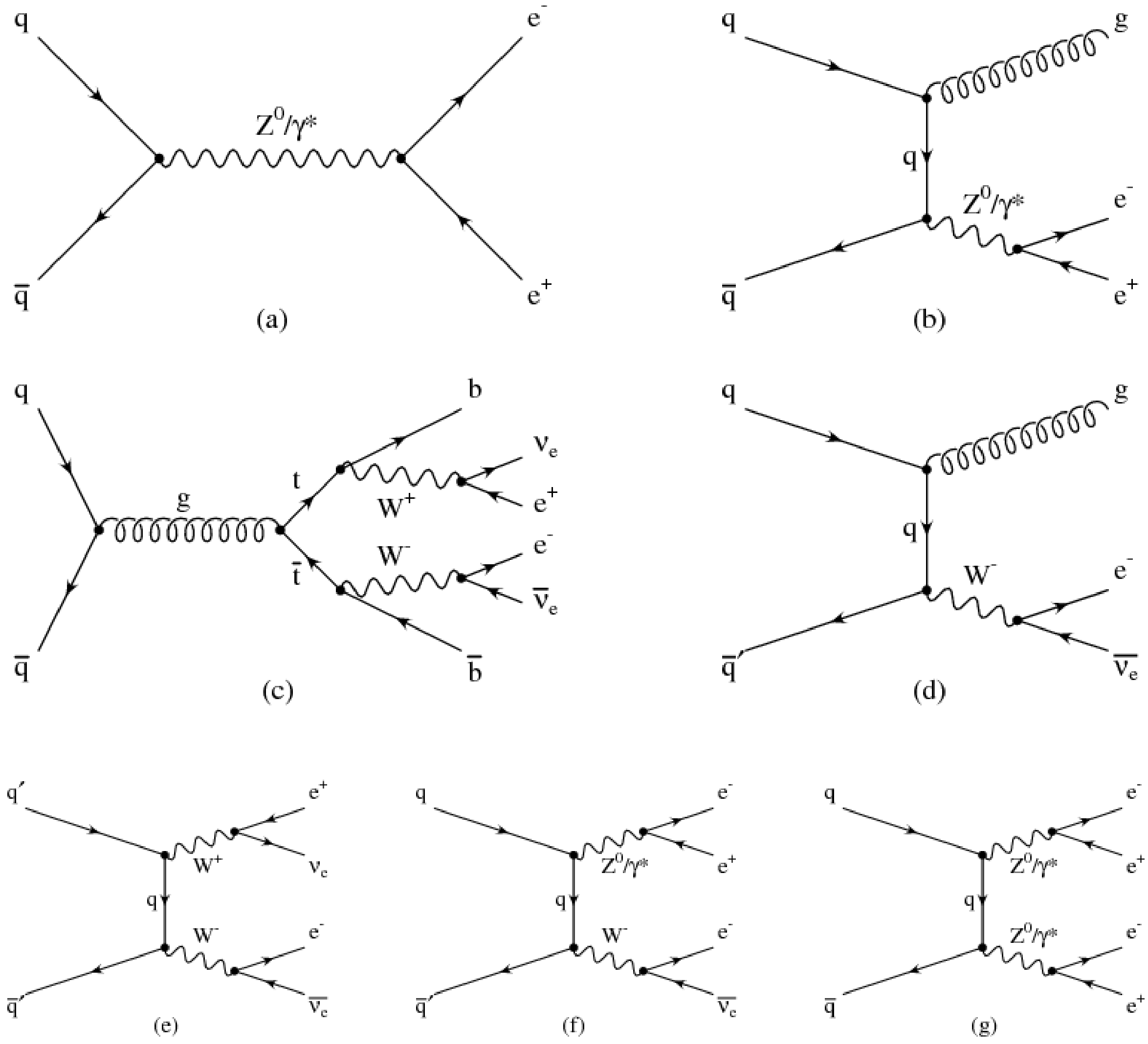

Figure 1.14: Feynman diagrams showing the leading order SM processes that are considered a background to an exotic high mass dielectron resonance search. The dominant process is Drell-Yan (a), which is added with the Drell-Yan plus jets background (b). Other non-negligible backgrounds that can mimic the signal process come from $t\bar{t}$ (c), $W+$jets (d), and dibosons: WW (e), WZ (f), or ZZ (g).

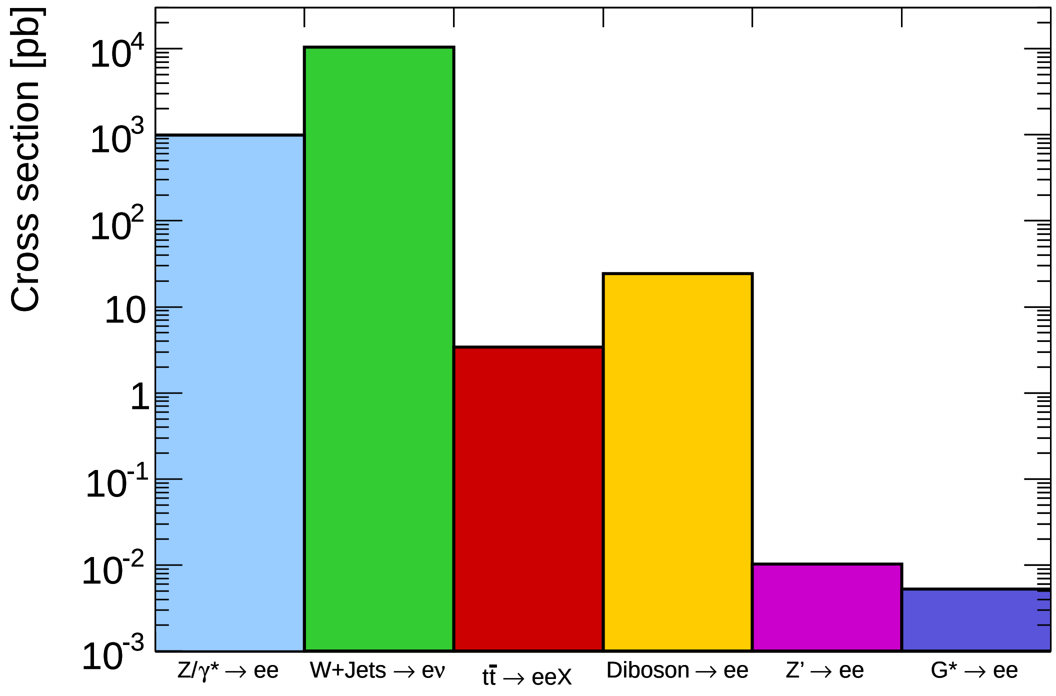

Figure 1.15: Cross sections for the SM background processes considered in this search (except QCD dijets) at $\sqrt{s}$ = 7 TeV. Expected cross sections for a 1.5 TeV Z'_{SSM} and RS G^* (k/$\overline{M}_{Pl}$ = 0.10) are also shown. A full list of cross sections is provided in Appendix B.

which is the *s*-channel process whereby $q\bar{q}$ fusion creates a Z^0 boson or virtual photon, which subsequently decays into two electrons. The difficulty in separating this type of event from that of the signal, is due to the processes being very similar, whereas other backgrounds such as $t\bar{t}$ and $W+$jets (see (c) and (d) of Figure 1.14 respectively) are reducible to an extent, as they are innately different processes which happen to have decay characteristics that can mimic the new physics signature. It is for this reason that despite the $W+$jets background having a larger cross section (see Figure 1.15), Drell-Yan is the dominant background in this search.

If a new gauge boson like the Z' or G^* is found, then the next immediate aim would be to determine its properties such as: the spin of the resonance to differentiate between the observation of a Z' (spin-1), and G^* (spin-2); Z'/G^* couplings to SM quarks and leptons; Z'/G^* couplings to exotic particles. It would also be desirable to probe the relative strength of the Z' gauge couplings, and the G^* coupling constant k/$\overline{M}_{Pl}$. While each of these tasks would require large amounts of data to study in detail, the spin of a new resonance is particularly interesting for its use in determining whether the particle is a Z', G^*,

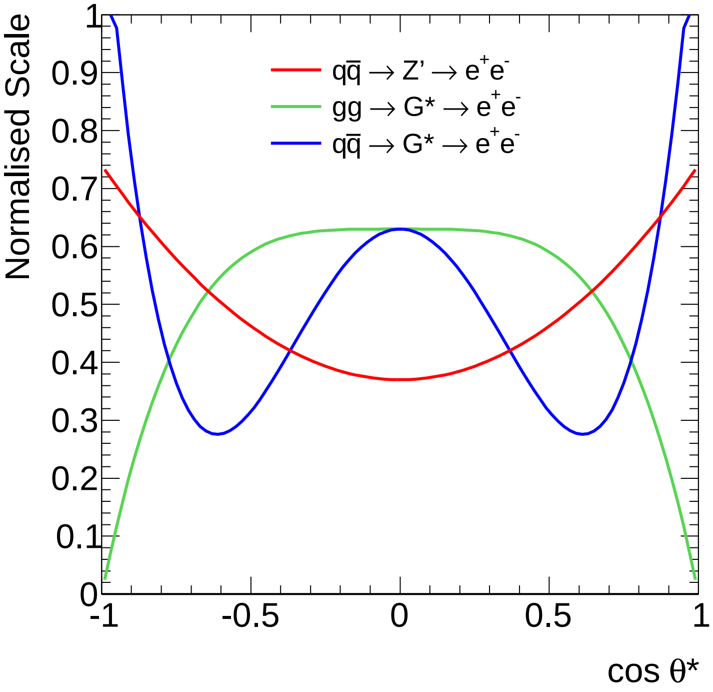

Figure 1.16: The $\cos\theta^*$ distribution for a Z' (spin-1), and RS G^* (spin-2) particle, decaying to two electrons. $q\bar{q}$ and gg production terms for the G^* are separated, as the $gg/q\bar{q}$ fraction depends on G^* mass. Distributions are from [48]

or otherwise. The angular distribution of events is used to differentiate between these possibilities, specifically the $\cos\theta^*$ spectrum, where θ^* is the angle of the outgoing electron from the Z'/G^* decay in the Collins-Soper Z'/G^* rest frame[8]. The predicted $\cos\theta^*$ distribution for a Z'/G^* is presented in Figure 1.16. Note that because the G^* has a $q\bar{q}$ and a gg production component, these are plotted separately, with the combination of the two not shown as the $gg/q\bar{q}$ fraction depends on G^* mass as presented in Figure 1.17. A measurement of the asymmetry between forward ($\cos\theta^* > 0$), and background ($\cos\theta^* < 0$) events, denoted A_{FB}, is quantified in Equation (1.26). A shift in A_{FB} from that predicted by the vector and axial-vector couplings of electroweak bosons to SM fermions [47] through the Drell-Yan process at the LHC, would be an indication of new physics, and so provides yet more fertile ground in which to search for a Z'/G^* resonance. Unfortunately, the size of the dataset available for this thesis means that the $\cos\theta^*$ distribution and A_{FB} would not yield a statistically significant deviation should a BSM high mass resonance be present. Therefore the search is only conducted using the dielectron invariant mass distribution, although $\cos\theta^*$ plots will be provided.

---

[8] The Collins-Soper frame has the z-axis aligned with the direction bisecting the incoming partons' momentum, and x-axis perpendicular to the partons' momentum plane.

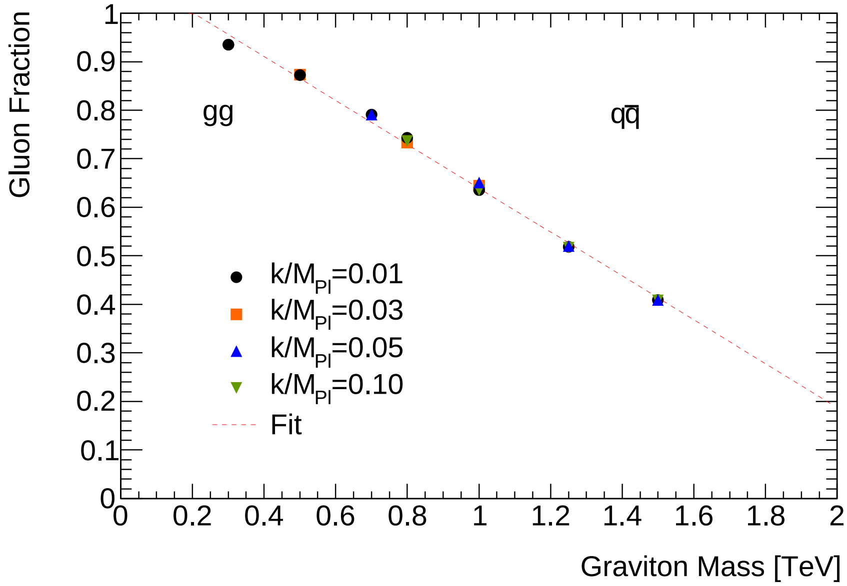

Figure 1.17: The contributions from gg and $q\bar{q}$, for RS G^* production at the LHC, using available Monte Carlo samples as listed in Appendix B.1, generated at $\sqrt{s}$ = 7 TeV. The points are fitted with a 1st degree polynomial.

$$A_{FB} = \frac{d\sigma(cos\theta^* > 0) - d\sigma(cos\theta^* < 0)}{d\sigma(cos\theta^* > 0) + d\sigma(cos\theta^* < 0)} = \frac{(N^+_{Obs} - N^+_{Bkg}) - (N^-_{Obs} - N^-_{Bkg})}{(N^+_{Obs} - N^+_{Bkg}) + (N^-_{Obs} - N^-_{Bkg})} \tag{1.26}$$

Chapter 2

The ATLAS Experiment at the Large Hadron Collider

In this section the experimental apparatus used to produce the results for this thesis will be discussed in detail.

2.1 The Large Hadron Collider

The LHC is currently the world's highest energy particle accelerator, capable of accelerating proton bunches up to an energy of 7 TeV, giving it a maximum centre of mass collision energy of $\sqrt{s} = 14$ TeV. Located at the European Organisation for Nuclear Research (CERN) site in Geneva, Switzerland, the LHC tunnel is 27 km in circumference and lies approximately 100 m below the surface near (indeed crossing) the Franco-Swiss border (see Figure 2.1). Originally constructed for the Large Electron-Positron Collider (LEP) between 1983 and 1988 (and operated from 1989-2000), the LHC inherited the tunnel and began dismantling the 30,000 tonnes of LEP equipment in 2001 to make way for the new accelerator. An equally large task was to excavate caverns for the four new LHC experiments; ALICE (A Large Ion Collider Experiment) [49] which was designed to study very high energy density environments with heavy ions, ATLAS (A Toroidal LHC ApparatuS) [50], and CMS (Compact Muon Solenoid) [51] which are general purpose detectors aiming to study a broad range of physics and be complimentary to each other, as well as LHCb (LHC beauty) [52] which was designed to look at B mesons and search for CP-Violation. Excavation for the experiments began in 1998 and was completed by

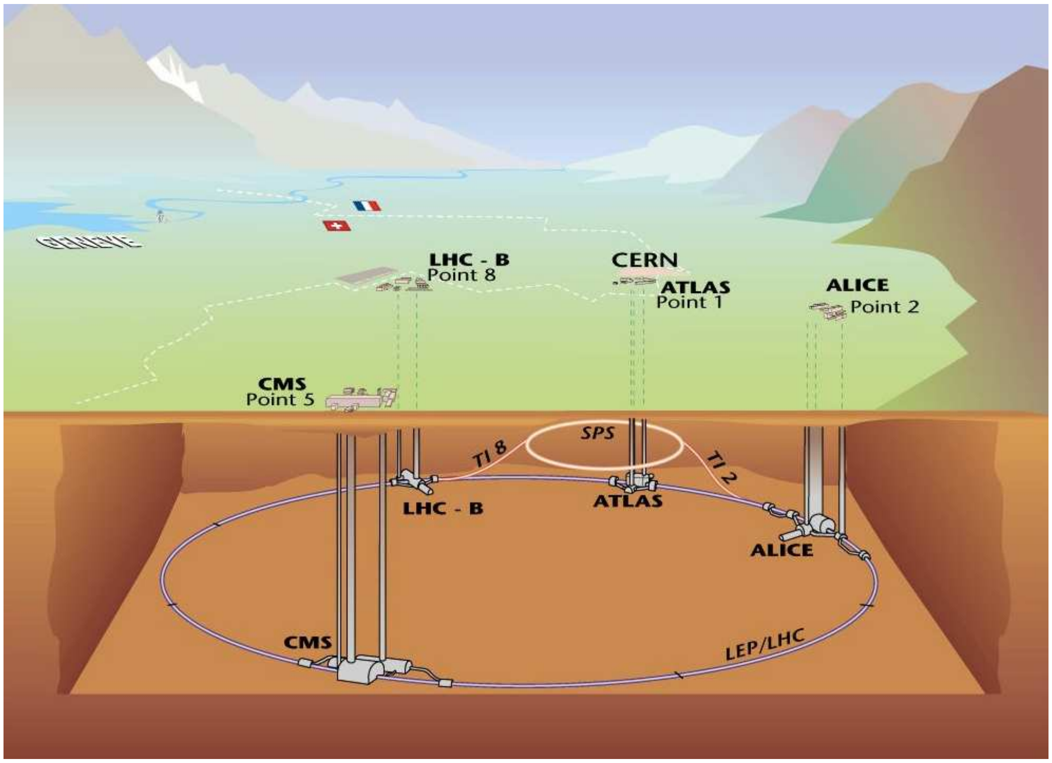

Figure 2.1: An artists illustration of the LHC showing the 27 km tunnel which houses the beam pipe and magnets, as well as the location of the 4 main LHC experiments; ATLAS, CMS, LHCb, and ALICE [56].

2001, with construction of the detectors themselves beginning in 2003, and proton beams first successfully circulated around the LHC on the 10th of September 2008. The LHC is a synchrotron machine and makes use of Nb-Ti superconducting magnets to control the beam, able to produce up to a 8.33 T field at a temperature of 1.9 K. The LHC was designed to achieve proton injection/collision energies of 450 and 7000 GeV respectively with up to 1.5×10^{11} particles per bunch and 2808 bunches per beam, giving a peak luminosity of 1×10^{34} cm^{-2}s^{-1} and a circulating beam current of 0.582 A (with a stored energy of 362 MJ per beam) [53]. As well as the four main detectors there are two smaller experiments that are part of the LHC, namely; TOTEM (TOTal Elastic and diffractive cross section Measurement) [54], and LHCf (LHC forward) [55]. These experiments have very specific purposes that are useful to the detector and accelerator teams, as well as other particle physics experiments worldwide. TOTEM does a range of studies including in depth studies of the proton structure, but importantly for the other experiments it can accurately monitor the LHC's luminosity. LHCf uses forward particles from the LHC as a source to simulate cosmic rays in laboratory conditions, which can help to interpret and calibrate large scale cosmic ray experiments.

2.1.1 Operation

The protons collided at the LHC must first be obtained and accelerated through a succession of injection stages, before they reach their desired energy, intensity, and bunch structure. All protons accelerated at the LHC start their journey being produced by a duo-plasmatron which accelerates electrons into a hydrogen filled chamber, ionising the gas. The resulting ions are accelerated through two highly charged grids, producing an ion beam which is then injected into the first LHC acceleration stage called Linac2. Here the proton beam is accelerated up to 50 MeV before being injected into the Proton Synchrotron Booster (PSB) which further accelerates the beam to 1.4 GeV. From the PSB the beam is passed to the Proton Synchrotron (PS), which with its larger radius, accepts the 1.4 GeV proton beam and provides acceleration up to 25 GeV as well as the desired proton train bunching and spacing using Radio Frequency (RF) harmonics. Due to the very high energy final proton beam required by the LHC, the PS then passes the beam to the Super Proton Synchrotron (SPS) which accelerates the beam up to its final injection energy of 450 GeV. When a flat top energy of 450 GeV has been achieved, the beam is injected into the 27 km circumference LHC main ring where the beam is accelerated to its final collision energy of 3.5 TeV per beam [57] (for 2010/11 running, with a maximum achievable 7 TeV per beam). The whole acceleration chain from first injection to ramped beam energy takes approximately 20 minutes; a full schematic overview of the LHC acceleration complex is illustrated in Figure 2.2.

Incident in September 2008

On the 19th of September 2008, during commissioning of sectors 3-4 up to a current of 9.4 kA for 5.5 TeV beam energy running, a resistive zone developed in the electrical bus between two of the magnets in the sector causing a quench. According to the official report covering the incident [59], the quench detection, power converter, and energy discharge systems, all behaved as expected, but within the first second an electrical arc developed and punctured one of the helium enclosures causing a pressure rise above the nominal 0.13 MPa. In the next few seconds, vacuum conditions were lost in the beam pipe, and within 20 seconds approximately 100 magnets quenched in the surrounding sectors. The quench relief valves on the helium enclosures opened at their set point of 1.7 MPa, and the spring-loaded relief discs on the vacuum enclosure opened when the

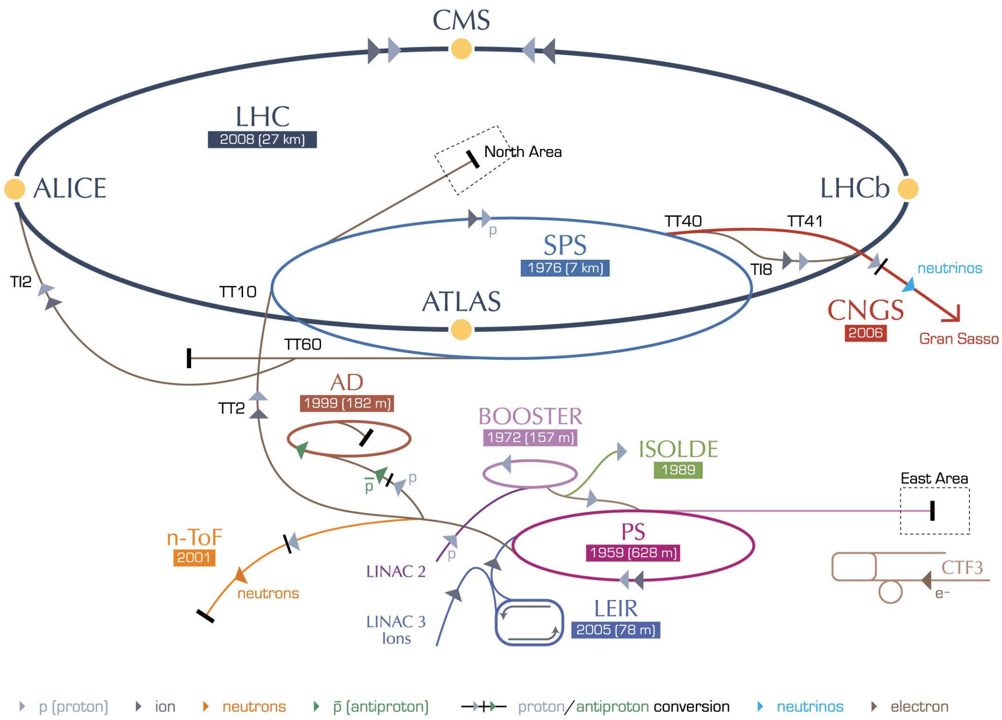

Figure 2.2: An artists illustration of the LHC accelerator complex. The main injection structure for protons is: Linac2 → PSB → PS → SPS → Main Ring. The accelerating structure for other LHC use is also shown, along with a pictorial key at the bottom of the figure [58].

pressure exceeded atmospheric, releasing ∼2 tonnes of helium into the tunnel. However, in subsectors 23-25 the vacuum enclosure was unable to contain the pressure rise above the nominal, causing large pressure forces to act on the magnets and their housing. This caused damage and movement to those systems, even managing to break the anchors in the concrete floor at some locations, bringing the total helium loss to approximately 6 tonnes. Postmortem of the incident diagnosed the need for repair to 5 quadrupole and 24 dipole magnets, with extensive beam pipe cleaning. Recommendations made by the report into the incident tried to address two goals; firstly to prevent another occurrence of the incident, and secondly to mitigate its consequences should it happen again. As a result, an improvement of the quench detection system was ordered to provide early warnings of such a type of event and to cover a wider range of systems. Also the relief devices on the cryostat vacuum vessels were increased both in discharge capacity and in number, so as to contain a possible pressure rise above 0.15 MPa even in the presence of an electrical arc, as well as the floor anchoring being reinforced to guarantee mechanical stability. The repairs to the LHC took almost one year, not becoming operational again until the 20th of November 2009, when low energy beams were circulated for the first time since the incident, marking the restart of the physics program. Before the winter shutdown, initial studies were done with $\sqrt{s}$ = 900 GeV collision energy (achieved on 23rd November), giving both the accelerator and physics teams a chance to study and understand the now operational LHC and its experiments. On the 30th of November, the LHC became the world's highest energy particle accelerator achieving an energy of 1.18 TeV per beam, beating the Tevatron's previous record of 0.98 TeV. After the winter shutdown, physics data taking restarted with the LHC setting the world record for high-energy collisions on the 30th of March 2010 with a centre of mass energy of $\sqrt{s}$ = 7 TeV, truly starting the exploration of an uncharted energy regime in particle physics.

2.1.2 Performance during data taking 2010/11

The performance of the LHC during 2010/11 exceeded all expectations, with various technical stops between data taking periods refining beam parameters which enabled the collection of nearly an order of magnitude more integrated luminosity than was first predicted. This enabled physics analysis teams to explore large areas of theoretical parameter space, despite being limited to $\sqrt{s}$ = 7 TeV. Proton collision data taking in 2010 took place between the 30th of March and 31st October, in which time 48.87 pb^{-1} of data was delivered to the experiments at a peak stable luminosity of 2.07×10^{32} $\text{cm}^{-2}\text{s}^{-1}$. After a successful start at the end of March, the accelerator team worked throughout the year to understand and optimise the operational machine. One of the important parameters worked on was β^*, which is the distance from the Interaction Point (IP) at which the emittance of the beam is double its size at the IP. The smaller β^* is, the larger the proton-proton beam cross section at the IP proportionally, with a β^* of 2 m corresponding to a beam size of just 45 μm at the IP. This process of reducing β^* is known as "squeezing" and uses the quadrupole magnets next to the experiments' IP to tightly focus the proton bunches. On the other side of the IP according to β^*, the bunches quickly become defocused due to the squeeze, making it difficult yet very important to control the post IP beam to avoid losses. In September of 2010, commissioning of the bunch trains increased the maximum number of bunches per beam from 50 to 368, with the number of colliding bunches increasing relatively from 35 to 348. By October 2010, β^* at ATLAS and CMS had been reduced from β^*_x=11 m, β^*_y=10 m to β^*_x=3.5 m, β^*_y=3.5 m, meaning that between the squeezing and the bunch train commissioning, the luminosity was increased by over an order of magni-

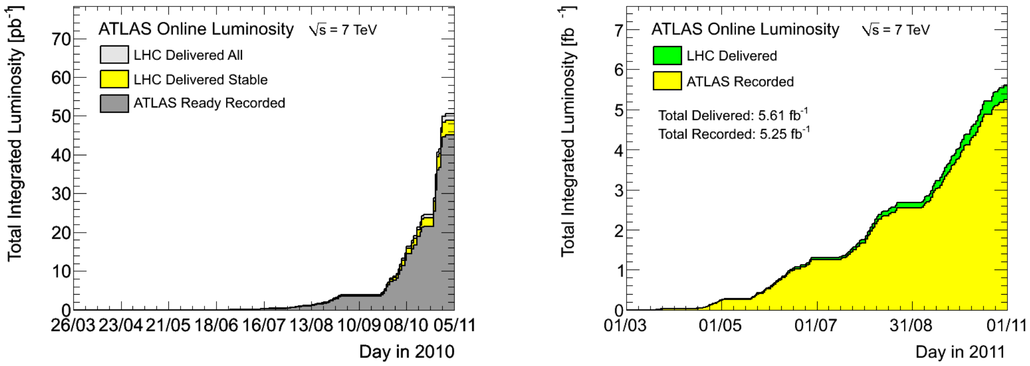

Figure 2.3: The total integrated luminosity, delivered and recorded by ATLAS during the 2010 (left) [60], and 2011 (right) [61], pp physics data taking period, with a centre of mass energy $\sqrt{s}$ = 7 TeV.

tude. Of the 48.87 pb^{-1} delivered to experiments in 2010, 40% was in the last week of data taking, with over 60% being delivered in the last month. Proton physics data taking in 2011 took place between the 12th of March and 22nd of November, delivering a total integrated luminosity of 5.61 fb^{-1} to the experiments. This astounding amount of data was taken due to the dedication and expertise of the accelerator team, who continued to optimise the machine actively during data taking, as well as targeted technical stops. By November the number of bunches per beam was up to 1380 with 1318 colliding bunches at ATLAS and CMS producing an instantaneous peak luminosity of 2.1×10^{33}cm^{-2}s^{-1}. The 2011 dataset up to the end of August (constituting 2.55 fb^{-1} delivered to ATLAS) will be predominantly used for this thesis as it is the largest dataset available at the time of writing with a constant collision energy, and can be used to explore a significant portion of Z'/G^* theoretical parameter space not previously accessible. Two plots showing the total integrated luminosity for ATLAS during 2010 and 2011 data taking are displayed in Figure 2.3.

2.2 A Toroidal LHC ApparatuS

2.2.1 Overview and Nomenclature

The ATLAS Detector is one of the four main experiments built for the LHC at CERN. It was designed to be a general purpose physics detector, studying collisions from the LHC to search for new physics BSM as well as make precision measurements of SM parameters. The structural design of ATLAS pushed the limits of current engineering

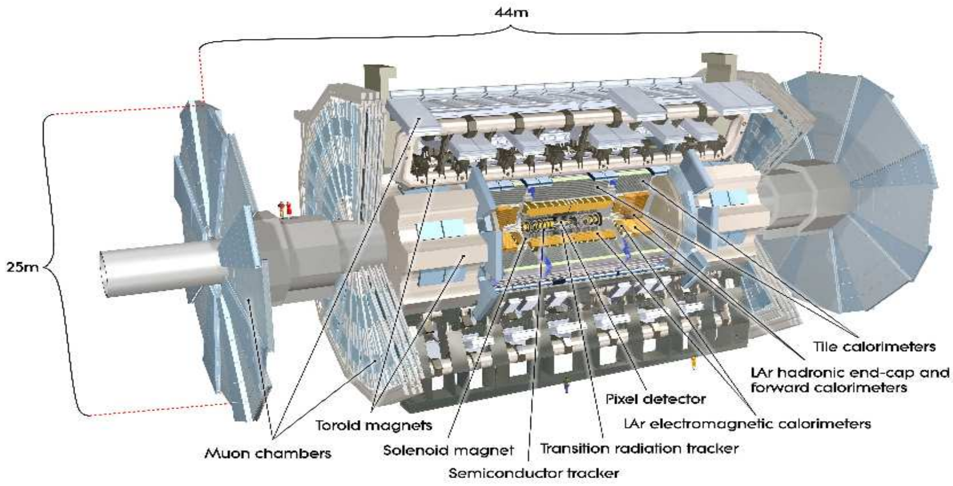

Figure 2.4: An overview of the ATLAS detector design, including dimensions, magnet systems and main detector components [62].

ability in an effort to provide a detector that fulfilled the physics program specification. Standing at 44 m in length, 25 m in diameter, and weighing approximately 7000 tonnes, ATLAS consists of many different detecting technologies spread over the main barrel and endcap sections, as well as the forward region and extended muon chamber endcap wheels. The main components of the ATLAS detector are shown in Figure 2.4. The Inner Detector (ID) and electromagnetic calorimetry are of direct importance to this thesis as the aim is to search for new physics in the high mass dielectron channel, therefore these parts of the detector are described in the greatest detail in the following subsections, and elaborated on for their identification and reconstruction of electrons in Chapter 3.5.

The coordinate system used in ATLAS is defined to have its origin at the nominal interaction point, with the beam line direction defining the z-axis, and the $x-y$ plane being perpendicular to this. The positive x-axis points towards the centre of the LHC ring, with positive y-axis vertically upwards, and positive z-axis in the direction of LHCb. The transverse radius from the beam line is denoted, r. Additional parameters are defined for their use with respect to interactions rather than detector geometry. The azimuthal angle ϕ, is measured around the z-axis clockwise for positive z, from x=0, with the polar angle θ, being the angle from the beam axis. A dimensionless measure of θ called the pseudo-rapidity η, is further defined in Equation (2.1).

$$\eta = -\ln[\tan(\frac{\theta}{2})] \tag{2.1}$$

Detector Component	Energy Resolution	Measurement Range	Trigger Range
Tracking	σ_{p_T}/p_T = 0.05% $p_T \oplus$ 1%	$\lvert\eta\rvert < 2.5$	-
EM Calorimetry	σ_E/E = 10%/$\sqrt{E} \oplus$ 0.7%	$\lvert\eta\rvert < 3.2$	$\lvert\eta\rvert < 2.5$
Hadronic Calorimetry:			
Barrel and Endcap	σ_E/E = 50%/$\sqrt{E} \oplus$ 3%	$\lvert\eta\rvert < 3.2$	$\lvert\eta\rvert < 3.2$
Forward	σ_E/E = 100%/$\sqrt{E} \oplus$ 10%	$3.1 < \lvert\eta\rvert < 4.9$	$3.1 < \lvert\eta\rvert < 4.9$
Muon Spectrometer	σ_{p_T}/p_T = 10% at p_T = 1 TeV	$\lvert\eta\rvert < 2.7$	$\lvert\eta\rvert < 2.4$

Table 2.1: The η coverage and resolution, of the ATLAS detector subsystems [62].

The pseudo-rapidity is more often used as η differences are invariant under Lorentz boosts to the z-axis for massless particles. Together η and ϕ are used to define the distance ΔR, which is the pseudo-rapidity-azimuthal angle space and is defined in Equation (2.2).

$$\Delta R = \sqrt{\Delta\eta^2 + \Delta\phi^2} \tag{2.2}$$

The transverse momentum p$_T$, transverse energy E$_T$, and missing transverse energy E$_T^{miss}$ are defined in the $x - y$ plane unless otherwise stated [62].

Covering the maximum possible solid angle around the interaction point is essential for a general purpose detector, as well as providing high energy resolution and precise tracking over the full coverage. ATLAS was designed to this end with details summarised in Table 2.1 showing the detector's ability to accurately measure the position and energy of leptons and hadrons coming from collisions, over a close to 4π range. To complement the hardware achievements of the physics and engineering teams, an equally important requirement for ATLAS was a robust and versatile software system. The Trigger and Data Acquisition systems (TDAQ) were designed to efficiently process the events being detected by ATLAS, with the trigger reducing the number of interesting events to a recordable level, and the Data Acquisition (DAQ) system monitoring the data flow as well as recording events to storage disk.

2.2.2 Magnet System

The ATLAS detector's magnet system consists of one solenoid and three toroidal superconducting magnets extending 22 m in diameter and 26 m in length. The system provides a magnetic field ($>$ 50 mT) over a volume of $\sim$12,000 m^3 with a stored energy of 1.6 GJ. A strong magnetic field throughout the detector is important as it enables measurements of particle momentum. Charged particles traversing a magnetic field feel a force perpen-

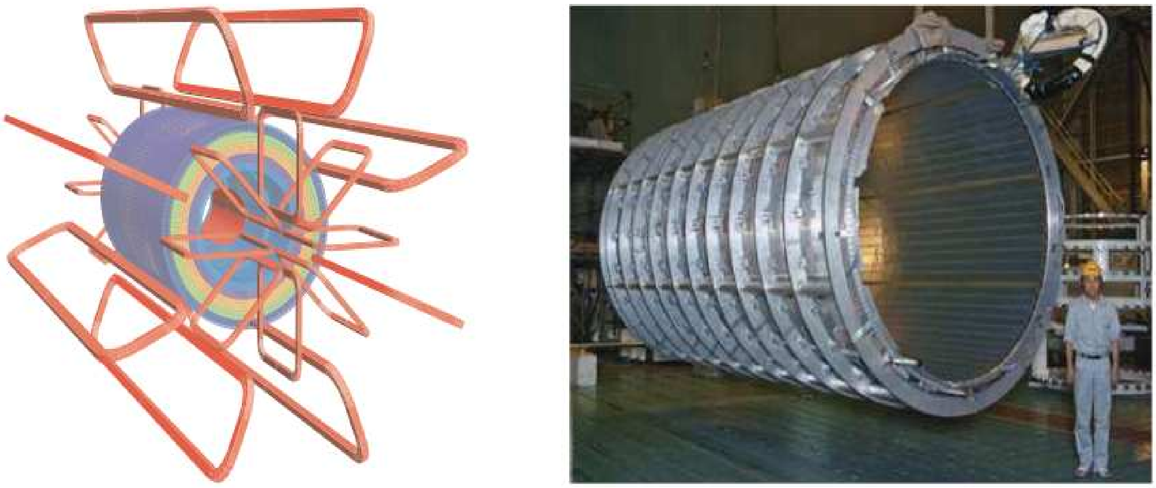

Figure 2.5: The ATLAS magnet system. Left: The magnet system with the centre solenoid surrounded by eight barrel toroid coils, and two endcap toroids each with eight coils. Right: The central solenoid in isolation after completion of the coil winding [63].

dicular to their direction of motion called the Lorentz force (Equation (2.3)), which is proportional to the strength of the magnetic field, $\vec{B}$, and electric field, $\vec{E}$, electric charge, q, and velocity of the particle, $\vec{v}$. This enables the determination of a particle's momentum from the deflection of the track as it travels through the detector (this is especially important for muons as they are not stopped in the detector). A view of the ATLAS magnet system is given in Figure 2.5.

$$\vec{F} = q[\vec{E} + (\vec{v} \times \vec{B})] \tag{2.3}$$

The solenoid was designed to minimise radiative thickness in front of the barrel Electromagnetic Calorimeter (ECAL), contributing only 0.63 radiation lengths at normal incidence. It is aligned to the beam axis providing a 2 T axial magnetic field for the ID and calorimetry systems, with a nominal current of 7.7 kA and temperature of 4.5 K [64]. To achieve the low radiative thickness, the solenoid windings and ECAL share a common vacuum vessel to avoid the need for two vacuum walls. The solenoid is 5.8 m in length with an inner/outer diameter of 2.46/2.56 m respectively, and weighs just 5.4 tonnes with a stored energy of 40 MJ. This is surrounded by the barrel toroid and two endcap toroids which produce a toroidal magnetic field of approximately 0.5 T and 1 T respectively for the muon spectrometer system. The barrel toroid is 25.3 m in length with inner/outer diameters of 9.4/20.1 m respectively, and a cold mass weight of over 360 tonnes. The nominal operating temperature is 4.6 K with a current of 20.5 kA, but extensive testing was done before installation to demonstrate the system's robustness during slow and fast quenches as well as a current of up to 500 A above nominal. The endcap toroids are similar in design to the barrel toroid, using the same conducting material (Al-stabilised Nb/Ti/Cu) and coil winding technology. These toroids were designed to provide an optimal magnetic field in the endcap regions of the muon spectrometer system to maintain bending power. Each endcap toroid weighs $\sim$140 tonnes (cold mass) [63].

2.2.3 Inner Detector

Particle tracks are reconstructed by the ATLAS Detector in the ID which covers a range of $|\eta| < 2.5$, and consists of 3 main detecting technologies: at smaller radii (1) Pixel Detectors (PD) consisting of silicon pixel layers, (2) Semi-Conductor Trackers (SCT) consisting of stereo pairs of silicon micro-strip layers, and (3) at larger radii, Transition Radiation Trackers (TRT) comprising of many layers of gaseous straw tube elements, interleaved with transition radiation material (Figure 2.6). This combination gives the ID an overall momentum resolution of σ_{p_T}/p_T = 0.05% $p_T \oplus$ 1% with the combination of precision trackers at small radii, and TRTs at larger radii enabling robust pattern recognition, and high spatial resolution of both primary and secondary vertices [65]. The ID system was designed to provide precision measurements for charged tracks above a nominal p_T theshold of 0.5 GeV (although measurements as low as 0.1 GeV have been achieved) up to $\sim$150 GeV within its coverage, which complements the measurements of the barrel and endcap EM calorimeters [65]. The ID also provides enhanced electron identification within the coverage of the TRT ($|\eta| < 2.0$), with the ability to distinguish between electrons and pions by the detection of high threshold transition radiation photons in the gas mixture within the straw tubes (electrons will on average produce more numerous high threshold hits than pions).

2.2.3.1 Pixel Detector

The PD is the closest subdetector to the beam line, meaning it has the least amount of material between it and the interaction point, but also the highest particle flux and thus need for radiation hardness. For the PD to maintain a good charge collection efficiency over the predicted lifetime of the LHC, as well as providing sufficiently high resolution

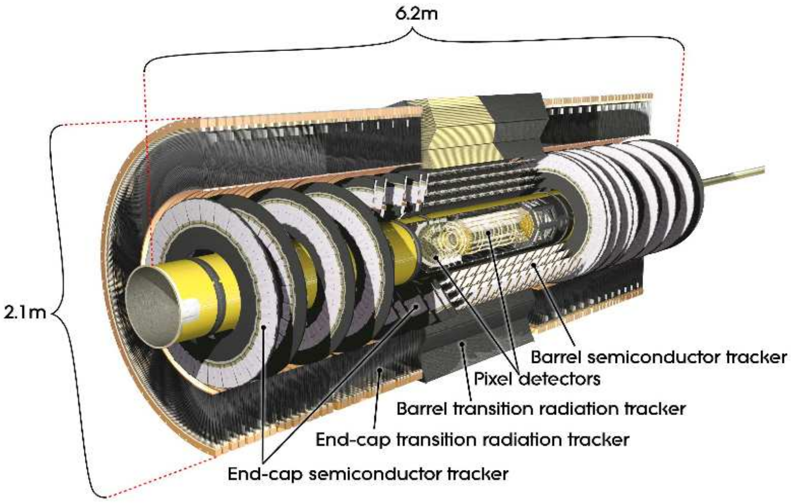

Figure 2.6: The Inner Tracking of the ATLAS Detector [62].

measurements of charged tracks, the design specification had to be leading edge. The PD consists of 1744 modules, arranged into one barrel and two endcap sections, each with three layers. Each module is 250μm thick with an area of 63.4$\times$24.4 mm^2, and a sensor made up of 47232 silicon pixels (each pixel is 50$\times$400 μm^2) [65]. The long term effects of irradiation to the PD had to be well understood, influencing the design to ensure a continued optimal performance. The sensor characteristics that are most sensitive to radiation are [66]:

1. The effective doping concentration. This is important as over time acceptor-like defects will cause an inversion of the conductor type from n to p.
2. The charge collection efficiency. This would subsequently be affected by (1) due to an increase in the depletion voltage with time.
3. Radiation induced leakage current. This causes an increase in noise and power consumption if the PD is not adequately cooled.

To address these issues, firstly the sensors use oxygenated n-type wafers with n-type implants, bump bonded to the front-end electronics which allow them to be operated partially depleted, and give increased radiation tolerance to charged hadrons [65]. To reduce leakage current, the sensors are operated within a -5°C to -10°C temperature range, and the sensor's n-side external to the active area is covered by an n$^+$ implant that is grounded externally [66]. Lastly due to the use of the n$^+$ implants, a p-spray was used to

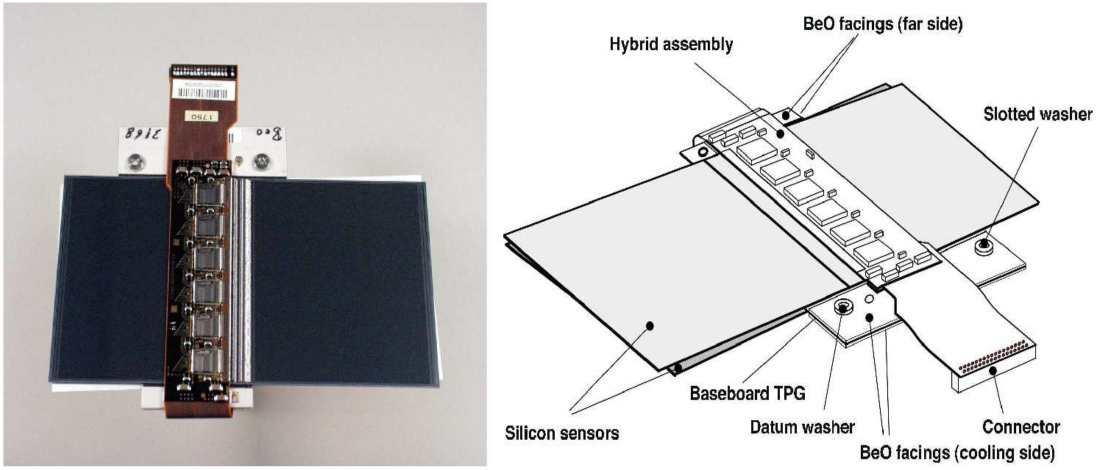

Figure 2.7: A barrel module from the ATLAS semi-conductor tracker with photograph (left) and drawing (right) showing the main components [65].

cover the n-side, providing high resistance between neighbouring cells. Extensive testing of the constructed pixel modules ranked them in order of quality so that the best were used in the layers closest to the interaction point (where radiation flux is highest), and the poorest kept as spares. The spatial resolution of individual pixel modules was measured with a test beam in both non-irradiated and fully irradiated states, showing an optimal resolution of 4.7 μm before, and 6.0 μm after irradiation, in r-ϕ at incidence angles 10-15° (at normal incidence the spatial resolution was measured to be 12 μm) [65].

2.2.3.2 Semi-Conductor Tracker

The SCT uses the same sensor technology as the PD, except with each module composed of two sensors glued back-to-back around a thermally conductive spine with a total nominal thickness of 90 μm (Figure 2.7). The spine was designed to transport heat away from the sensors to cooling and mounting points at the ends of each module, while providing support and the readout connector. The two micro-strip sensors in each module have a strip pitch of 80 μm, and while glued back-to-back, are at a relative rotation of ±20 mrad which helps achieve the nominal resolution of 17 μm in r-ϕ (tested with a beam at normal incidence). The SCT consists of 4088 modules, which tile four cylindrical layers in the barrel, and nine disk layers in each of the two endcaps, providing almost full coverage over the range of the ID. The nominal SCT operating temperature is -7°C to reduce leakage current due to radiation damage [65].

2.2.3.3 Transition Radiation Tracker

The TRT makes use of (cathode) polyimide straw tubes (4 mm in diameter and 144/37 cms in length, for the barrel/endcap respectively), each containing a 31 μm diameter, gold plated tungsten wire (anode). These straws are interleaved with polypropylene fibres in the barrel and foils in the endcap, which act as the transition radiation material. The gas used as the detecting medium in the straw tubes is a mixture of 70% Xe, 26% CO_2, and 3% O_2 at an overpressure of 5-10 mbar. Stable TRT operation requires a re-circulating gas system with continuous monitoring and a filter to maintain gas quality. To avoid contamination due to gas permeating through the straw tubes, an envelope of CO_2 is used, as well as the option to operate with an $Ar/CO_2/CF_4$ gas mixture for a few days of operation to clean Si-based deposits from the anode wire. The CO_2 envelope also serves as the method for which heat dissipation can be conducted away from the straw tubes to two cooling tubes located in the corners of each module. The straws are arranged into modules, with 73/160 straw layers per module, and 96/20 modules in the barrel/endcaps respectively. This provides a nominal > 36 straw hits for traversing charged particles with $p_T > 0.5$ GeV and $|\eta| < 2.0$, lowering to a minimum of 22 straw hits in the barrel-endcap transition region ($0.8 < |\eta| < 1.0$). The TRT is designed to operate at room temperature, and has a nominal tracking resolution of 130 μm in r-ϕ.

2.2.4 Calorimeters

The ATLAS calorimetry system consists of a number of sampling detectors with full ϕ-symmetry and $|\eta|$ coverage up to 4.9 [67]. The system was designed to provide precision measurements of electrons, photons, jets, and E_T^{miss} (as well as their associated triggering) in the high luminosity and extreme energy density conditions produced by the LHC [68]. The calorimeter geometry closest to the beam line (radii $<$ 2.2 m) is housed in three cryostats (one barrel, and two endcaps). The central cryostat contains the barrel ECAL, as well as the superconducting solenoid. Each endcap cryostat contains one Electromagnetic Endcap Calorimeter (EMEC), two Hadronic Endcap Calorimeter (HEC) wheels, and a Forward Calorimeter (FCal). All of the inner calorimeters use Liquid Argon (LAr) as their detecting medium because of its intrinsic linear behaviour and response stability over time, even in high radiation environments [67]. The calorimeter geometry at larger radii (where there is a lower radiation level), consists of one barrel and two extended barrel,

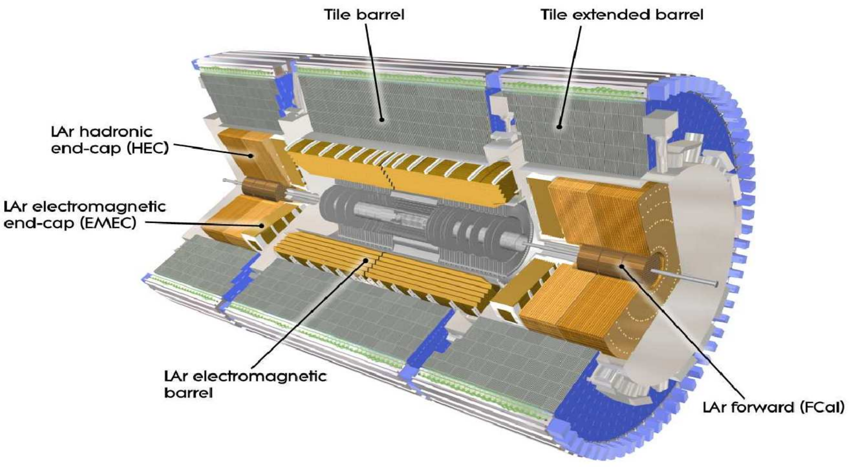

Figure 2.8: A cut-away view of the ATLAS calorimetry system, showing the main components [67].

Component	Barrel		Endcap	
	Coverage (η)	Thickness	Coverage (η)	Thickness
EM Calorimeter	$\|\eta\| < 1.475$	22 X_o	$1.375 < \|\eta\| < 3.2$	24 X_o
LAr Hadronic Endcap	-	-	$1.5 < \|\eta\| < 3.2$	10 λ
LAr Forward Calorimeter	-	-	$3.1 < \|\eta\| < 4.9$	10 λ
Tile Calorimeter	$\|\eta\| < 1.0$	9.7 λ	$0.8 < \|\eta\| < 1.7$	10 λ

Table 2.2: The η coverage and radiative thickness for different components of the ATLAS calorimetry system [67]. The radiation length X_o (g/cm^2), is used to describe high-energy electromagnetic cascades as it is the mean distance at which high energy electrons lose 1/e ($\sim$1/3) of their energy due to bremsstrahlung/pair production. For hadronic showers a more appropriate measure is the interaction length λ (g/cm^2), which is the mean path length required to reduce the number of relativistically charged particles to 1/e.

tile calorimeters, also known as Hadronic Calorimeters (HCAL) which use steel as the absorber material and scintillators as the active detecting medium. An important requirement of the ATLAS calorimetry was to provide adequate containment of electromagnetic and hadronic showers, while limiting leakage into the muon spectrometer, and this was taken into account when considering the radiative depth of the calorimeter systems. An illustrative overview of the ATLAS calorimetry system is presented in Figure 2.8, with the η coverage and radiative thicknesses for the main components listed in Table 2.2.

2.2.4.1 Electromagnetic Calorimeters

The Electromagnetic Calorimetry of the ATLAS detector is designed to stop electromagnetic showers within its volume, making precise measurements of the energy deposited and facilitating the triggering of interesting events. It is entirely contained within three

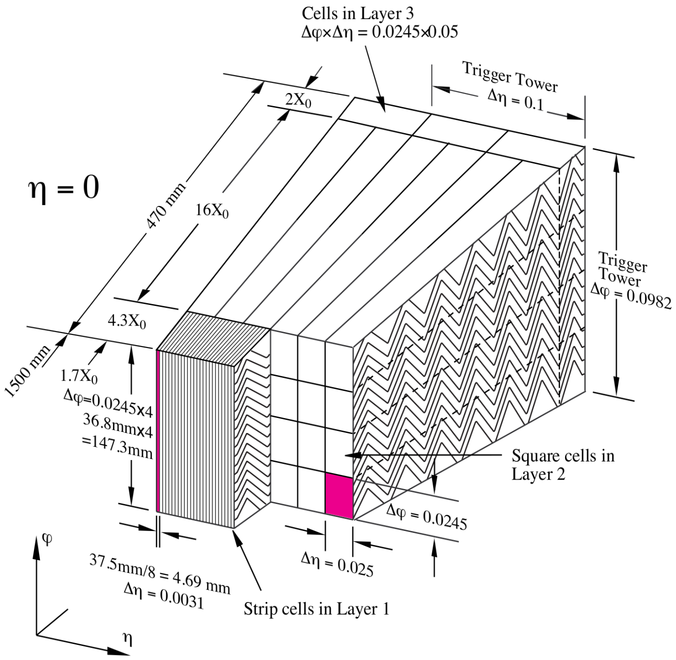

Figure 2.9: Schematic illustration of a barrel ECAL module [67]. The accordion structure is clearly visible with the three module layers shown with associated cell granularity in η and ϕ.

cryostat vessels, divided into one barrel and two endcap components. As the superconducting solenoid is located in front of the ECAL, it is also housed in the central cryostat section to optimise material in front of the ECAL. By removing the need for two separate vacuum walls, the system is optimised for performance with the solenoid amounting to a contribution of 0.63 X_o [68]. The barrel ECAL is split into two half-barrels separated by a 4 mm gap at $z = 0$, while each EMEC is split into two coaxial wheels separated by 3 mm at $|\eta| = 2.5$. The ATLAS EM calorimetry system uses LAr as the active detecting medium, with lead accordion-shaped absorbers. The accordion geometry ensures a uniform performance in terms of linearity and resolution over full ϕ coverage, and allows for multiple active layers (three in the precision region $|\eta| < 2.5$, and two in the range $2.5 < |\eta| < 3.2$). A schematic illustration of one of the barrel ECAL modules is shown in Figure 2.9, with the layout, dimensions, and accordion geometry. Extra coverage is provided at the highest η range by the FCal, whereas presamplers (an instrumented LAr layer) at $|\eta| < 1.8$ provide complementary measurements of energy lost in front of the barrel and endcap EM calorimetry. A summary of the overall energy resolution for the EM calorimetry system is listed in Table 2.1.

2.2.4.2 Hadronic Calorimeters

The ATLAS hadronic calorimeter was designed to contain highly energetic hadron showers, preventing them from leaking into the muon spectrometer after having already passed through the ID, and EM calorimetry system. The hadronic calorimetry system is made up of three different components: The tile calorimeter (HCAL), LAr hadronic endcap calorimeter (HEC), and the hadronic component of the FCal. The tile calorimeter uses steel absorbers and scintillating tiles as the active medium. It is located immediately outside of the EM calorimetry envelope, and comprises of a barrel ($|\eta| < 1.0$), and two extended barrels ($0.8 < |\eta| < 1.7$), each segmented into three layers. Each HEC consists of two (back-to-back) wheels, placed directly behind the EMEC. As the HECs are located inside the LAr cryostat vessel, they use a different technology to the tile calorimeter to optimise their performance. Each wheel consists of two layers made of parallel copper plates interleaved with 8.5 mm LAr gaps which provide the active medium. The HECs are also designed to bridge the material density drops between the tile calorimeter, endcap, and FCal by extending out to $|\eta| = 3.2$. Similarly to the HECs, each endcap cryostat also houses an FCal. The FCal is made up of three modules, with the first (made of copper) optimised for electromagnetic measurements, and the other two made of tungsten optimised for the measurement of hadronic interactions. Each module contains a metal matrix of channels filled with the readout electrode structure and LAr which acts as the detecting medium [62].

2.2.5 Muon Spectrometer

The muon spectrometer makes use of the large superconducting air-core toroids to continue deflecting muons trajectories in the outer reaches of the ATLAS detector. The system provides triggering of muons and high precision measurements within a coverage $|\eta| < 2.7$, and consists of 4 main components: Monitor Drift Tubes (MDT), Cathode Strip Chambers (CSC), Resistive Plate Chambers (RPC), and Thin Gap Chambers (TGC). The MDTs provide precision tracking for muons over the full spectrometer coverage, complemented by the CSCs at ranges $2.0 < |\eta| < 2.7$, which were designed with higher granularity and better performance/hardness in higher radiation environments. The RPCs and TGCs were designed to handle the triggering of muons, as well as secondary track measurements. RPCs are used in the barrel region covering the range $|\eta| < 1.05$, with the TGCs located in the endcap regions triggering in the range $1.05 < |\eta| < 2.4$ (2.7 for tracking). These trigger systems also serve to provide the bunch crossing identification, and well defined p_T thresholds for the muon spectrometer. One of the greatest factors affecting the overall performance of the muon spectrometer system is the alignment of the muon chambers with respect to each other and the overall detector. The tolerance of the relative alignment for the muon chambers is necessarily 30 μm to provide the required muon momentum measurement accuracy [62].

2.2.6 The Trigger and Data Acquisition System

The TDAQ system collectively handles the triggering and readout/storage of interesting physics events. The ATLAS trigger consists of three distinct levels of event selection: Level-1 (L1), Level-2 (L2), and Event Filter (EF). Together the L2 and EF form the High-Level Trigger (HLT) which is based on commercially available computing, where as the L1 trigger is implemented with custom made electronics to satisfy ATLAS specifications [69].

2.2.6.1 The Level-1 Trigger

The L1 trigger is designed to be sensitive to signatures from high p_T leptons, photons, and jets, as well as events with large E_T or E_T^{miss}. High p_T muons are triggered using the RPC and TGC subdetectors. The L1 trigger has 2.5 μs after each associated bunch crossing to reach its decision with a maximum accept rate of 75 kHz (upgradable to 100 kHz) [69]. To be able to make the most efficient L1 decision given the time restraints, the L1 trigger uses reduced granularity information from both the muon and calorimeter subsystems.

2.2.6.2 The Level-2 Trigger

The L2 trigger is seeded by Regions of Interest (ROIs), which are regions of the detector designated by the L1 trigger to possibly contain trigger objects from the event. The L2 trigger reduces the event rate to below 3.5 kHz with a decision time per bunch crossing of $\sim$40 ms [69]. The time constraints on the L2 decision means that as with L1, limited information is read out from the detector to reach a decision. This process is optimised by using the L1 ROI location, energy, and signature type, to transfer data from selected parts of the detector at full granularity, as well as using track matching from the ID.

2.2.6.3 The Event Filter

The EF is the final stage of the ATLAS trigger system, and is designed to reduce the event rate down to the recordable rate of 200 Hz, with an average processing time of $\sim$4 s [69]. The EF uses offline algorithms and analysis procedures to fully reconstruct events that are accepted at L2, using information from the whole detector to make the final decision whether to write the event to permanent storage for offline analysis.

2.2.6.4 Data Acquisition

The ATLAS DAQ system is multi-functional in its design. It has the ability to receive and buffer event data at the L1 rate, transferring relevant information from the detector to the trigger system as required to enable each trigger level to reach its decision. The DAQ system also writes the selected event data to permanent storage for offline analysis, as well as continually controlling and monitoring the ATLAS detector systems during data taking.

Chapter 3

Event Simulation and Reconstruction

To perform a detailed search analysis in this thesis, it is vital to have an accurate simulation of events at the LHC, and an understanding of how objects are reconstructed in ATLAS as they traverse the detector medium and its various components. To this end, the ATLAS collaboration has created the ATHENA framework [70], which can create and analyse simulated data called Monte Carlo (MC) samples, carrying events from their generation through to output in a format which is identical to that of the true detector. The simulation chain will be discussed in this chapter with particular focus on the reconstruction of electrons. Generally the chain can be divided into three stages: event generation, detector simulation and physics interactions, and digitisation of readout. Structuring the ATLAS event simulation in this way is an effective use of resources, and simplifies software validation. For example, as each stage has an output format which is in turn input to the next, a large dataset of generated events can be re-simulated with different detector conditions or software version, without having to re-generate the events.

3.1 Simulation Chain

Event Generation

The generators used by the ATLAS collaboration are generally FORTRAN based, producing events in standard HepMC format [71], and are responsible for the generation of particles as well as handling prompt decays from particles such as the $W^{\pm}$ and Z^0 boson. This information, along with any particle which is “stable”, i.e. does not promptly decay and so travels through the detector medium, is stored in the event generation record. A filter can be applied to the event generation stage, only storing information relevant to a certain process or decay channel. For example in this thesis when generating the G^* and Z' MC samples, these were created independently for each channel, filtering out all decays of the signal process that were not directly to the channel of interest. As this stage handles particle generation and only prompt decays, there is no need to simulate any detector geometry information, which allows for a faster generation time. A history of the particles and their interactions is also stored at this stage, known as "truth" information.

Detector Simulation

The simulation stage retains a record of all particles produced by the generator, to which cuts can be applied, limiting simulation to only certain particles if required. For all MC samples in this thesis, full detector simulation was used with GEANT 4 [72]. For the various signal samples, validation was first required before the full simulation sample was run, to ensure the target processes were being correctly generated and processing time was not wasted. For this validation step the fast simulation program ATLFAST-I was used.

Full Simulation

For full simulation, each particle is propagated through the full ATLAS detector description by GEANT 4, with the ability to set variable detector information such as configuration and/or misalignment at run time. During the simulation stage, information such as $\sum E$, position, and time, are stored for energy deposits in sensitive detector components. These deposits are known as "hits", and output from the detector simulation stage is in a hit-file format. The detector simulation stage also stores its own truth information, in the form of truth tracks, decays, and location of conversions.

ATLFAST-I Simulation

Because of the complex physics description provided by GEANT 4, and the detailed detector description, full simulation is not always a viable option for processes such as QCD dijets faking electrons which would require literally billions of simulated events to statistically describe the background expected in a Z^0 boson like analysis with $\sim$1fb^{-1}.

This can also be applicable for SUSY/Exotic searches in which there are many theoretical parameters to test, meaning a large number of high statistic samples are required. In full simulation, over 75% of the processing time is spent simulating electromagnetic particles [70], whereas ATLFAST-I performs a fast simulation of the detector using parameterisations of detector and simulation effects, such as reconstructed energy smearing for electrons which is taken from fully simulated events, to decrease overall processing time by a factor of 1000 compared to full simulation [70]. ATLFAST-I takes the same HepMC input and produces the same hits file format output as full simulation.

Digitisation

The digitisation stage of event simulation at ATLAS first creates Simulation Data Objects (SDO), which are maps linking the hit-file deposit information to the particles in the simulation truth record. This stage also handles the rates of particular types of events such as: beam halo, beam gas, and pile-up, which help reproduce realistic detector conditions. Pile-up is particularly important, as it describes the number of interactions per bunch crossing (In-Time Pile-up), and residual energy deposition in the calorimeter (Out-Of-Time Pile-up). Also incorporated at this stage is the hardware based L1 trigger (albeit in a pass through mode) and any detector noise simulation. The digitisation uses all of this information to generate the detector signal, i.e. voltages and time responses, proceeded by simulation of the Read Out Drivers (RODs), and finally creating an output in Raw Data Object (RDO) format. The ATLAS detector itself has a bytestream output format, however this is easily converted to and from RDO format, which forms the basis for all subsequent analysis formats.

3.2 Data Samples

The data storage infrastructure of the ATLAS collaboration allows physics analysis groups to have great flexibility in their choice of analysis procedure. The data taken by the detector is first stored in RDO format, subsequently being written to Analysis Object Dataset (AOD) and Event Summary Dataset (ESD) format which can then be used for data analysis, containing nearly all of the variables recorded in data. As individual analyses often only require a subset of these variables it is sometimes desirable to have a data format with only the variables relevant to the given analysis stored. This reduced data format is based on flat ROOT ntuples called DnPD (Derived nth Physics Dataset), of which this analysis uses the n=3 derivation, and is generally favoured as the dataset size is smaller than that of the AOD/ESD format, leading to faster analysis times. It is sometimes required to further reduce the D3PD format in size, to give the final format used for analyses, called D3PD skims. As D3PDs are generally created on a per physics group basis, there is still a degree of generality in the choice of variables, which can be stripped away for a specific search channel (called slimming). On top of this there is a level of basic analysis which is unlikely to change over time for a search, such as requiring at least two electrons with a minimum p_T requirement (this process is called thinning). Therefore it is prudent to apply this slimming and thinning process to the D3PD format, producing highly specialised D3PD skims for a specific search channel which take orders of magnitude less time to analyse, while producing the same results. The author of this thesis produced skims for all 2010/11 data in the electron channel, from D3PDs originally produced for the e/γ group. For approximately 1fb^{-1} of data in 2011, the total unskimmed D3PD format dataset size was 2738 GB, with an average size of 25 KB per event; after slimming/thinning the skimmed D3PD format size was just 109 GB (96% reduction), with an average event size of 4.5 KB. These skims were used by the dilepton exotic physics group to do the entire analysis in the dielectron channel during 2010/11, while colleagues produced similar skims based on dimuon and diphoton channel search requirements. In the author's role as data manager for the dilepton exotics group in 2010/11, it was important to validate the data format chain from AOD $\rightarrow$ D3PD $\rightarrow$ Skim, checking that at each format level the number of candidate events passing the event selection as described in Chapter 5, were identical, and thus no analysis specific information was lost during the reduction process.

The dataset used for this thesis was collected from the 23rd of March to 22nd of August 2011 at a centre of mass energy $\sqrt{s} = 7$ TeV. The physics data collected totalled an integrated luminosity of 2.12 fb^{-1}. A list of the runs that make up this dataset can be found in Appendix A.

3.3 Monte Carlo Samples

The MC samples used in this thesis are in the same format as the data samples, processed into D3PD format from AOD, but without the requirement of the extra skimming stage due to the relatively short analysis time for MC samples. All MC was generated using GEANT 4 full simulation in ATHENA release 16; the production version used was MC10b which importantly simulates an LHC proton bunch spacing of 50 ns, which was the most appropriate for 2011 data taking, requiring the minimal amount of MC pileup reweighting. The MC samples analysed fall into two distinct categories: Signal, and Background. The MC signal samples used represent the processes which are of interest to the search analysis, with MC background samples consisting of any background process which is not negligible with respect to the signal. The signal processes of interest to this thesis are $Z' \rightarrow e^+e^-$ and $G^* \rightarrow e^+e^-$ which were generated using PYTHIA with the MRST2007LO* PDF set[1], at various masses (and couplings for G^*). A list of the signal MC samples used in this thesis is provided in Appendix B.1. MC samples were also produced for the SM backgrounds not deemed negligible to this search, using a variety of generators at Next-to-Leading Order (NLO) accuracy. The Z^0/γ^* background was generated with PYTHIA using the MRST2007LO* PDF set as was done for the signal samples. The $W+$jets background was generated with ALPGEN for the matrix elements, JIMMY to describe multiple parton interactions, and HERWIG for the remaining underlying event and parton shower. The $t\bar{t}$ sample was generated in a similar manner to $W+$jets but with MC@NLO for the matrix elements. The diboson samples were generated using HERWIG, with a single lepton filter applied. All background MC samples are supplied in Appendix B.2. A list of the relevant software and versions used for MC10b generation is shown in Table 3.3.

Program	Version	Reference
ATHENA	16	[70]
PYTHIA	6.421	[74]
ALPGEN	2.1.3	[75]
CompHEP	4.4.3	[76]
MC@NLO	3.41	[77]
JIMMY		[78]
HERWIG	6.510	[79, 80]

Table 3.1: List of the important simulation/generation software used for MC10b production.

---

[1] LO* denotes the use of a LO PDF set, with theoretical NLO coupling and scale factor corrections [73]

To increase the precision of the Z^0/γ^* estimate further, as well as that for Z'/G^* where applicable, QCD and EW K-factors were used to improve cross section calculations from LO* to Next-to-Next-to-Leading Order (NNLO) accuracy. Appendix B.3 provides the details of the QCD K-factor NNLO calculations using PHOZPR [81], resulting in an invariant mass dependent QCD K-factor that is applied to MC on an event by event basis. Similarly, Appendix B.4 details the EW K-factor NNLO calculations obtained using HORACE [82]. Table 3.3 summarises some representative values of the mass dependent QCD and EW K-factors used in this search.

Mass [GeV]	500	750	1000	1250	1500	1750	2000
$K^*_{QCD} = \frac{\sigma_{NNLO}}{\sigma_{LO*}}$	1.131	1.109	1.080	1.041	0.990	0.929	0.860
$K^*_{EW} = \frac{\sigma_{NNLO}}{\sigma_{LO*}}$	1.032	1.016	1.000	0.986	0.971	0.956	0.941

Table 3.2: Representative values of the mass dependent K-factors applied to Drell-Yan background, and Z'/G^* signal, where applicable.

In the case of setting exclusion limits on a signal process, it was identified that a discrete number of mass points as provided by the individual MC samples listed for the Z' (Table B.1) and G^* (Table B.2), would lead to a limit with large interpolated regions between mass points. To avoid this for the Z', a template sample was used (the G^* template was not yet available) when setting limits on the signal process (shown as the first entry in Table B.1). A template sample is one that is made by modifying PYTHIA to produce a "flat" sample where the Breit-Wigner resonance terms have been removed in the generation, along with parton luminosity effects, and in the case of the G^*, mass dependent factors accounting for the mixed $gg/q\bar{q}$ production terms. This leads to a very broad signal mass distribution (colloquially called "flat"), with events populating the whole spectrum from low to high mass (see Figure 3.1 (left)). The relevant resonance terms and effects removed from the generation can then be re-added at a later stage of the analysis using the flat sample to produce a resonance at any mass (or coupling) desired (see Figure 3.1 (right)), using the theoretical dependence of the signal process parameters. This allowed limits to be set on mass points every 40 GeV in the search region, producing a far smoother exclusion limit, without the need for production and validation of numerous individual mass point samples. The author of this thesis helped validate the Z' template sample for the mass range 130 GeV to 3 TeV, which was subsequently used in the ATLAS dilepton 2010/11 analyses [83, 84]. The author also designed and validated a G^* template

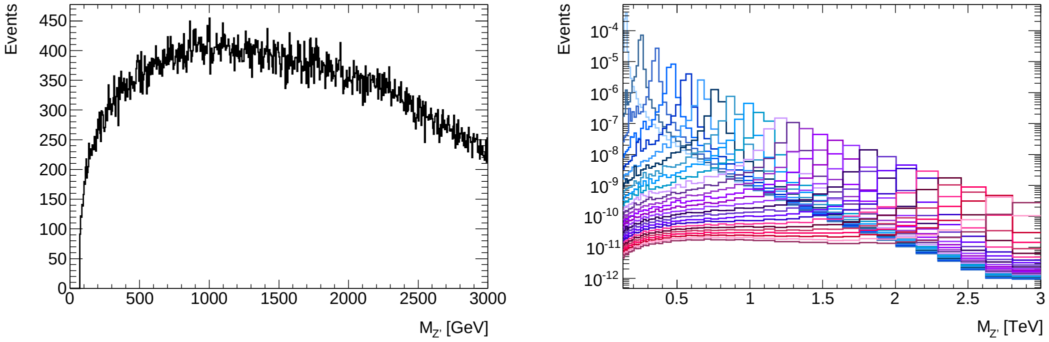

Figure 3.1: An example of the template sample production method showing the "flat" Z' truth mass spectrum (left), and the result of reweighting to various Z' masses (right). For limit setting mass points are generated every 40 GeV (displayed here every 80 GeV) from 130-3000 GeV.

sample, taking into account the extra complication due to $gg/q\overline{q}$ production terms, but this sample was not available in MC10b at the time of writing this thesis. However, the G^* template is currently being used in MC11c by the ATLAS dilepton and diphoton analyses for 2011/12. Validation of the template sample was undertaken by comparing dedicated production at a range of mass points (and couplings in the case of G^*) with the reweighted template, checking for any discrepancies in the line shape, and agreement close to within statistical error.

3.4 Analysis Software Versions

A summary of the software and versions used for the dielectron resonance search in this thesis are presented in Table 3.4. AOD analysis was performed entirely within the ATHENA framework, using PYTHON as an object orientated scripting and interpreter language to configure and load the required C++ libraries. In contrast, the D3PD analysis used C++ compiled ROOT code, which linked to specific ATHENA packages as needed. The specific ATHENA packages used are listed in the latter section of Table 3.4.

3.5 Electron Reconstruction and Identification

As the main focus of this thesis is to search for the decay of exotic heavy resonances to two electrons, it is important to understand the process and effects of electron reconstruction in the ATLAS detector. The unprecedented level of QCD processes created at the LHC mean that efficient and precise reconstruction/identification of electrons is a difficult task,

Purpose	Version/Package	Reference
ATHENA	16.6.5	[70] [85]
PYTHON	2.6.5	-
ROOT	15.28/00c	[86]
Analysis	AnalysisExamples-00-22-00	[87]
Pileup Reweighting	PileupReweighting-00-00-12	[88]
Good Runs Lists	GoodRunsLists-00-00-89	[89]

Table 3.3: Software and versions used for the analysis performed in this thesis.

with the expected ratio of electron/jets $\sim 10^{-5}$ at p_T = 40 GeV [90]. This section will describe the performance and calibration of the ID and ECAL with respect to electrons, as well as their electron reconstruction and identification procedures.

Electron Algorithms

Each of the two ATLAS subdetector systems important for electron reconstruction and identification, namely the ID and ECAL, use separate reconstruction algorithms which are combined using a likelihood ratio to make best possible use of the tracking and electron identification capabilities of the TRT in the ID, as well as the granularity of the ECAL. Both of these algorithms are discussed here.

Inner Detector

The inner detector measures charged particles with $p_T > 0.5$ GeV and $|\eta| < 2.5$, playing a central role in electron identification at ATLAS below energies of 25 GeV. To create tracks, raw information is first taken from the PD and SCT subsystems, with hits on adjacent strips merged to form clusters. The clusters are then associated with each other and transformed into space points. Track-finding seeds are created from a combination of these space points using the three PD layers and first SCT layer, and extended into the outer SCT layers to form a track candidate. Next the candidates are fitted using a suite of track-fitting tools, with outlying clusters removed and fake tracks rejected. These selected tracks are further extended into the TRT which uses raw timing information to construct calibrated drift circles. If a given candidate track is associated with a TRT drift circle, then the track is refitted using all three subdetector systems. Dedicated post processing tools are used for primary and secondary vertex finding, which is associated to the reconstructed tracks. At energies < 25 GeV, flexibility in the electron track fitter allows for compensation for effects like bremsstrahlung, which is especially important for electrons that have radiated a large fraction of their energy ($\sim$50%) in the silicon layer, and enables significant improvements for reconstructed track parameters and electron energies in this energy region [90]. The TRT is of particular importance for electron identification as it checks for electron tracks from photon conversions, which is vital considering on average 10-50% of photons convert to an e^+e^- pair within the ID at energies < 25 GeV.

Electromagnetic Calorimeter

Electron and photon reconstruction in the ECAL is seeded using a 5x5 ($\eta \times \phi$) cell sliding window algorithm in the middle layer. A cluster of fixed cell size is then reconstructed around the seed with 3x7 cells used in the barrel ECAL for electrons and converted photons, and a 3x5 cell cluster size for photons. In the end-cap region a 5x5 cell cluster size is used for both electron and photons. The most important corrections to the calculated cluster energy are the η dependent weights, which simultaneously optimise the energy resolution and response linearity of the ECAL. Four distinct weights are used: s(η), an overall scale factor; c(η), an offset weight; $w_0(\eta)$, to correct for energy losses upstream of the presampler; and $w_3(\eta)$, to correct for longitudinal leakage. The incorporation of these weights into the total cluster energy calculation is shown in Equation (3.1), where E_{PS}, E_{Strips}, E_{Middle}, and E_{Back}, are the energies calculated from the Presampler, Strip, Middle, and Back, calorimeter layers respectively (see Figure 2.9). The weights were initially determined using simulated single particle events with energies in the range 5-200 GeV, however with the advent of real data these maps were regularly calibrated and tuned. As disclosed in Chapter 4, some outlying electron energies were due to over calibrations in these weight maps, and information from the study was given as feedback to further improve the maps.

$$E = s(\eta)[c(\eta) + w_0(\eta).E_{PS} + E_{Strips} + E_{Middle} + w_3(\eta).E_{Back}] \tag{3.1}$$

Standard Electron Reconstruction and Identification

Standard electron reconstruction and identification with the ATLAS detector makes use of both the ID and ECAL electron algorithms. A calorimeter seed (identified using a

5×5 cell, sliding-window algorithm in the middle layer of the ECAL) is loosely matched to a reconstructed track, and a flag set if it matches a photon conversion reconstructed from the ID. Electron identification requires that the ECAL seed is associated to a track with no conversion flagged. All electron shower shape variables are calculated using the ECAL, with some combined reconstruction properties such as E/p which is the ratio of the calorimeter energy and the ID measured momentum, and $\Delta\eta$, $\Delta\phi$, which is the difference between the ID extrapolated value into the calorimeter, and the cluster value, compared at the first layer of the calorimeter. These shower shape variables are used to identify isolated electrons and reject fake signals such as those from QCD dijets, on a cut based approach. Low p_T electrons $<$ 25 GeV rely more on the ID subsystems, whereas high p_T electrons (above 25 GeV) solely use the ECAL for energy calculations, and the ID for direction information such as η and ϕ. This is because at lower energies a greater fraction of the electron energy is lost before leaving the ID, giving greater weight to the use of tools such as bremsstrahlung recovery, whereas at higher energy most of the electron energy is contained within the ECAL, but the direction is still more precisely measured by the ID. Another useful combined reconstruction property for identification of electrons is the ratio of high threshold TRT hits to low threshold track hits, which distinguishes electrons from pions, thus helping to reject the charged QCD dijet background.

Inner Detector and Electromagnetic Calorimeter Performance

Due to the large volume of the ATLAS detector, material effects are of great importance to the performance of its subdetectors. The material in front of the ECAL and its presamplers, including the ID itself (which in turn has losses due to material thickness), require a high level of calibration to ensure performance is maximised and true electron energies/directions are preserved. Figure 3.2 shows the energy lost by electrons before the ECAL (left) and from the ID material (right), as a function of $|\eta|$. The left plot in Figure 3.2 demonstrates that extra material due to cabling in the crack region between the barrel and endcap sections of the ECAL seriously affect the performance of the calorimetry in that region. It is for this reason that in Chapter 5, the crack region ($1.37 < |\eta| < 1.52$) is excluded from the search analysis.

It is also important to consider the ATLAS detector's electron energy, and dielectron invariant mass, resolution. This is to understand the restrictions when observing high

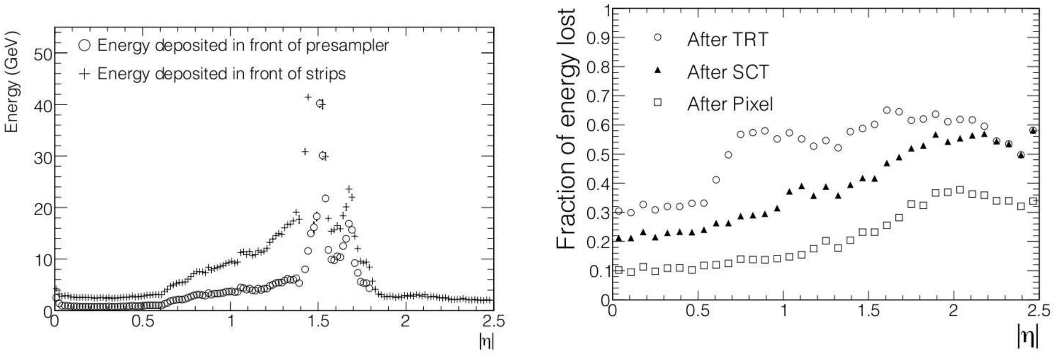

Figure 3.2: The average energy loss for (left) 100 GeV electrons before the ECAL/presamplers, and (right) fractionally for electrons with p_T = 25 GeV from the ID. Both results are displayed as a function of $|\eta|$. The fraction of energy lost from the ID is not found to be a strong function of the electron energy above 25 GeV [90].

mass resonances of sufficiently narrow width (such as a G^* with low k/$\overline{M}_{Pl}$ value), and study the expected response of the detector in cases where the signal width is resolution dominated. The expected form of the energy resolution is shown in Equation (3.2), where a corresponds to a stochastic term [67], b describes the contamination due to electronic noise and pile-up [91], and c is a constant term reflecting local non-uniformities in the response of the calorimeter [67]. The general performance goals of the ATLAS detector for these parameters, as described in Table 2.1 from [67], and [91], are 10%, 0.5 GeV, and 0.7% respectively for a, b, and c, across the η and energy ranges relevant to this search (these example values are used for comparison purposes in both the barrel and endcap).

A resolution study performed by the author of this thesis using Z' MC is presented here. Figure 3.3 shows the electron energy resolution in the (upper) barrel and (lower) endcap. Figure 3.4 shows the dielectron invariant mass resolution for (upper) Barrel-Barrel (BB), and (lower) Barrel-Endcap (BE) / Endcap-Endcap (EE) events. This study uses Z' events that pass the MC event selection described in Chapter 5.2, and requires that the two candidate electrons are matched to respective truth electrons originating from the Z'. For electrons that meet these requirements, the resolution is calculated as $\frac{E_{reco}-E_{truth}}{E_{truth}}$ and stored in bins of E_{truth} (or M^{ee}_{reco} and M^{ee}_{truth}). A Gaussian is then fitted to the resolution distributions in each E_{truth} bin, in a range ±RMS from the mean of the distribution. For each E_{truth} bin, the width (σ) of the Gaussian fit is then plotted versus the E_{truth} central bin value, and a line fitted through the values of the form shown in Equation 3.2.

$$\frac{\sigma(E)}{E} = \frac{a}{\sqrt{E}} \oplus \frac{b}{E} \oplus c \tag{3.2}$$

The electron energy resolution is shown to be well modelled in Figure 3.4, and although the result is slightly worse than the target resolution, it is in approximate agreement with other studies [91]. Above 1000 GeV the energy resolution becomes essentially constant at 0.84% for the barrel and 0.85% for the endcap. The dielectron invariant mass resolution is shown to be in close agreement with the target performance with a constant component of 0.67%/0.88% for BB and BE/EE events respectively. The difference between the barrel and endcap resolutions in both cases is due to the ECAL region $|\eta| > 2$, where the strip granularity of the endcap becomes progressively coarser than the barrel. The increase in mass resolution compared to the electron energy is due to the added information provided by the ID which gives track and opening angle information to the electrons used in the invariant mass calculation (Equation 5.3). A further study by the author of this thesis was designed to investigate the effect of the ATLAS detector resolution on observed signal resonance widths. The upper plot in Figure 3.5 shows the resonance width versus MC truth mass for Z'_{SSM} and RS G^* with various k/$\overline{M}_{Pl}$ values. The data points represent the resolving width of the ATLAS detector, calculated as the difference between the true and reconstructed mass width from Z'_{SSM} MC. At the point where the theoretical (truth) width for a given resonance falls below the resolving width, the signal is deemed to have become resolution dominated which means the observed invariant mass distribution will effectively be smeared out to the resolving width. It is presented here that at low invariant masses ($<$ 200 GeV) most Z'/G^* resonances would become resolution dominated, whereas at higher invariant masses ($>$ 200 GeV) the Z'_{SSM} width could be resolved by the ATLAS detector. For the RS G^* it is evident from this plot that at some value of k/$\overline{M}_{Pl}$ the resonance would become resolution dominated at all masses. Therefore by parameterising the RS G^* theory lines on the upper plot of Figure 3.5 and scanning through in steps of k/$\overline{M}_{Pl}$ = 0.001, the lower plot of Figure 3.5 presents the mass below which a RS G^* resonance becomes resolution dominated versus k/$\overline{M}_{Pl}$ coupling value. It is shown that for an RS G^* with k/$\overline{M}_{Pl} < 0.073$, the resonance would always be resolution dominated below a mass of 3 TeV. These restrictions mean that any observed signal resonance with detector resolution width could only set an upper limit on k/$\overline{M}_{Pl}$ of 0.073. A variation of the observed signal cross section could be used to infer couplings below this value, however varying the G^* coupling to SM particles could also give this effect meaning the result would be inconclusive in this respect.

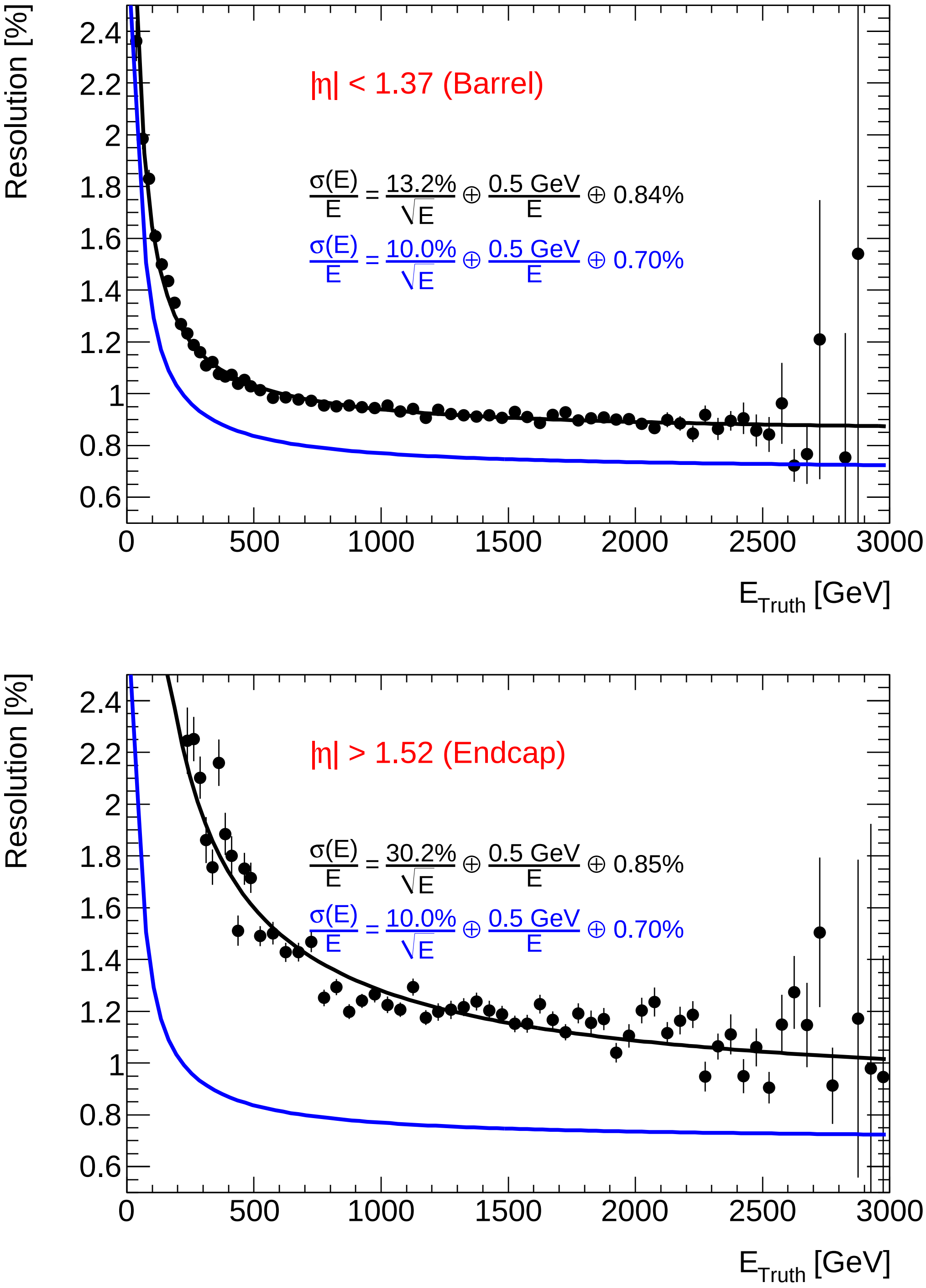

Figure 3.3: Electron energy resolution for (upper) barrel, and (lower) endcap electrons in Z' MC. The blue line shows the target design energy resolution of the ATLAS detector [67, 91]. E_{truth} is binned every 25 GeV from 0-500 GeV, and every 50 GeV from 500-3000 GeV.

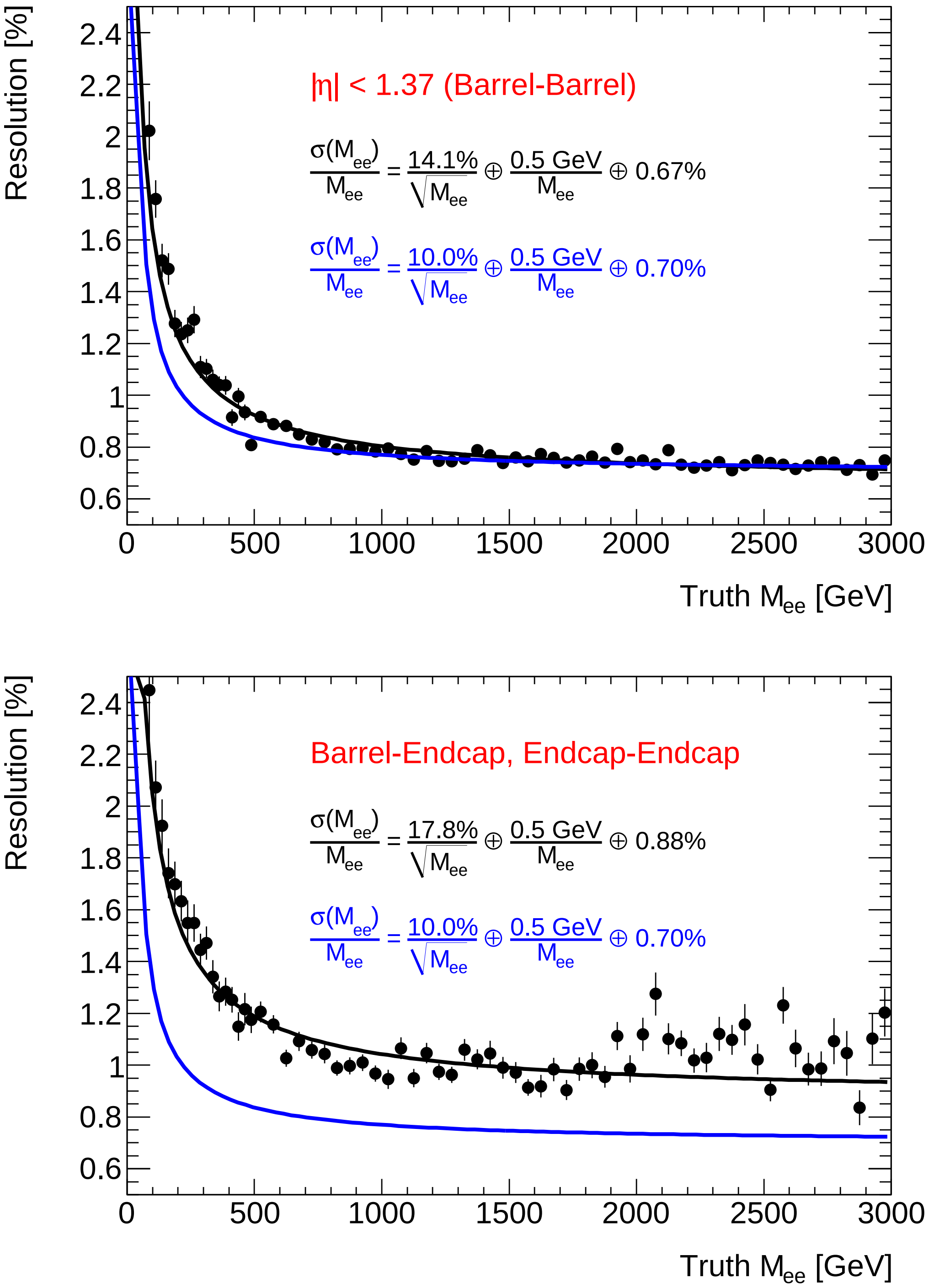

Figure 3.4: Dielectron invariant mass resolution for (upper) barrel-barrel, and (lower) barrel-endcap/endcap-endcap events in Z' MC. The blue line shows the target design energy resolution of the ATLAS detector [67, 91]. M_{ee} is binned every 25 GeV from 0-500 GeV, and every 50 GeV from 500-3000 GeV.

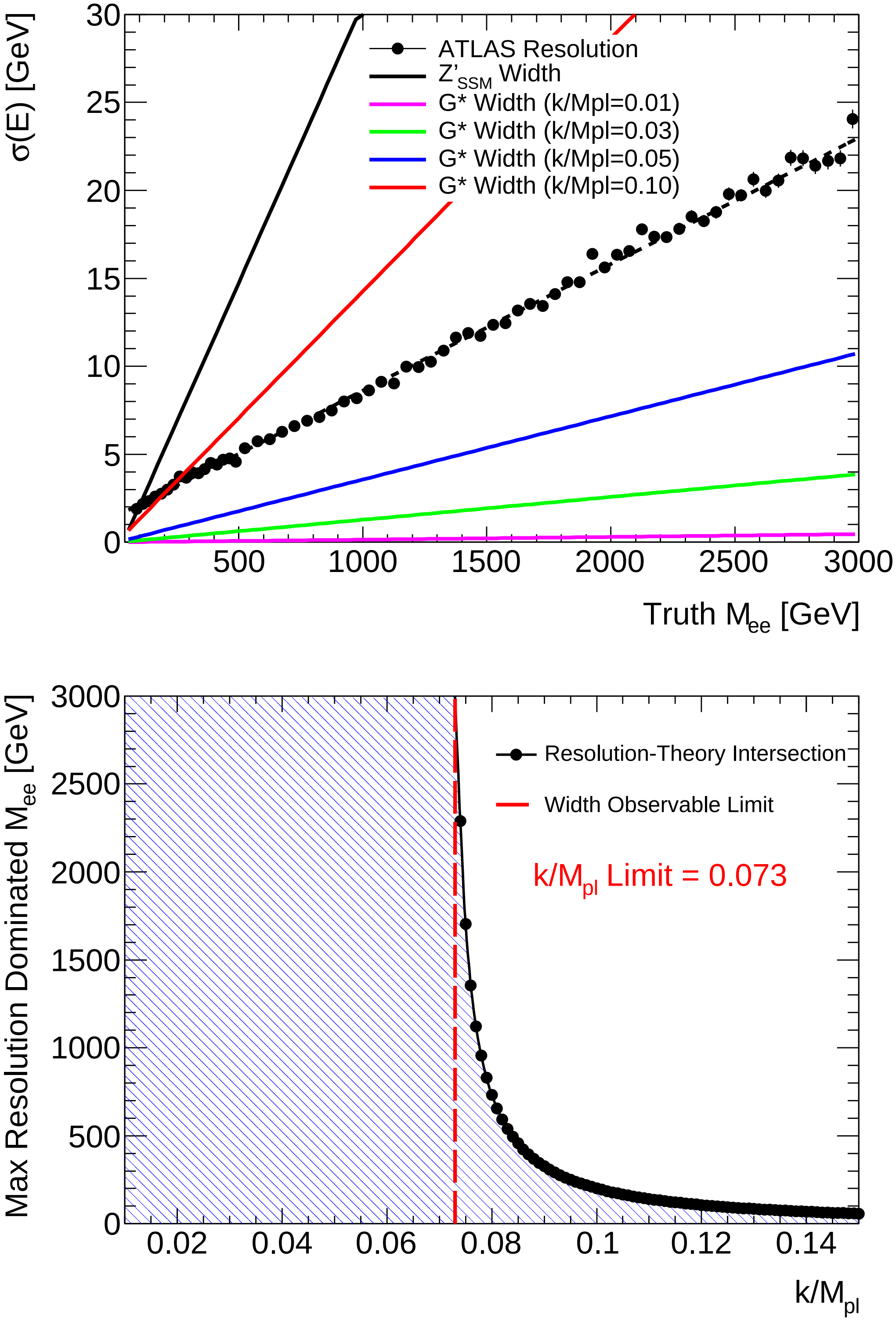

Figure 3.5: The effect of ATLAS detector resolution (BB/BE/EE) on the observation of Z'/G^* resonance width. The Z'/G^* width, and ATLAS resolving width, versus mass is shown (upper). Also shown (lower) is the maximum resolution dominated G^* mass for a given k/$\overline{M}_{Pl}$ value. The excluded region (blue-striped) indicates resolution dominated G^* parameters. The limit line (red-dashed) shows the k/$\overline{M}_{Pl}$ below which all masses considered are resolution dominated for a G^* resonance.

Chapter 4

High E_T Electron Outlier Study

4.1 Motivation

This study was performed to ascertain how consistently electron E_T is reconstructed between different trigger levels of the ATLAS trigger system (EM objects will be mentioned instead of specifically electrons from now on as at L1 objects are not yet defined). The study will investigate any inter-trigger level outliers found to feedback and improve performance, or identify defects in the detector which require further understanding. An initial study was done with early data at $\sqrt{s}$ = 900 GeV during the commissioning phase, and then followed up with a re-assessment study at $\sqrt{s}$ = 7 TeV.

4.2 High E_T Electrons and the ATLAS Trigger System

The three trigger levels of the ATLAS trigger system (L1, L2, and EF) use different subsets of detector components to make their decision on whether to accept or reject a given event. The number of systems available to the trigger level is constrained by the amount of time each level is allowed to make its decision. The L1 trigger decision is based on reduced granularity information from the ECAL, giving only GeV resolution estimates of E_T. The L2 trigger looks at ROIs, identified by the information from L1 (such as position in η and ϕ, as well as E_T estimates of the candidate). The L2 trigger makes its decision using the ROIs with full precision and granularity of the calorimeter, along with track information from the ID, and the TRT if required. This enables the L2 trigger to give MeV resolution estimates of object E_T. The last stage of the trigger system is the EF. After an event has passed the L2 trigger it is evaluated by the EF which, while online, uses offline algorithms and methods to make its decision based on the most accurate information available. The EF uses offline calibration and alignment as well as a magnetic field map that accurately represents the online environment at the time. The EF confirms and then uses the L2 information to run more refined and complex algorithms which were not possible at L2 due to time constraints [69]. While the energy resolution may be the same as at L2, the E_T of the object is recalculated with the more complex methods (including bremsstrahlung recovery for electrons), meaning that the estimate can be different from that at L2.

4.3 Inter-Trigger Level Study at $\sqrt{s}$ = 900 GeV

An outlier study was initially performed at $\sqrt{s}$ = 900 GeV as part of the commissioning of the ATLAS detector. It was aimed at investigating the highest E_T inter-trigger level outliers found in early data to help understand how the detector responds to high energy collisions, and so that as the centre of mass energy was increased, the collaboration could go forward with knowledge of how discrepancies seen at lower energies might manifest themselves in the new energy regime. The study also served as a channel for feedback to enable re-calibration of detector components if necessary, and to identify defects if a solution to an outlier could not be found.

This study was performed on a list of runs contained within one of the first so called "Good Runs Lists" (a list released by performance groups to indicate which luminosity blocks[1] during any given run, had stable beam conditions where all the required subsystems to do with an analysis have been judged to be working nominally). The data constituted an integrated luminosity of a few nb^{-1}, and was recorded between the 6th and 15th of December 2009. The only other requirement made on these events were that they passed the lowest electron trigger in the trigger menu at the time, L1_EM3, which resulted in 1136 events that were suitable for this initial study. The EM objects within these events, then underwent a series of selection criteria, mainly to assess the suitability of the objects. A fiducial cut of $|\eta| < 2.5$ was applied to select barrel and endcap EM objects, with a spatial matching cut of $\Delta\text{R} < 0.15$ applied between the same object at the

---

[1] Luminosity blocks contain roughly 2 minutes of data taking, but can vary depending on run conditions.

two trigger levels being compared. The E_T of the EM objects passing these cuts were then compared at the different trigger levels in detail, searching for outliers. A lower E_T threshold of 4 GeV was also applied to avoid low energy noise not of interest to this study.

The definition of an outlier for the study was based on the aim of looking at the highest energy outliers, as these are of most interest to this thesis, and also because the software/hardware being used was (or in the near future would be) accessing a new, higher energy regime that had not previously been experienced. The mean of the energy resolution distribution between the two trigger levels being compared was used to set the nominal difference expected (Resolution = $(A_{E_T}\text{-}B_{E_T})/B_{E_T}$, where A and B are the two trigger levels to be compared [1]), and a Gaussian fitted, with events found to be $\pm 2\ \sigma$ from the mean of the distribution being classified as outliers in this study. Degeneracy in the EM object combinations (at different trigger levels) was also considered, as for each event multiple EM objects could be accepted; sometimes more than 10 objects at a trigger level would pass the cuts. However, each object was only matched (if possible) once, and then taken out of the selection, leaving only those objects that had not yet been matched to be selected from upon the next iteration, until no more matches were possible. A summary of the EM objects studied, and the number of outliers found, at each trigger level for the $\sqrt{s}$ = 900 GeV study can be found in Table 4.1.

Comparison	L1 vs L2	L1 vs EF	L2 vs EF
EM Objects	620	585	591
Outliers	67	53	42

Table 4.1: Summary of $\sqrt{s}$ = 900 GeV study to find and identify high E_T EM outliers during the commissioning stage of the ATLAS detector.

Level-1 versus Level-2 Study

This section describes the results of the L1 vs L2, EM object comparison. In Figure 4.1 the distribution of the resolution vs $L1_{E_T}$ is shown (upper left), with a dashed line representing the mean resolution, bounded by two solid lines denoting the $\pm 2\ \sigma$ outlier boundary. The upper right plot of Figure 4.1 indicates the remaining candidates after those objects determined not to be outliers were removed from the sample. The lower two plots mirror the above by showing the $L2_{E_T}$ vs $L1_{E_T}$ before (lower left), and after (lower right), non-outlier subtraction from the plots.

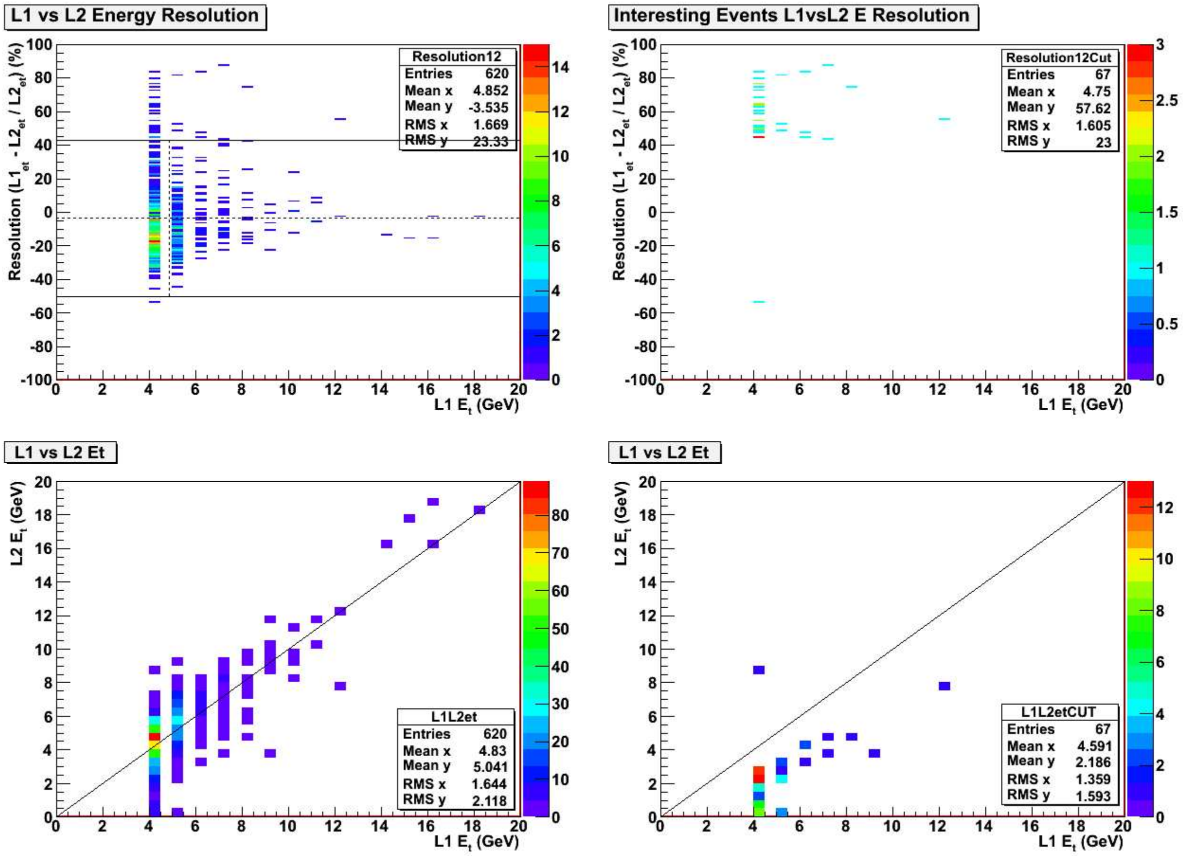

Figure 4.1: Level-1 vs Level-2 object comparison from upper left clockwise; Resolution vs L1$_{E_T}$ of all objects passing cuts; Resolution vs L1$_{E_T}$ of object comparisons determined to be outliers; L2$_{E_T}$ vs L1$_{E_T}$ of object matches determined to be outliers; L2$_{E_T}$ vs L1$_{E_T}$ matches for all objects that pass cuts.

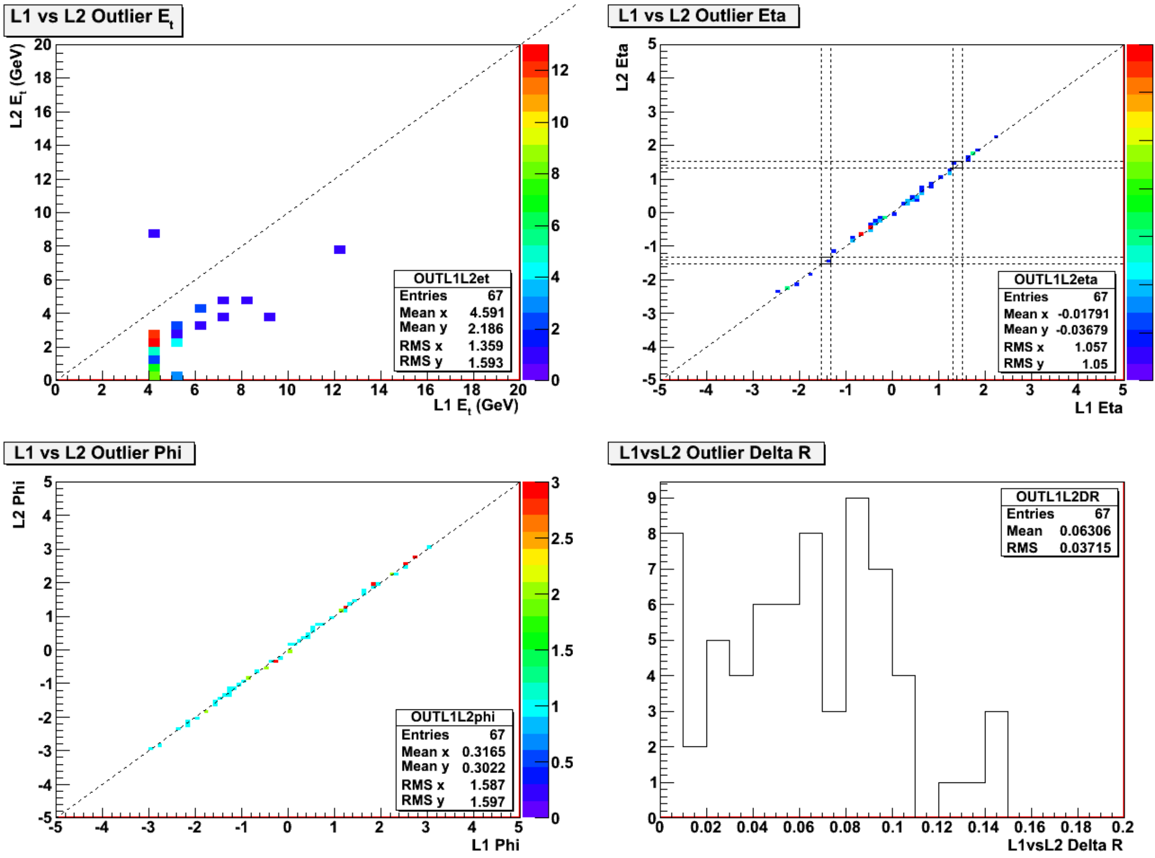

Figure 4.2: Level-1 vs Level-2 object comparison for outlier objects from upper left clockwise; $L2_{E_T}$ vs $L1_{E_T}$, $L2_\eta$ vs $L1_\eta$ with dashed lines highlighting the crack region, ΔR between objects at L1 and L2, $L2_\phi$ vs $L1_\phi$.

Once the outlying EM objects were selected, basic kinematic variables were investigated. Figure 4.2 shows η, ϕ and ΔR inter-trigger level comparisons for the outlying EM objects. Two of the objects are clearly in the crack region between the barrel and the endcap (see upper right plot of Figure 4.2), and offer the most likely cause of their outlier status. Interestingly all of the outliers can be seen to have good η and ϕ matching between trigger levels, and most are far away from the cut of $\Delta R < 0.15$. In the discussion section of this study, the cause of these remaining outliers will be investigated further, along with those found in the other inter-trigger level studies.

Level-1 versus Event Filter Study

The same study was performed with L1 and EF objects. This study is of particular importance because the EF is the final trigger level before events are written out and stored for physics analysis. In this study for brevity the inter-trigger level resolution plot (as Fig-

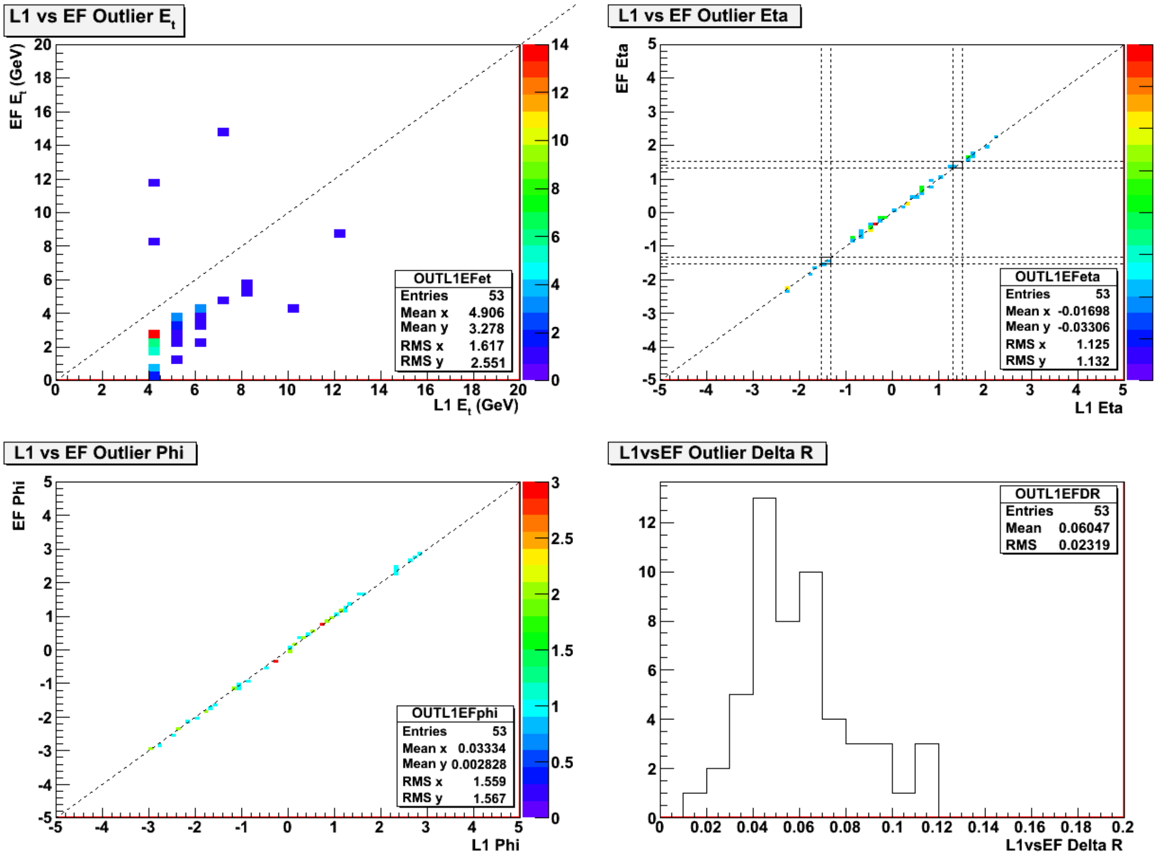

Figure 4.3: Level-1 vs Event Filter object comparison for outlier objects from upper left clockwise; EF_{E_T} vs $L1_{E_T}$, EF_η vs $L1_\eta$ with dashed lines highlighting the crack region, ΔR between objects at L1 and EF, EF_ϕ vs $L1_\phi$.

ure 4.1 was to the L1 vs L2 study) has been moved to Appendix D.1 due to the principle and procedure being exactly the same as was done previously. In Figure 4.3 the L1 vs EF outlying objects are displayed in further detail, with results of the investigation into the cause of the outliers given in the discussion section.

Level-2 versus Event Filter Study

For completeness in this thesis, a study of L2 and EF objects was also undertaken, even though there is some degeneracy in this after the previous two studies. The final study therefore serves as a robust cross check, to ensure that no outliers were missed. Information on the resulting outliers from L2 vs EF comparisons are presented in Figure 4.4, and a summary of the investigation into the cause of all of the inter-trigger level comparison outliers is presented and discussed in the next subsection.

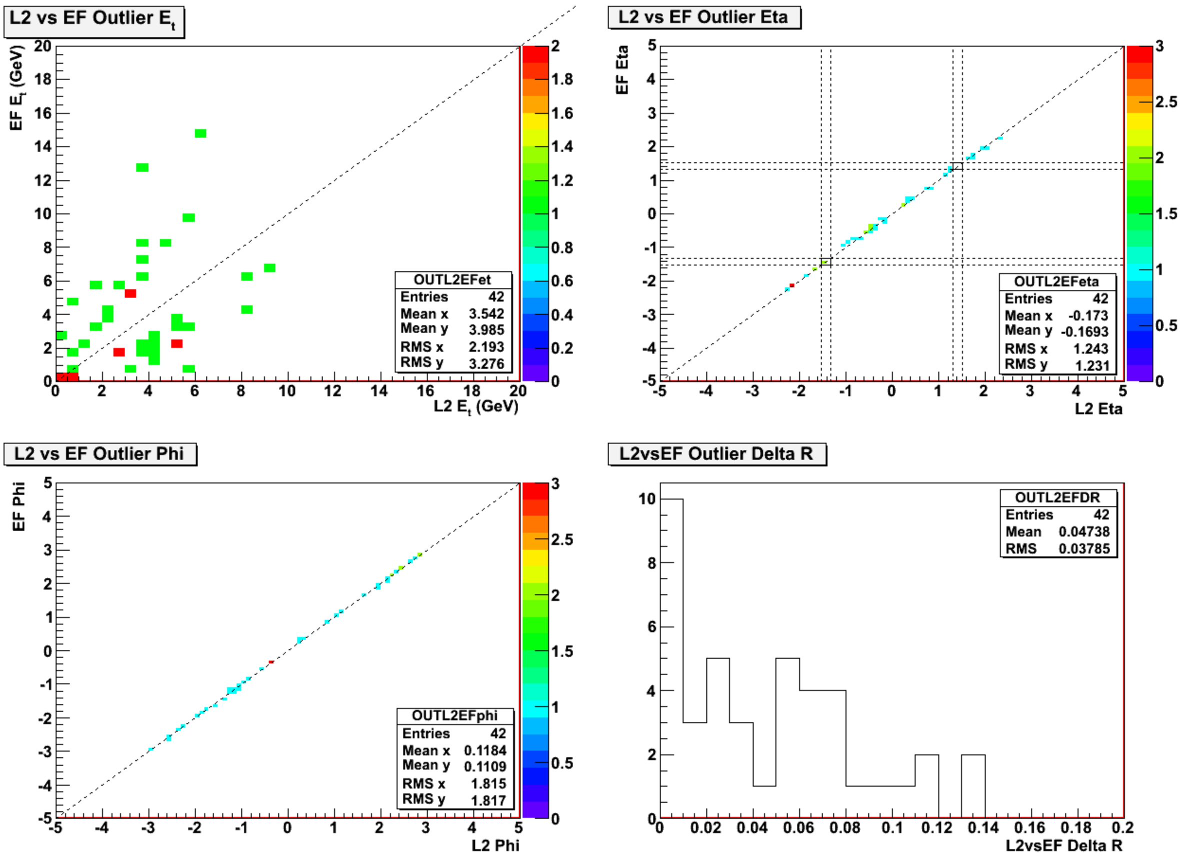

Figure 4.4: Level-2 vs Event Filter object comparison for outlier objects from upper left clockwise; EF$_{E_T}$ vs L2$_{E_T}$, EF$_\eta$ vs L2$_\eta$ with dashed lines highlighting the crack region, ΔR between objects at L2 and EF, EF$_\phi$ vs L2$_\phi$.

Discussion on Cause and Implications of Outliers at $\sqrt{s}$ = 900 GeV

The cause of outliers found in this study were investigated, and in collaboration with both detector component and software experts, categorised as described in Table 4.2. The association of the outliers to the classes described in Table 4.2 can be seen in Table 4.3. Here it is evident that a large fraction of the outliers were found to have no discernible cause as far as non-nominal software or hardware behaviour was concerned, and so were deemed “miscellaneous” outliers. However, many of this type of outlier can be attributed to the natural tails of the energy resolution distribution, and none of those without known cause indicated severe problems that required immediate investigation.

Outlier Category	Description
Crack	If the object falls in the crack region ($1.37 < \eta < 1.52$), some variables may not be reconstructed properly and thus this is considered an outlier category.
Bad Channel	Some outlier cases where $L1_{E_T} > L2_{E_T}$ are due to a mistiming of the L1Calo readout pulse, which are linked to known bad channels.
Nearby Clusters	Arises when there are many L2 or EF clusters close together, sometimes causing the wrong cluster to be matched.
f3	f3 is defined as the fraction of energy in the third layer of the EM Calorimeter. Some outlier events were found that seemed to have a particularly high f3.
False EF Cluster	Caused when no true EF cluster for that object exists, but the nearest EF cluster has been taken. This is a mis-match in clusters, giving E_T values that are not expected to be correlated.
Bad Calibration	Some events were found with very large calibration values because they happen to fall into specific η bins that have been determined to need improved calibrations when applied to fakes. In newer versions of these calibration tables produced in part with the help of this study, the values were corrected.
L1 Summing	These outliers arise because the cell size sometimes causes a nearby ROI to be included into the energy calculation, giving a $L1_{E_T}$ that is effectively the sum of two different objects.
Hot L1 Spot	A small number of events showed some noisy hot spots at L1 possibly leading to the erroneous energy values.

Table 4.2: Summary of outlier classes identified to be possible causes of discrepancies between different trigger levels estimation of electron E_T in the commissioning phase of the ATLAS detector with $\sqrt{s}$ = 900 GeV data [1].

As a final check that the outlier objects were real, and not for example, all found in a

Outlier Category	L1 vs L2	L1 vs EF	L2 vs EF
Crack ($1.37 < \eta < 1.52$)	1	1	0
Known Bad Channel (L1Calo)	1	0	1
Nearby Clusters	2	0	0
f3	1	2	4
False EF Cluster	1	3	1
Bad Calibration (Bin Factors)	0	0	3
L1 Summing	2	1	0
Hot L1 Spot	1	0	0
Miscellaneous	10	15	18
Total	19	22	27

Table 4.3: A summary of the causes attributed to outliers found in the $\sqrt{s}$ = 900 GeV study [1].

particular run with specific beam conditions, the results of the study are also presented by run number in Table 4.4, from which it is shown that there is no particular clustering of outliers in any given run used in this study. The results of this study were written up as part of an E/γ trigger study [1], and one particular outcome was to identify that the calorimeter calibration map which is dependent on both η and E_T, needed adjustments where objects found in certain specific η bins were receiving a disproportionate scale factor, causing the object's outlier status (this is the "bad calibration" class of outlier in Table 4.2).

Run	# Events	Total Outliers	L1 vs L2	L1 vs EF	L2 vs EF
141749	12	0	0	0	0
141811	34	5 (14.71%)	3	1	1
142149	8	1 (12.50%)	1	0	0
142154	8	0	0	0	0
142165	153	15 (9.80%)	4	6	5
142166	82	8 (9.76%)	2	1	5
142171	71	6 (8.45%)	1	3	2
142174	21	1 (4.76%)	1	0	0
142189	55	3 (5.45%)	0	2	1
142193	162	21 (12.96%)	5	6	10
142195	50	6 (12.00%)	2	2	2
142383	159	2 (1.26%)	0	1	1
Total	815	68 (65 Unique)	19	22	27

Table 4.4: Summary of outliers in $\sqrt{s}$ = 900 GeV study by run number [1].

4.4 Inter-Trigger Level Study at $\sqrt{s}$ = 7 TeV

Once the LHC began running with pp collisions at $\sqrt{s}$ = 7 TeV, the outlier study first performed at $\sqrt{s}$ = 900 GeV was repeated, both to check that fixes implemented from the first study were still effective, and to provide feedback for further detector recalibration, while checking that the ATLAS detector was performing nominally in this new energy regime. The difference in the volume of data between the two studies was the first challenge encountered, with the first study looking at data with a total integrated luminosity of a few inverse nanobarns, compared to this study which used a subset of the data with a integrated luminosity of order 15 pb^{-1}. The solution to this problem was to focus on the highest energy EM objects, with those that were the most outlying of greatest interest to the purpose of the study. For this reason an E_T threshold cut was applied to only select EM objects above 100 GeV at each trigger level, compared to the 4 GeV threshold cut of the previous study. The definition of an outlier was also slightly changed, with resolution = $(A_{E_T} - B_{E_T}) / (A_{E_T} + B_{E_T})$, to avoid cases seen in the previous study where resolutions could be greater than $|100\%|$. The threshold deviation from the mean of the energy resolution distribution to be considered an outlier was also changed from $\pm 2\,\sigma \rightarrow \pm 3\,\sigma$ to ensure the study selected only the most outlying EM objects. This study was performed on data taken between the 30th of June and 7th of October 2010, requiring the runs were in the respective good runs list and that events minimally passed the L2_e20_medium and EF_e20_medium triggers, which constituted an integrated luminosity of $\sim$15 pb^{-1}. Again a fiducial cut of $|\eta| < 2.5$ was used, and $\Delta R < 0.15$ required between the two respective trigger level objects being compared. Applying these requirements to the data sample resulted in $\sim$2.5 million events being suitable for the second study, of which 328 EM objects were determined to be outliers, selected by the updated definition. The breakdown of the 328 outlying objects into trigger level comparisons is as follows; L1 vs L2: 123, L1 vs EF: 79, L2 vs EF: 126. All of the plots related to this study at $\sqrt{s}$ = 7 TeV can be found in Appendix A.2, and follow a very similar form to the $\sqrt{s}$ = 900 GeV study, albeit with orders of magnitude higher numbers of events.

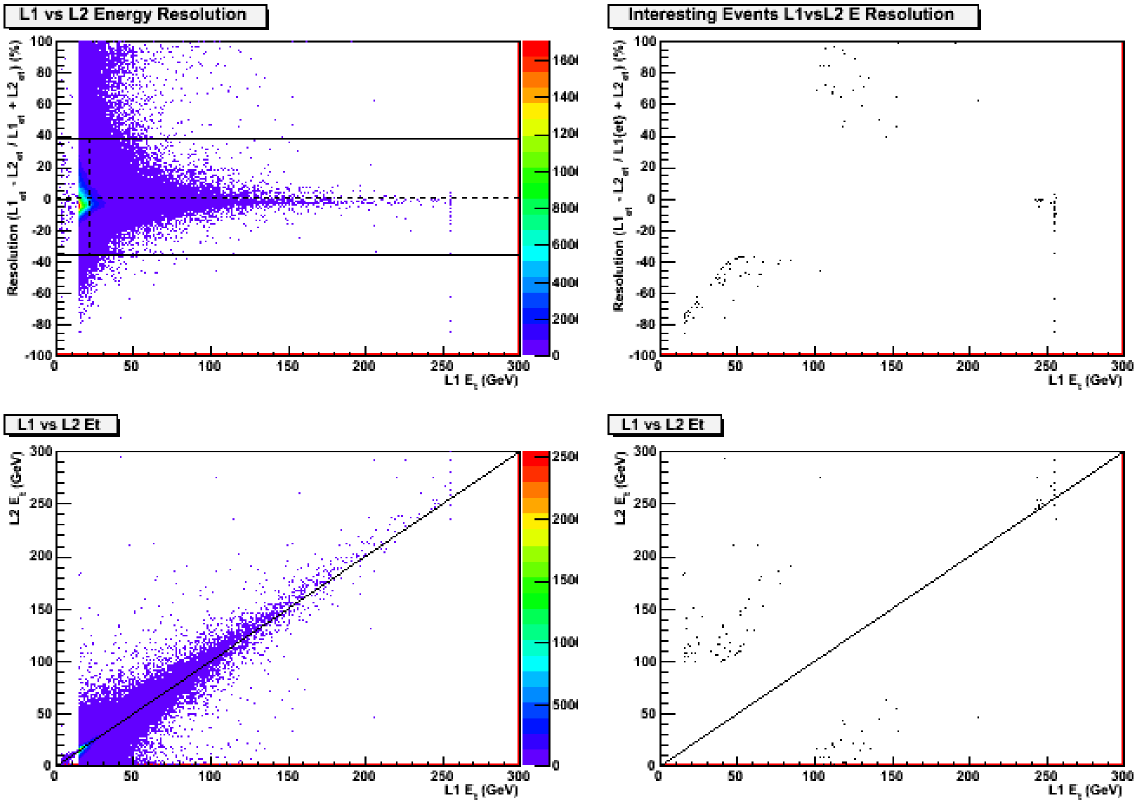

Figure 4.5: Level-1 vs Level-2 object comparison from upper left clockwise; Resolution vs L1$_{E_T}$ of all objects passing cuts; Resolution vs L1$_{E_T}$ of object comparisons determined to be outliers; L2$_{E_T}$ vs L1$_{E_T}$ object matches determined to be outliers; L2$_{E_T}$ vs L1$_{E_T}$ matches for all objects that pass cuts.

Discussion on Cause and Implications of Outliers at $\sqrt{s}$ = 7 TeV

The sources of outliers found in this study were a subset of those seen in the previous study (referring again to Table 4.2). To this degree, the study was successful in confirming the general type of rare discrepancies that can be seen with respect to inter-trigger level E_T estimation comparisons with EM objects, and that no new software or hardware defects had become apparent with a change of centre of mass energy. It is worth noting an interesting side effect of this study in the form of observing the known L1$_{E_T}$ saturation at ∼250 GeV (see Figure 4.5). Though at this stage in data taking the relative number of events with L1$_{E_T}$ $\geq$ 250 GeV was low, this would be a continued small source of known “false” outliers in the study, termed as such because if the E_T of the object was higher than 250 GeV, this would not be seen at L1 making it more likely to be deemed an outlier despite the detector behaving as expected.

4.5 Conclusions of Outlier Study

The high E_T electron outlier study was designed to look at high E_T objects in early data with the ATLAS detector. During this commissioning phase, it was important to check that the detector was working nominally, and that any defects seen (if any) were understood and accounted for. The first study done at $\sqrt{s}$ = 900 GeV, was a first look at how the detector was performing, and despite a few rare discrepancies, the detector performed above and beyond expectations. The feedback from this first study led to improvements in the calibration maps for the calorimeter, and seem to have been effective as only a few "Bad Calibration" type outliers were seen in the follow up study at $\sqrt{s}$ = 7 TeV (which is significant considering the relative size of the datasets used in the two studies). The second study was performed as a follow up check for the ATLAS detector, once the LHC had reached its initial physics data taking beam energy of 3.5 TeV per beam ($\sqrt{s}$ = 7 TeV). The experience gained from the first study enabled the second study to quickly target any sources of outliers seen, and designate the outlying events into these classes, to see if any new sources of outlier could be found. All the outliers seen in the second study had previously been identified by the first, with the exception of the $\mathrm{L1}_{E_T}$ saturation at $\sim$250 GeV, which had not been seen in the first study but was expected and known. Fewer outliers were seen at higher E_T in the second study proportionally when compared to the first study. This is especially important for this thesis, as the importance is on accurately identifying the highest E_T objects available in data. A way that this study is continually being used to benefit the collaboration, is when very high invariant mass objects are observed in data, one can go back and check the inter-trigger level comparisons of the objects that go into the combination, as a sanity check that these objects are real, and not outliers caused by an effect as found and defined by this study.

Chapter 5

High Mass Dielectron Event Selection

5.1 Data Selection

The criteria used to select possible high mass dielectron resonance candidates from data were chosen to provide the highest signal efficiency, while simultaneously minimising background contributions (see signal/background efficiencies in Section 5.2). The selection criteria require that an event has at least two “good” electrons to be considered a candidate event, where a good electron is one that passes the cut flow as will be motivated/described in this section, and summarised in Table 5.1.

Firstly, the events must have occurred during a period in which the ATLAS detector was discerned to be working optimally for an electron analysis. This is achieved by requiring that events are present in the e/γ Good Runs List (GRL), which comprises of the luminosity blocks in data where detector components vital for a given analysis, such as the inner detector and electromagnetic calorimetry in the case of this search, were operating nominally. Table 5.2 lists full details of the e/γ GRL requirements.

After the GRL requirement, the number of primary vertices in the event is taken into account, ensuring that there is at least one Primary Vertex (PV) with greater than 2 tracks in the event, to be confident that the detector is not seeing a cosmic event or, an out of time pile-up effect. The event also has to have triggered the EF_e20_medium or EF_e22_medium trigger (depending on the run number), which is seeded by L1_EM14 (note that “medium” here does not pertain to the isEM identification but a trigger based measure, also named medium [93]). The justification for using these triggers, despite their relatively low E_T threshold given a high mass resonance search, is that they are the

Criterion	Description
GRL	Event must be in the e/γ good runs list (Table 5.2).
PV	Event has at least one primary vertex with > 2 tracks.
Trigger	Event passes the EF_e20_medium trigger for runs before 182873, and EF_e22_medium trigger from that run onwards.
Author	Each electron has Author 1 or 3.
η	Each electron must pass a fiducial cut of $\lvert\eta\rvert < 2.47$, and not be located in the crack region $1.37 < \lvert\eta\rvert < 1.52$.
E_T	Each electron must have an $E_T > 25$ GeV.
OQ	The cluster associated to each electron must pass calorimeter quality requirements. Each electron must not be located in a region of the calorimeter that shows a LAr error. Together these requirements are denoted as the OQ cut [92].
isEM Id	Each electron must pass at least isEM *medium* identification requirements (Table 5.3).
B-layer	Each electron must have a b-layer hit, if one is expected.
Isolation	The two highest E_T electrons passing the above cuts, form a pair. The leading electron of this pair, must have calorimeter isolation < 7 GeV.
Invariant Mass	The dielectron pair must have an invariant mass ≥ 70 GeV.

Table 5.1: Summary of the dielectron resonance event selection criteria. The first section (delineated by double lines) shows the event level selection criteria, the next section summarises the electron level cuts, and the final section presents the requirements made on selected dielectron pairs.

GRL Requirement	Description
Ready for physics	Accelerating beams are stable and ready for physics
Solenoid on	Solenoid is turned on
ATLGL	DQ status green: Runs where DQ information was reviewed
ATLSOL	DQ status green: Solenoid on and stable
L1CTP	DQ status green: No clock or data header problems
L1CAL	DQ status green: Level 1 calorimeter working
TRELE	DQ status green: Electron trigger operating normally
TRGAM	DQ status green: Photon trigger operating normally
cp eg electron barrel	Include barrel region of the detector for electrons
cp eg electron endcap	Include endcap region of the detector for electrons
IDVX	DQ status green: ID vertexing quality
LUMI	DQ status green: Offline luminosity OK

Table 5.2: Data quality requirements included in the e/γ good runs list.

highest E_T single electron triggers that are unprescaled and preserve the Z^0 peak, which is used as the control region for data/MC normalisation. These triggers are also well documented/supported by the e/γ performance group, who provide accurate trigger efficiency measurements which were also studied as part of the 2011 dilepton analysis using the tag and probe method [83]. If a trigger such as EF_e150 was used, which might appear to be a more natural choice of trigger for a search of this kind with a high E_T threshold, it would in fact be much more difficult to obtain an accurate efficiency measurement and normalisation, because of the implied cut on the Z^0 region. The higher E_T threshold triggers are also not currently supported by the e/γ performance group to the level required by this search analysis.

If an event passes the trigger requirement, then individual electron criteria are applied within the event to search for at least two good electrons which pass all of the proceeding requirements. At each stage, if an electron fails a criterion, it is excluded from the list of candidate good electrons. If the number of candidate electrons in the event falls below two, the event is rejected from the analysis. The first criterion each electron must pass is the Author cut, requiring the electron has been reconstructed by either a calorimeter seed (Author = 1) or, a calorimeter seed and the track algorithm (Author = 3). The next electron criterion is a fiducial cut in η, which checks both that electrons are located in the barrel and/or endcap electromagnetic calorimetry systems ($|\eta| < 2.47$), and that they do not fall into the crack region between the barrel and endcap ($1.37 < |\eta| < 1.52$). This requirement specifically implies that electrons are not located in the FCal which has not currently been studied to a high enough precision to be used in this search analysis.

An $E_T > 25$ GeV cut is applied to all electrons to ensure that low E_T electrons most likely originating from QCD dijets, are minimised while preserving the Z^0 peak and any BSM high mass resonances. In electron and photon analyses, it is important to check the quality of the clusters associated with candidate EM objects, to reject bad quality or fake clusters due to calorimeter problems. The two criteria proceeding the E_T cut focus on this aspect, rejecting bad clusters using calorimetry information, and checking for LAr noise bursts or data integrity errors, stored from data on an event by event basis. Following these Object Quality (OQ) criteria, the analysis applies a *medium* electron identification requirement (where *medium* is described in Table 5.3 and all isEM identification characteristics are described in [94]). The last criterion applied to all electrons is the b-layer requirement, which checks if the innermost layer of the pixel detector contains a track hit from the associated cluster if one is expected. This cut is very effective at rejecting converted photons from the analysis that would otherwise be accepted. If at least two electrons in an event satisfy the cut flow conditions described above, the two highest E_T electrons are selected to form a pair. Two final criteria are then applied: firstly the highest E_T electron of the pair is required to pass a p_T corrected isolation cut < 7 GeV in a cone of $\Delta R = 0.2$, and secondly the invariant mass of the pair must be ≥ 70 GeV. The isolation requirement is made to further remove QCD events (see Figure 7.3 in Chapter 7), and is only made on the leading electron, as requiring isolation on both provided little further gain in signal purity at the cost of statistics. The invariant mass cut is invoked as the search analysis is aimed at high mass resonances but requires preservation of the Z^0 peak for normalisation and extrapolation purposes. If both of these criteria are met then the event is accepted as a candidate event and stored, otherwise it is rejected. It should be noted that no opposite charge requirement is made on the final two candidate electrons because of possible charge mis-identification due to either bremsstrahlung or, limited momentum resolution of the inner detector at very high E_T. While a study of the charge mis-id rate was not performed for this thesis, a check on the selected number of candidate events in the 2.12 fb^{-1} dataset finds that 1.8% are apparently same sign pairs.

Studies carried out by performance groups within ATLAS, designed to understand the response of the detector to the underlying events it records, sometimes lead to modifications of the variables recorded from data. For instance, the e/γ performance group's study

isEM *medium* criteria	Description
Cluster η Range	Fiducial requirement to check cluster is within detector range.
Cluster Hadronic Leakage	Ratio of cluster E_T leakage into the HCAL to cluster E_T.
Cluster Middle Energy	Energy in the 2nd sampling layer of the ECAL in a window of 7×7 cells (E277). This is where electrons are expected to deposit most of their energy.
Cluster Middle Energy Ratio 37	Energy ratio in the 2nd sampling layer of the ECAL in window sizes 3×7/7×7 cells (E237/E277). Electrons are expected to show a peak near unity in this variable, due to small lateral leakage.
Cluster Middle Width	The lateral width calculated with a window of 3×5 cells using the energy weighted sum over all cells, which depends on the particle impact point inside the cell: weta2 $= \sqrt{\frac{\sum E_i \eta^2}{(\sum E_i) - (\frac{\sum E_i \eta}{\sum E_i})^2}}$, where E_i is the energy of the i-th cell.
Cluster Strips ΔE	As pions are often found to give two maxima, a cut is made on the difference $E_{Max2} - E_{min}$ of the energy associated with the 2nd maximum (E_{Max2}) and the energy reconstructed in the strip with the minimal value between the first and second maximum (E_{min}).
Cluster Strips ΔE$_{Max2}$	To ensure insensitivity to fluctuations, E_{Max2} has to be greater than a threshold which depends linearly on E_T.
Cluster Strips W_{tot}	Shower width in first sampling layer, determined in a window ΔR corresponding typically to 40 strips in η : $W_{tot} = \sqrt{\frac{\sum E_i (i - i_{max})^2}{\sum E_i}}$, where i is the strip number and i_{max} is the strip number of the first local maximum.
Cluster Strips Fracm (Fside)	Shower shape in the shower core : [E(+/-3)-E(+/-1)]/E(+/-1), where E(+/-n) is the energy in n strips around the strip with highest energy.
Cluster Strips Weta1c	Shower width weighted by distance from the maximum.
Cluster Strips ΔE$_{Maxs1}$	Difference between maximum and 2nd maximum reconstructed energy in the strips.
Track Match η	η difference between cluster and extrapolated track in the 1st sampling.
Track Pixel	Number of pixel hits.
Track Silicon	Number of pixel and semi-conductor tracker hits.
Track A0	Transverse impact parameter. Distance of closest approach to the beam-line.

Table 5.3: List of requirements to pass isEM *medium* identification [94]. The specific cuts on each of the variables are not shown as they are E_T and η dependent, but matrices of the values exist in the reference.

of the electron cluster energy recorded by the ATLAS detector, using $Z^0 \rightarrow ee$ events as a standard candle with $\sim$420 pb^{-1} of data, showed that an energy scale correction needed to be applied depending on the cluster location in η and ϕ. The full study that made the recommendations on this correction can be found in [92], and was taken into account for the data selection presented here, as well as an equivalent correction applied to MC to ensure a meaningful data/MC comparison. The correction was important for this search as the calculation of E_T (Equation (5.1)) and p_T (Equation (5.2)) rely on accurate energy values, along with the dielectron invariant mass calculation (Equation (5.3)). It is assumed here that the electron mass is negligible compared to its energy and momentum, meaning $E_T \approx p_T$, and the invariant mass can be written in the form of Equation (5.3).

$$E_T = \sqrt{p_T^2 + m_T^2} \tag{5.1}$$

$$p_T = \begin{cases} \frac{E_{cluster}}{\cosh(\eta_{cluster})} & \text{for } \mathrm{N}_{SCT+Pixel} \text{ hits} < 4 \\ \frac{E_{cluster}}{\cosh(\eta_{track})} & \text{otherwise} \end{cases} \tag{5.2}$$

$$M_{ee} = \sqrt{2(E_1E_2 - P_1 \cdot P_2)} \tag{5.3}$$

When considering the OQ check made on electrons, it is important to understand what effect this has on the final distributions in data. The OQ check assesses whether a cluster has passed through a non-nominal/dead high voltage region or, parts of the calorimeter that have non-functioning LAr Front End Boards (FEBs). During the data taking period between runs 180614 and 185352 (43% of the data in this thesis), 6 FEBs became unusable due to hardware failure of the optical transmitters that connect to the readout boards. This covered a region $\Delta\phi$ = 0.2, $\Delta\eta$ = 1.4, centred at ϕ = -0.7, η = 0.7, and corresponds to a 0.8% loss in the ECAL coverage over the precision region [83]. An η-ϕ map showing electrons that pass the event selection is presented in Figure 5.1, with the missing FEB hole clearly visible. This effect causes a slight asymmetry in the η and ϕ distributions, which is not modelled in MC but can be accounted for using event weights as described in Section 5.2.

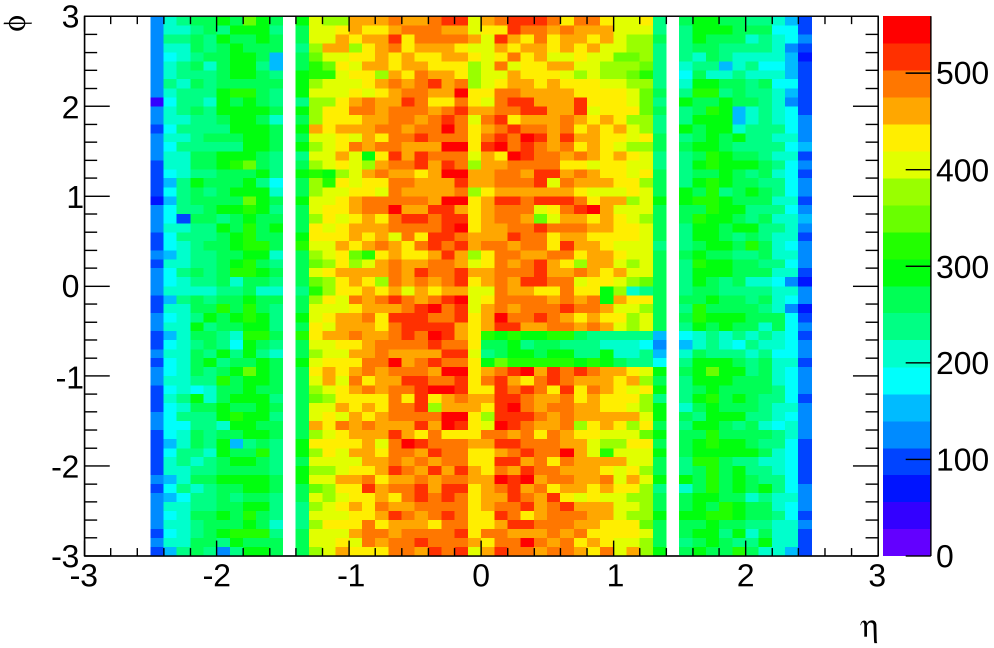

Figure 5.1: η-φ map of electrons passing the event selection cut flow using 2.12 fb^{-1} of 2011 data. The crack and missing FEB regions are clearly visible.

5.2 Monte Carlo Selection

The MC simulation analysis uses the same procedures where possible as those performed for the data analysis. However, in certain instances a cut does not apply to MC, or quantities are not simulated sufficiently when compared to data, meaning that compensation methods have to be employed to achieve the closest possible comparison between data and MC. The same cut flow as presented in the previous section is used for MC, except the GRL criterion, which does not apply to MC due to its generation under nominal detector and beam conditions. There are however additional Scale Factors (SF) and reweighting applied to MC objects/events to ensure complete compatibility with data, which are summarised in Table 5.4. These corrections to MC are studied and supported by the e/γ performance group [92].

Signal Efficiencies

The signal process efficiencies using the MC event selection can be found in Table 5.5, based on a 1.5 TeV Z'_{SSM} and RS G^* ($k/\overline{M}_{Pl}$ = 0.10). Figure 5.2 shows the final event selection efficiency versus signal truth mass using the corresponding template samples from the limit setting procedure. All signal samples can be found in Appendix B.1.

Correction	Description
Pile-up	Reweighting of MC events depending on the number of primary vertices is done to ensure the in-time and out-of-time pile-up conditions present in data are accurately simulated. This reweighting is done on a per event basis.
Trigger SF	To account for the efficiency of the trigger in data. The correction depends on the η location of both electrons, and is applied on a per event basis.
Id SF	This scale factor accounts for the identification efficiency of the reconstruction algorithms. It is p_T and η dependent, applied on a per electron basis.
Energy Correction	Corrections to the electron cluster energy are applied, equivalent to that described previously for data. It is applied on a per electron basis and is dependent on energy, as well as position in η and ϕ.
OQ	To account for the FEB holes in data, a map is applied to a fraction of MC events corresponding to the fraction of corrupted data. The correction is η-ϕ dependent and applied on a per electron basis.
K-factor	To account for NNLO QCD and EW loop corrections, a K-factor is applied to the Drell-Yan background, and Z'/G^* signal MC (which are generated at LO* with PYTHIA). This is done on a per event basis, and in the case of signal processes, depends on the truth mass of the resonance.

Table 5.4: The corrections applied to MC, to accurately simulate data conditions in 2011 during pp collisions.

Criterion	Z' Efficiency [%]		G^* Efficiency [%]	
	Relative	Total	Relative	Total
Primary Vertex	100.00 ± 0.00	99.82 ± 0.03	100.00 ± 0.00	99.75 ± 0.05
Trigger	98.50 ± 0.09	98.32 ± 0.09	97.91 ± 0.15	97.66 ± 0.16
Author	98.12 ± 0.10	96.47 ± 0.13	98.08 ± 0.15	95.79 ± 0.21
η	95.73 ± 0.15	92.35 ± 0.19	97.13 ± 0.18	93.04 ± 0.27
E_T	93.42 ± 0.18	86.27 ± 0.24	95.23 ± 0.23	88.60 ± 0.34
Object Quality	99.14 ± 0.07	85.53 ± 0.25	99.04 ± 0.11	87.75 ± 0.35
isEM Id	85.96 ± 0.27	73.52 ± 0.31	87.08 ± 0.38	76.41 ± 0.45
B-Layer	97.13 ± 0.14	71.41 ± 0.32	98.01 ± 0.17	74.89 ± 0.46
Isolation	98.55 ± 0.10	70.37 ± 0.32	98.73 ± 0.14	73.94 ± 0.46
Invariant Mass	100.00 ± 0.00	70.37 ± 0.32	100.00 ± 0.00	73.94 ± 0.46
After Weights	95.79 ± 0.17	67.41 ± 0.33	96.36 ± 0.23	71.25 ± 0.48

Table 5.5: Relative and total, signal efficiencies using MC event selection criteria, for an example signal resonance mass of 1.5 TeV (and $k/\overline{M}_{Pl}$ = 0.10 for G^*). The samples used here are listed in Appendix B.1.

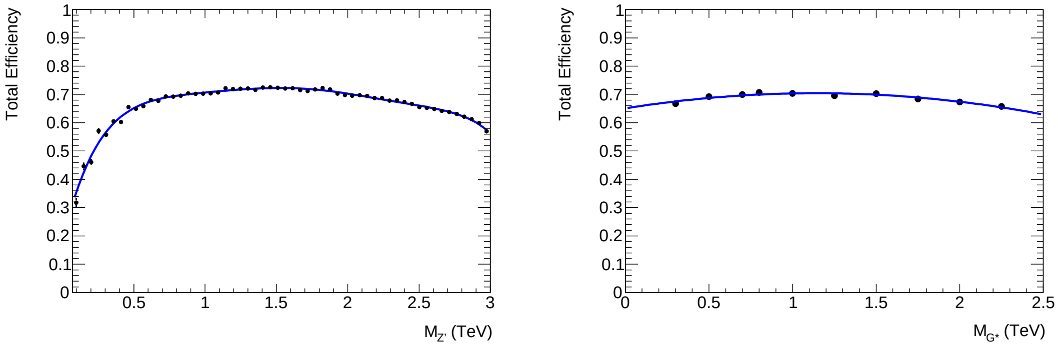

Figure 5.2: The total efficiency versus signal truth mass after applying the MC event selection criteria to the Z' template (left), and available G^* mass points (right) respectively.

Background Efficiencies

The event selection criterion efficiencies for background processes considered in this thesis to be relevant to a high mass dielectron resonance search, are presented in Table 5.6 using the MC samples as listed in Appendix B.2. The Drell-Yan process returns the highest efficiency due to its irreducible nature with respect to the signal signature. All other backgrounds (except $t\bar{t}$) have vastly lower efficiencies, showing strong background rejection within the analysis. Comparing the relative cut efficiencies for signal (Table 5.5) and background (Table 5.6), it is observed that the E_T and isEM Identification (Id) criteria have the largest effect on the cut flow. The $E_T > 25$ GeV criterion is relatively fixed as preservation of the Z^0 peak is required in this search for normalisation purposes. As the effect of the isEM Id criteria is large, a study is provided in the next subsection to justify the use of isEM *medium*, over the other options that were considered, namely *loose* and *tight* [94].

isEM Identification Study

A study was carried out in this thesis to compare the signal and background efficiencies using the MC event selection, while varying the isEM Id cut between *loose*, *medium*, and *tight*. The results of this study are presented in Figure 5.3, and show that while the diboson and $W+$jets backgrounds are relatively unaffected by the change of isEM cut, the signal, Drell-Yan, and $t\bar{t}$ processes have a notable change in efficiency. In the case of both *loose* and *tight* cuts, the signal and Drell-Yan background have comparable efficiencies, whereas *medium* shows a higher signal efficiency. As both of these processes are

Cut	Drell-Yan Efficiency [%]		$t\bar{t}$ Efficiency [%]	
	Relative	Total	Relative	Total
Primary Vertex	100.00 ± 0.00	99.79 ± 0.01	100.00 ± 0.00	80.02 ± 0.14
Trigger	94.48 ± 0.05	94.28 ± 0.05	94.77 ± 0.09	75.84 ± 0.15
Author	93.86 ± 0.05	88.49 ± 0.07	99.94 ± 0.01	75.79 ± 0.15
η	94.42 ± 0.05	83.55 ± 0.08	99.66 ± 0.02	75.53 ± 0.15
E_T	89.71 ± 0.07	74.95 ± 0.10	85.71 ± 0.14	64.74 ± 0.17
Object Quality	99.19 ± 0.02	74.35 ± 0.10	99.42 ± 0.03	64.37 ± 0.17
isEM Id	85.83 ± 0.09	63.81 ± 0.11	60.81 ± 0.22	39.15 ± 0.17
B-Layer	96.55 ± 0.05	61.61 ± 0.11	94.35 ± 0.13	36.93 ± 0.17
Isolation	98.85 ± 0.03	60.90 ± 0.11	98.21 ± 0.08	36.27 ± 0.17
Invariant Mass	99.97 ± 0.01	60.88 ± 0.11	97.19 ± 0.10	35.25 ± 0.17
After Weights	97.93 ± 0.04	59.62 ± 0.11	97.41 ± 0.09	34.34 ± 0.17
Cut	$W+$jets Efficiency [%]		Diboson Efficiency [%]	
	Relative	Total	Relative	Total
Primary Vertex	100.00 ± 0.00	99.77 ± 0.00	100.00 ± 0.00	99.80 ± 0.01
Trigger	53.32 ± 0.02	53.20 ± 0.02	34.21 ± 0.05	34.14 ± 0.05
Author	66.83 ± 0.02	35.55 ± 0.02	87.82 ± 0.06	29.98 ± 0.05
η	96.21 ± 0.01	34.20 ± 0.02	96.73 ± 0.04	29.00 ± 0.05
E_T	15.80 ± 0.02	5.40 ± 0.01	37.57 ± 0.10	10.89 ± 0.04
Object Quality	99.18 ± 0.01	5.36 ± 0.01	99.22 ± 0.03	10.81 ± 0.04
isEM Id	0.93 ± 0.01	0.05 ± 0.00	53.38 ± 0.18	5.77 ± 0.03
B-Layer	50.39 ± 0.74	0.03 ± 0.00	92.87 ± 0.12	5.36 ± 0.03
Isolation	83.99 ± 0.77	0.02 ± 0.00	99.58 ± 0.03	5.34 ± 0.03
Invariant Mass	72.06 ± 1.03	0.02 ± 0.00	95.91 ± 0.10	5.12 ± 0.03
After Weights	97.19 ± 0.45	0.01 ± 0.00	97.18 ± 0.08	4.97 ± 0.03

Table 5.6: Relative and total, background process efficiencies using the MC event selection criteria, on samples as listed in Appendix B.2.

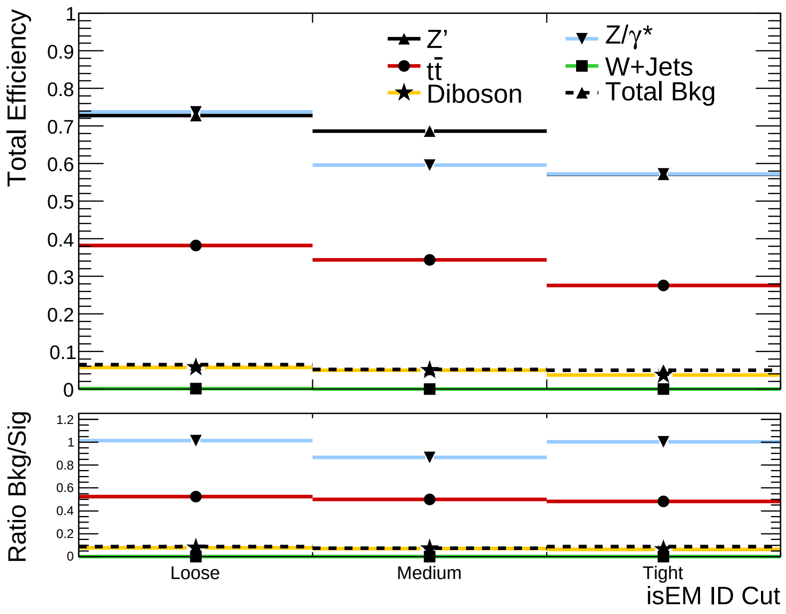

Figure 5.3: Comparison of signal (1.5 TeV Z'_{SSM}) and background efficiencies, using MC event selection with varying isEM Id cuts. The absolute efficiencies for each process are presented for isEM *loose*, *medium*, and *tight*. The subplot shows the corresponding ratio of background to signal efficiency in each case. A Total background efficiency is also provided, where each background is weighted by its cross section proportionally as listed in Appendix B.

inherently the same, in similar mass regions one finds that there is no actual difference in efficiency. However, the comparison shown is for signal and background selected by the search criteria, and so essentially compares low mass Drell-Yan to high mass signal, which results in an overall efficiency difference, as well as shape differences in the electron identification criteria. $t\bar{t}$ rejection increases with tightness of Id cut, but the ratio subplot reveals this is nullified by a correlated increase in signal rejection. Therefore as *medium* provides the highest background rejection while relatively preserving the signal, *medium* was the optimal choice for this search. This is backed up by *medium* resulting in the highest signal significance with respect to the backgrounds considered, in a mass window $\pm 3\sigma$ of the signal resonance mass.

For completeness, a MC study showing the applicable isEM *medium* criteria variable distributions, with cut thresholds displayed, was conducted for this thesis. Here a 1 TeV Z'_{SSM} and all relevant MC backgrounds, were analysed with the selection criteria up to but not including the isEM Id cut. A data-driven method was used for the QCD dijet background, which will be described in Section 6.1. The resulting distributions were normalised to unity for each contributing process and displayed together so that proportionally the cut threshold effect could be observed. Note that the thresholds displayed on

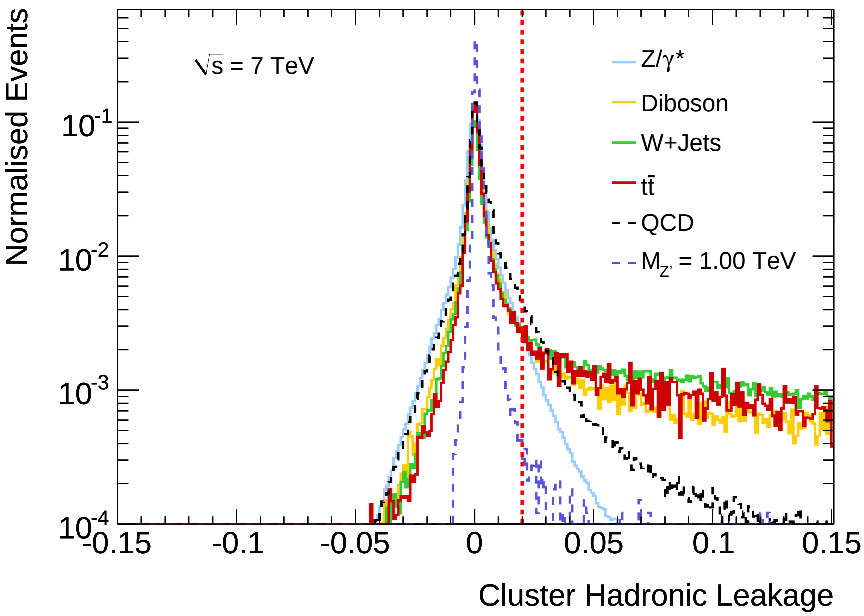

Figure 5.4: Process normalised Cluster Hadronic Leakage distribution. The red dashed line shows the minimum cut value.

these plots by the red dashed line, show only the most stringent cut value for electrons relevant to this search, where in reality the cut threshold values vary depending on electron η and E_T. The 4 variables with cut thresholds showing greatest effect are displayed here, namely: Cluster Hadronic Leakage (Figure 5.4), Cluster Middle Energy Ratio 37 (Figure 5.5), Cluster Strips ΔE_{Maxs1} (Figure 5.6), and Cluster Strips W_{tot} (Figure 5.7). All other applicable isEM *medium* criteria variable distributions are provided in Appendix E.

A further study to investigate the optimisation of a subset of isEM *medium* Id criteria thresholds was undertaken with a Toolkit for Multivariate Data Analysis (TMVA). Using a 1 TeV Z'_{SSM} signal sample, and relevant background MC, the isEM *medium* criteria as listed in Table 5.3 were used as differentiating variables in a genetic algorithm analysed with TMVA. Correlations between the variables were taken into account so that only the most essential cuts were made (see Figure 5.8 for signal (left) and background (right) correlation matrices). After optimising the variable cuts for a Z' search (rather than a Z^0 analysis, for which the isEM criteria were originally tuned), this resulted in a *medium*++ definition which provided the signal acceptance of *medium* and background rejection of *tight*. However, as only the standard isEM Id cuts are supported by the e/γ performance group at the time of writing this thesis, and the acceptance/rejection increase was not significant, the standard *medium* criteria were used for this search analysis.

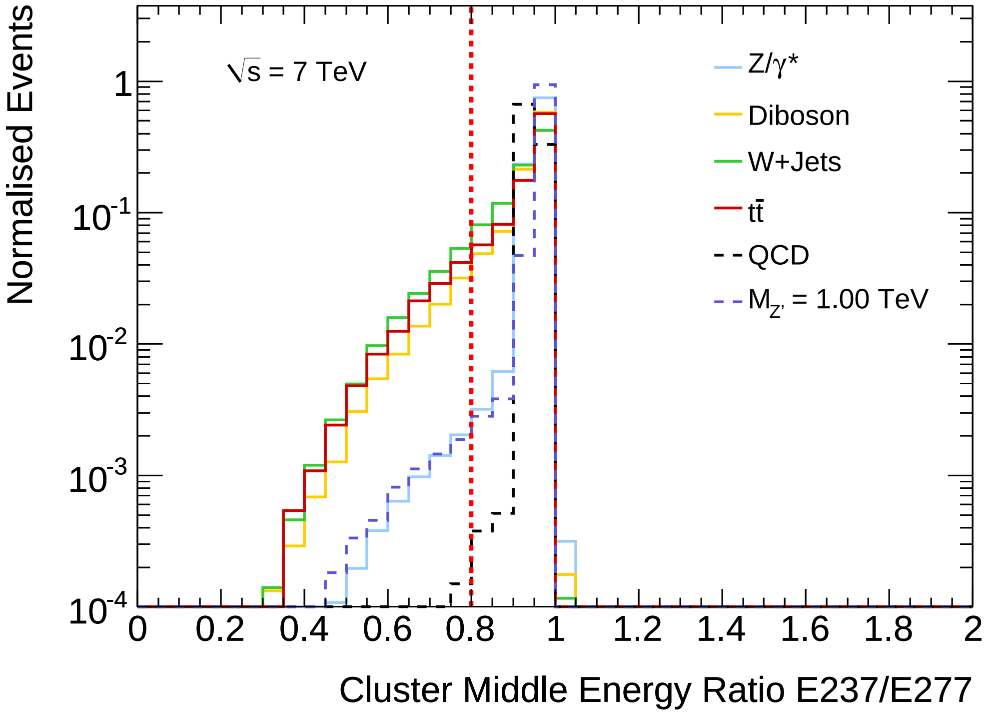

Figure 5.5: Process normalised Cluster Middle Energy Ratio 37 distribution. The red dashed line shows the maximum cut value.

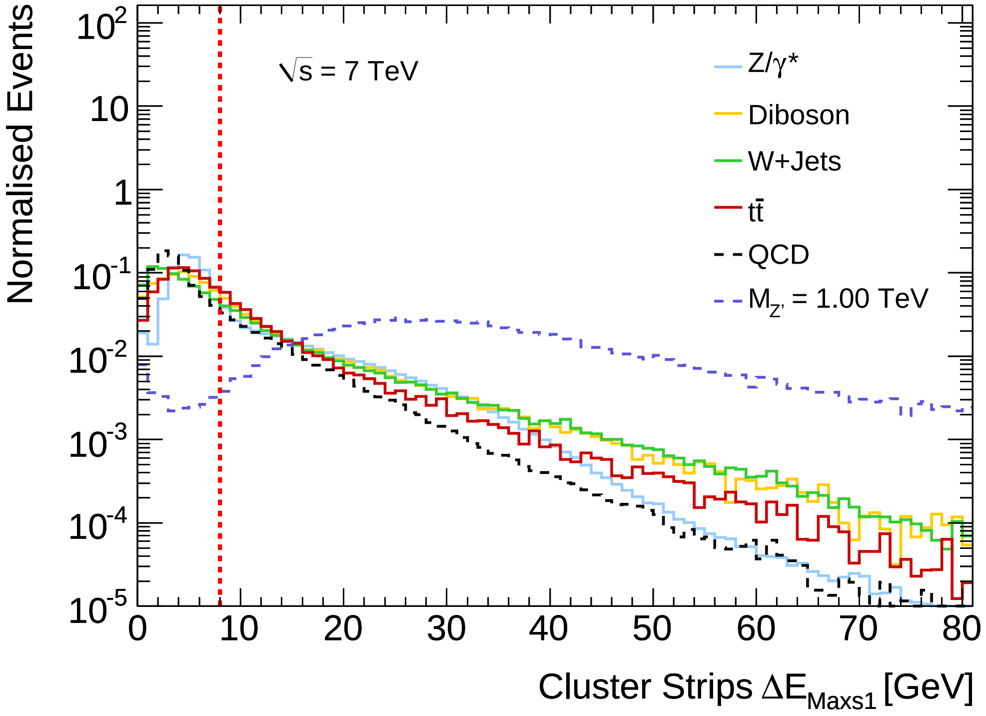

Figure 5.6: Process normalised Cluster Strips ΔE_{Maxs1} distribution. The red dashed line shows the maximum cut value.

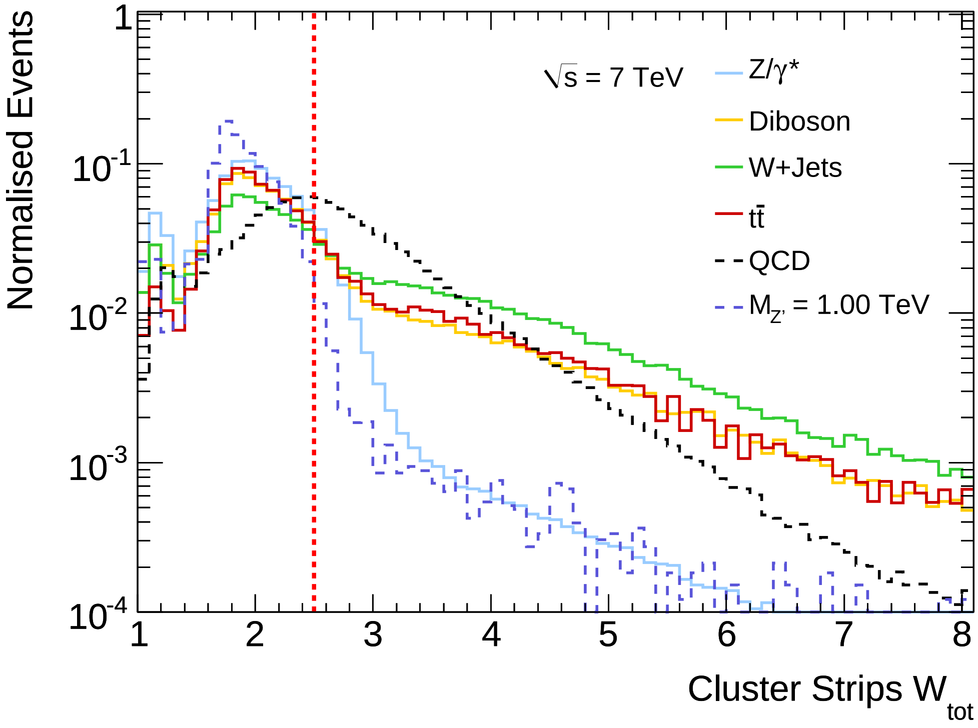

Figure 5.7: Process normalised Cluster Strips W_{tot} distribution. The red dashed line shows the minimum cut value.

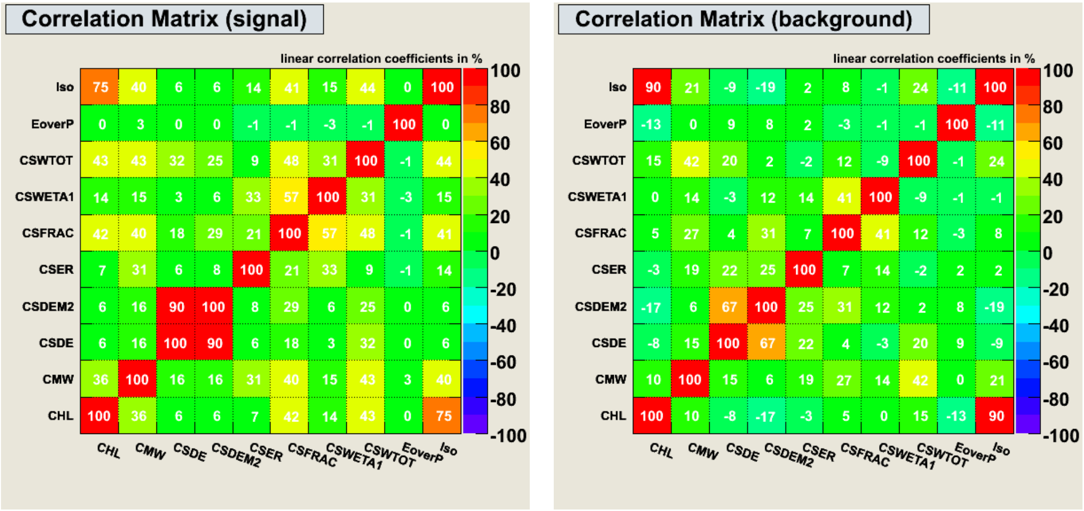

Correlation Matrix (signal)

	CHL	CMW	CSDE	CSDEM2	CSER	CSFRAC	CSWETA1	CSWTOT	EoverP	Iso
Iso	75	40	6	6	14	41	15	44	0	100
EoverP	0	3	0	0	-1	-1	-3	-1	100	0
CSWTOT	43	43	32	25	9	48	31	100	-1	44
CSWETA1	14	15	3	6	33	57	100	31	-3	15
CSFRAC	42	40	18	29	21	100	57	48	-1	41
CSER	7	31	6	8	100	21	33	9	-1	14
CSDEM2	6	16	90	100	8	29	6	25	0	6
CSDE	6	16	100	90	6	18	3	32	0	6
CMW	36	100	16	16	31	40	15	43	3	40
CHL	100	36	6	6	7	42	14	43	0	75

Correlation Matrix (background)

	CHL	CMW	CSDE	CSDEM2	CSER	CSFRAC	CSWETA1	CSWTOT	EoverP	Iso
Iso	90	21	-9	-19	2	8	-1	24	-11	100
EoverP	-13	0	9	8	2	-3	-1	-1	100	-11
CSWTOT	15	42	20	2	-2	12	-9	100	-1	24
CSWETA1	0	14	-3	12	14	41	100	-9	-1	-1
CSFRAC	5	27	4	31	7	100	41	12	-3	8
CSER	-3	19	22	25	100	7	14	-2	2	2
CSDEM2	-17	6	67	100	25	31	12	2	8	-19
CSDE	-8	15	100	67	22	4	-3	20	9	-9
CMW	10	100	15	6	19	27	14	42	0	21
CHL	100	10	-8	-17	-3	5	0	15	-13	90

Figure 5.8: Correlation matrices for a 1 TeV Z'_{SSM} signal (left), and all relevant backgrounds processes (right), between various isEM Id criteria of interest. This study was carried out using a genetic algorithm with TMVA.

Chapter 6

Standard Model Background Estimation

In order to search for new physics at the TeV scale, it is imperative to understand the physical phenomena that are already a part of the SM. It is only once an accurate SM background estimate has been compared to data that one can be sure if there is the presence of new physics. In this chapter the procedure for estimating the SM background shape will be explained. Most background processes can be sufficiently well modelled with MC, however in the case of the QCD dijet background it was found that MC did not accurately model some variables, and was severely lacking in statistics, therefore a Data-Driven (DD) QCD estimation method was used to provide the required level of precision.

6.1 Data-Driven QCD Estimate

The QCD dijet background is defined as any candidate event where both of the selected electrons are either a fake from a misidentified hadron, or non-isolated from a hadronic decay, as opposed to one of the other backgrounds or signal. The DD QCD estimation method was designed to obtain a sample which was mutually exclusive of the signal selection and based on “reverse identification” cuts that select a QCD enriched sample from events in data, estimating the shape of QCD contamination in the signal sample. This method was developed for the 2010 Z'/G^* analysis [95, 2] and minimally updated for the 2011 analysis [83, 3]. The QCD selection is the same as for signal but for a few key differences. Firstly, the trigger cut is looser, requiring EF_2g20_loose instead of a medium-based trigger to reduce the identification separation between isolated electrons and jets faking electrons. Secondly, the Id cut is altered to require that both electrons pass isEM *loose* but fail at least one of two specific strip cuts from isEM *medium*. Passing isEM *loose* maintains some prerequisites of the *medium* cut integral to the signal selection, such as hadronic leakage, and passing of certain shower shape variables in the second layer of the calorimeter, as well as having an associated track. Requiring that electrons fail either $\Delta \mathrm{E}_{Maxs1}$, or W_{tot} (described in Table 5.3) in addition to this, then preferentially selects non-isolated electrons that would usually be excluded by these cuts in the first precision layer of the calorimeter, and would have a similar shaped distribution in the signal sample. The isolation requirement made at the end of the signal selection is still applied in the QCD selection; this is to ensure the most electron like contamination in the signal sample is obtained. A dijet function similar to one used by the dijet resonance group [96] (Equation (6.1)) is fitted to the resulting reverse Id invariant mass spectrum (where x is M_{ee}, and p_0, p_1, p_2, are fit parameters) around the Z^0 peak from 70-200 GeV. This is to obtain a parameterisation of the QCD dijet mass distribution from data, that can be extrapolated into the high mass region. In the 2010/11 dilepton analyses [2, 3], two other methods were also used to estimate the QCD dijet mass distribution, namely an isolation method (similar to reverse Id, but performs a fit using the isolation distribution), and a fake rate measurement using inclusive jet samples. All three methods showed good agreement, with the reverse Id method subsequently used as the default method [95, 83].

$$f(x) = p_0 x^{p_1} x^{p_2 \cdot \log x} \tag{6.1}$$

The reversing of other possible isEM cuts was also explored to understand the systematic uncertainty due to cut choice. This is presented in Figure 6.1, with the maximum difference between cut choices propagated to the nominal QCD selection as a systematic. The systematic uncertainty due to a varying fit range around the Z^0 peak was negligible. For completeness the DD QCD selection was also performed on all other MC backgrounds, to assess the level of their contamination in the QCD estimate. The total level of MC background passing the DD QCD selection was found to be $< 0.05\%$ and so deemed negligible. The statistical uncertainty on the fit was calculated using the fit parameter uncertainty for p_0, p_1, and p_2. The nominal reverse Id mass distribution using 2.12 fb^{-1}, together with the dijet function fit and all uncertainties, are presented in Figure 6.2.

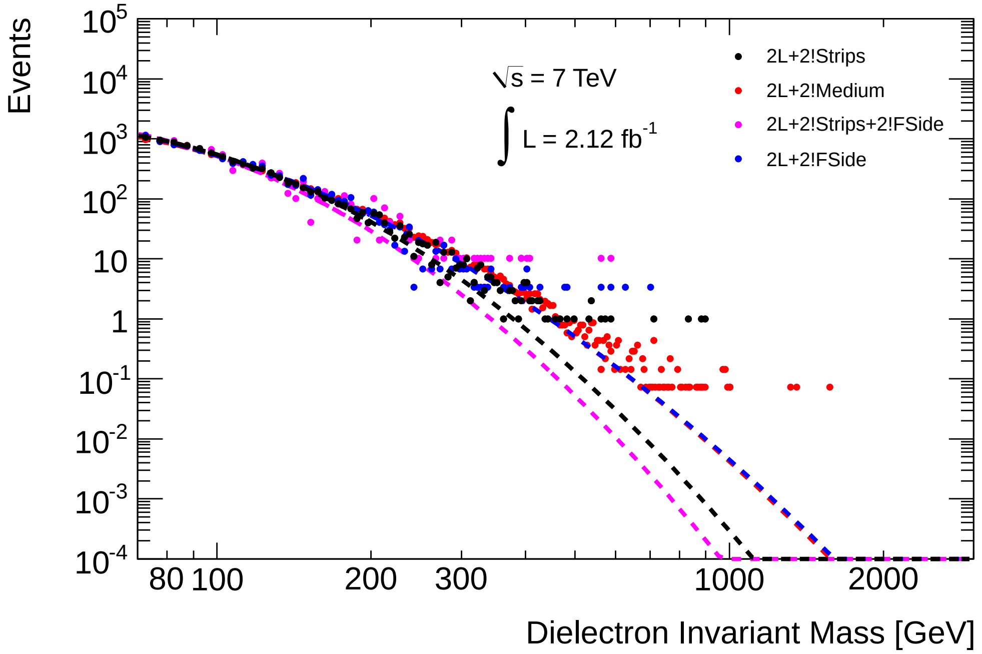

Figure 6.1: Results of the reverse identification selection method with varying cut choices. The different cut selections always require two isEM *loose* electrons ("2L"), varying the other QCD enriching cut between electrons failing: ("2!Strips") at least one of two specific strip cuts (ΔE_{Maxs1} or W_{tot}); ("2!Medium") isEM *medium*; ("2!Strips+2!FSide") at least one of the two strip cuts or FSide<0.63; ("2!FSide") FSide<0.63. The "2L+2!Strips" cut choice was taken as the nominal, with the other estimates normalised to this selection and used as systematics.

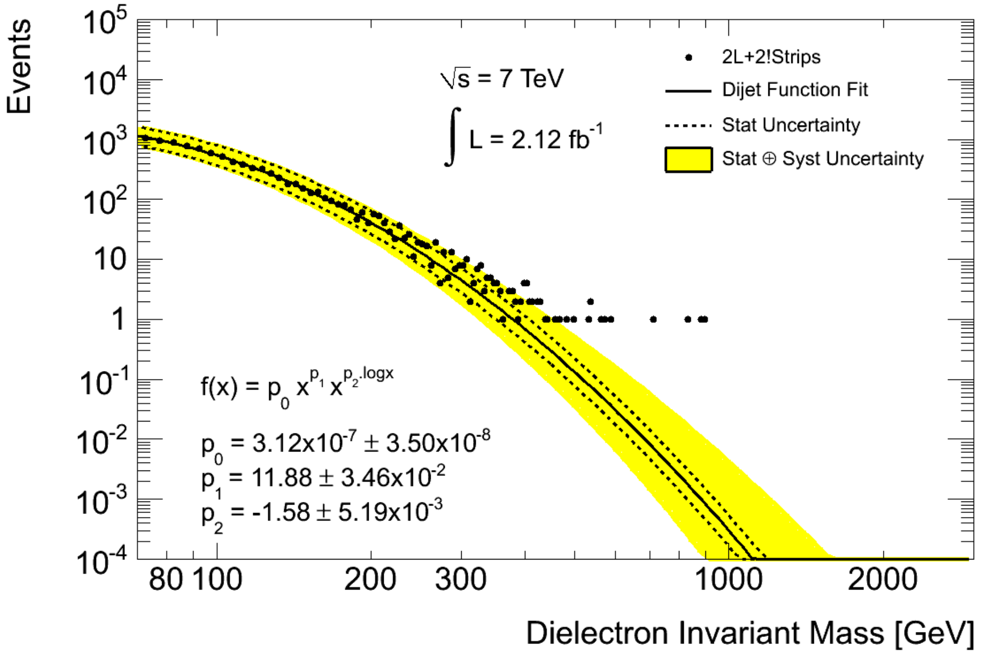

Figure 6.2: Nominal reverse identification method result performed with 2.12 fb^{-1}. The invariant mass spectrum of selected candidates is used to fit a dijet function enabling the data-driven estimate to be extrapolated into the tail of the distribution. The systematic uncertainty on this estimate was taken as the maximum variation using similar selections as shown in Figure 6.1, and statistical uncertainty was taken as the fit parameter uncertainty.

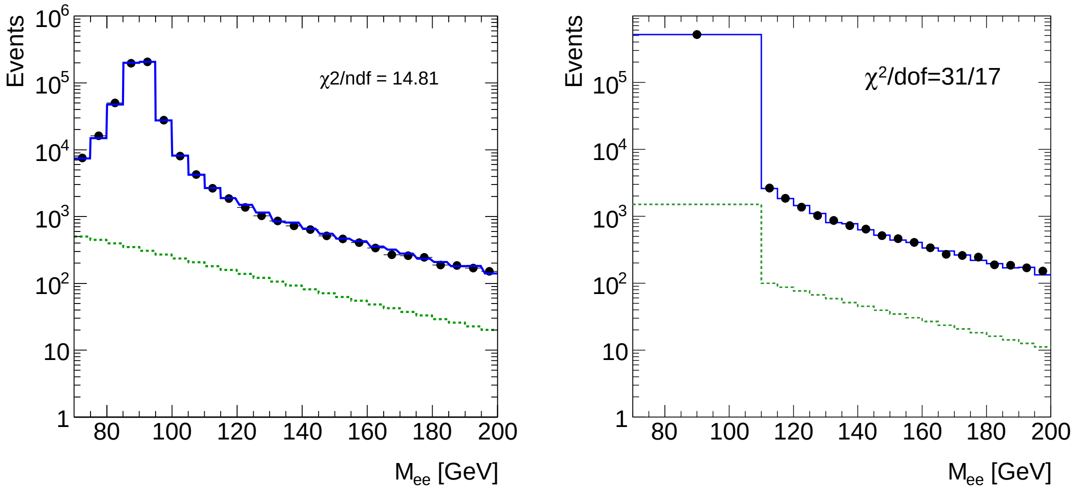

Figure 6.3: Normalisation for the data/MC comparison in the control region 70-200 GeV using a log likelihood fit. The two plots show normalisation using the standard fit (left), and one bin Z^0 peak method (right). The green dotted line shows the QCD component, with the blue solid line showing the total background estimate including QCD.

6.2 Background Normalisation

The procedure for estimating the contribution from background processes in this thesis relied on using the distributions resulting from the applied MC selection described in Chapter 5.2 and the DD QCD estimate as described in Section 6.1. The MC background processes considered, namely: Drell-Yan, $W+$jets, $t\bar{t}$, and dibosons (Figure 1.14), were analysed and normalised relatively to each other using their corresponding sample size and cross section as listed in Appendix B.2. The MC templates were then added together to create an overall MC background template and combined with the DD QCD template, normalising to data in a control region around the Z^0 peak from 70-200 GeV, allowing both the MC and DD QCD template components to vary in the fit. Furthermore, as this search is only concerned with the normalisation scale in the Z^0 region (and not the exact shape of the Z^0 peak), a single binned approach was used for the range immediately around the Z^0 peak from 70-110 GeV. The integral of the fit in the control region is used to calculate the normalisation factor for each template component. The result of the normalisation procedure is shown in Figure 6.3.

The Z^0 peak was chosen for the normalisation region as it is the highest mass dielectron resonance that can be used as a standard candle from the SM in this search. Normalising the background estimate in this way provides immunity from luminosity uncertainty as well as any mass independent uncertainties. Crucially, this does not bias the search as

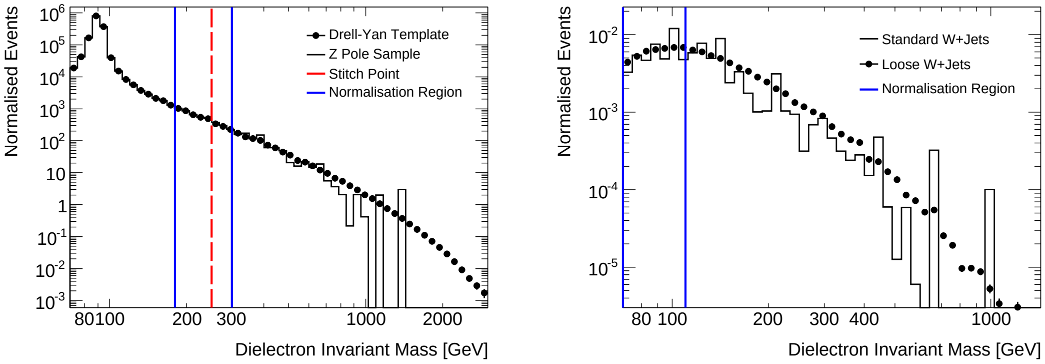

Figure 6.4: The Drell-Yan estimate sample stitching result (left), and $W+$jets loose sample selection normalisation to the standard $W+$jets selection (right).

it scales the background to a well known resonance which is not of interest to the search analysis, allowing an unbiased extrapolation into the tail region to look for signal.

To accurately estimate the Drell-Yan background a combination of MC samples was used. The first $Z^0/\gamma^* \rightarrow ee$ sample listed in Table B.4 refers to a dedicated high statistics Z^0 pole sample, but lacks statistics at high mass. The other samples listed in Table B.4 are samples dedicated to Drell-Yan production in specific mass bins, extending out to beyond 2 TeV. These samples have adequate statistics in the high mass region but could be improved in the low mass region which the high statistics sample covers. Therefore a sample stitching procedure was used when considering the Drell-Yan background in this search, with the shape at masses below 250 GeV coming from the high statistics sample, and above 250 GeV from the combined binned sample which is normalised (using the integral from 180 GeV to 300 GeV) to the high statistic sample at the stitch point. Figure 6.4 (left) shows the result of this procedure.

For this search the $W+$jets sample was found to lack statistics in the tail of the invariant mass distribution. To rectify this issue, a looser $W+$jets selection was applied in parallel to the standard MC selection to obtain a $W+$jets distribution shape which extended into the search region. The looser $W+$jets selection consisted of removing the isEM Id, b-layer, and isolation cut from the standard MC selection. The resulting distribution was normalised to the standard $W+$jets result after data/MC normalisation, in the control region 70-110 GeV, and used as the $W+$jets estimate in this search analysis. Figure 6.4 (right) shows the comparison between the standard and loose $W+$jets selection.

Chapter 7

Results

During pp physics data taking in 2011 more than 5 fb^{-1} of data was recorded by the ATLAS detector at a centre of mass energy $\sqrt{s} = 7$ TeV. The dataset for this thesis is based on the data collected between the 23rd of March and 22nd of August 2011. This amounts to an integrated luminosity of 2.52 fb^{-1} with stable beam conditions, 2.12 fb^{-1} of which was deemed to be suitable for analysis in the electron channel after GRL. The results for this dataset after event selection as described in Chapter 5.1, are shown in Table 7.1, with 529,874 candidate events accepted out of a total of 258,002,456. As data taking is spread over a period of time, it is also interesting to represent the results of the data cut flow as a yield plot across each individual run, that when combined make up the complete dataset. One would expect the distribution of this yield plot (Figure 7.1) to be relatively flat across all runs when normalised to run integrated luminosity, and indeed this is the case apart from runs 182013 and 185353 which show an apparent higher than average yield due to low statistics in those runs. For completeness it should be noted that the event selection was also run over the debug stream for all runs in this dataset, returning zero events. The debug stream contains events that for reasons such as system timeout were not included in the physics stream.

The equivalent selection was applied to MC simulation (Chapter 5.2), enabling a comparison between observed data and the expected SM result, with any discrepancy to be quantified in Chapter 9. Details of the comparison procedure were explained in Chapter 6 along with the determination of the data-driven QCD estimate. The main backgrounds to a Z'/G^* signal are: Drell-Yan, W+Jets, $t\bar{t}$, QCD dijets, and Dibosons. All of these backgrounds are taken into account for the comparison, with Drell-Yan being by far the

Cut	Number of Events	Relative Efficiency [%]	Total Efficiency [%]
Total	258,002,456	1	1
GRL	224,696,451	87.09	87.09
Primary Vertex	224,566,313	99.94	87.04
Trigger	115,285,581	51.34	44.68
Author	76,194,882	66.09	29.53
η	69,194,762	90.81	26.82
E_T	3,463,877	5.01	1.34
Object Quality	3,413,843	98.56	1.32
isEM Id	595,732	17.45	0.23
B-Layer	546,515	91.74	0.21
Isolation	544,422	99.62	0.21
Invariant Mass	529,874	97.33	0.21

Table 7.1: Event selection cut flow summary for the high mass dielectron resonance search analysis, using 2.12 fb^{-1} of ATLAS data taken during the 2011 pp physics run at $\sqrt{s}$ = 7 TeV. Poisson errors on the efficiencies were calculated, but are not shown as all are below 0.05%.

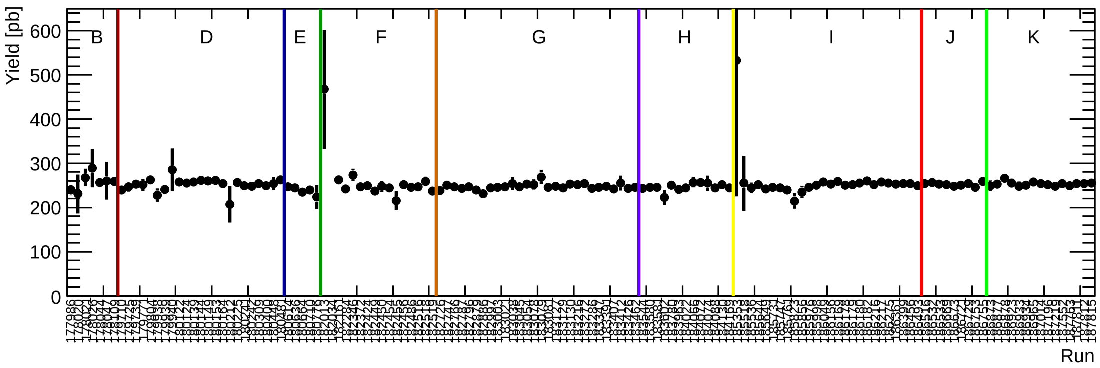

Figure 7.1: Yield plot showing the results of the high mass dielectron resonance search analysis with 2.12 fb^{-1} at $\sqrt{s}$ = 7 TeV. Results are displayed as events per run, per pb^{-1}.

most dominant component. Table 7.2 presents a binned numerical comparison of the data and SM background estimate, followed by kinematic plots for a visual comparison with various possible Z'/G^* signal scenarios displayed with the observed data and SM background prediction. E_T distributions of the leading and subleading electrons are shown in Figure 7.2, with subsequent isolation spectra in Figure 7.3. The η and ϕ distributions of both electrons are displayed in Figure 7.4, followed by the isEM *medium* variable distributions that were used in the DD QCD estimate, presented in Figure 7.6 (All applicable isEM *medium* variable distributions not shown, are provided with data/MC comparison in Appendix F.1). Lastly, the dielectron invariant mass spectrum is presented in Figure 7.7, and the $\cos\theta^*$ distribution of both electrons, as described in Chapter 1.2.3, is displayed in Figure 7.8. All of the presented plots include the expected variable shape should a Z' signal be present, with all equivalent G^* plots provided in Appendix F.2 (except invariant mass and $\cos\theta^*$, which are displayed here). Note that in the case of the $\cos\theta^*$ distribution, a Z' signal with increased cross section by a factor of 1000, and G^* by a factor 100, are plotted, as the expected observable deviation due to a new physics signal above the SM background would require a large dataset of $O(100\ \text{fb}^{-1})$, and would otherwise not be clearly visible in the 2.12 fb^{-1} dataset of this thesis.

M_{ee} [GeV]	70-110	110-130	130-150	150-170	170-200
Drell-Yan	512917.0 ± 716.7	6270.0 ± 79.7	2267.6 ± 48.1	1203.9 ± 35.2	908.4 ± 30.6
QCD	1497.6 ± 39.2	330.7 ± 18.7	194.1 ± 14.4	115.1 ± 11.2	93.0 ± 10.2
Diboson	669.1 ± 26.4	53.6 ± 7.8	41.3 ± 6.9	25.6 ± 5.6	25.3 ± 5.5
W+Jets	293.2 ± 17.6	110.6 ± 11.0	77.9 ± 9.3	53.3 ± 7.8	51.6 ± 7.7
$t\bar{t}$	452.1 ± 21.8	167.0 ± 13.4	120.9 ± 11.5	99.6 ± 10.5	102.7 ± 10.6
Total	515829.0 ± 718.7	6931.8 ± 83.8	2701.8 ± 52.5	1497.4 ± 39.2	1181.0 ± 34.9
Observed	515829	6880	2739	1476	1200
Difference	0.0	-51.8	37.2	-21.4	19.0

M_{ee} [GeV]	200-240	240-300	300-400	400-800	800-3000
Drell-Yan	595.2 ± 24.9	389.2 ± 20.2	213.4 ± 15.1	110.2 ± 11.0	6.2 ± 3.0
QCD	54.3 ± 7.9	27.6 ± 5.8	10.1 ± 3.7	2.1 ± 2.0	0.0 ± 0.0
Diboson	22.2 ± 5.2	12.3 ± 4.0	12.5 ± 4.1	5.5 ± 2.9	0.4 ± 1.2
W+Jets	38.2 ± 6.7	27.9 ± 5.8	17.6 ± 4.7	9.0 ± 3.5	0.4 ± 1.2
$t\bar{t}$	72.3 ± 9.0	58.8 ± 8.2	28.7 ± 5.9	10.6 ± 3.8	0.2 ± 1.1
Total	782.2 ± 28.5	515.9 ± 23.2	282.3 ± 17.3	137.3 ± 12.2	7.1 ± 3.2
Observed	785	521	304	132	8
Difference	2.8	5.1	21.7	-5.3	0.9

Table 7.2: Numerical Data/MC comparison for the 2.12 fb^{-1} search analysis, using the dielectron invariant mass spectrum. The table binning is more coarse in the tail of the distribution to account for the low number of observed/expected events. The errors given are Poisson statistical.

The observed data shows good agreement with the SM prediction across the invariant mass range 70-3000 GeV, with only a few regions showing either a slight excess or deficit of observed events. All invariant mass bins in Table 7.2 agree between data and SM background within Poisson statistical errors, except the bin 300-400 GeV which shows a small excess. Other variable distributions also show good agreement between MC and data, with the slight asymmetry in the η distribution, and deficit around 0.8 in ϕ (Figure 7.4), understood by accounting for the missing FEB regions in the ECAL as discussed in Chapter 5.1 and illustrated in Figure 5.1. The isolation spectrum for leading and subleading electrons in Figure 7.3, shows some minor known mismodelling issues in MC, also accounted for by the relatively low statistics in the tail of the $W+$jets and $t\bar{t}$ backgrounds. The leading electron isolation distribution is displayed without the < 7 GeV criterion applied, so that the effect of making this requirement is clear. If the selected region of the leading electron isolation distribution is considered, it is evident that a large fraction of the QCD dijet background is removed, as well as an improvement observed in the data/MC comparison. The W_{tot} distribution shown in the lower plot of Figure 7.6 shows an apparent discrepancy. However, apart from some minor MC mismodelling in the shape causing a small shift in W_{tot}, the disagreement seen at large values is due to the nature of the reverse Id method, in which W_{tot} was specifically chosen as one of the variables to select the QCD dijet background from data. The apparent over estimation in QCD at high values is therefore due to few events passing the signal event selection because of the W_{tot} criterion, and conversely a large amount of QCD selected upon the reversing of this criterion. The $\cos\theta^*$ distribution appears to have a small excess around $\cos\theta^* = 0$, however the effect from a Z'/G^* resonance with this dataset is not expected to be visible. To investigate whether this excess appears to be signal like in nature, the Z'/G^* signals were scaled by a factor of 1000/100 respectively. It is then evident that this excess does not immediately correlate to a Z'/G^* signal (Figure 1.16). Though a high mass G^* signal via $q\bar{q}$ production would show a centrally peaked distribution in $\cos\theta^*$, there would be an even greater excess in the distribution tails which are not observed in this result.

The three highest invariant mass candidate dielectron resonance events, selected in the 2.12 fb^{-1} search, are listed with detailed kinematic information in Table 7.3. The highest invariant mass event is displayed using Atlantis [97], in Figure 7.9, with the other two high invariant mass events displayed in Appendix G.

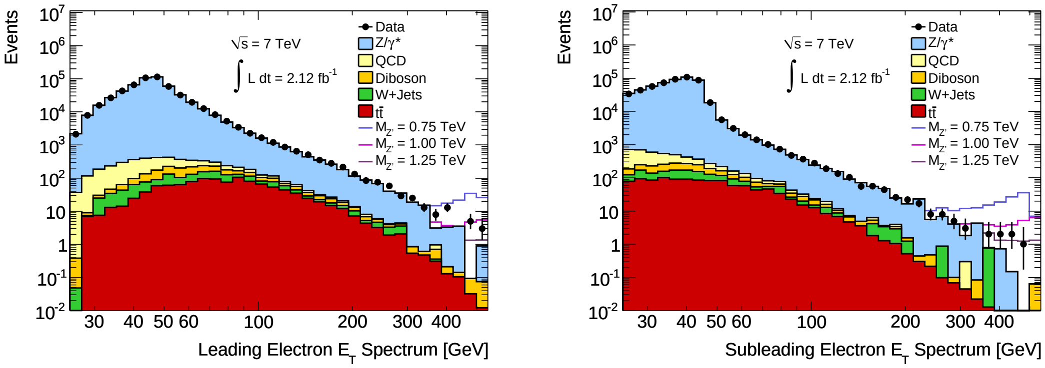

Figure 7.2: E_T distribution for the leading (left) and sub-leading (right) electron after event selection. The comparison is between 2011 data and all relevant background processes, as well as various possible Z'_{SSM} resonance signals.

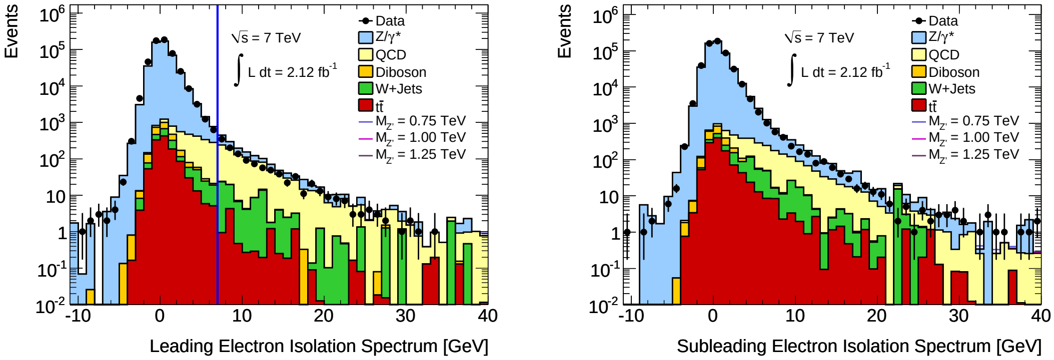

Figure 7.3: Isolation distribution for the leading electron (left) with event selection excluding the isolation requirement (vertical blue line indicates the 7 GeV cut value). Also shown is the subleading electron (right) after full event selection. The comparison is between the 2.12 fb^{-1} dataset and all relevant background processes, as well as various possible Z'_{SSM} resonance signals (barely visible due to dataset size).

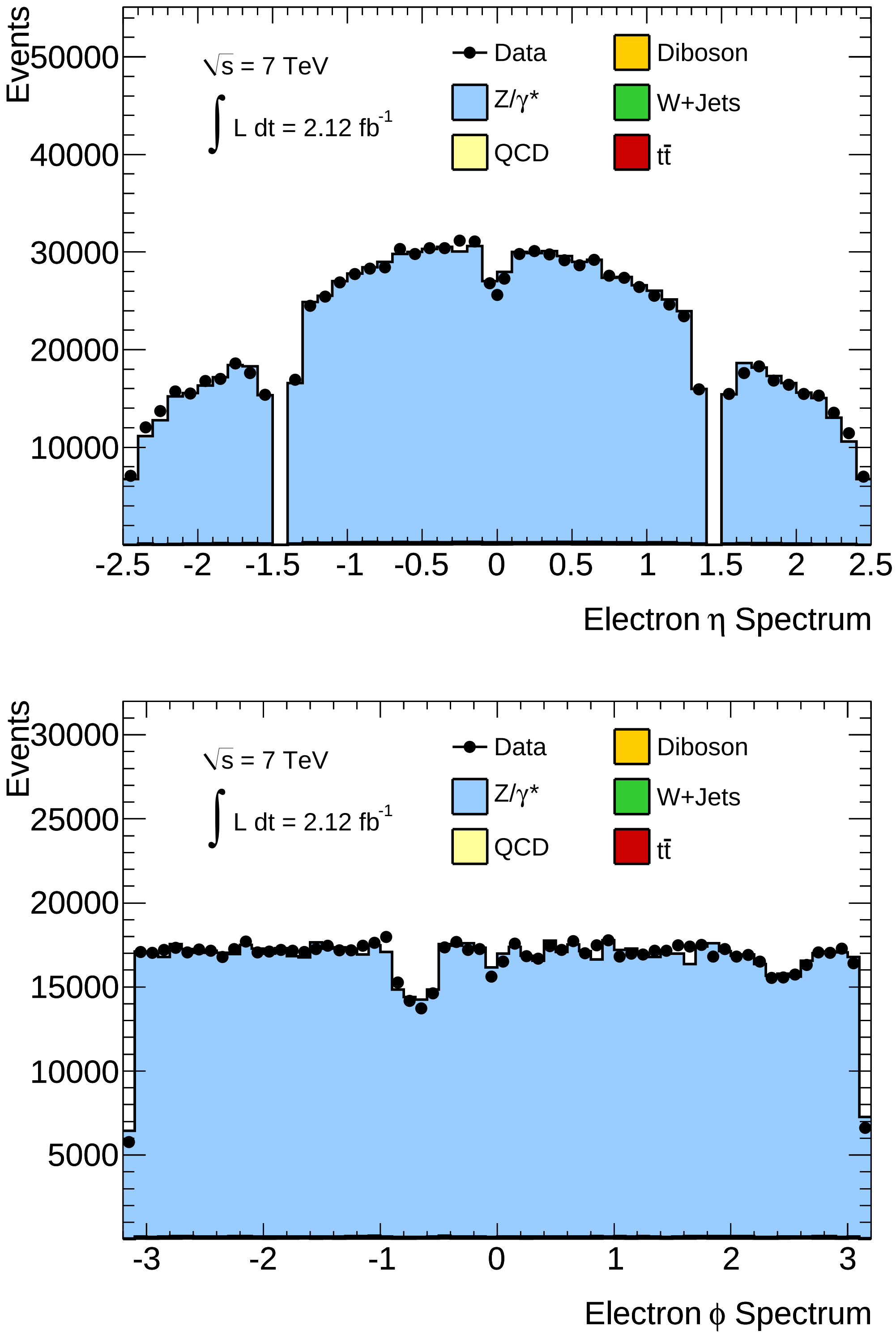

Figure 7.4: Distributions of η (upper) and ϕ (lower), for both electrons in candidate events selected by the search analysis. The comparison is between the 2.12 fb^{-1} dataset and all relevant background processes, as well as various possible Z'_{SSM} resonance signals (not visible due to dataset size).

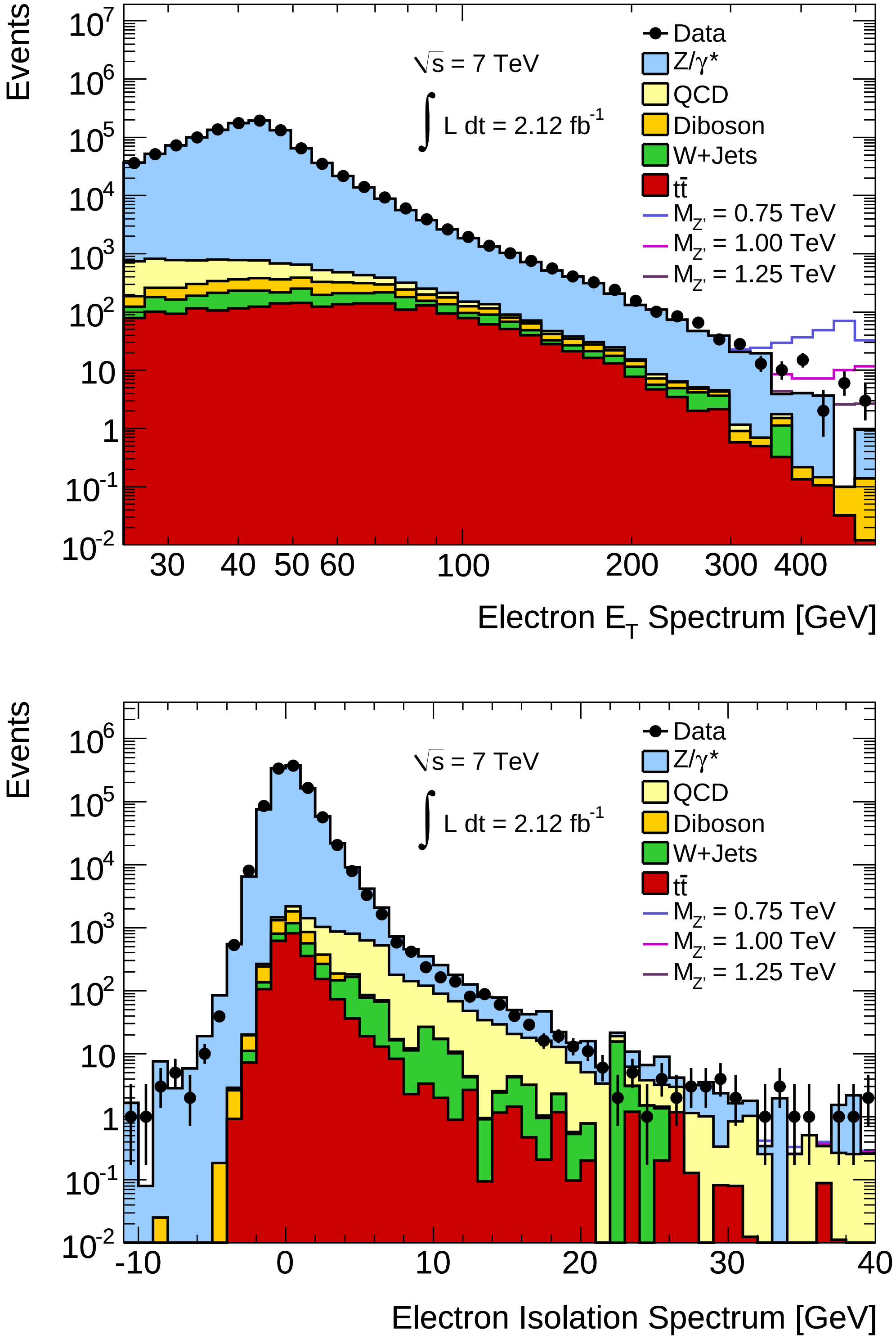

Figure 7.5: Distribution for both electrons in candidate events showing the E_T spectrum (upper) and Isolation spectrum (lower), after event selection. The comparison is between the 2.12 fb^{-1} dataset and all relevant background processes, as well as various possible Z'_{SSM} resonance signals.

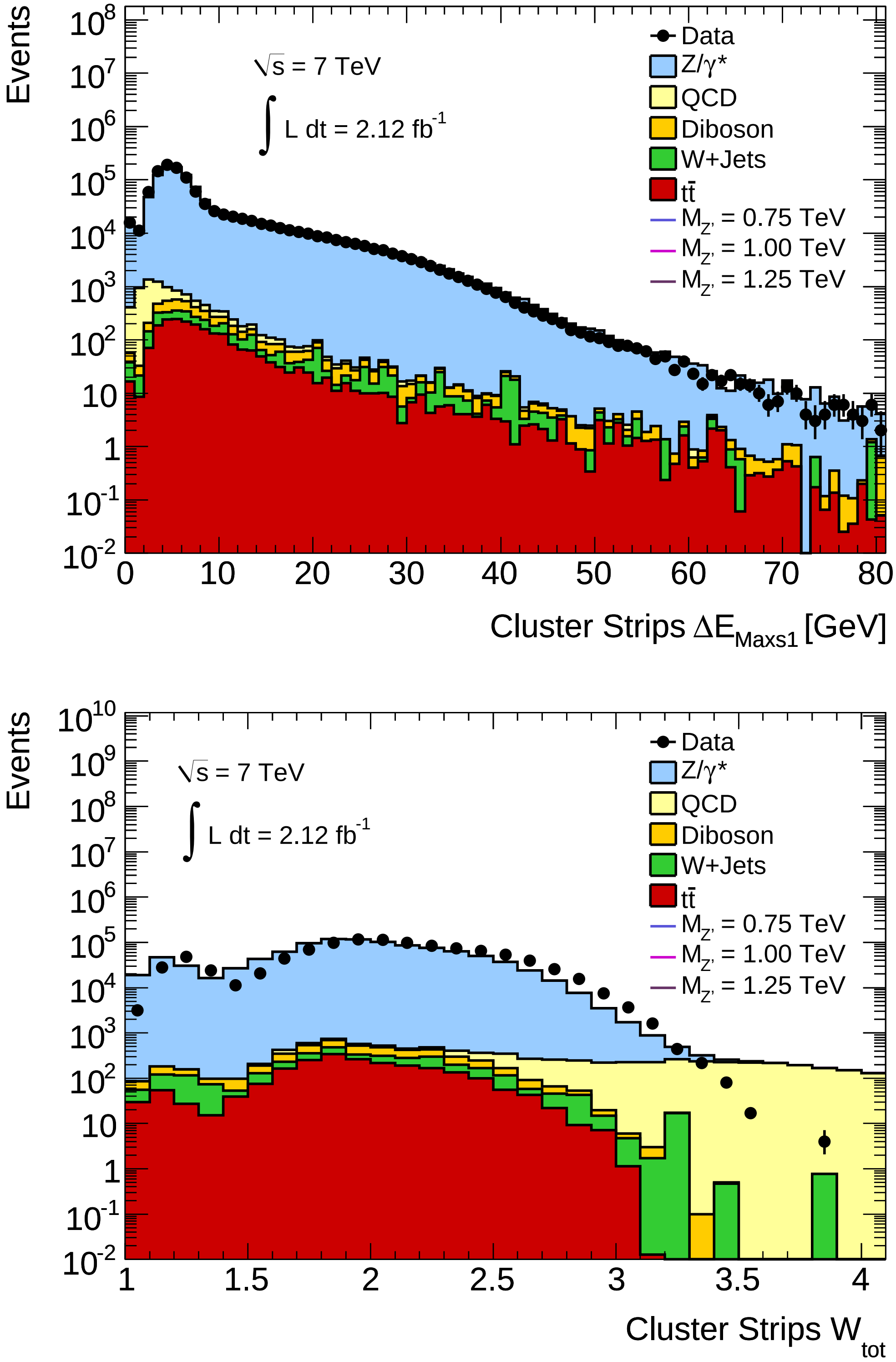

Figure 7.6: Distribution for both electrons in candidate events showing the Cluster Strips ΔE_{Maxs1} spectrum (upper) and Cluster Strips W_{tot} spectrum (lower), after event selection. The comparison is between the 2.12 fb^{-1} dataset and all relevant background processes, as well as various possible Z'_{SSM} resonance signals.

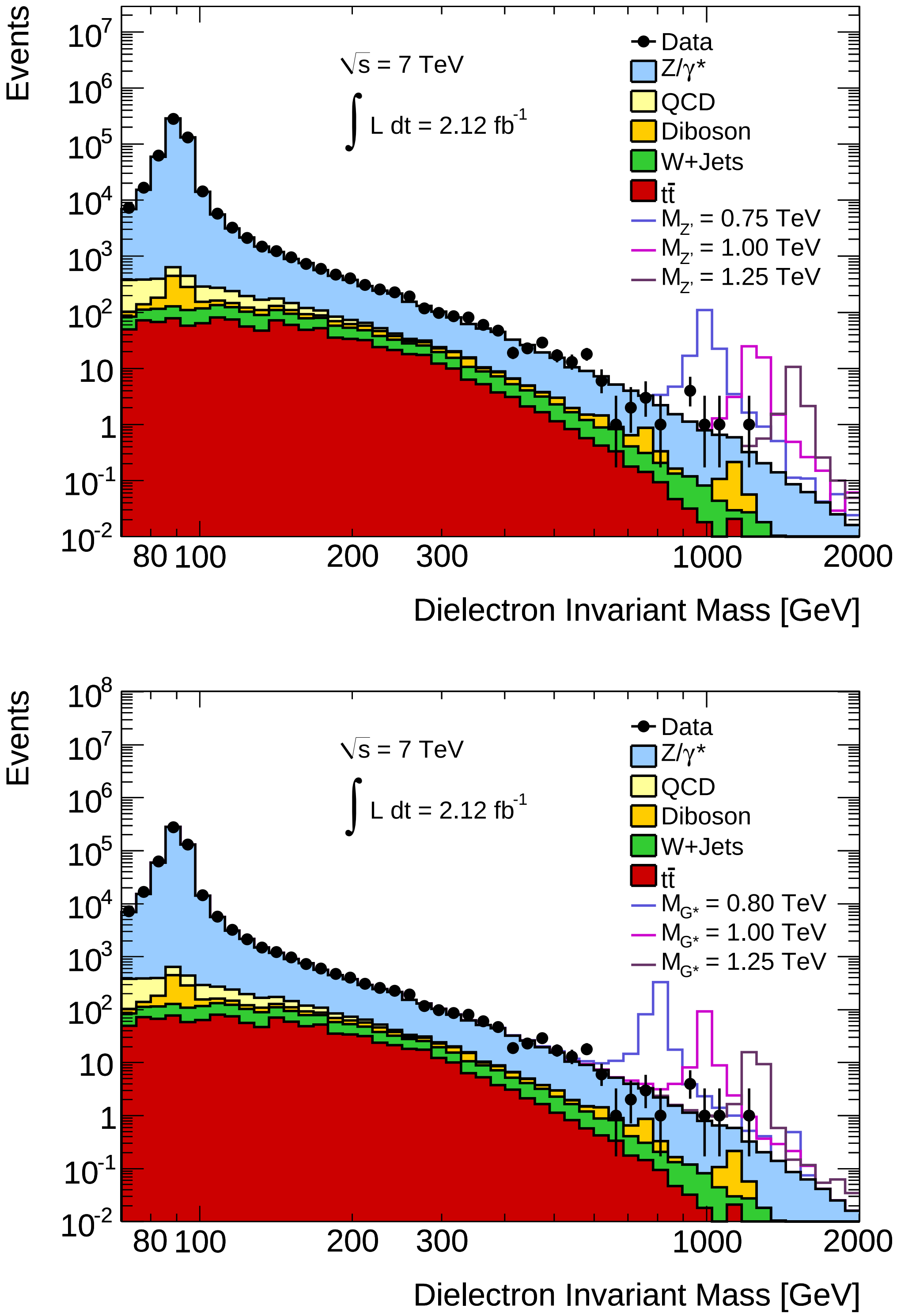

Figure 7.7: Dielectron invariant mass distribution for candidate events selected by the search criteria. The comparison is between the 2.12 fb^{-1} dataset and all relevant background processes, as well as various high-mass resonance signals for the Z'_{SSM} (upper) and RS G^* (lower). The G^* resonances shown are for a coupling, k/$\overline{M}_{Pl}$ = 0.10.

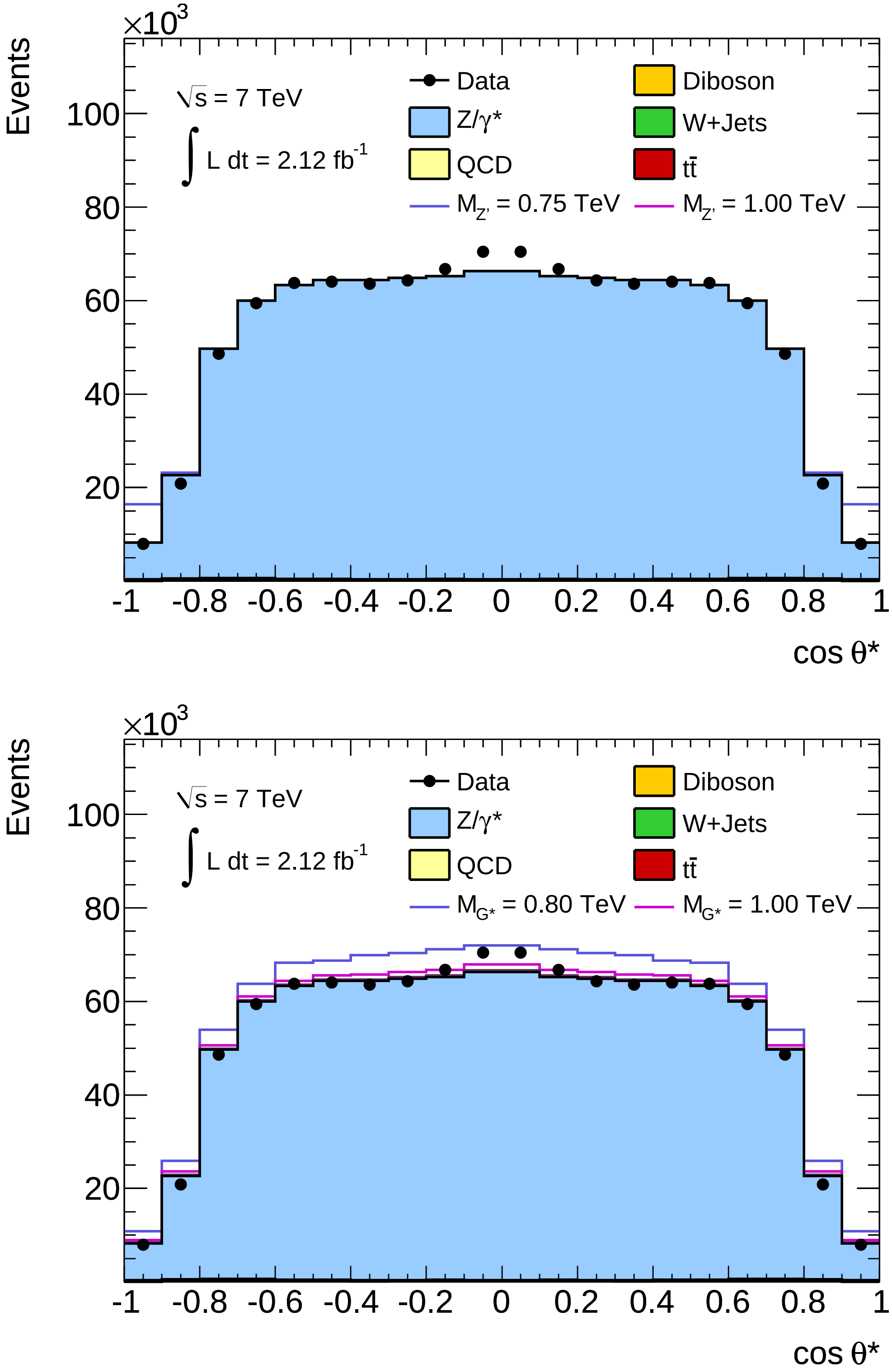

Figure 7.8: cosθ* distribution for both electrons in candidate events after selection criteria. The comparison is between the 2.12 fb^{-1} dataset and all relevant background processes, as well as high-mass resonance signals for the Z'_{SSM} (upper) and RS G^* (lower). The G^* resonances shown are for a coupling, k/$\overline{M}_{Pl}$ = 0.10. The Z'/G^* signal cross sections are increased by a factor of 1000/100 respectively, to make the distribution observable given the relatively small dataset size.

Run Number	Event Number	M_{ee} [GeV]	E_T [GeV]	η	ϕ [rad]	q	d_0 [mm]	z_0 [mm]	Calo Iso [GeV]	Had Leak	FSide	Pixel Hits	SCT Hits	TRT Hits	isEM Id
183462	48979599	993.29	256.64	-0.76	1.14	-1	0.53	1.01	3.54	-0.001	0.26	3	8	26	Tight
			206.61	2.05	-2.05	+1	-0.61	3.79	3.79	0.004	0.18	3	10	12	Tight
186721	111269544	1213.94	459.13	-0.42	2.51	+1	-0.78	100.16	-0.45	0.006	0.20	3	10	37	Tight
			445.22	1.18	-0.73	-1	0.73	100.93	0.33	0.001	0.29	3	8	34	Tight
187811	12520737	1068.25	507.87	0.62	1.43	+1	0.20	-48.01	-2.73	-0.001	0.23	3	10	36	Tight
			460.13	1.54	-1.72	-1	-0.24	-45.13	-1.34	0.004	0.23	3	8	39	Tight

Table 7.3: Kinematic information for the three highest invariant mass events from the 2011 dataset used for this thesis comprising of 2.12 fb^{-1}. For each event, the first three columns show: the run number, event number, and invariant mass of the event. For the columns proceeding these, the first line represents the kinematic information of the leading electron in the event, and the second line represents that of the subleading electron. These electron columns from left to right present: E_T, η, ϕ, charge, transverse impact parameter d_0 (distance of closest approach to local z-axis), longitudinal impact parameter z_0 (z-value at the perigee), calorimeter isolation (pt corrected in a cone of $\Delta R = 0.2$), hadronic leakage, fraction of energy outside the shower core (FSide), number of pixel hits, number of SCT hits, number of TRT hits, and isEM identification status.

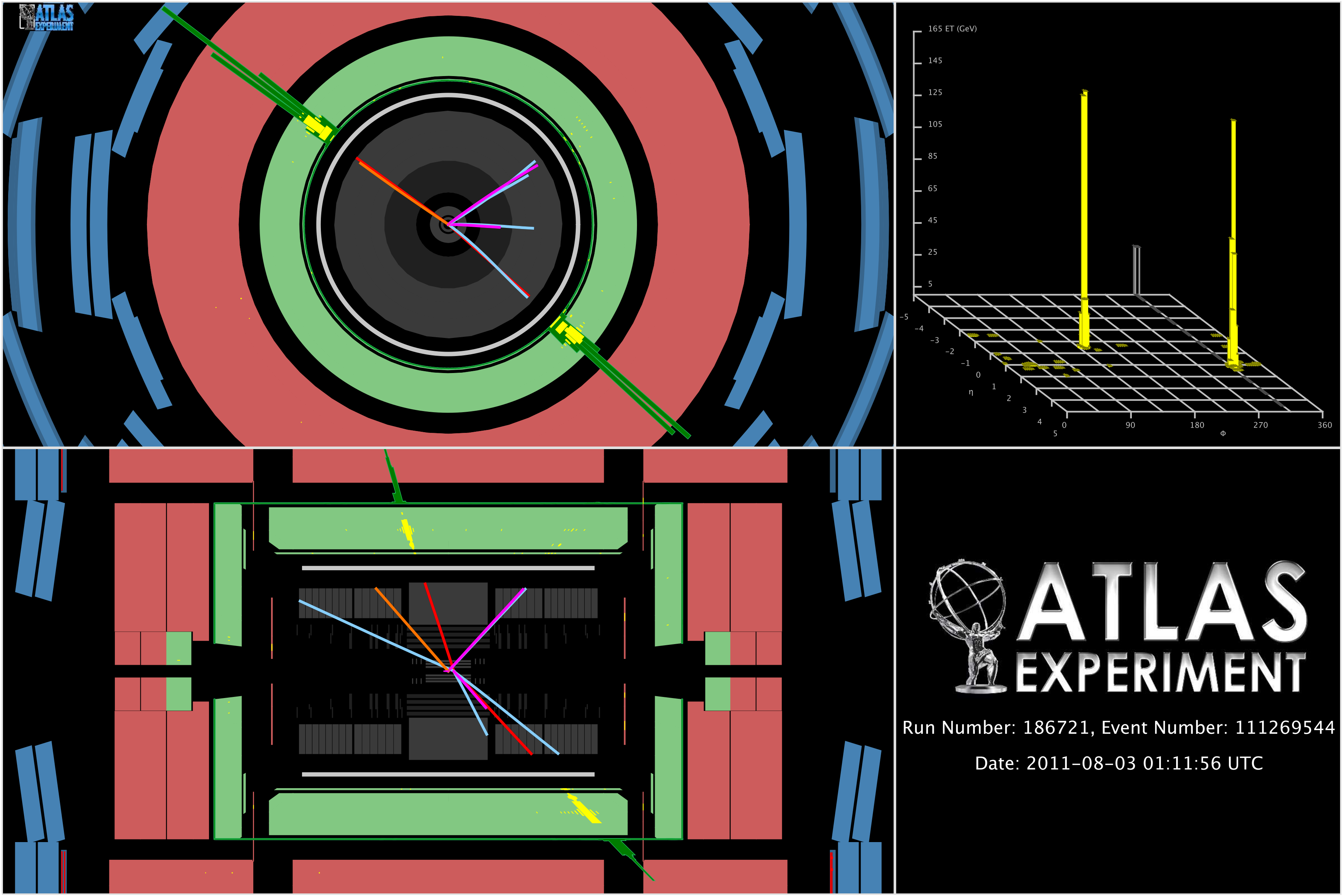

Figure 7.9: Atlantis event display showing the highest invariant mass dielectron event selected by the 2.12 fb^{-1} analysis presented in this thesis, recorded by the ATLAS detector in 2011. This event has an invariant mass of 1213.94 GeV. Views in X-Y (upper left), p_Z (lower left), and ECAL lego plot (upper right) are shown.

Chapter 8

Systematic Uncertainties

The systematic uncertainties in this analysis are reduced due to the normalisation of MC to data in a control region around the Z^0 peak as described in Chapter 6. This procedure removes any luminosity uncertainty as the fit provides the necessary normalisation scale without the use of an integrated luminosity estimate. Any mass independent systematic uncertainties are also removed as they are folded into the scale provided by the normalisation procedure. It is important therefore to understand the mass dependent normalisation systematic uncertainties which are summarised for a 1.5 TeV signal search in Table 8.1. Any systematic uncertainty that after investigation is found to contribute less than 1.5% uncertainty, is deemed negligible and therefore not included in the final estimate (individual systematics are added in quadrature). The applicable systematics are displayed across the full invariant mass range in Figure 8.1.

Source	Z' Signal	G^* Signal	Background
Normalisation	5%	5%	N/A
PDF/α_s	10%	12%	10%
QCD K-factor	3%	N/A	3%
Weak K-factor	N/A	N/A	4.5%
Efficiency	1.5%	1.5%	1.5%
Resolution	-	-	-
QCD Background	N/A	N/A	1.5%
Total	12%	13%	12%

Table 8.1: Summary of the mass dependent systematic uncertainties considered in this analysis. Values given are examples for a 1.5 TeV Z'_{SSM}, and 1.5 TeV RS G^* with $k/\overline{M}_{Pl} = 0.10$. “N/A” indicates that the uncertainty is not applicable, and “-” denotes sources with a negligible contribution (below 1.5%). The individual uncertainties are added in quadrature to give the total estimated systematic uncertainty.

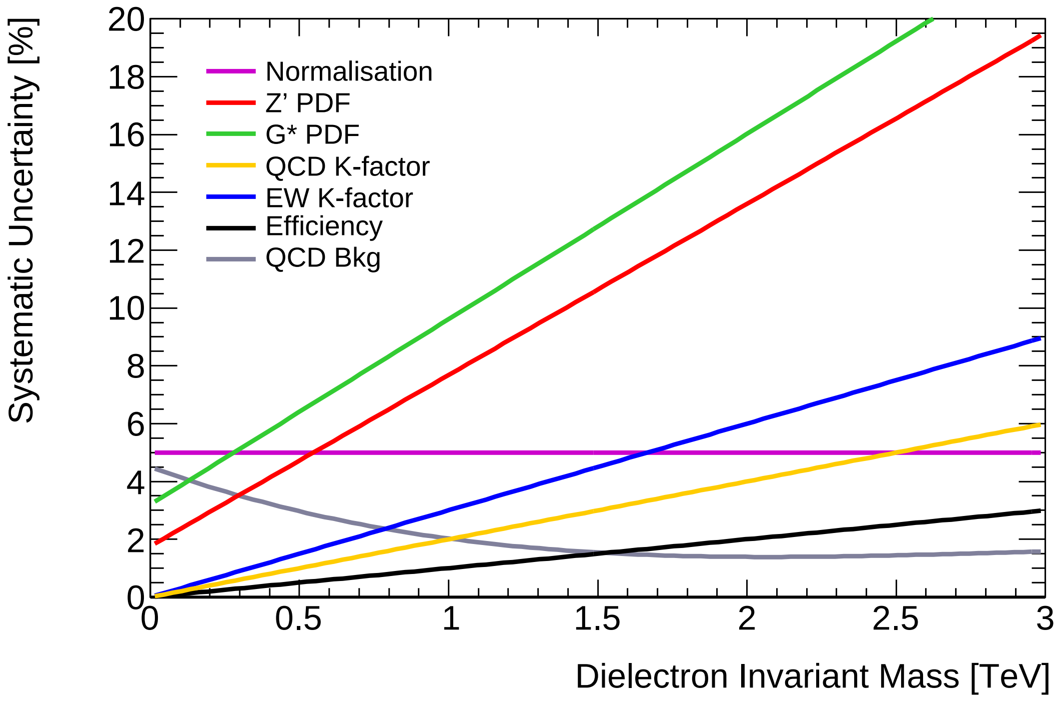

Figure 8.1: All mass dependent systematic uncertainties taken into account for the 2.12 fb^{-1} dielectron channel search analysis, which were derived as part of the 2010/11 dilepton analyses [83, 84]. These values are used as nuisance parameters in the limit setting procedure.

The systematic uncertainties presented, are considered as correlated between signal and background processes across all invariant mass bins in the search region, except for the weak K-factor which is only applied to the Drell-Yan background. The uncertainties are incorporated into the limit setting procedure as nuisance parameters, integrating over the variation, for the computation of the likelihood function as described in Chapter 9.

The systematic uncertainty estimation methods and results presented here, were studied as part of the 2010/11 dilepton analyses [83, 84]. The QCD K-factor uncertainty is obtained by varying the renormalisation and factorisation scales by a factor of two around the nominal scale, adding linearly the largest K-factor difference (this study is presented in Appendix B.3). The QCD K-factor is not applied to the G^* signal as no estimate at $\sqrt{s} = 7$ TeV is currently available [98, 99]. The weak K-factor uncertainty was studied by incorporating the electroweak scheme difference between PYTHIA and HORACE, as well as accounting for real W/Z emission and higher order corrections, as presented in Appendix B.4. This K-factor is only applied to the Drell-Yan background as the weak K-factor does not apply to the other backgrounds or G^*, and cannot be directly applied to the Z' as the triple gauge couplings vanish in contrast to the SM Z^0. The Parton Distribution Function (PDF) and α_s uncertainties are obtained by varying the MSTW2008 eigenvector PDF sets, and the PDF sets corresponding to variations of α_s, both at 90% CL (this study is described in Appendix C). A mass independent 5% uncertainty on the Z^0/γ^* cross section [100] is included for the signal, as luminosity scaling was achieved using the Z^0 peak instead of a luminosity estimate.

The experimental systematic uncertainties on efficiency, resolution, and the QCD dijet background were also considered. The efficiency uncertainty was estimated by studying the mass dependence of adding the calorimeter isolation criterion. This resulted in a 1.5% systematic uncertainty at 1.5 TeV for the electron reconstruction and identification efficiency. The resolution uncertainty was assessed by using the resolution smearing correction uncertainty recommended by the e/γ working group study [92], and was found to be negligible. The calorimeter energy calibration uncertainty is between 0.5% and 1.5%, depending on p_T and η, with the non-linearity of the calorimeter response being negligible according to test beam data and MC studies [101]. All of these resolution effects have a minimal impact on the sensitivity of this search, as the main effect would be to shift any potential peak in the dielectron invariant mass spectrum, without greatly affecting the line shape. The DD QCD background estimate was assigned a systematic uncertainty of 1.5%. This was calculated by taking the ratio of total background, where the QCD background estimate was increased by 1σ, and the nominal case. The effect of using a non-nominal DD QCD selection was also studied, comparing the ratio of total background where the QCD estimate was taken as the maximum systematic, to the nominal case (see Figure 6.2). This had a negligible effect after the normalisation procedure ($\sim$0.01%).

Chapter 9

Statistical Interpretation of Results

To quantify the level of agreement between observed data and SM predictions (as well as any BSM prediction), a statistical treatment of the results is used. The broad regimes of statistical methodology fall into two categories: Frequentist, and Bayesian. In this thesis both approaches will be used to interpret the results, with the Frequentist method used as a benchmark for the Bayesian treatment which will be presented as the main statistical result. The Bayesian result is obtained using a software package called the Bayesian Analysis Toolkit (BAT) [102], which offers ease of incorporating multiple channels into the analysis, as well as marginalisation of nuisance parameters through integration using Markov Chain Monte Carlo (MCMC). A two dimensional signal scan is performed to search for a Z' resonance with unknown mass and production rate. p-values are evaluated for the background only hypothesis, and in the absence of a significant excess, exclusion limits are set at 95% Confidence Level (CL) on the cross section times branching ratio (σB) of the signal process for various Z' models, and RS G^* $k/\overline{M}_{Pl}$ couplings. The 2.12 fb^{-1} dielectron result of this thesis is then combined with the equivalent 1.21 fb^{-1} dimuon channel [3], and 2.12 fb^{-1} diphoton channel [4] search results, to set stringent mass exclusion limits on the models considered.

9.1 Methodology

Frequentist Approach

The Frequentist methodology defines probability as the relative frequency of the occurrence of an event, in a number of repetitions of the experiment. This was a paradigm shift from the approach taken before the mid-19th century, which stated that the probability of an event was equal among all possible outcomes. This section will employ Frequentist methods to interpret the 2.12 fb^{-1} dielectron analysis result.

Single Binned Counting Experiment

A single binned counting experiment was used to analyse the results and set limits on Z'/G^* models at a number of test mass points, counting observed and expected events in a single bin above a given threshold. In this analysis the counting threshold was set to 70% of the resonance test mass point, i.e. for a 1 TeV resonance, events are counted above a mass of 700 GeV, and so on. This boundary was chosen to take into account the varying width of resonances in this search.

The expected number of events, μ, is the sum of the expected background (μ_b) and signal (μ_s). Using Poisson statistics, the likelihood to observe n events is:

$$\mathcal{L}(n|\mu) = \frac{\mu^n e^{-\mu}}{n!} \quad \text{, where} \quad \mu = \mu_b + \mu_s \tag{9.1}$$

Uncertainty in any of the free parameters of the likelihood are included as nuisance parameters by multiplying by the probability density function (pdf) characterising that uncertainty. If N_{sys} such nuisance parameters $\theta_1, \ldots, \theta_{N_{sys}}$ are identified (collectively denoted by the vector, $\overline{\theta}$), then the likelihood becomes:

$$\mathcal{L}(n|\mu, \overline{\theta}) = \frac{\mu^n e^{-\mu}}{n!} \prod_{i=1}^{N_{sys}} G(\theta_i, 0, 1) \quad \text{, where} \quad \mu = \sum_j \mu_j (1 + \sum_i \theta_i \varepsilon_{ji}) \tag{9.2}$$

$G(\theta_i, 0, 1)$ is the pdf for nuisance parameter θ_i and is chosen to be a unit Gaussian centred at zero. ε_{ji} is then the relative change in normalisation of process j for each source of systematic uncertainty i, which controls the width of the nuisance parameter.

CL_s Method

The CL_s method [103] is a Modified Frequentist technique that uses a log likelihood ratio (LLR) test statistic, Q, to quantify agreement between observed and expected results:

$$Q = -2 \ln \frac{\mathcal{L}(n|\mu)}{\mathcal{L}(n|\mu_b)} \tag{9.3}$$

A Modified Frequentist technique is used to avoid excluding or discovering a signal that the search analysis is not sensitive to, and is a conscious decision not to insist on the classical Frequentist concept of full coverage[1]. Where a small number of signal events are expected, there is the possibility of an observation of less than the mean number of background events due to a downward fluctuation, resulting in limits on the signal process that effectively exclude even zero signal events at greater than 95% CL. Though this is a valid result, it has been argued [103] that in these limiting cases there is not enough information to clearly distinguish between signal and signal+background hypotheses. The CL_s method addresses this issue by normalising the observed signal+background hypothesis confidence level, CL_{s+b}, to the background only confidence level, CL_b. This is a generalisation of the modified classical calculation of confidence limits for single channel counting experiments as presented in [104]. The result is a conservative limit on the signal hypothesis, that remains sensible in the limit of no signal events and a downward fluctuation of the background.

The CL_s method involves computing the p-values of CL_{s+b} and CL_b, which correspond to the confidence level for the test hypothesis H_1, and null hypothesis H_0, respectively. These confidence levels are evaluated by integrating the LLR distributions populated using MCMC to simulate 100,000 pseudo-experiments. CL_{s+b} and CL_b are defined as below:

$$1 - CL_b = p(Q \leq Q_{obs}|H_0) \tag{9.4}$$

$$CL_{s+b} = p(Q \geq Q_{obs}|H_1) \tag{9.5}$$

Here Q_{obs} is the value of the test statistic observed in data. $1 - CL_b$ is the probability that an upward fluctuation of the background provides a H_1 like outcome, given H_0. CL_{s+b} corresponds to the probability of a downward fluctuation in the total signal plus background, given H_1. A small value of CL_{s+b} would therefore show inconsistency with the H_1 hypothesis. One then defines the CL_s result as the ratio of p-values obtained in Equations (9.4) and (9.5) such that:

$$CL_s = \frac{CL_{s+b}}{CL_b} \tag{9.6}$$

---

[1] Full coverage guarantees that the confidence interval does not include the true parameter value for a fixed fraction of experiments

The exclusion limit is determined by increasing the signal cross section until $CL_s = 1 - \alpha$, therefore setting $\alpha = 0.05$ defines the signal cross section excluded at 95% CL.

Bayesian Approach

The Bayesian branch of statistics uses a subjective interpretation of probability, representing a measure of belief in a given hypothesis [105]. The Frequentist approach can be incorporated into this methodology by making a hypothesis that a measurement will have a given fractional outcome. The strength of a Bayesian approach is in its ability to also assign a degree of belief to the value of unknown parameters such as the mass of an exotic resonance. One can set for example a 95% credibility interval on a given parameter value. This is not meaningful in the Frequentist interpretation which assumes an exact value of the parameter that does not change with repetition of the experiment. Bayes theorem applied to the analysis of a new theory BSM given the observed data can be expressed as:

$$P(theory|data) = \frac{P(data|theory)P(theory)}{P(data)} \tag{9.7}$$

Where $P(data|theory)$ is the probability of observing the data given that the theory is true, $P(theory)$ is the prior probability that the theory is true, and $P(data)$ is the prior probability of observing the data which by construction $P(data) \neq 0$, and through Bayesian inference is assumed to be constant. $P(theory|data)$ is then the posterior probability that the theory is true given the observed data, and can be written as:

$$P(theory|data) \propto P(data|theory)P(theory) \tag{9.8}$$

The prior probability $P(theory)$ is the subjective part of this interpretation, and is assumed to be a uniform positive prior in σB for this analysis, such that $\pi(\sigma B) = 1$ (π denotes a prior distribution), for $\sigma B \geq 0$, and 0 otherwise. Other possible priors such as a uniform prior depending on the expected theoretical σB versus resonance mass could have been used, however for simplicity and to make the statistical treatment as general as possible for high mass resonances, $\pi(\sigma B) = 1$ was used.

Template Method

A template method was used for the Bayesian interpretation of the results. This has an advantage over the simple counting method shown in Section 9.1 as the signal shape from MC is used as a template to include bin by bin kinematic information that is lost when simply looking for an excess of events above a cut threshold using the dielectron invariant mass spectrum. In this way the method is sensitive when distinguishing between an excess due to resonant signatures of new physics, as opposed to models which predict broad non-resonant excesses such as the ADD [30] or contact interaction [106] model, which could also manifest in the dielectron channel should they exist. Furthermore this method is resilient to false positive signal excesses due to experimental bias or background prediction mismodelling/normalisation, as any effect would have to appear resonant in nature to fake the signal.

Signal templates for Z' and G^* resonances (as described in Chapter 3.3) are used to test the consistency of the SM with observed data across the mass range 130 GeV to 2.5 TeV, in 40 GeV steps for the Z', and at the 9 available test masses for the G^*. The template method is essentially a counting experiment in many bins of the observable distribution (in this case the dielectron invariant mass spectrum), meaning the likelihood function can be represented as the product of the single binned counting experiment from Equation (9.1) over all bins in the distribution, N_{bin}. Bin by bin systematic variations (ε_{ji}) of the template shapes (T_{jk}) modify the expected number of events in each bin for the total background ($j = 1$) and signal ($j = 2$) components of the likelihood function. As the main parameter of interest to test at each mass point is more specifically the potential signal σB, a substitution is made to convert from μ using the relation μ_j = $(\sigma\text{B})_j A_j L$, where A_j is the template acceptance (Figure 5.2) and L is the luminosity/normalisation factor. This then finally leads to the expression for the likelihood shown in Equation (9.9).

$$\mathcal{L}(n|\sigma B,\overline{\theta}) = \prod_{k=1}^{N_{bin}} \frac{\mu_k^{n_k} e^{-\mu_k}}{n_k!} \prod_{i=1}^{N_{sys}} G(\theta_i,0,1) \quad , \text{ where } \quad \mu_k = \sum_j (\sigma B)_j A_j L T_{jk}\left(1+\sum_i \theta_i \varepsilon_{jik}\right) \tag{9.9}$$

To account for systematic uncertainties and remove nuisance parameters to reduce the likelihood function to only one parameter of interest (σB), θ_i are treated as Gaussian priors and integrated out through marginalisation using BAT. The resulting marginalised likelihood function is given in Equation (9.10).

$$\mathcal{L}'(n|\sigma B) = \int \mathcal{L}(n|\sigma B, \overline{\theta})d\overline{\theta} \tag{9.10}$$

This is converted into a posterior probability density using Bayes theorem from Equation (9.7), treating P(theory) as a uniform positive prior in σB so that π(σB)=1. The maximum of P(theory|data) i.e. P(σB|n) then corresponds to the most likely signal excess in data, with 95% CL extracted for the upper limit of σB by integrating the posterior probability density as shown in Equation (9.11). The σB limits are converted into mass limits using the theoretical dependence of σB versus resonance mass for each signal model considered.

$$0.95 = \frac{\int_0^{\sigma B_{95}} \mathcal{L}'(\sigma B)\pi(\sigma B)d(\sigma B)}{\int_0^{\infty} \mathcal{L}'(\sigma B)\pi(\sigma B)d(\sigma B)} \tag{9.11}$$

9.2 Signal Discovery Scan

In this section the template method will be used to perform a 2D signal scan, searching for a Z' signal of unknown mass and σB, with the 2.12 fb^{-1} dielectron channel result. The significance of any excess can be interpreted through a *p*-value of the background only hypothesis, which is the probability of observing an excess at least as extreme as the one observed, given that the null hypothesis is true. The commonly accepted *p*-value for evidence of a signal is 1.35×10^{-3} (3σ), with a *p*-value of 2.87×10^{-7} (5σ) required to claim a discovery. The Neyman-Pearson lemma [107] states that when performing a hypothesis test between two point hypotheses H_0 (background only) and H_1 (signal + background), a LLR test is favoured for rejecting a H_0 hypothesis in place of H_1. The likelihood used is similar to that of Equation (9.3), however as the mass and σB of the theoretical Z' is not known a priori, the LLR test for this 2D search is performed simultaneously for the best fit number of signal events ($\text{N}_{Z'}$) and mass ($\text{M}_{Z'}$) to account for the so called "look elsewhere effect"[2]. Systematic uncertainties are also taken into account through nuisance parameters leading to the log likelihood ratio shown in Equation (9.12), where $\hat{N}_{Z'}$ and $\hat{M}_{Z'}$ are the best fit values for the number of Z' events and mass respectively. The nui-

---

[2] The look elsewhere effect describes the increased probability of observing an apparent signal from statistical fluctuations, the more places in parameter space that are tested.

sance parameters $\hat{\theta}$ and $\hat{\hat{\theta}}$ represent the values which maximise $\mathcal{L}$ assuming the H_1 and H_0 hypothesis respectively.

$$Q = -2\ln \frac{\mathcal{L}(n|\hat{N}_{Z'}, \hat{M}_{Z'}, \hat{\theta})}{\mathcal{L}(n|(N_{Z'} = 0), \hat{\hat{\theta}})} \tag{9.12}$$

The likelihood is reduced through marginalisation using BAT so that it only depends on the parameters of interest, $\hat{N}_{Z'}$ and $\hat{M}_{Z'}$. The posterior probability density as a function of $\hat{N}_{Z'}$ (converted to σB) and $\hat{M}_{Z'}$, for the 2.12 fb^{-1} result is presented in Figure 9.1. “Hot” regions in this 2D plane represent values of Z' mass and σB which are favoured for a H_1 like hypothesis, with the colour axis normalised to the observed test statistic (Q_{obs}) of the greatest excess. 1,500 pseudo experiments each containing 100,000 events, were used to simulate the expected LLR distribution assuming the H_0 hypothesis, taking into account all sources of systematic uncertainty. p-values were evaluated by taking the integral of the LLR distribution for values below Q_{obs} as a fraction of the overall distribution so that $p = p(Q \leq Q_{obs}|H_0)$ as in Equation (9.4). The expected LLR distribution and Q_{obs}, for the greatest excess in the 2.12 fb^{-1} dielectron channel search, are presented in Figure 9.2, corresponding to a p-value of 9% at 580 GeV. In terms of statistical significance as a one sided integral of a Gaussian distribution, this represents a 1.34 σ excess.

9.3 Limit Setting

As no significant excess is observed in the dataset of this thesis, lower mass exclusion limits are proceeded to be set at 95% CL, using both the Modified Frequentist, and Bayesian, approaches as described in Section 9.1.

9.3.1 Modified Frequentist Result

The 95% CL exclusion limit from the CL_s interpretation of the 2.12 fb^{-1} dielectron channel search result, is presented in Figures 9.3 and 9.4 for various Z' models and RS G^* k/$\overline{M}_{Pl}$ couplings respectively. A tabulation of the lower mass exclusion limits is provided in Table 9.1.

These lower mass limits are conservative due to the Modified Frequentist approach used. While this interpretation is useful for quantifying an overall excess or deficit in

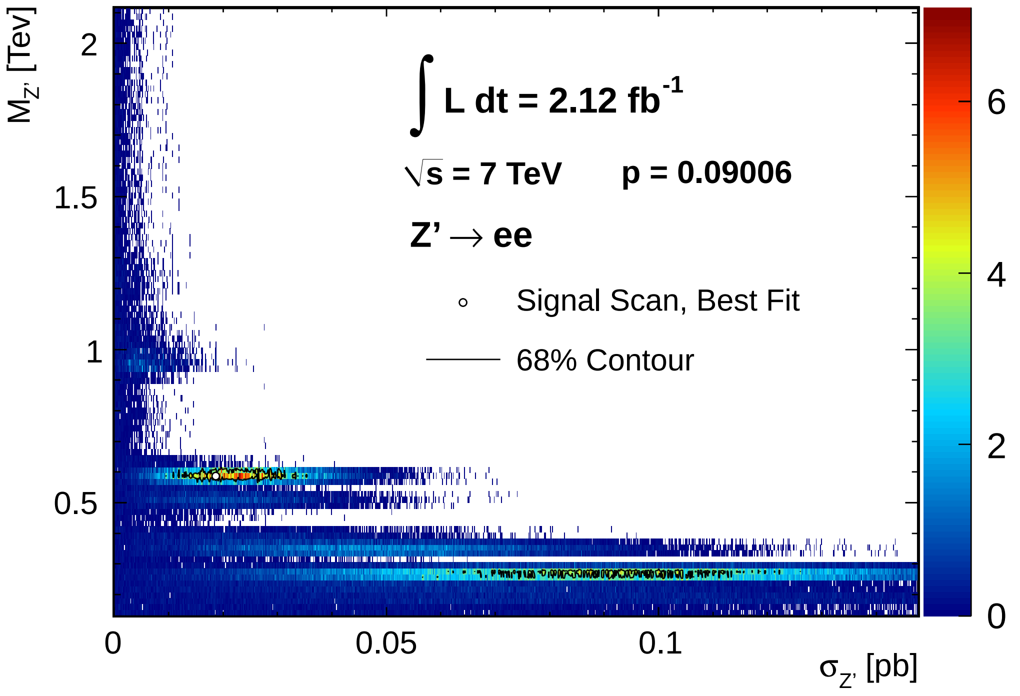

Figure 9.1: 2D signal scan of the 2.12 fb^{-1} dielectron channel result. $\mathcal{L}$ is simultaneously maximised for $\hat{N}_{Z'}$ and $\hat{M}_{Z'}$ against the SM expectation. Hot scale units are normalised to the observed test statistic. The white marker points to the greatest excess observed in this dataset.

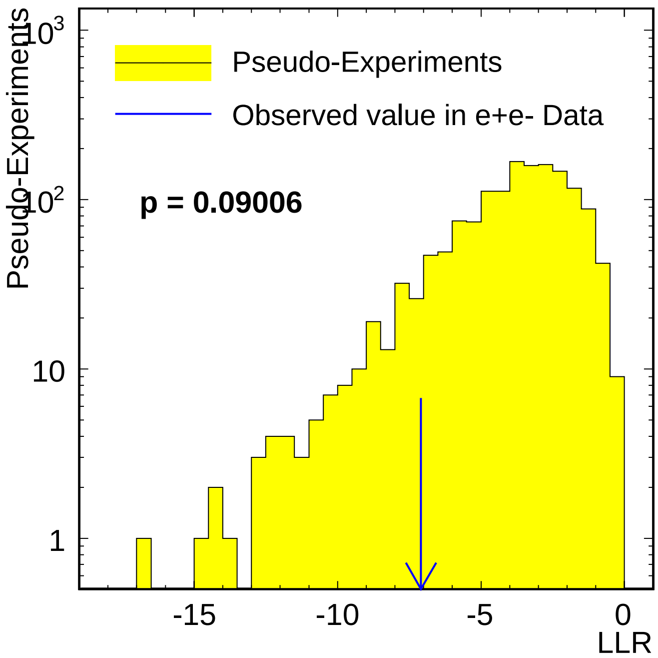

Figure 9.2: LLR distribution for the greatest excess observed in the 2.12 fb^{-1} dielectron channel resonance search. 1,500 pseudo-experiments each with 100,000 events, were run to simulate the SM expectation. The distribution is integrated over values less than the observed test statistic, Q_{obs} (shown by the vertical arrow), to yield a p-value of 9% for the background only hypothesis.

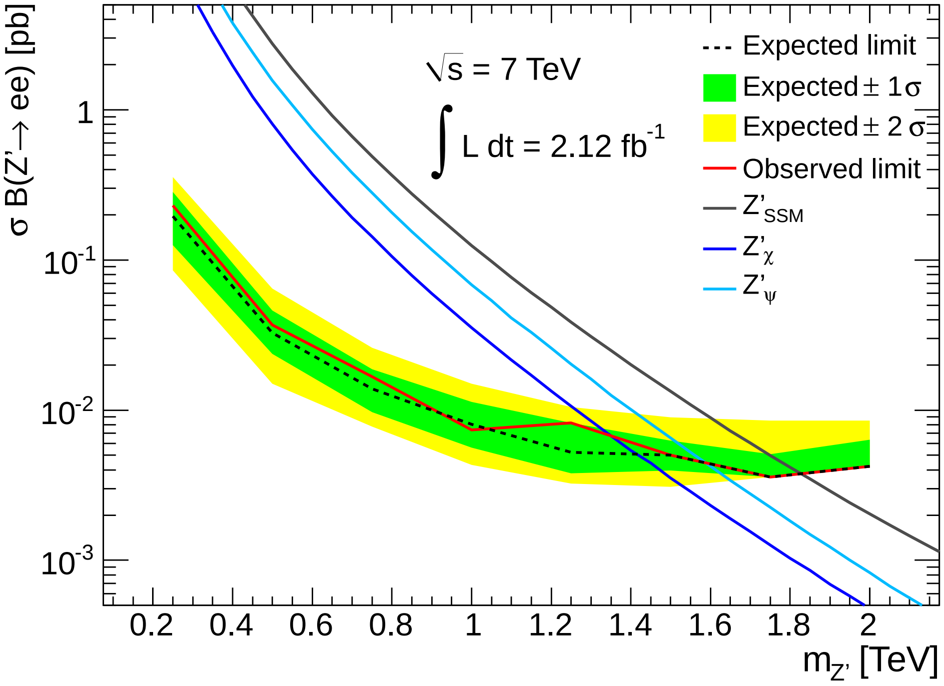

Figure 9.3: Expected and observed 95% CL upper limits on σB(Z'→ee) as a function of Z' mass, using the CL$_s$ method. The Z'_{SSM} theory curve is overlaid, along with a selection of E$_6$ motivated Z' models.

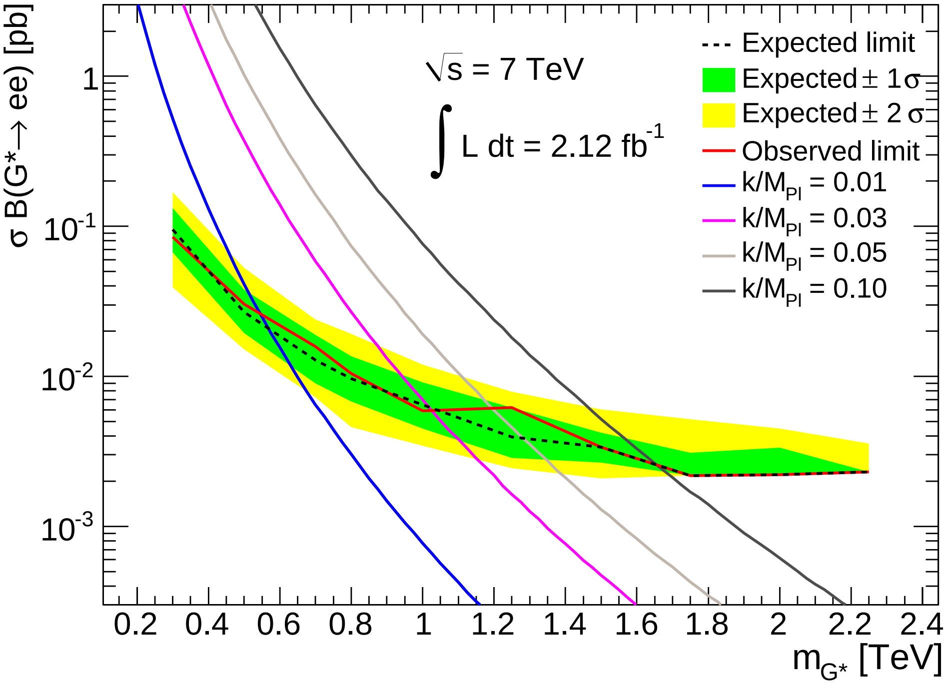

Figure 9.4: Expected and observed 95% CL upper limits on σB(G^*→ee) as a function of G^* mass, using the CL$_s$ method. Theory curves for a RS G^* resonance with various k/$\overline{M}_{Pl}$ coupling values are overlaid.

E_6 Z′ Models	Z'_ψ	Z'_N	Z'_η	Z'_I	Z'_S	Z'_χ	Z'_{SSM}
Expected Mass Limit [TeV]	1.42	1.44	1.46	1.49	1.53	1.58	1.83
Observed Mass Limit [TeV]	1.34	1.38	1.41	1.48	1.53	1.58	1.83

RS Graviton Coupling [$k/\overline{M}_{Pl}$]	0.01	0.03	0.05	0.10
Expected Mass Limit [TeV]	0.56	1.02	1.28	1.65
Observed Mass Limit [TeV]	0.54	1.02	1.19	1.65

Table 9.1: Expected and observed 95% CL lower mass limits for various Z' models and RS G^* $k/\overline{M}_{Pl}$ couplings. Limits were determined from the 2.12 fb^{-1} dielectron channel result of this thesis, using the CL_s method.

data, it neglects the signal resonance shape which adds useful extra kinematic information. Therefore a template method was also used, and incorporated into the Bayesian interpretation of the results in the following section.

9.3.2 Bayesian Result

The results of the Bayesian approach are presented in this section, with 95% CL upper σB exclusion limits set on various Z' models and RS G^* $k/\overline{M}_{Pl}$ couplings in the dielectron channel. The upper σB exclusion limits are presented in Figures 9.5 and 9.6 for the Z' and G^* respectively. The corresponding mass exclusion values (converted using the theoretical dependence of σB on resonance mass) are listed in Table 9.2. No significant excess is observed in data that would correspond to a dielectron resonance signal, however the most significant test mass, identified by the 2D signal scan, is clearly visible at 580 GeV. Note that due to the G^* MC template not being available at the time of writing this thesis, only the available dedicated samples could be used in the limit setting. This leads to larger interpolated regions between points on the G^* limits, and thus explains why the fluctuations seen in the Z' limits are not visible for G^*.

E_6 Z′ Models	Z'_ψ	Z'_N	Z'_η	Z'_I	Z'_S	Z'_χ	Z'_{SSM}
Expected Mass Limit [TeV]	1.53	1.55	1.58	1.60	1.63	1.68	1.88
Observed Mass Limit [TeV]	1.54	1.56	1.58	1.61	1.64	1.68	1.88

RS Graviton Coupling [$k/\overline{M}_{Pl}$]	0.01	0.03	0.05	0.10
Expected Mass Limit [TeV]	0.73	1.13	1.35	1.66
Observed Mass Limit [TeV]	0.78	1.08	1.31	1.66

Table 9.2: Expected and observed 95% CL lower mass limits for various Z' models and RS G^* $k/\overline{M}_{Pl}$ couplings. Limits were determined from the 2.12 fb^{-1} dielectron channel result of this thesis, using BAT.

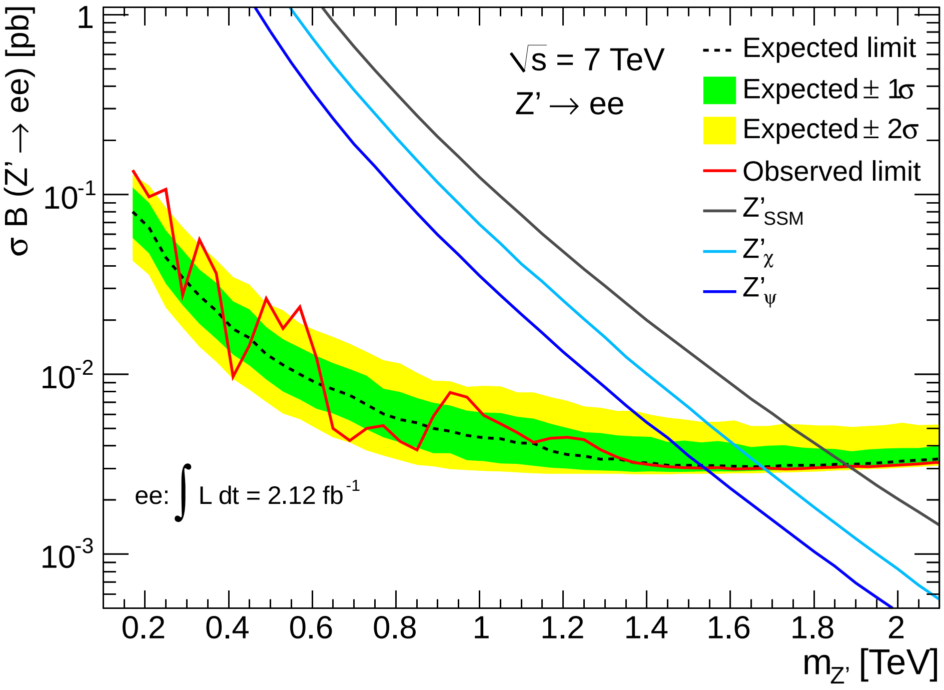

Figure 9.5: Expected and observed 95% CL upper limits on σB(Z′→ee) as a function of Z' mass, using BAT. The Z'_{SSM} theory curve is overlaid, along with a selection of E_6 motivated Z' models.

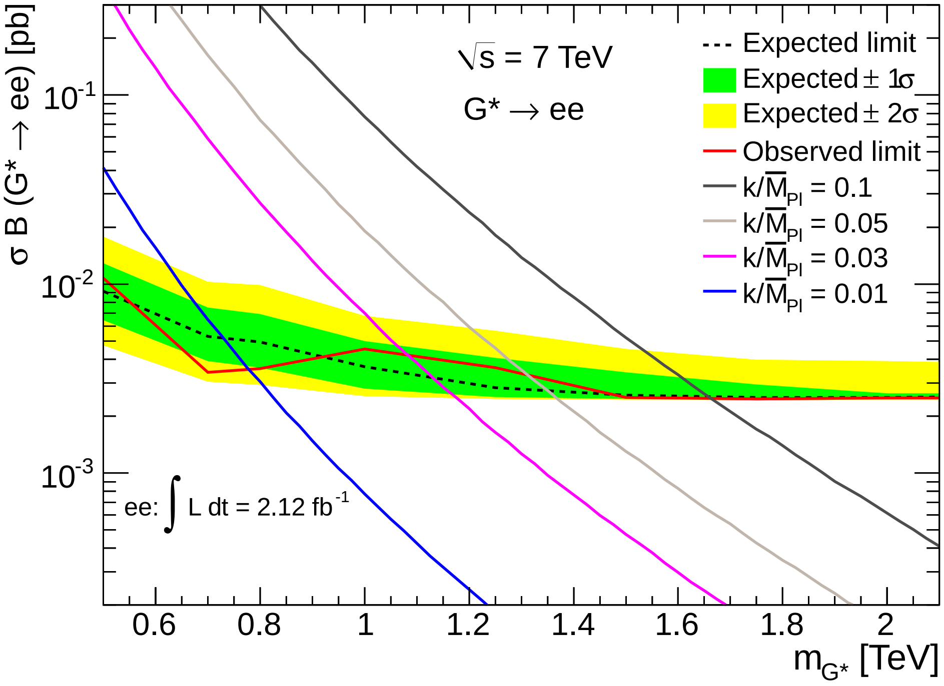

Figure 9.6: Expected and observed 95% CL upper limits on σB(G^*→ee) as a function of G^* mass, using BAT. Theory curves for a RS G^* resonance with various k/$\overline{M}_{Pl}$ coupling values are overlaid.

Combined Channel Result

To set the strongest exclusion limits possible, for models considered in this thesis given the dataset available, individual search channel results are combined using BAT. This is achieved by modifying Equation (9.9) to account for multiple search channels, taking the product for each channel across all bins in the distribution (see Equation (9.13)). For the Z' search, the 2.12 fb^{-1} dielectron channel result from this thesis is combined with the latest 1.21 fb^{-1} dimuon channel result [3]. For the RS G^* search, the dielectron channel result from this thesis is combined with both the latest dimuon channel result [3], and the latest 2.12 fb^{-1} diphoton channel result [4].

$$\mathcal{L}(n|\sigma B, \bar{\theta}) = \prod_{l=1}^{N_{channel}} \prod_{k=1}^{N_{bin}} \frac{\mu_{lk}^{n_{lk}} e^{-\mu_{lk}}}{n_{lk!}} \prod_{i=1}^{N_{sys}} G(\theta_i, 0, 1) \tag{9.13}$$

The systematic uncertainties for each channel are taken into account for both signal and background, combining those that are correlated where possible to reduce the number of degrees of freedom that have to be analysed in the marginalisation. For the Z' search, the normalisation, PDF/α_s, and QCD/Weak K-factor, uncertainties were correlated between the dielectron and dimuon channel. For the RS G^* search, the normalisation, and PDF/α_s, uncertainties were correlated across all three channels, with the QCD background systematic correlated between the dielectron and diphoton channel additionally.

Equation (9.13) is used to obtain the marginalised likelihood, and Bayes theorem applied. Solving for $(\sigma B)_{95}$, the 95% CL upper σB exclusion limits are extracted for $Z' \rightarrow ee+\mu\mu$ and $G^* \rightarrow ee+\mu\mu+\gamma\gamma$ as displayed in Figures 9.7 and 9.8 respectively. Table 9.3 lists the numerical values of the corresponding lower mass limits.

E_6 Z' Models	Z'_ψ	Z'_N	Z'_η	Z'_I	Z'_S	Z'_χ	Z'_{SSM}
Expected Mass Limit [TeV]	1.60	1.61	1.64	1.66	1.70	1.74	1.95
Observed Mass Limit [TeV]	1.61	1.63	1.66	1.67	1.71	1.75	1.96

RS Graviton Coupling [k/$\overline{M}_{Pl}$]	0.01	0.03	0.05	0.10
Expected Mass Limit [TeV]	0.87	1.35	1.60	1.95
Observed Mass Limit [TeV]	0.80	1.32	1.50	1.95

Table 9.3: Expected and observed 95% CL lower mass limits for various Z' models and RS G^* k/$\overline{M}_{Pl}$ couplings. Limits were determined from combined dielectron, dimuon (and diphoton for G^*) channel search results, using BAT.

These results represent the world's current highest observed mass exclusion limits for

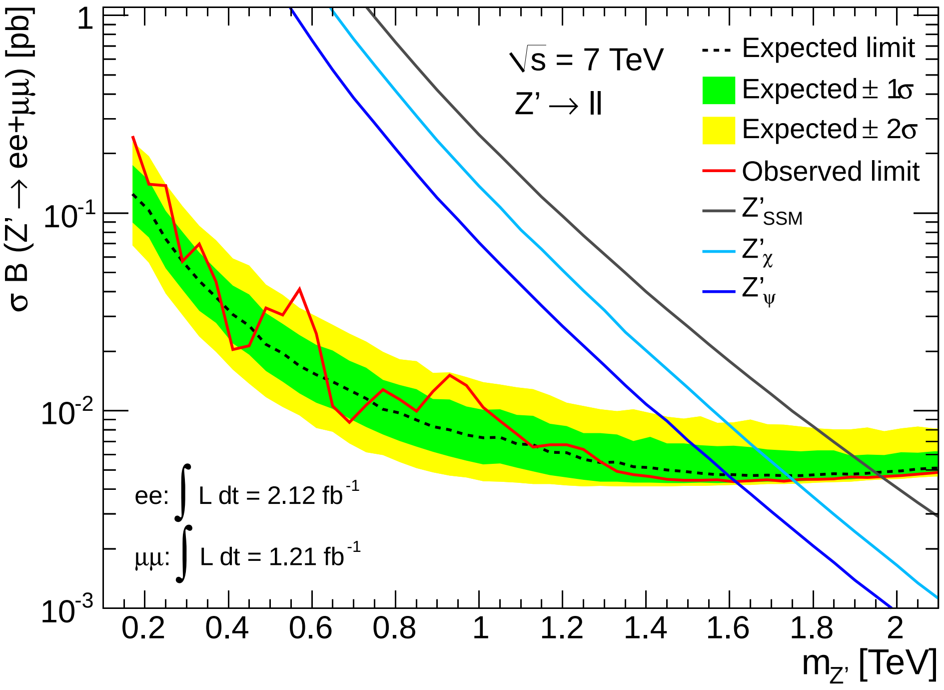

Figure 9.7: Expected and observed 95% CL upper limits on σB($Z' \to ee+\mu\mu$) as a function of Z' mass. The Z'_{SSM} theory curve is overlaid along with a selection of E_6 motivated Z' models.

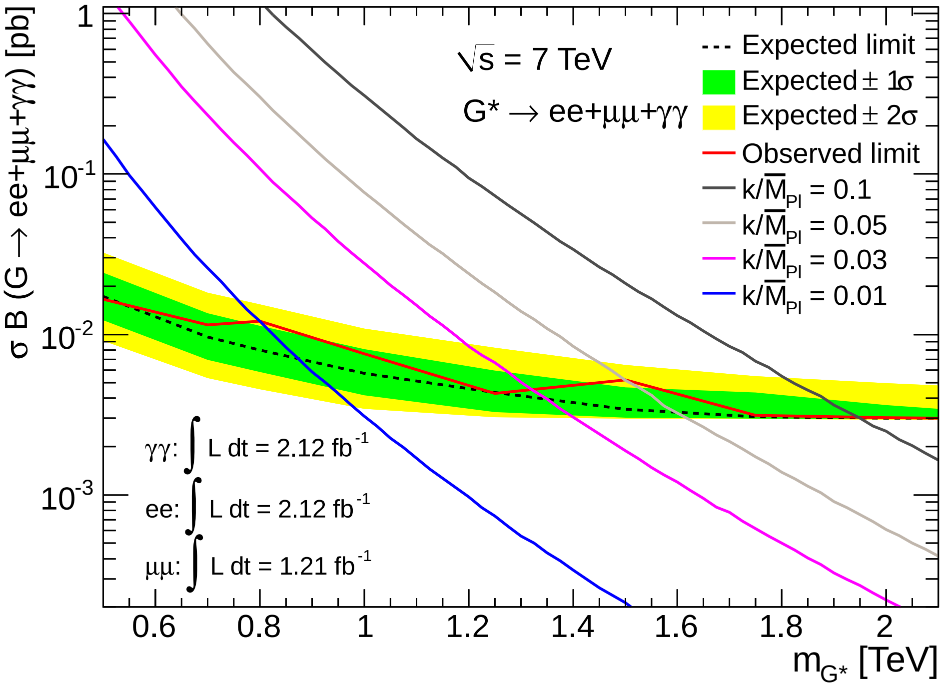

Figure 9.8: Expected and observed 95% CL upper limits on σB($G^* \to ee+\mu\mu+\gamma\gamma$) as a function of G^* mass. Theory curves for G^* resonances with various $k/\overline{M}_{Pl}$ coupling values are overlaid.

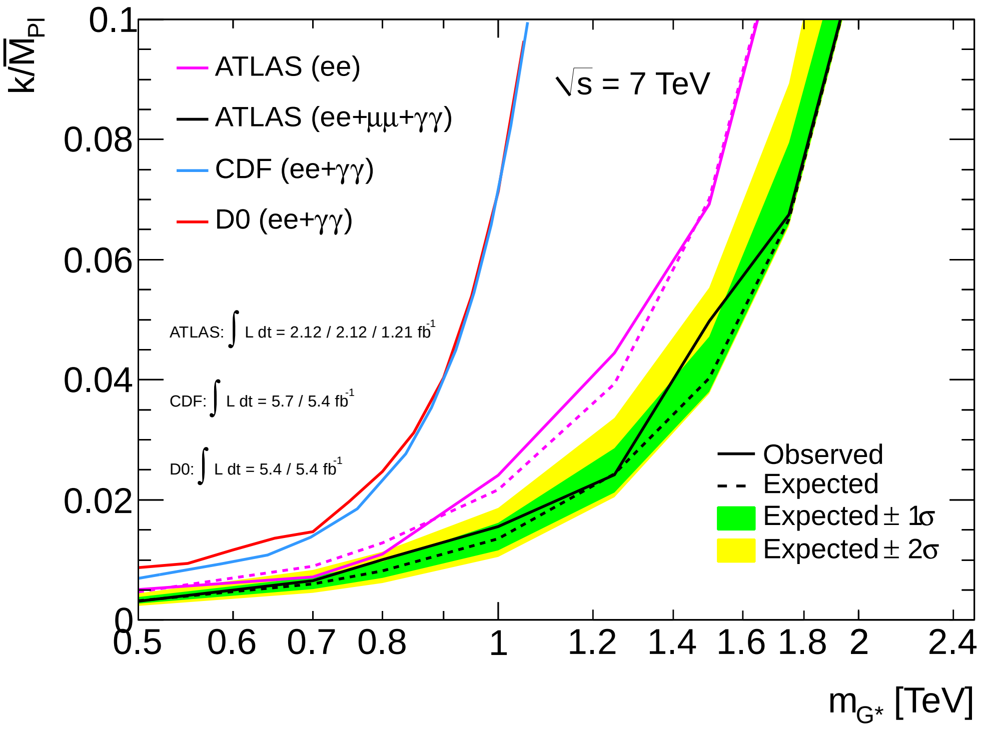

Figure 9.9: 95% CL G^* exclusion limits in the $k/\overline{M}_{Pl}$ versus resonance mass plane. The dielectron and combined results are displayed, as well as latest results available from other experiments [44, 43].

the Z'_{SSM}, E_6 motivated Z' models, and RS model G^*, at the time of writing this thesis. It is interesting to display the RS G^* combined results as exclusion limits in the $k/\overline{M}_{Pl}$ coupling versus resonance mass plane (Figure 9.9). This plot is overlaid with exclusion regions from precision electroweak measurements and theoretical restrictions on the new physics energy scale Λ_π (Figure 9.10). This yields the most complete current picture available for the RS G^*.

9.4 Near Future Discovery Potential

At the end of pp collisions in 2011, an integrated luminosity of more than 5 fb^{-1} had been recorded by the ATLAS detector at $\sqrt{s}$ = 7 TeV. This dataset combined across various search channels, in a similar manner to the methods shown in this thesis, would considerably improve the lower mass exclusion limits presented, should a significant resonant excess not be present. Furthermore, as of March 2012 with the planned restart of the LHC and its experiments, an average of 500 pb^{-1} a week is expected at $\sqrt{s}$ = 8 TeV. If data taking proceeds at this rate, within one year it should be possible to either discover,

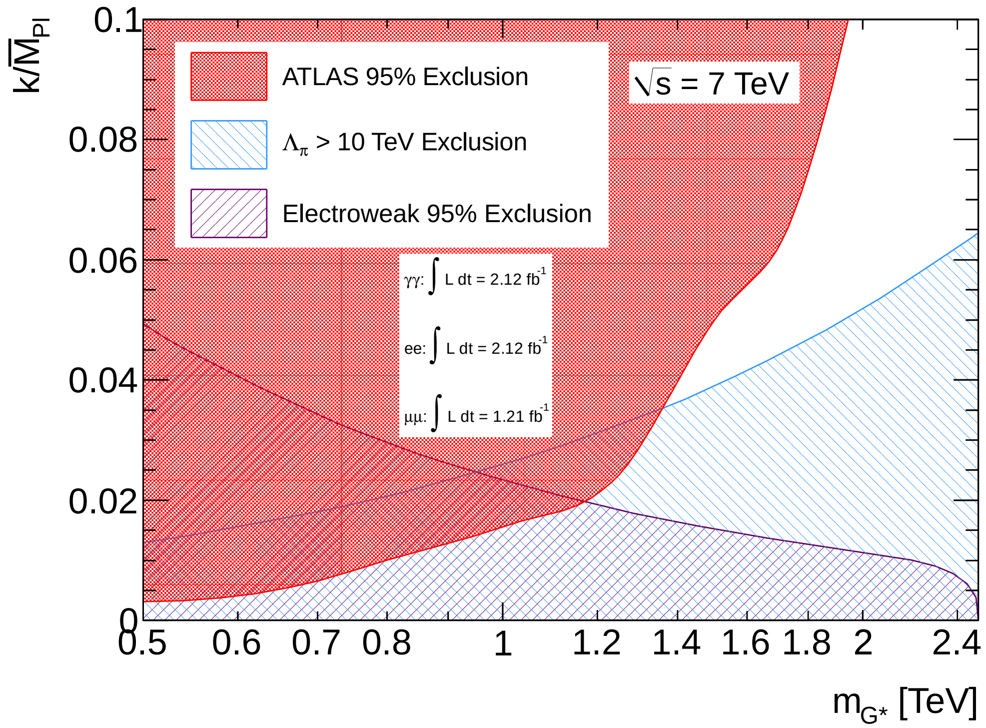

Figure 9.10: Exclusion region for the RS model G^* in the $k/\overline{M}_{Pl}$ versus resonance mass plane. The combined observed limit of this thesis is displayed, as well as excluded regions from electroweak precision measurements and theoretical restrictions on the new physics scale Λ_π.

or completely rule out, the RS model G^* (see Figure 1.11 in Chapter 1). The Z' models discussed will also come into contention if exclusion limits reach above 3 TeV [20].

With a dataset as large as the one predicted by the end of 2012, it should then be possible to also conduct meaningful searches for new physics such as the Z' and G^* using angular distribution methods such as $\cos\theta^*$ and A_{FB}.

Using feedback from the physics community in 2010/11, especially what theorists would like to see from new physics searches, results will also start to be displayed in more model independent ways. One such method for the Z' would be to display results in the so called $C_u - C_d$ plane, where the coupling of the new resonance to the u and d quark respectively, contains the information for the dependence of the Z' coupling to all quarks and leptons. A contour exclusion plot in this plane could then be populated with the Z'_{SSM} and E_6 models for example, also allowing for varying parameters within these models (which affect the couplings) to be displayed, while keeping them distinct from other models.

Chapter 10

Conclusions

The Standard Model of particle physics has proved to be an excellent theory for describing three of the four known forces of nature, standing the test of time for more than 35 years. But ultimately there must be more, even if the Higgs boson is found within the next year around 126 GeV by the LHC, a GUT scale theory, and a theory that incorporates gravity into our understanding of the Universe, must exist.

This thesis has presented a search for new heavy particles, beyond the Standard Model of particle physics, which may indicate the presence of a GUT scale theory through observation of a Z' gauge boson, and/or a paradigm shift in our understanding of gravity and the hierarchy problem, via extra spatial dimensions and the observation of an RS model G^*.

Both of these particles would appear as resonances in the invariant mass spectrum as measured by the ATLAS detector, and would be clearly visible above SM background processes. An overview of the ATLAS detector, and subsystems important for a neutral heavy resonance search in the dielectron channel, were discussed in Chapter 2. In Chapter 3, the MC simulation used to estimate relevant SM background contributions to this search were presented, as well as a study of the MC signal samples with an emphasis on electron reconstruction, identification, and resolution, using the ATLAS detector. Investigating electrons from data, and in the same kinematic regime as those important to the search analysis, Chapter 4 considered high E_T electron outliers, providing feedback to reduce the number of misidentified electron energies in the 2.12 fb^{-1} dataset used in this thesis. Chapter 5 motivated and presented the event selection applied to data in search of a Z'/G^* resonance, including how this translated to cuts made on MC simulation. Given these selection criteria, Chapter 6 then laid out the procedure by which an accurate SM background estimation was obtained, dealing with both the MC simulation, and data-driven QCD dijet background components to form an overall SM background template. Applying the event selection criteria to data, and constructing the SM background estimate, Chapter 7 proceeded to present the 2.12 fb^{-1} dielectron channel search results, comparing data and MC for a number of kinematic distributions that would indicate if new physics was present. Chapter 9 then used both Frequentist and Bayesian techniques to interpret the 2.12 fb^{-1} dielectron channel result, using the invariant mass spectrum as the kinematic variable of interest. A 2D signal scan was performed to find the most significant excess in data, maximising both the number of Z' events, and the most likely Z' mass to control the look elsewhere effect. The greatest excess in this dataset is located at 580 GeV, with a p-value of 9%, which corresponds to a significance of 1.34 σ. As no significant excess was observed, upper limits were set on the cross section of the signal processes, times branching ratio into two electrons, at 95% CL. These limits were then converted into lower mass limits on various Z' models and RS G^* $\text{k}/\overline{M}_{Pl}$ couplings. Finally the results of the 2.12 fb^{-1} dielectron channel search were combined with the 1.21 fb^{-1} dimuon channel, and 2.12 fb^{-1} diphoton channel, search results. This enabled lower mass limits to be set on the Z'_{SSM}, E_6 motivated Z' models, and RS model G^*, that are at the time of writing this thesis, currently the most stringent from any particle physics experiment in the world.

Despite the fact that no evidence for new physics was observed in the dataset presented in this thesis, by the end of pp collisions in 2011, 5 fb^{-1} of data had been collected by the ATLAS detector, more than doubling the data in each channel considered here. Add to that the realisation that CMS also collected a similar amount of data, and it soon becomes apparent that with the overall 2011 dataset, new physics could very quickly become apparent should it be hiding just beyond the reach of the search presented here. Equally, if no new physics exists at the TeV scale, then with the 2011 dataset, and furthermore the coming 2012 dataset which is expected to achieve more than 15 fb^{-1} at $\sqrt{s} = 8$ TeV (possibly up to 9 TeV) if predictions are to be believed (and 2011 far exceeded the initial estimate of 1-2 fb^{-1}), then searches such as this will start to exclude models like the E_6 motivated Z', and RS model G^*, pointing theorists in new directions to try and understand the Universe in which we live.

Appendix A

Dataset 2011

Table A.1: Data runs comprising the dataset used for this thesis. Runs listed here amount to an integrated luminosity of 2.12 fb^{-1} taken between the 23rd of March and 22nd of August 2011. The columns from left to right list the run number, data period, physics stream, and 3 data formats used for the analysis.

Run	#	Stream	AOD	D3PD	Skim	Run	#	Stream	AOD	D3PD	Skim
177986	B	E/γ	✓	✓	✓	179940	D	E/γ	✓	✓	✓
178020	B	E/γ	✓	✓	✓	180122	D	E/γ	✓	✓	✓
178021	B	E/γ	✓	✓	✓	180124	D	E/γ	✓	✓	✓
178026	B	E/γ	✓	✓	✓	180139	D	E/γ	✓	✓	✓
178044	B	E/γ	✓	✓	✓	180144	D	E/γ	✓	✓	✓
178047	B	E/γ	✓	✓	✓	180149	D	E/γ	✓	✓	✓
178109	B	E/γ	✓	✓	✓	180153	D	E/γ	✓	✓	✓
179710	D	E/γ	✓	✓	✓	180164	D	E/γ	✓	✓	✓
179725	D	E/γ	✓	✓	✓	180212	D	E/γ	✓	✓	✓
179739	D	E/γ	✓	✓	✓	180224	D	E/γ	✓	✓	✓
179771	D	E/γ	✓	✓	✓	180225	D	E/γ	✓	✓	✓
179804	D	E/γ	✓	✓	✓	180241	D	E/γ	✓	✓	✓
179938	D	E/γ	✓	✓	✓	180242	D	E/γ	✓	✓	✓
179939	D	E/γ	✓	✓	✓	180309	D	E/γ	✓	✓	✓
180400	D	E/γ	✓	✓	✓	182879	G	E/γ	✓	✓	✓
180448	D	E/γ	✓	✓	✓	182886	G	E/γ	✓	✓	✓
180481	D	E/γ	✓	✓	✓	182997	G	E/γ	✓	✓	✓

Continued on next page

Run	#	Stream	AOD	D3PD	Skim
180614	E	E/γ	✓	✓	✓
180636	E	E/γ	✓	✓	✓
180664	E	E/γ	✓	✓	✓
180710	E	E/γ	✓	✓	✓
180776	E	E/γ	✓	✓	✓
182013	F	E/γ	✓	✓	✓
182161	F	E/γ	✓	✓	✓
182284	F	E/γ	✓	✓	✓
182346	F	E/γ	✓	✓	✓
182372	F	E/γ	✓	✓	✓
182424	F	E/γ	✓	✓	✓
182449	F	E/γ	✓	✓	✓
182450	F	E/γ	✓	✓	✓
182454	F	E/γ	✓	✓	✓
182455	F	E/γ	✓	✓	✓
182456	F	E/γ	✓	✓	✓
182486	F	E/γ	✓	✓	✓
182516	F	E/γ	✓	✓	✓
182518	F	E/γ	✓	✓	✓
182519	F	E/γ	✓	✓	✓
182726	G	E/γ	✓	✓	✓
182747	G	E/γ	✓	✓	✓
182766	G	E/γ	✓	✓	✓
182787	G	E/γ	✓	✓	✓
182796	G	E/γ	✓	✓	✓
183078	G	E/γ	✓	✓	✓
184066	H	E/γ	✓	✓	✓
184072	H	E/γ	✓	✓	✓
184074	H	E/γ	✓	✓	✓
184088	H	E/γ	✓	✓	✓
184130	H	E/γ	✓	✓	✓
184169	H	E/γ	✓	✓	✓
183003	G	E/γ	✓	✓	✓
183021	G	E/γ	✓	✓	✓
183038	G	E/γ	✓	✓	✓
183045	G	E/γ	✓	✓	✓
183054	G	E/γ	✓	✓	✓
183079	G	E/γ	✓	✓	✓
183081	G	E/γ	✓	✓	✓
183127	G	E/γ	✓	✓	✓
183129	G	E/γ	✓	✓	✓
183130	G	E/γ	✓	✓	✓
183216	G	E/γ	✓	✓	✓
183272	G	E/γ	✓	✓	✓
183286	G	E/γ	✓	✓	✓
183347	G	E/γ	✓	✓	✓
183391	G	E/γ	✓	✓	✓
183407	G	E/γ	✓	✓	✓
183412	G	E/γ	✓	✓	✓
183426	G	E/γ	✓	✓	✓
183462	G	E/γ	✓	✓	✓
183544	H	E/γ	✓	✓	✓
183580	H	E/γ	✓	✓	✓
183581	H	E/γ	✓	✓	✓
183602	H	E/γ	✓	✓	✓
183780	H	E/γ	✓	✓	✓
183963	H	E/γ	✓	✓	✓
184022	H	E/γ	✓	✓	✓
186361	I	E/γ	✓	✓	✓
186399	I	E/γ	✓	✓	✓
186456	I	E/γ	✓	✓	✓
186493	I	E/γ	✓	✓	✓
186516	J	E/γ	✓	✓	✓
186532	J	E/γ	✓	✓	✓

Continued on next page

Run	#	Stream	AOD	D3PD	Skim	Run	#	Stream	AOD	D3PD	Skim
185353	I	E/γ	✓	✓	✓	186533	J	E/γ	✓	✓	✓
185518	I	E/γ	✓	✓	✓	186669	J	E/γ	✓	✓	✓
185536	I	E/γ	✓	✓	✓	186673	J	E/γ	✓	✓	✓
185644	I	E/γ	✓	✓	✓	186721	J	E/γ	✓	✓	✓
185649	I	E/γ	✓	✓	✓	186729	J	E/γ	✓	✓	✓
185731	I	E/γ	✓	✓	✓	186753	J	E/γ	✓	✓	✓
185747	I	E/γ	✓	✓	✓	186755	J	E/γ	✓	✓	✓
185761	I	E/γ	✓	✓	✓	186873	K	E/γ	✓	✓	✓
185823	I	E/γ	✓	✓	✓	186877	K	E/γ	✓	✓	✓
185856	I	E/γ	✓	✓	✓	186878	K	E/γ	✓	✓	✓
185976	I	E/γ	✓	✓	✓	186923	K	E/γ	✓	✓	✓
185998	I	E/γ	✓	✓	✓	186933	K	E/γ	✓	✓	✓
186049	I	E/γ	✓	✓	✓	186934	K	E/γ	✓	✓	✓
186156	I	E/γ	✓	✓	✓	186965	K	E/γ	✓	✓	✓
186169	I	E/γ	✓	✓	✓	187014	K	E/γ	✓	✓	✓
186178	I	E/γ	✓	✓	✓	187196	K	E/γ	✓	✓	✓
186179	I	E/γ	✓	✓	✓	187219	K	E/γ	✓	✓	✓
186180	I	E/γ	✓	✓	✓	187552	K	E/γ	✓	✓	✓
186182	I	E/γ	✓	✓	✓	187763	K	E/γ	✓	✓	✓
186216	I	E/γ	✓	✓	✓	187811	K	E/γ	✓	✓	✓
186217	I	E/γ	✓	✓	✓	187812	K	E/γ	✓	✓	✓
186275	I	E/γ	✓	✓	✓	187815	K	E/γ	✓	✓	✓

Appendix B

Monte Carlo: Samples, Cross Sections, and Corrections

B.1 Signal samples

Relevant properties of the MC signal samples used for this thesis can be found in this section. Table B.1 lists the Z'_{SSM} MC properties which are all generated with PYTHIA using MRST2007LO*. The individual mass point Z' samples include Drell-Yan interference above a mass threshold of 0.5 times the pole mass. For the limit setting, a flat template covering 130-3000 GeV was created from the 1 TeV Z'_{SSM} sample, without Drell-Yan interference.

Table B.2 lists the properties of the G^* MC samples used in this thesis for a range of masses and couplings k/M_{pl}.

Table B.3 displays the leading order Z' cross sections used in the limit calculation as theory curves, for various masses. These samples like the template sample, were generated without the Drell-Yan production interference, meaning the cross sections shown are for Z' production only. The actual mass spacing used in the limit calculation is 40 GeV.

B.2 Background samples

Tables B.4 to B.6 list the background samples used in this thesis.

Mass [GeV]	Threshold [GeV]	Γ [GeV]	$B(Z' \to e^+e^-)$ [%]	Run Number	σB [fb]		N_{evt} [k]	L_{int} [fb^{-1}]
					Generated	Calculated		
130-3000	-	-	-	115494	-	-	400	-
250	125	6.87	3.36	115272	36447.8	41878.5	20	0.478
500	250	14.56	3.20	115273	2625.3	2969.2	20	6.736
750	375	22.64	3.10	115274	481.026	533.5	20	37.49
1000	500	30.64	3.06	105603	129.074	139.4	20	143.5
1250	625	38.60	3.05	105549	40.9309	42.6	20	469.5
1500	750	46.55	3.04	105624	15.3947	15.24	20	1312
1750	875	54.49	3.03	105554	5.9892	5.56	20	3597
2000	1000	62.43	3.03	105409	2.5528	2.20	20	9091

Table B.1: MC Z'_{SSM} samples. The columns from left to right give the: mass, mass threshold, width, electron branching fraction, and MC run number. This is followed by the cross section times branching fraction calculated by the generator, and then after applying a QCD NNLO correction factor. The last two columns give the number of generated events and corresponding integrated luminosity using the modified cross section. The integrated luminosity of these MC samples provide a good statistical sample for use with the 2.12 fb^{-1} ATLAS dataset.

Mass [GeV]	k/M$_{pl}$	Γ [GeV]	$B(G^* \to e^+e^-)$ [%]	Run Number	σB [fb] Generated	N_{evt} [k]	L_{int} [fb^{-1}]
300	0.01	0.041	2.1	105298	521.6	10	19.17
500	0.01	0.069	2.1	105586	40.46	10	247.2
800	0.01	0.113	2.1	105299	2.996	10	3337
1000	0.01	0.142	2.0	105587	0.7839	10	12756
500	0.03	0.625	2.1	105562	369.5	10	27.06
800	0.03	1.016	2.0	105563	26.98	10	370.6
1000	0.03	1.274	2.0	105564	6.925	10	1444
700	0.05	2.482	2.1	105898	163.7	10	61.09
1000	0.05	3.565	2.0	105982	19.42	10	514.9
1250	0.05	4.463	2.0	105983	4.567	10	2190
1500	0.05	5.360	2.0	105984	1.324	10	7553
800	0.1	11.377	2.1	105937	298.2	10	33.53
1000	0.1	14.261	2.0	105588	77.34	10	129.3
1250	0.1	17.854	2.0	105938	18.38	10	544.1
1500	0.1	21.440	2.0	105939	5.288	10	1891

Table B.2: MC G^* samples. The columns from left to right show: mass, k/M$_{pl}$, width, electron branching fraction, and MC run number. This is followed by the cross section times branching fraction from the generator. The last two columns give the number of generated events, and corresponding integrated luminosity. Again it can be seen, that these MC samples comprise a statistical dataset that is appropriate for use with the 2.12 fb^{-1} ATLAS dataset taken during 2011.

B.3 QCD Corrections

The work presented in this section was undertaken by the ATLAS Exotics working group for the 2011 dilepton analysis [83]. The Drell-Yan process in MC10b is simulated using

Mass [GeV]	$\sigma B(Z'_{\mathrm{SSM}})$ [fb]	$\sigma B(Z'_{\mathrm{S}})$ [fb]	$\sigma B(Z'_{\mathrm{N}})$ [fb]	$\sigma B(Z'_{\psi})$ [fb]	$\sigma B(Z'_{\chi})$ [fb]	$\sigma B(Z'_{\eta})$ [fb]	$\sigma B(Z'_{I})$ [fb]
250	2.735e+04	1.471e+04	9.223e+03	8.132e+03	1.589e+04	9.566e+03	1.330e+04
500	2.038e+03	1.080e+03	683.0	596.8	1.163e+03	694.6	951.8
750	366.8	188.5	119.7	106.9	210.1	123.2	170.0
1000	94.77	46.90	30.32	26.90	51.83	31.40	41.51
1250	29.60	13.63	9.069	8.171	15.56	9.704	11.87
1500	10.33	4.310	3.003	2.732	5.064	3.229	3.741
1750	3.876	1.440	1.037	9.833e-01	1.747	1.195	1.219
2000	1.579	5.090e-01	3.793e-01	3.706e-01	6.410e-01	4.550e-01	4.221e-01
2250	6.935e-01	1.911e-01	1.440e-01	1.422e-01	2.493e-01	1.775e-01	1.571e-01
2500	3.296e-01	8.032e-02	5.754e-02	5.668e-02	1.044e-01	7.255e-02	6.530e-02

Table B.3: Leading order cross sections used in the limit calculation for all Z' models

Process	Mass [GeV]	Run Number	σB [pb] Generated	Calculated	N_{evt} [k]	L_{int} [fb^{-1}]
$Z^0/\gamma^* \to ee$	91.2	106046	856	989	5000	5.056
$Z^0/\gamma^* \to ee$	70-120	105466	819.921	948	20	0.021
$Z^0/\gamma^* \to ee$	120-250	105467	8.711	9.99	20	2.002
$Z^0/\gamma^* \to ee$	250-400	105468	0.416	0.461	20	43.38
$Z^0/\gamma^* \to ee$	400-600	105469	0.0671	0.0729	20	274.3
$Z^0/\gamma^* \to ee$	600-800	105470	0.0111	0.0118	20	1695
$Z^0/\gamma^* \to ee$	800-1000	105471	0.00275	0.0028	20	7143
$Z^0/\gamma^* \to ee$	1000-1250	105472	0.000919	0.000912	20	21930
$Z^0/\gamma^* \to ee$	1250-1500	105473	0.000249	0.000235	20	85106
$Z^0/\gamma^* \to ee$	1500-1750	105474	0.000077	0.0000687	20	291121
$Z^0/\gamma^* \to ee$	1750-2000	105475	0.000026	0.0000217	20	921659
$Z^0/\gamma^* \to ee$	2000+	105476	0.000015	0.0000173	20	1156069

Table B.4: MC Drell-Yan samples used in this thesis. The columns from left to read give the: physical process, mass, MC run number, cross section times branching ratio given by the generator, followed by the calculated value after applying a QCD NNLO correction factor. The last two columns list the number of generated events and the corresponding integrated luminosity of the sample.

the PYTHIA LO generator and MRST2007LO* PDFs. The Drell-Yan cross section has been calculated at NNLO using the PHOZPR [81] program with various PDF sets. These results can be used to correct the PYTHIA data sets to NNLO precision by applying a K-factor to the PYTHIA cross section. The ATLAS Standard Model group has performed extensive studies of the Drell-Yan cross section and associated uncertainties. The results of their study [108] for the differential production cross section $M^2_{\ell\ell}\mathrm{d}\sigma_{\mathrm{NNLO}}/\mathrm{d}M^2_{\ell\ell}$ calculated at NNLO using the MSTW2008NNLO PDF for dilepton masses 10 GeV $< M_{\ell\ell} <$

Process	Run Number	σB [pb]		N_{evt}	L_{int}
		Generated	Calculated	[k]	[pb^{-1}]
$W \rightarrow e\nu$ + 0 parton	107680	6913.3	8296	3456.5	416.6
$W \rightarrow e\nu$ + 1 parton	107681	1293.0	1551.6	632.5	407.6
$W \rightarrow e\nu$ + 2 partons	107682	377.1	452.5	756	1671
$W \rightarrow e\nu$ + 3 partons	107683	100.9	121.1	202	1668
$W \rightarrow e\nu$ + 4 partons	107684	25.3	30.4	52	1711
$W \rightarrow e\nu$ + 5 partons	107685	6.9	8.3	14	1687
WW	105985	11.49	17.46	250	14318
WZ	105987	3.481	5.543	250	45102
ZZ	105986	0.976	1.261	250	198255

Table B.5: MC W/Z background samples used in this thesis. The columns from left to right give the: physical process, MC run number, and cross section times branching ratio given by the generator, followed by the calculated value after NNLO correction factors have been applied. The last two columns list the number of generated events and the corresponding integrated luminosity of the sample.

Process	M_{ee}	Run	σB [pb]		N_{evt}	L_{int}
	[GeV]	Number	Generated	Calculated	[k]	[pb^{-1}]
$t\bar{t} \rightarrow eeX$		105200	80.2	89.4	1000	11200
$t\bar{t} \rightarrow eeX$	30-150	115400	2.7104	3.0240	20	6490
$t\bar{t} \rightarrow eeX$	150-300	115401	0.31148	0.34669	20	57300
$t\bar{t} \rightarrow eeX$	300-450	115402	0.025219	0.028065	20	713000
$t\bar{t} \rightarrow eeX$	450+	115403	0.004321	0.00481	20	4160000

Table B.6: MC $t\bar{t}$ background samples used in this thesis. The columns from left to right give the: physical process, mass, MC run number, and cross section times branching fraction given by the generator, followed by the calculated value after NNLO correction factors have been applied. The last two columns list the number of generated events and the corresponding integrated luminosity.

3000 GeV are provided in Table B.7. The mass dependent cross section ratios K$_{NLO}(M_{\ell\ell})$, K$_{NNLO}(M_{\ell\ell})$, and K$^{*}{}_{NNLO}(M_{\ell\ell})$ are also provided. The equivalent K$^{*}{}_{NNLO,Z'}(M_{\ell\ell})$ is shown in Table B.8. As the MRST2007LO* PDF is used in ATLAS MC10b production, K$^{*}{}_{NNLO}(M_{\ell\ell})$ defines an event specific weight for Drell-Yan events generated with a LO event generator (i.e. PYTHIA and HERWIG) to obtain a normalisation and a dilepton invariant mass shape which is accurate to NNLO (Figure B.1). The following uncertainties on the NNLO cross section for the production of Z^0/γ^* (Table B.7) or Z' (Table B.8) can be interpreted as uncertainties on the QCD K-factor. The α_s and PDF uncertainties are evaluated using the MSTWNNLO2008 eigenvector PDF sets and the PDF sets corresponding to variations of α_s, both at the 68% and 90% CL. The α_s uncertainties at

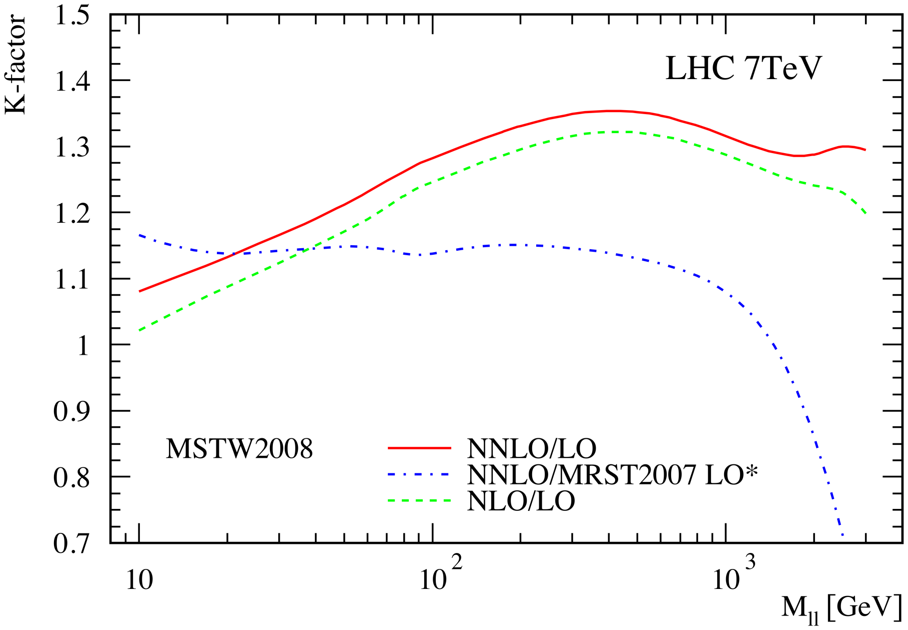

Figure B.1: Cross section ratios (QCD K-factors) for Drell-Yan lepton-pair production as a function of dilepton invariant mass M_{ll} [83], calculated with PHOZPR.

68%/90% CL are within 1.5% (4%) up to 1.75 TeV, and are considerably smaller than the PDF uncertainties. Therefore the combined α_s and PDF uncertainties which are obtained by adding the contributions in quadrature, are only slightly larger than the PDF uncertainties.

B.4 Electroweak Corrections

The work presented in this section was undertaken by the ATLAS Exotics working group for the 2011 dilepton analysis [83]. Electroweak corrections to the $Z^0/\gamma^* \rightarrow l^+l^-$ and $Z' \rightarrow l^+l^-$ cross sections also need to be considered in addition to the higher order QCD corrections described in the previous section. These corrections include those coming from initial/final state radiation photons, and electroweak loop corrections. The final state radiation can be accurately simulated using PHOTOS [109] and full detector simulation. To evaluate the other electroweak corrections, the HORACE event generator v3.1 [110] is used. Cross section correction factors are defined as a function of the l^+l^- invariant mass with further details of the electroweak correction determination in this thesis found

$M_{\ell\ell}$ [GeV]	$M_{\ell\ell}^2 \frac{d\sigma_{\rm NNLO}}{dM_{\ell\ell}^2}$ [nb]	$\frac{\sigma_{\rm NLO}}{\sigma_{\rm LO}}$	$\frac{\sigma_{\rm NNLO}}{\sigma_{\rm LO}}$	$\frac{\sigma_{\rm NNLO}}{\sigma_{\rm LO}}$	Δ_r [%]	Δ_r^+ [%]	Δ_r^- [%]	Δ_r [%]	Δ_r^+ [%]	Δ_r^- [%]
	MSTW	MSTW	MSTW	MSTW/MRST	PDF uncert.			PDF uncert.		
	2008NNLO	2008NLO/LO	2008NNLO/LO	2008NNLO/2007LO*	68% C.L.			90% C.L.		
10	0.465E+01	1.022	1.081	1.166	5.5	7.5	-4.5	9.3	12.2	-8.8
20	0.917E+00	1.088	1.133	1.138	2.3	3.1	-2.0	4.5	5.5	-4.3
30	0.327E+00	1.124	1.166	1.142	1.8	2.1	-1.8	3.7	4.0	-3.7
40	0.154E+00	1.150	1.191	1.146	1.7	1.8	-1.7	3.5	3.6	-3.5
50	0.884E-01	1.171	1.212	1.149	1.7	1.7	-1.7	3.4	3.5	-3.3
60	0.633E-01	1.190	1.231	1.148	1.7	1.7	-1.6	3.3	3.5	-3.2
70	0.665E-01	1.208	1.248	1.144	1.7	1.7	-1.6	3.3	3.5	-3.2
80	0.155E+00	1.225	1.262	1.138	1.7	1.7	-1.6	3.3	3.5	-3.2
91.12	0.113E+02	1.239	1.275	1.136	1.6	1.7	-1.6	3.3	3.5	-3.1
100	0.236E+00	1.246	1.282	1.138	1.6	1.7	-1.6	3.2	3.5	-3.1
125	0.207E-01	1.263	1.299	1.145	1.6	1.7	-1.5	3.2	3.5	-3.0
150	0.784E-02	1.277	1.312	1.149	1.6	1.7	-1.5	3.1	3.5	-3.0
175	0.405E-02	1.287	1.323	1.151	1.6	1.7	-1.5	3.2	3.5	-2.9
200	0.239E-02	1.296	1.331	1.151	1.6	1.7	-1.5	3.2	3.6	-2.9
250	0.104E-02	1.308	1.342	1.149	1.6	1.8	-1.4	3.3	3.7	-3.0
300	0.528E-03	1.316	1.349	1.146	1.6	1.8	-1.5	3.4	3.9	-3.1
400	0.179E-03	1.322	1.354	1.139	1.7	2.0	-1.5	3.6	4.2	-3.3
500	0.750E-04	1.321	1.352	1.131	1.8	2.1	-1.6	3.9	4.5	-3.5
600	0.357E-04	1.316	1.347	1.123	1.9	2.3	-1.7	4.1	4.8	-3.7
700	0.185E-04	1.310	1.339	1.114	2.0	2.5	-1.7	4.4	5.1	-3.8
800	0.101E-04	1.302	1.332	1.104	2.2	2.7	-1.8	4.6	5.5	-4.0
900	0.582E-05	1.295	1.324	1.093	2.3	2.9	-1.8	5.0	6.0	-4.1
1000	0.346E-05	1.288	1.316	1.080	2.5	3.2	-1.9	5.4	6.6	-4.3
1250	0.105E-05	1.271	1.300	1.041	3.2	4.1	-2.3	6.7	8.4	-5.3
1500	0.353E-06	1.257	1.290	0.990	4.2	5.4	-3.2	8.8	11.0	-7.0
1750	0.127E-06	1.247	1.286	0.929	5.5	7.1	-4.4	11.6	14.5	-9.3
2000	0.473E-07	1.241	1.288	0.860	7.3	9.2	-6.1	15.3	19.1	-12.3
2500	0.687E-08	1.230	1.300	0.712	11.9	14.5	-10.7	24.8	30.8	-20.3
3000	0.949E-09	1.199	1.295	0.563	17.2	20.3	-16.2	35.4	43.7	-29.6

Table B.7: NNLO Drell-Yan to lepton-pair production cross section $M_{\ell\ell}^2 d\sigma_{\rm NNLO}/dM_{\ell\ell}^2$ as function of dilepton mass $M_{\ell\ell}$ calculated with PHOZPR [81] and the MSTW2008NNLO PDF set, cross section ratios (K-factors) based on the MSTW2008 LO, NLO, and NNLO and MRST2007* PDF sets, symmetric and asymmetric PDF uncertainties for the NNLO cross section at 68% and 90% CL, respectively.

$m_{\ell\ell}$	$K^*_{\mathrm{NNLO},Z'}$	$\Delta K_{Z^0/\gamma*,Z'}$	scale unc.		68% C.L. uncertainties							90% C.L. uncertainties					
					α_S		PDF			α_S+PDF		α_S		PDF			α_S+PDF	
			Δ_r^+	Δ_r^-	Δ_r^+	Δ_r^-	Δ_r	Δ_r^+	Δ_r^-	Δ_r^+	Δ_r^-	Δ_r^+	Δ_r^-	Δ_r	Δ_r^+	Δ_r^-	Δ_r^+	Δ_r^-
[GeV]		[%]	[%]	[%]	[%]	[%]	[%]	[%]	[%]	[%]	[%]	[%]	[%]	[%]	[%]	[%]	[%]	[%]
10	1.160	-0.5	2.5	-9.8	1.7	-1.5	5.5	7.5	-4.5	7.7	-4.7	3.9	-3.8	9.3	12.2	-8.8	12.8	-9.5
20	1.123	-1.3	1.6	-3.9	1.5	-1.5	2.3	3.1	-2.0	3.4	-2.5	3.5	-3.7	4.5	5.5	-4.3	6.5	-5.7
30	1.123	-1.6	1.3	-2.4	1.4	-1.4	1.8	2.1	-1.8	2.5	-2.3	3.2	-3.5	3.7	4.0	-3.7	5.1	-5.1
40	1.126	-1.8	1.1	-1.7	1.3	-1.3	1.7	1.8	-1.7	2.2	-2.2	3.0	-3.3	3.5	3.6	-3.5	4.7	-4.8
50	1.129	-1.8	0.9	-1.3	1.2	-1.2	1.7	1.7	-1.7	2.1	-2.1	2.8	-3.1	3.4	3.5	-3.3	4.5	-4.6
60	1.131	-1.5	0.8	-1.1	1.2	-1.2	1.7	1.7	-1.6	2.1	-2.0	2.7	-3.0	3.3	3.5	-3.2	4.4	-4.4
70	1.133	-1.0	0.7	-0.9	1.1	-1.1	1.7	1.7	-1.6	2.1	-2.0	2.5	-2.8	3.3	3.5	-3.2	4.3	-4.3
80	1.135	-0.3	0.6	-0.8	1.1	-1.1	1.7	1.7	-1.6	2.0	-1.9	2.4	-2.7	3.3	3.5	-3.2	4.2	-4.2
91	1.136	-0.0	0.5	-0.7	1.0	-1.0	1.6	1.7	-1.6	2.0	-1.9	2.3	-2.6	3.3	3.5	-3.1	4.2	-4.1
100	1.137	-0.1	0.4	-0.6	1.0	-1.0	1.6	1.7	-1.6	2.0	-1.9	2.2	-2.5	3.2	3.5	-3.1	4.1	-4.0
125	1.139	-0.5	0.3	-0.5	0.9	-0.9	1.6	1.7	-1.5	1.9	-1.8	2.0	-2.3	3.2	3.5	-3.0	4.0	-3.8
150	1.140	-0.8	0.3	-0.4	0.8	-0.8	1.6	1.7	-1.5	1.9	-1.7	1.7	-2.1	3.1	3.5	-3.0	3.9	-3.6
175	1.140	-0.9	0.2	-0.3	0.7	-0.7	1.6	1.7	-1.5	1.8	-1.6	1.6	-1.9	3.2	3.5	-2.9	3.8	-3.5
200	1.140	-0.9	0.2	-0.3	0.6	-0.7	1.6	1.7	-1.5	1.8	-1.6	1.4	-1.7	3.2	3.6	-2.9	3.8	-3.4
250	1.139	-0.9	0.2	-0.4	0.5	-0.6	1.6	1.8	-1.4	1.8	-1.5	1.1	-1.4	3.3	3.7	-3.0	3.9	-3.3
300	1.137	-0.8	0.3	-0.4	0.4	-0.4	1.6	1.8	-1.5	1.9	-1.5	0.8	-1.2	3.4	3.9	-3.1	3.9	-3.3
400	1.132	-0.6	0.3	-0.5	0.2	-0.2	1.7	2.0	-1.5	2.0	-1.5	0.3	-0.7	3.6	4.2	-3.3	4.2	-3.4
500	1.127	-0.4	0.4	-0.6	0.0	-0.1	1.8	2.1	-1.6	2.1	-1.6	0.0	-0.2	3.9	4.5	-3.5	4.5	-3.5
600	1.120	-0.2	0.5	-0.7	0.1	-0.2	1.9	2.3	-1.7	2.3	-1.7	0.2	-0.6	4.1	4.8	-3.7	4.8	-3.7
700	1.113	-0.1	0.5	-0.8	0.2	-0.4	2.0	2.5	-1.7	2.5	-1.7	0.6	-0.9	4.4	5.1	-3.8	5.2	-4.0
800	1.104	-0.0	0.6	-0.9	0.4	-0.5	2.2	2.7	-1.8	2.7	-1.8	1.0	-1.3	4.6	5.5	-4.0	5.6	-4.2
900	1.093	0.0	0.7	-1.0	0.5	-0.6	2.3	2.9	-1.8	3.0	-1.9	1.3	-1.6	5.0	6.0	-4.1	6.2	-4.4
1000	1.081	0.1	0.7	-1.1	0.7	-0.8	2.5	3.2	-1.9	3.3	-2.0	1.7	-1.9	5.4	6.6	-4.3	6.8	-4.7
1250	1.041	0.0	0.9	-1.4	1.0	-1.0	3.2	4.1	-2.3	4.2	-2.5	2.5	-2.4	6.7	8.4	-5.3	8.8	-5.8
1500	0.988	-0.2	1.1	-1.6	1.3	-1.2	4.2	5.4	-3.2	5.5	-3.4	3.3	-2.7	8.8	11.0	-7.0	11.5	-7.5
1750	0.923	-0.7	1.3	-1.9	1.5	-1.3	5.5	7.1	-4.4	7.2	-4.6	4.0	-2.7	11.6	14.5	-9.3	15.1	-9.7
2000	0.850	-1.2	1.5	-2.1	1.7	-1.2	7.3	9.2	-6.1	9.4	-6.2	4.6	-2.3	15.3	19.1	-12.3	19.7	-12.5
2500	0.696	-2.2	1.9	-2.7	1.9	-0.9	11.9	14.5	-10.7	14.6	-10.7	5.4	-0.3	24.8	30.8	-20.3	31.2	-20.3
3000	0.549	-2.5	2.4	-3.4	1.9	-0.1	17.2	20.3	-16.2	20.3	-16.2	5.9	0.0	35.4	43.7	-29.6	44.1	-29.6

Table B.8: $K^*_{\mathrm{NNLO},Z'}$ for Z' production as function of dilepton mass $M_{\ell\ell}$ calculated with ZWPROD and the MSTW2008NNLO and MRST2007LO* PDF sets, its relative difference to $K^*_{\mathrm{NNLO},Z^0/\gamma^*}$ for Z^0/γ^* production, and the relative uncertainties on the NNLO cross section due to variations of factorisation and renormalisation scales, α_s, PDF, and α_s and PDF added in quadrature, at 68% and 90% CL, respectively.

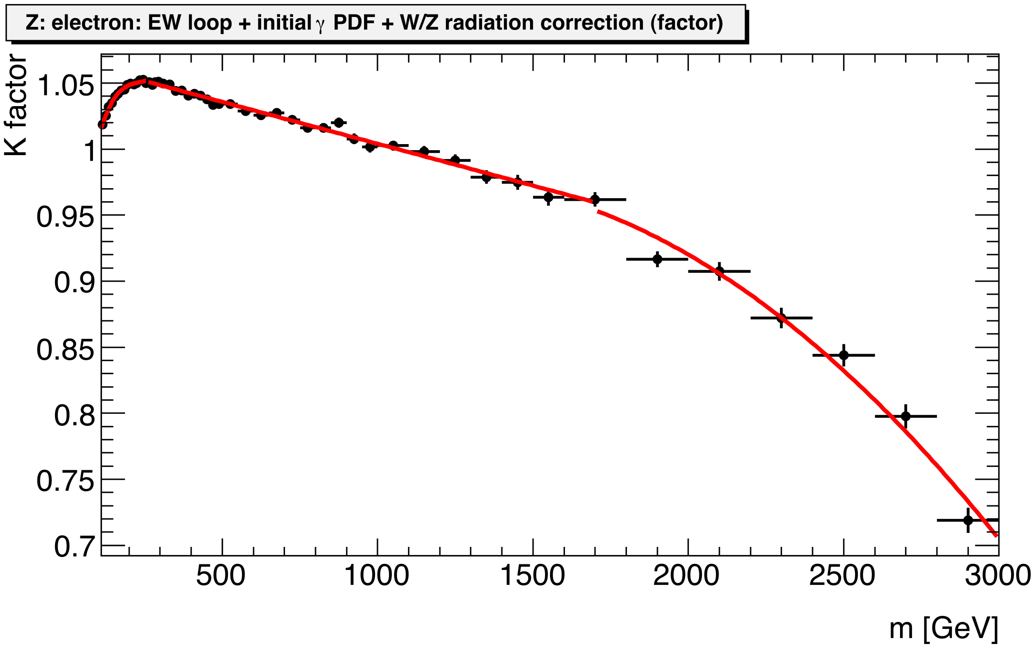

Figure B.2: Electoweak K-factor for $Z^0/\gamma^* \rightarrow l^+l^-$ production as a function of the dilepton mass taking into account corrections due to processes with initial photons, electroweak loops, and real radiation of W and Z bosons [83].

in [83]. The finally derived combined electroweak K-factor correction for the dielectron channel is presented in Figure B.2. A systematic uncertainty on the electroweak K-factor of 4.5% is estimated by taking into account the individual uncertainties for the calculation of the real boson radiation (1%), potential contributions from $O(\alpha)$ corrections (1%) [82], higher order electroweak corrections (1.5%) [111], an assumed uncertainty of 10% on the contribution from photon induced processes (1%), and a difference in the definition of the electroweak scheme used in the event generation with PYTHIA and in the calculation of the electrweak corrections with HORACE (3%). This electroweak K-factor is not applied to the Z' signal, although it is expected to have a similar correction. This is because the calculation cannot be directly applied as the triple gauge coupling $Z'W^+W^-$ vanishes (or is at least model dependent) in contrast to the SM $Z^0W^+W^-$ coupling.

Appendix C

Signal Cross-Section Parton Distribution Function Uncertainties

The method and results presented in this section are those as were studied by the ATLAS Exotics working group for the 2010 dilepton analysis [84], and used unchanged in the 2011 dilepton analysis for EPS [83].

The variation of the signal PDF has an effect on the cross section as a function of mass. Each PDF has a set of independent parameters associated with it known as eigenvectors. These eigenvectors can be varied orthogonally to quantify the systematic uncertainty of a given PDF variation. For each eigenvector, the Z'/G^* cross section was calculated as a function of mass by generating 100,000 events per simulation in PYTHIA. The asymmetric uncertainty at each mass point was then calculated with Equations (C.1) and (C.2).

$$\Delta\sigma^{+} = \sqrt{\sum_{i=1}^{n}(max(\sigma_i^{+} - \sigma_0, \sigma_i^{-} - \sigma_0, 0))^2} \tag{C.1}$$

$$\Delta\sigma^{-} = \sqrt{\sum_{i=1}^{n}(max(\sigma_0 - \sigma_i^{+}, \sigma_0 - \sigma_i^{-}, 0))^2} \tag{C.2}$$

Where n is the number of PDF eigenvectors, σ_i^{+} is the cross section for the higher value of the i$^{\text{th}}$ PDF eigenvector, σ_i^{-} is the cross section for the lower value of the i$^{\text{th}}$ PDF eigenvector, and σ_0 is the cross section for the central value PDF. The larger of the positive and negative variation is taken as the systematic uncertainty on the $Z'G^*$ cross section.

As PYTHIA is a LO generator, LO PDF sets have to be used as input. However AT-

LAS makes use of a modified LO PDF set called MRST2007LO* which factors in the theoretical expected difference between LO and NLO cross section calculations. Since only the central value is available for the modified LO PDF set, the closest LO set: MSTW2008LO90cl, is used to estimate the PDF uncertainties, as per the MC group recommendations [112]. This set has 1 central PDF and 20 orthogonal eigenvector variations with a high and low value for each eigenvector. Further information on MSTW2008 can be found in reference [113]. The Z' results are shown in Table C.1. The spin-2 G^* has the additional complication due production proceeding through $q\bar{q}$ annihilation as well as gg fusion. The PDF uncertainty for the spin-2 RS G^* production is given in Table C.2 as a function of the G^* mass. These are slightly larger compared to the uncertainties obtained for the Z'.

Z' mass [GeV]	MRST2007lomod Cross section [fb]	MSTW2008lo90cl Cross section [fb]	Uncertainty
100	641000	556000	+3.0% -2.1%
200	69700	58800	+2.6% -2.6%
500	2380	2040	+4.4% -3.7%
1000	114.6	94.8	+5.5% -7.1%
1500	13.2	10.3	+8.0% -9.8%
2000	2.18	1.58	+8.5% -13.3%

Table C.1: Z' LO(mod) cross sections and their fractional uncertainty due to PDF variation (at 90% C.L.).

As an additional test, Z' cross sections calculated with CTEQ and MSTW sets of PDFs are compared. This comparison is shown in Table C.3. The difference between the two is always smaller than the uncertainty within a given set (in this case MSTW). Following official recommendations [112], the predictions from different PDFs are not combined to determine the PDF error contribution.

G^* Mass [GeV]	k/M_{Pl}	MSTW2008lo90cl Uncertainty
100	0.01	+4.2% -2.9%
200	0.01	+4.6% -3.6%
500	0.01	+6.5% -5.8%
1000	0.01	+7.5% -8.5%
1500	0.01	+9.6% -11.1%
2000	0.01	+12.2% -16.3%
100	0.1	+3.8% -3.6%
200	0.1	+4.9% -4.0%
500	0.1	+5.8% -6.1%
1000	0.1	+7.5% -8.6%
1500	0.1	+9.0% -11.2%
2000	0.1	+13.1% -15.2%

Table C.2: Uncertainty on G* cross-sections due to PDF variation (at 90% C.L.).

Z' mass [GeV]	CTEQ6LL σ [fb]	MSTW2008lo90cl σ [fb]	$\sigma_{\mathrm{MSTW}}/\sigma_{\mathrm{CTEQ}} - 1$ [%]
100	541 000	556 000	+2.7%
200	58 100	58 800	+1.2%
500	2010	2040	+1.5%
1000	92.4	94.8	+2.5%
1500	9.98	10.3	+3.1%
2000	1.52	1.58	+3.8%

Table C.3: Difference in Z' LO cross sections between CTEQ and MSTW PDF sets.

Appendix D

Outlier Study

D.1 Inter-Trigger Level Study at $\sqrt{s}$ = 900 GeV

Figures D.1 and D.2, present the inter-trigger level study plots at $\sqrt{s}$ = 900 GeV, not displayed in Chapter 4.3.

D.2 Inter-Trigger Level Study at $\sqrt{s}$ = 7 TeV

Figures D.3-D.8, present the inter-trigger level study plots at $\sqrt{s}$ = 7 TeV, not displayed in Chapter 4.4.

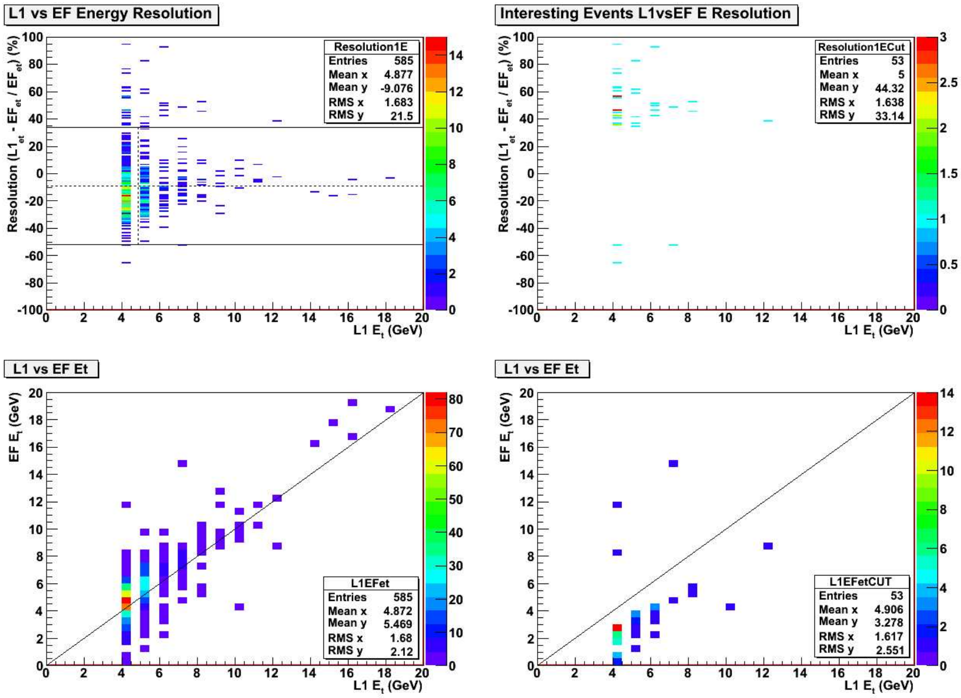

Figure D.1: Level-1 vs Event Filter object comparison from upper left clockwise; Resolution vs $L1_{E_T}$ of all objects passing cuts; Resolution vs $L1_{E_T}$ of object comparisons determined to be outliers; EF_{E_T} vs $L1_{E_T}$ object matches determined to be outliers; EF_{E_T} vs $L1_{E_T}$ matches for all objects that pass cuts.

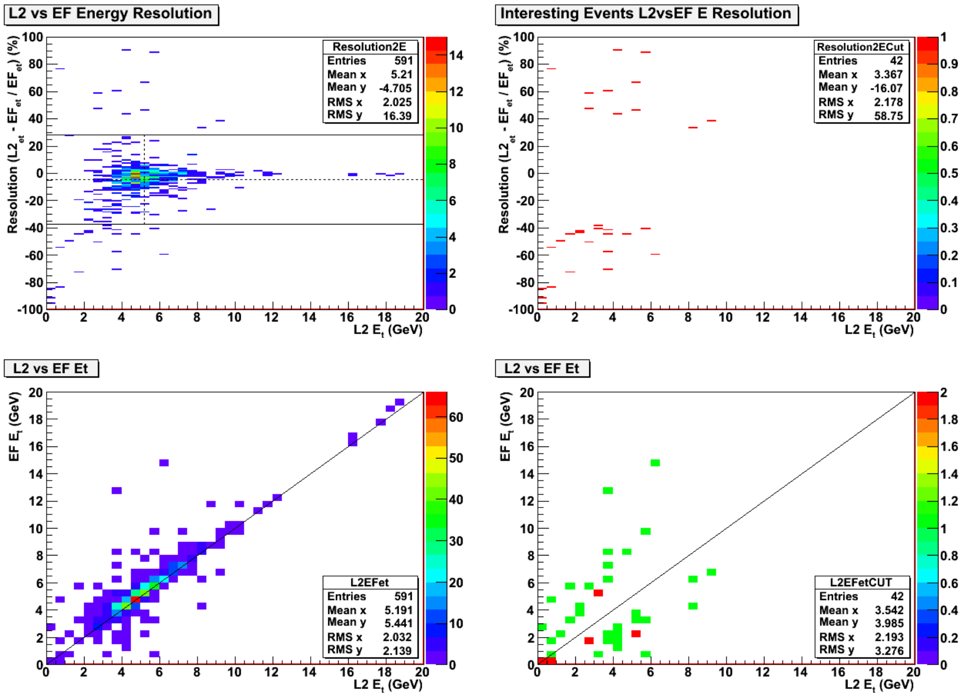

Figure D.2: Level-2 vs Event Filter object comparison from upper left clockwise; Resolution vs $L2_{E_T}$ of all objects passing cuts; Resolution vs $L2_{E_T}$ of object comparisons determined to be outliers; EF_{E_T} vs $L2_{E_T}$ object matches determined to be outliers; EF_{E_T} vs $L2_{E_T}$ matches for all objects that pass cuts.

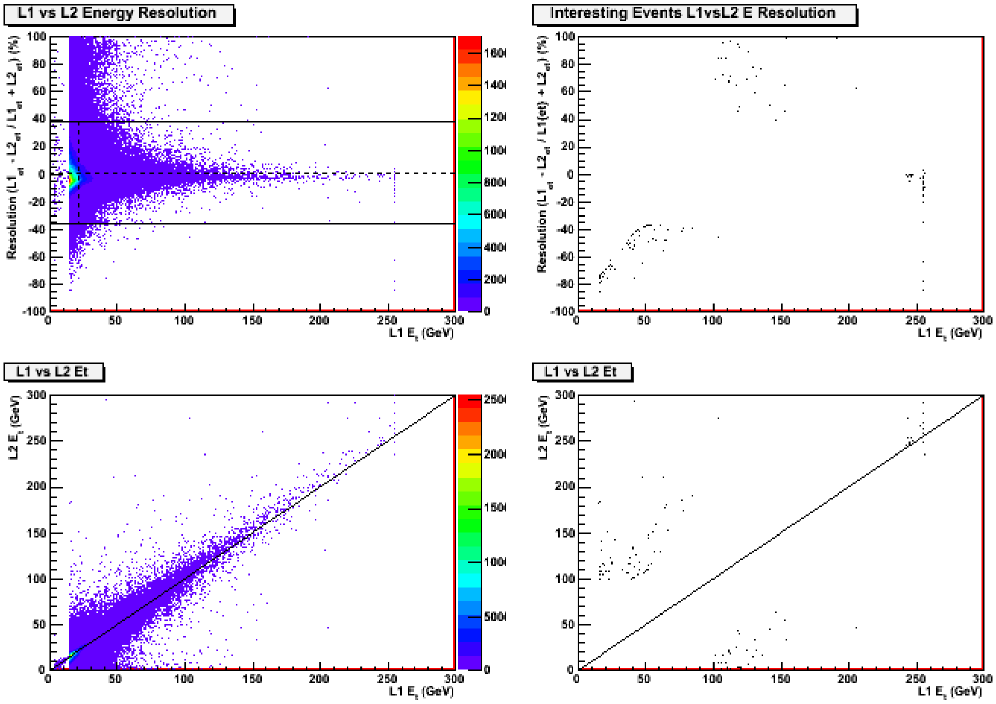

Figure D.3: Level-1 vs Level-2 object comparison from upper left clockwise; Resolution vs $L1_{E_T}$ of all objects passing cuts; Resolution vs $L1_{E_T}$ of object comparisons determined to be outliers; $L2_{E_T}$ vs $L1_{E_T}$ object matches determined to be outliers; $L2_{E_T}$ vs $L1_{E_T}$ matches for all objects that pass cuts.

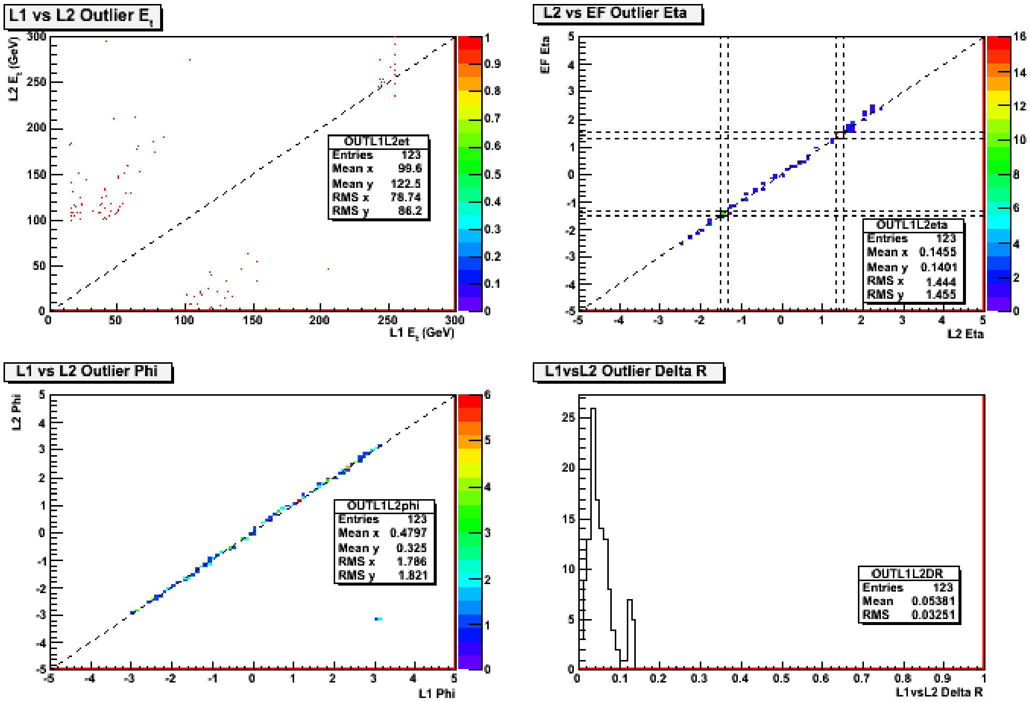

Figure D.4: Level-1 vs Level-2 object comparison for outlier objects from upper left clockwise; $L2_{E_T}$ vs $L1_{E_T}$, $L2_\eta$ vs $L1_\eta$ with dashed lines highlighting the crack region, ΔR between objects at L1 and L2, $L2_\phi$ vs $L1_\phi$.

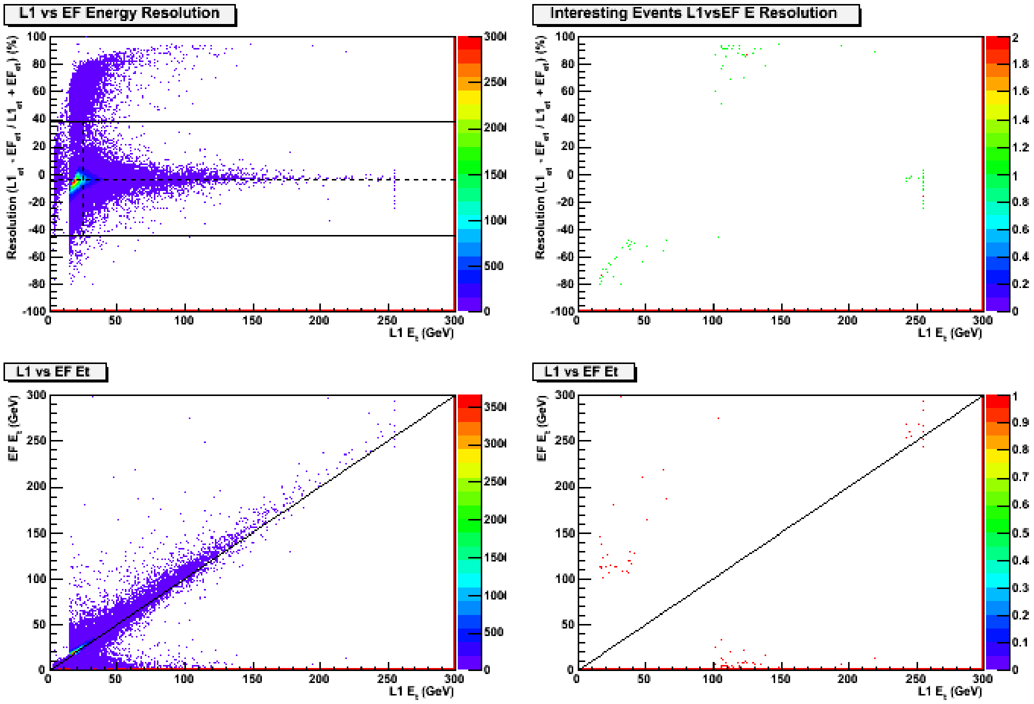

Figure D.5: Level-1 vs Event Filter object comparison from upper left clockwise; Resolution vs $L1_{E_T}$ of all objects passing cuts; Resolution vs $L1_{E_T}$ of object comparisons determined to be outliers; EF_{E_T} vs $L1_{E_T}$ object matches determined to be outliers; EF_{E_T} vs $L1_{E_T}$ matches for all objects that pass cuts.

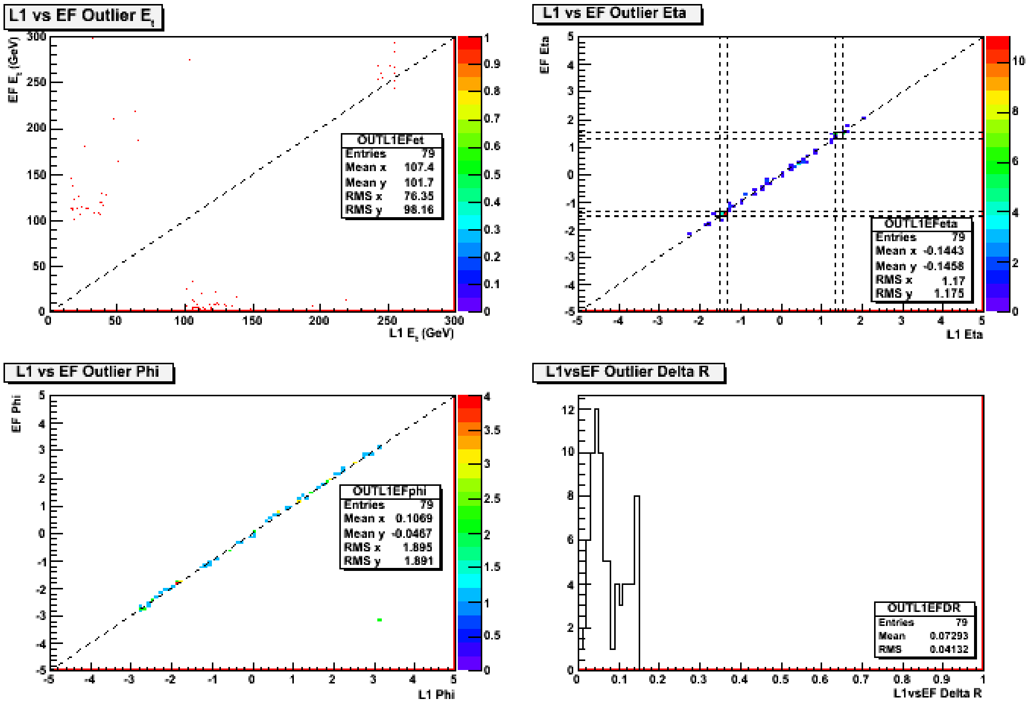

Figure D.6: Level-1 vs Event Filter object comparison for outlier objects from upper left clockwise; EF_{E_T} vs $L1_{E_T}$, EF_η vs $L1_\eta$ with dashed lines highlighting the crack region, ΔR between objects at L1 and EF, EF_ϕ vs $L1_\phi$.

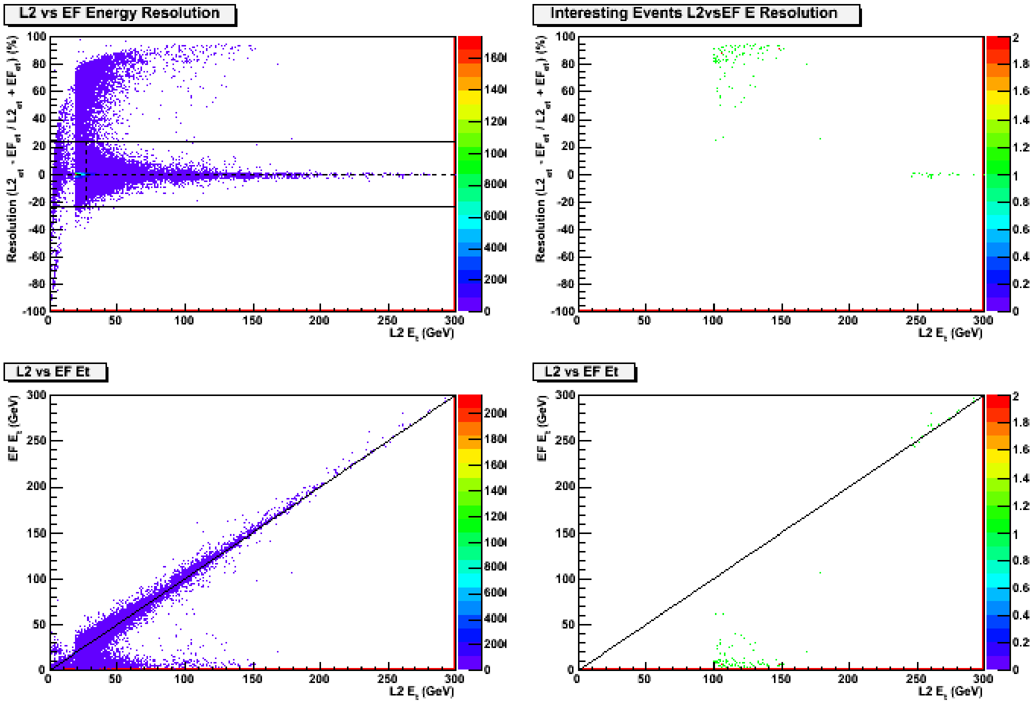

Figure D.7: Level-2 vs Event Filter object comparison from upper left clockwise; Resolution vs $L2_{E_T}$ of all objects passing cuts; Resolution vs $L2_{E_T}$ of object comparisons determined to be outliers; EF_{E_T} vs $L2_{E_T}$ object matches determined to be outliers; EF_{E_T} vs $L2_{E_T}$ matches for all objects that pass cuts.

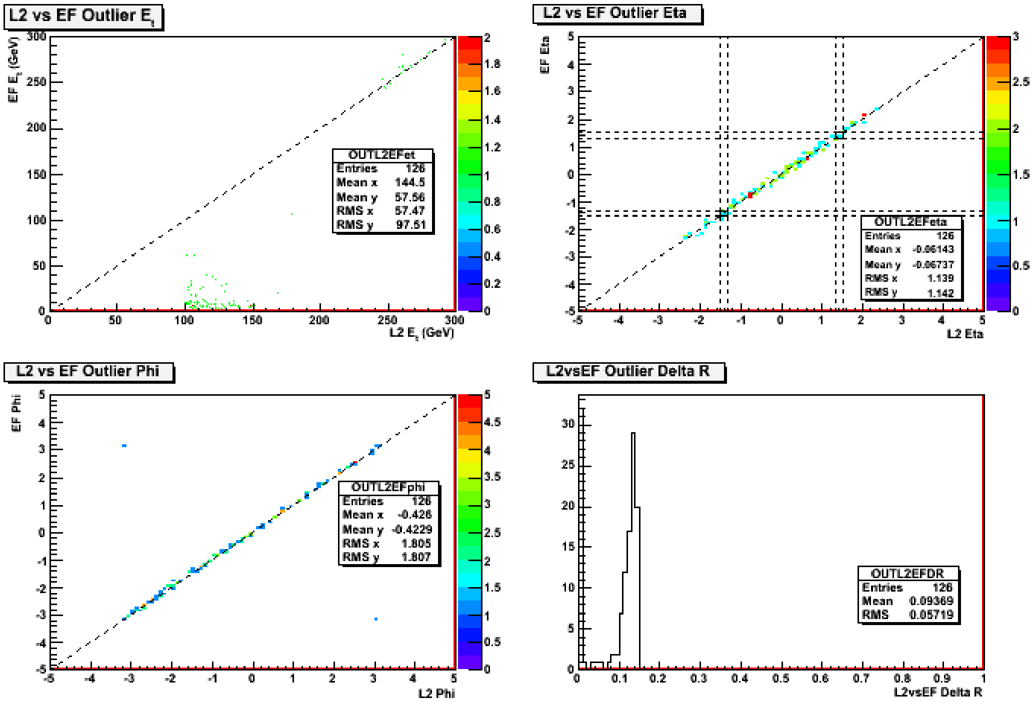

Figure D.8: Level-2 vs Event Filter object comparison for outlier objects from upper left clockwise; EF_{E_T} vs $L2_{E_T}$, EF_η vs $L2_\eta$ with dashed lines highlighting the crack region, ΔR between objects at L2 and EF, EF_ϕ vs $L2_\phi$.

Appendix E

isEM Study Extra Plots

This section presents the applicable remaining isEM *medium* criteria variable distributions not displayed in Chapter 5.2. A full description of the methods and MC used to produce these plots can be found in the text of Chapter 5. All plots are shown with a potential 1 TeV Z'_{SSM} signal.

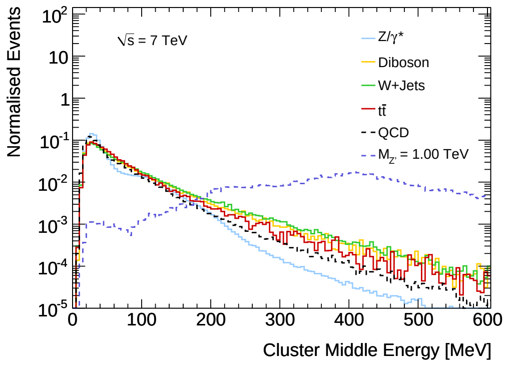

Figure E.1: Process normalised Cluster Middle Energy distribution.

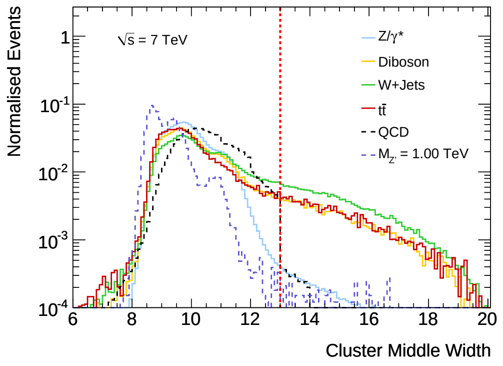

Figure E.2: Process normalised Cluster Middle Width distribution. The red dashed line shows the minimum cut value.

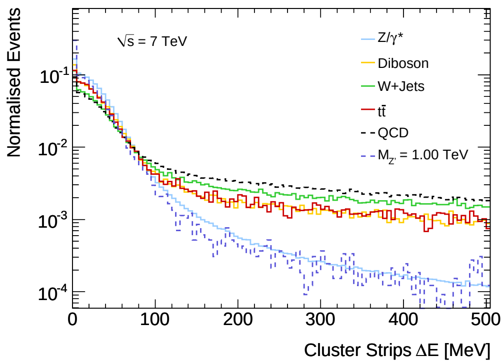

Figure E.3: Process normalised Cluster Strips ΔE distribution.

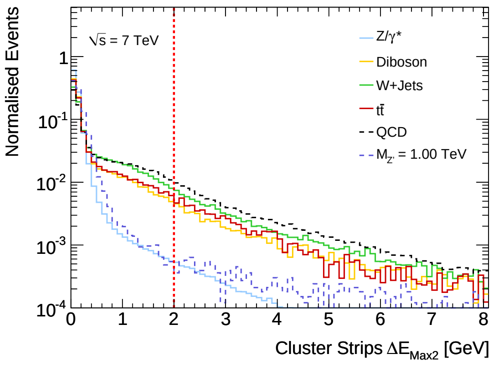

Figure E.4: Process normalised Cluster Strips ΔE_{Max2} distribution. The red dashed line shows the minimum cut value.

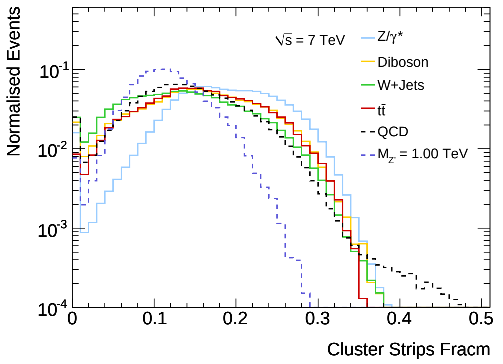

Figure E.5: Process normalised Cluster Strips Fracm.

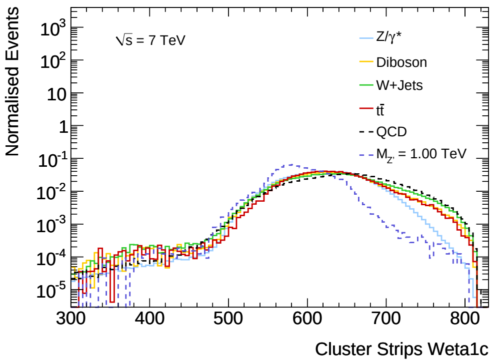

Figure E.6: Process normalised Cluster Strips Weta1c distribution.

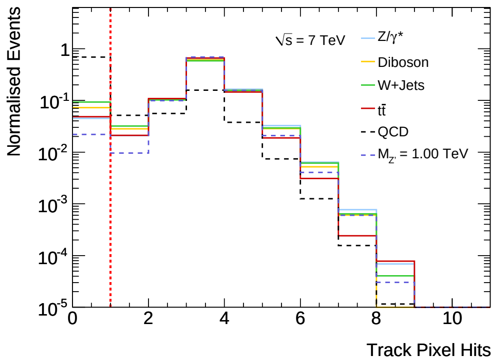

Figure E.7: Process normalised Track Pixel Hits distribution. The red dashed line shows the threshold cut value.

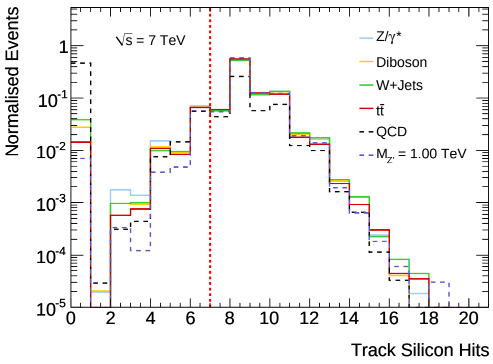

Figure E.8: Process normalised Track Silicon Hits distribution. The red dashed line shows the maximum cut value.

Appendix F

Extra Data/MC Kinematic Plots

F.1 isEM *medium* Kinematic Plots

Figures F.1-F.10 present the applicable isEM *medium* variable distribution data/MC plots, which were not displayed in Chapter 7. All plots presented show various possible Z'_{SSM} resonance signals. RS G^* equivalent plots are not provided in the next section, as due to the relatively small dataset size, no expected BSM deviation is visible.

F.2 G^* Kinematic Plots

Figures F.11-F.14 present the RS G^* equivalent plots to those found in Chapter 7 for a Z'_{SSM} resonance signal.

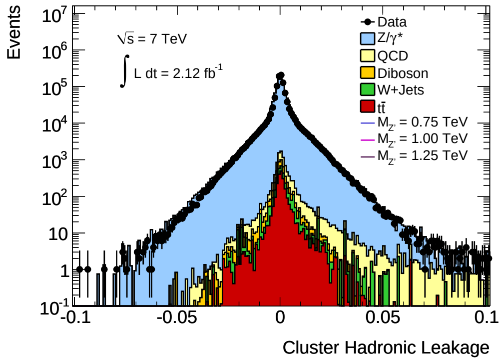

Figure F.1: Cluster Hadronic Leakage distribution for both electrons in candidate events. The comparison is between the 2.12 fb^{-1} dataset and all relevant background processes.

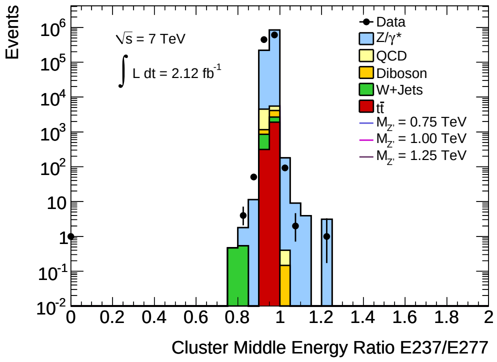

Figure F.2: Cluster Middle Energy Ratio 37 distribution for both electrons in candidate events. The comparison is between the 2.12 fb^{-1} dataset and all relevant background processes.

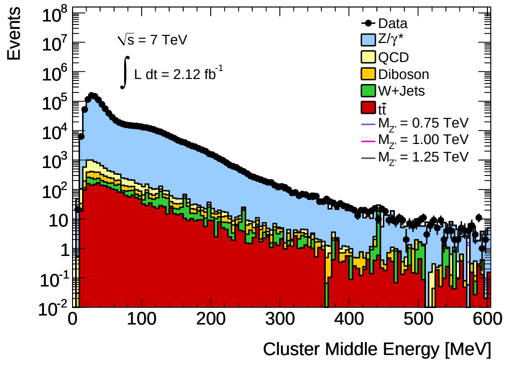

Figure F.3: Cluster Middle Energy distribution for both electrons in candidate events. The comparison is between the 2.12 fb^{-1} dataset and all relevant background processes.

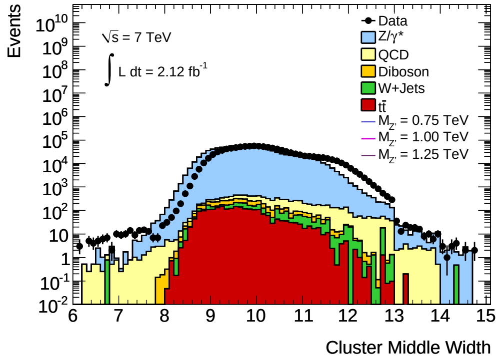

Figure F.4: Cluster Middle Width distribution for both electrons in candidate events. The comparison is between the 2.12 fb^{-1} dataset and all relevant background processes.

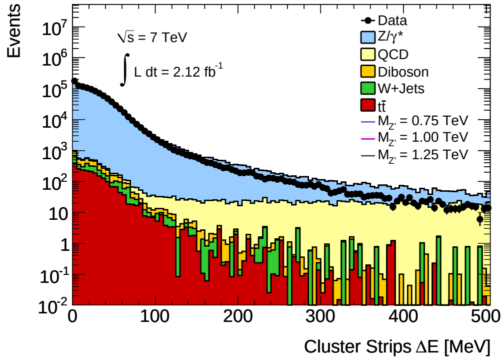

Figure F.5: Cluster Strips ΔE distribution for both electrons in candidate events. The comparison is between the 2.12 fb^{-1} dataset and all relevant background processes.

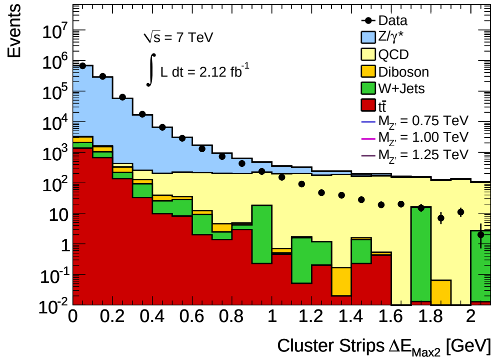

Figure F.6: Cluster Strips ΔE_{Max2} distribution for both electrons in candidate events. The comparison is between the 2.12 fb^{-1} dataset and all relevant background processes.

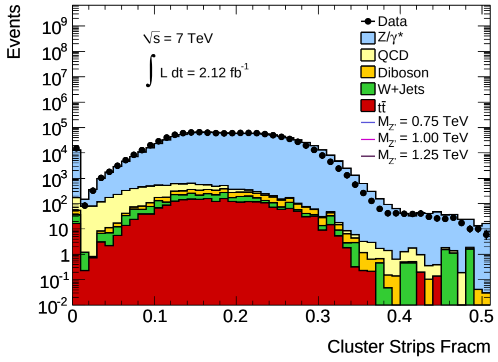

Figure F.7: Cluster Strips Fracm distribution for both electrons in candidate events. The comparison is between the 2.12 fb^{-1} dataset and all relevant background processes.

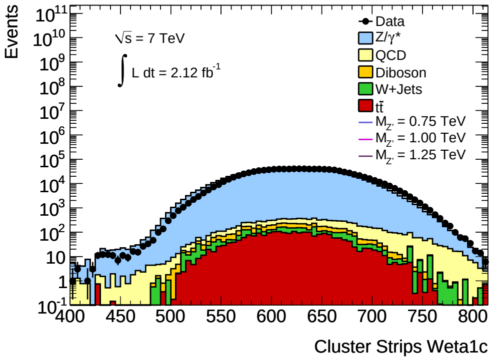

Figure F.8: Cluster Strips Weta1c distribution for both electrons in candidate events. The comparison is between the 2.12 fb^{-1} dataset and all relevant background processes.

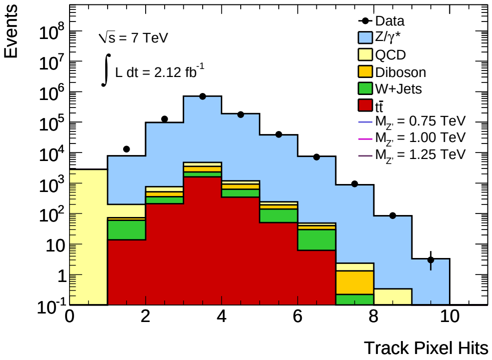

Figure F.9: Track Pixel Hits distribution for both electrons in candidate events. The comparison is between the 2.12 fb^{-1} dataset and all relevant background processes.

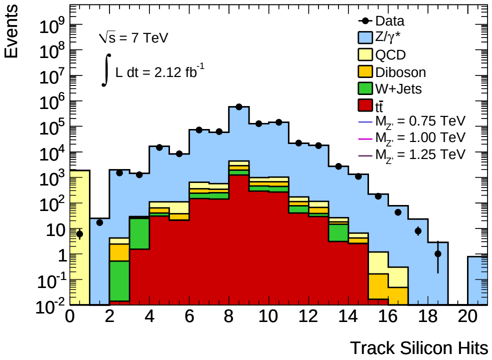

Figure F.10: Track Silicon Hits distribution for both electrons in candidate events. The comparison is between the 2.12 fb^{-1} dataset and all relevant background processes.

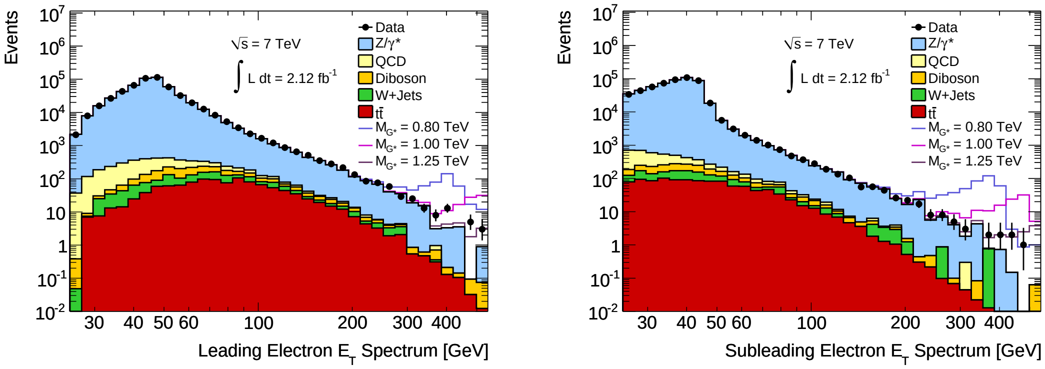

Figure F.11: E_T distribution for the leading (left) and subleading (right) electron after event selection. The comparison is between 2011 data and all relevant background processes, as well as various possible G^* resonance signals for k/$\overline{M}_{Pl}$ = 0.10.

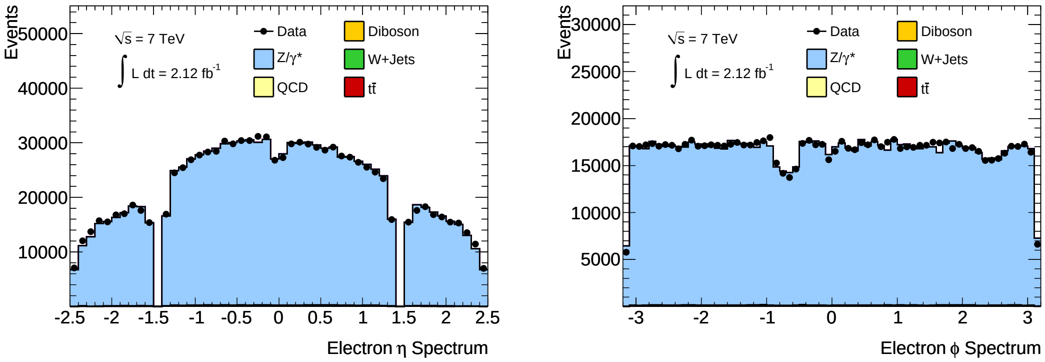

Figure F.12: Distributions of η (left) and ϕ (right) for the electrons that are paired in the candidate event after selection. The comparison is between 2011 data and all relevant background processes, as well as various possible G^* resonance signals for k/$\overline{M}_{Pl}$ = 0.10.

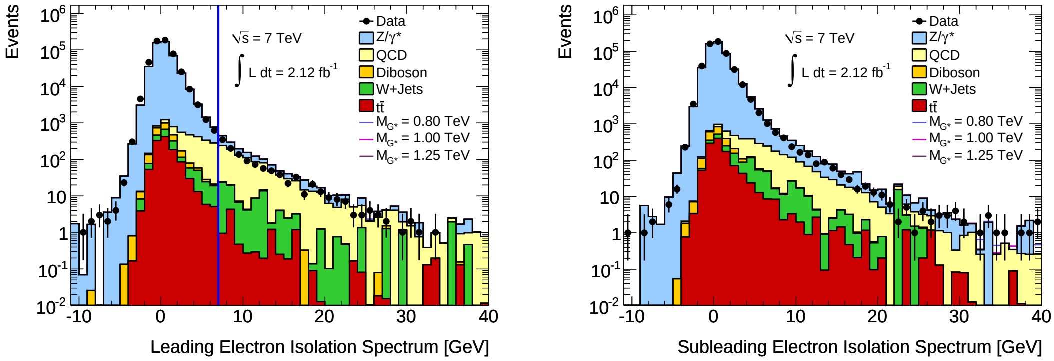

Figure F.13: Isolation distribution for the leading electron (left) with event selection excluding the isolation requirement (blue line indicates the 7 GeV cut value). Also shown is the subleading electron (right) after event selection. The comparison is between 2011 data and all relevant background processes, as well as various possible G^* resonance signals for $k/\overline{M}_{Pl} = 0.10$.

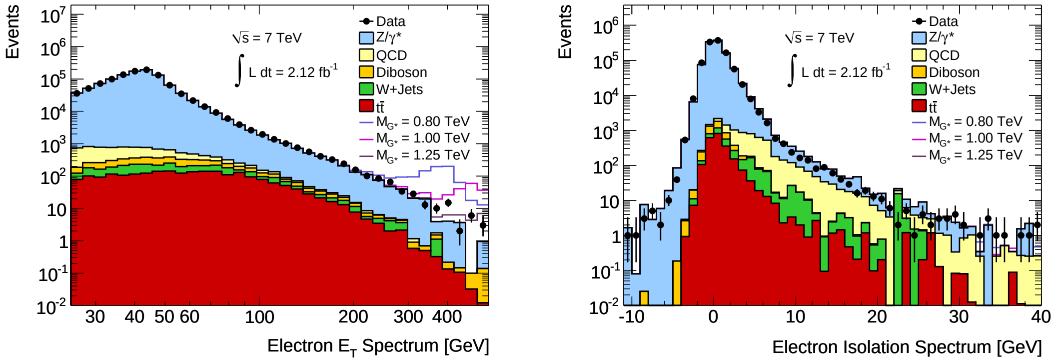

Figure F.14: Distributions for both electrons in candidate events showing (top) E_T spectrum and (bottom) Isolation spectrum, after event selection. The comparison is between 2011 data and all relevant background processes, as well as various possible G^* resonance signals for $k/\overline{M}_{Pl} = 0.10$.

Appendix G

Atlantis Event Displays

This section presents the Atlantis event displays for the second and third highest invariant mass dielectron events selected by the analysis presented in this thesis with 2.12fb^{-1} of data recorded by the ATLAS detector in 2011.

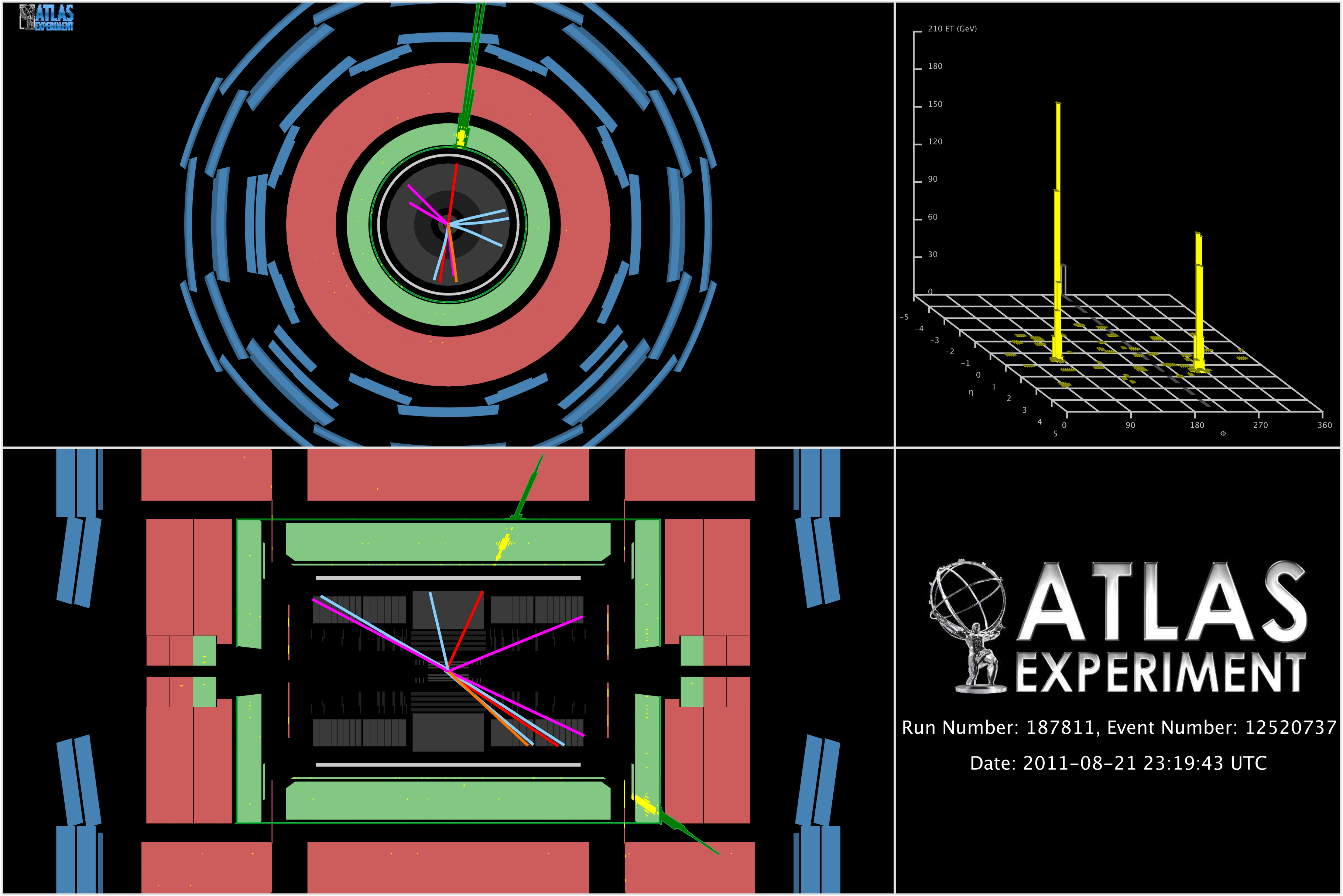

Figure G.1: Atlantis event display showing the second highest invariant mass dielectron event selected by the analysis presented in this thesis with 2.12fb^{-1} of data recorded by the ATLAS detector in 2011. This event has an invariant mass of 1068.25 GeV. Views in X-Y (upper left), p_Z (lower left), and ECAL lego plot (upper right) are shown.

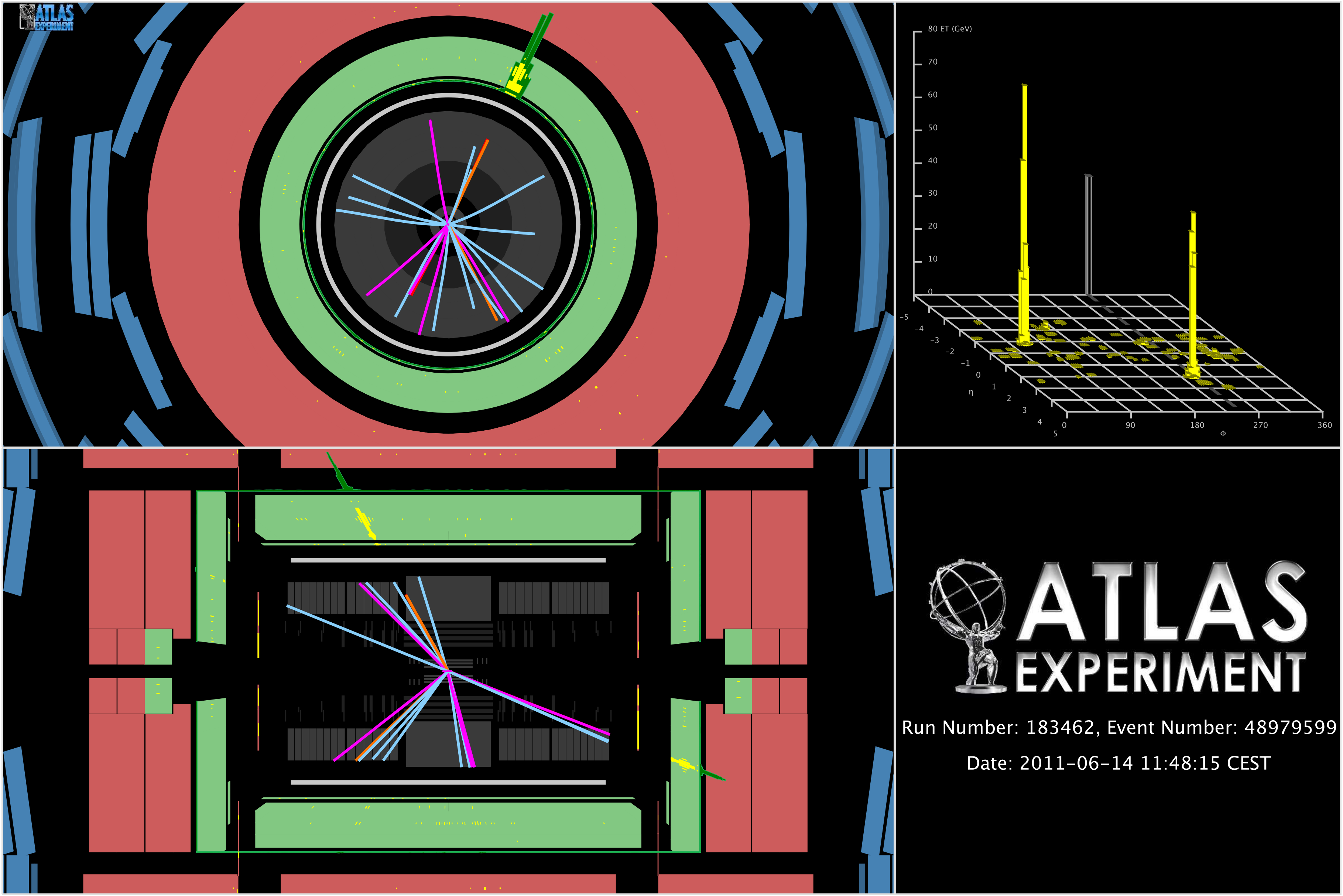

Run Number: 183462, Event Number: 48979599

Date: 2011-06-14 11:48:15 CEST

Figure G.2: Atlantis event display showing the third highest invariant mass dielectron event selected by the analysis presented in this thesis with 2.12fb^{-1} of data recorded by the ATLAS detector in 2011. This event has an invariant mass of 993.29 GeV. Views in X-Y (upper left), p_Z (lower left), and ECAL lego plot (upper right) are shown.

Bibliography

[1] D. Damazio et al, Trigger Egamma 2009 Collision Studies, ATL-COM-DAQ-2010-032 (2010) 17–21.

[2] The ATLAS Collaboration, Search for high-mass dilepton resonances in pp collisions at $\sqrt{s} = 7$ TeV with the ATLAS detector, Phys. Lett. B700 (2011) 163–180.

[3] The ATLAS Collaboration, Search for dilepton resonances in pp collisions at $\sqrt{s} = 7$ TeV with the ATLAS detector, Phys. Rev. Lett 107 (2011) 27.

[4] The ATLAS Collaboration, Search for Extra Dimensions using diphoton events in 7 TeV proton-proton collisions with the ATLAS detector, arXiv:1112.2194v1 [hep-ex] Accepted by Phy. Rev. Lett. B (2011) .

[5] David Griffiths, Introduction to Elementary Particles, second revised edition Edition, Wiley-VCH Verlag GmbH & Co. KGaA (Wiley-VCH), 2009.

[6] B. R. Martin & G. Shaw, Particle Physics, second edition Edition, John Wiley & Sons, 1997.

[7] K. Nakamura et al. (Particle Data Group), 2011 Review of Particle Physics, J. Phys G 37 (2010) 075021.

[8] David Griffiths, Introduction to Elementary Particles, second revised edition Edition, Wiley-VCH Verlag GmbH & Co. KGaA (Wiley-VCH), 2009, p. 355.

[9] N. Cabibbo, Unitary Symmetry and Leptonic Decays, Phys. Rev. Lett 10 (1963) 531–533.

[10] M. Kobayashi and T. Maskawa, CP-Violation in the Renormalizable Theory of Weak Interaction, Prog. Theor. Phys 49 (1973) 652–657.

[11] S. L. Glashow, Partial symmetries of weak interactions, Nucl. Phys 22 (1961) 579–588.

[12] S. Weinberg, A model of leptons, Phys. Rev. Lett 19 (1967) 1264–1266.

[13] A. Salam, Weak and electromagnetic interactions, Proceedings of the 8th Nobel Symposium on Elementary particle theory, relativistic groups and analyticity (1968) 367–377.

[14] P. W. Higgs, Broken symmetries and the masses of gauge bosons, Phys. Rev. Lett 10 531 (1964) 508–509.

[15] Luis Álvarez-Gaumé and John Ellis, Eyes on a prize particle, Nature Physics 7 (2011) 2–3.

[16] B. Lee, C. Quigg, and H. Thacker, Weak interactions at very high energies: The role of the Higgs-boson mass, Phys. Rev D 16 (1977) 1519–1531.

[17] D. Dicus and V. Mathur, Upper Bounds on the Values of Masses in Unified Gauge Theories, Phys. Rev D 7 (1973) 3111–3114.

[18] The ATLAS Collaboration, Combination of Higgs Boson Searches with up to 4.9 fb^{-}1 of pp Collisions Data Taken at a center-of-mass energy of 7 TeV with the ATLAS Experiment at the LHC, ATLAS-CONF-2011-163 (2011) .

[19] T. Hambye and K. Riesselmann, SM Higgs mass bounds from theory, arXiv:hep-ph/9708416v1 (1997) .

[20] P. Langacker, The Physics of Heavy Z' Gauge Bosons, Rev. Mod. Phys 81 (2009) 1199–1228.

[21] A. Leike, S. Riemann, T. Riemann, ZZ' Mixing in Presence of Standard Weak Loop Corrections, arXiv:hep-ph/9808374v1 (1998) .

[22] J. L. Hewett and T. G. Rizzo, Low-energy phenomenology of superstring-inspired E6 models, Physics Reports 183 (1989) 193–381.

[23] R. W. Robinett and J. L. Rosner, Minimally extended electroweak gauge theories in SO(10) and E6, AIP Conf. Proc. 99 (1983) 193–201.

[24] D. London and J. L. Rosner, Extra gauge bosobs in E6, Phys. Rev. D 34 (1986) 1530–1546.

[25] H. Georgi and S. L. Glashow, Unity of All Elementary-Particle Forces, Phys. Rev. Lett 32 (1974) 438–441.

[26] CMS Collaboration, Search for Resonances in the Dilepton Mass Distribution in pp Collisions at $\sqrt{s} = 7$ TeV, CMS PAS EXO-11-019 (2011) .

[27] CDF Collaboration, Search for High-Mass e^+e^- Resonances in $p\overline{p}$ Collisions at $\sqrt{s} = 1.96$ TeV, Phys. Rev. Lett 102 (2009) 031801.

[28] CDF Collaboration, Search for New High-Mass Particles Decaying to Lepton Pairs in pp Collisions at $\sqrt{s} = 1.96$ TeV, Phys. Rev. Lett 95 (2005) 252001.

[29] D0 Collaboration, Search for a heavy neutral gauge boson in the dielectron channel with 5.4 fb^{-1} of ppbar collisions at $\sqrt{s} = 1.96$ TeV, arXiv:1008.2023v2 [hep-ex] (2011) .

[30] N. Arkani-Hamed, S. Dimopoulos, and G. Dvali, The Hierarchy Problem and New Dimensions at a Millimeter, Phys. Lett. B 3-4 (1998) 263–272.

[31] T. G. Rizzo, Pedagogical Introduction to Extra Dimensions, arXiv:hep-ph/0409309v2 (2004) .

[32] L. Randall and R. Sundrum, A Large Mass Hierarchy from a Small Extra Dimension, Phys. Rev. Lett 83 (1999) 3370–3373.

[33] H. Davoudiasl, J. L. Hewett, B. Lillie, T. G. Rizzo, Higgsless Electroweak Symmetry Breaking in Warped Backgrounds: Constraints and Signatures, hep-ph/0312193 (2003) .

[34] N. Arkani-Hamed and M. Schmaltz, Hierarchies without Symmetries from Extra Dimensions, arXiv:hep-ph/9903417v1 (1999) .

[35] K. R. Dienes, E. Dudas, T. Gherghetta, Grand Unification at Intermediate Mass Scales through Extra Dimensions, arXiv:hep-ph/9806292v2 (1998) .

[36] G. Servant and T. Tait, Is the Lightest Kaluza-Klein Particle a Viable Dark Matter Candidate, arXiv:hep-ph/0206071v2 (2002) .

[37] S. Dimopoulos and G. Landsberg, Black Holes at the LHC, arXiv:hep-ph/0106295v1 (2001) .

[38] H. Davoudiasl, J. L. Hewett, and T. G. Rizzo, Experimental probes of localized gravity: On and off the wall, Phys. Rev D 63 (2001) .

[39] C. D. Hoyle et al, Sub-millimeter Tests of the Gravitational Inverse-square Law, Phys. Rev D 70 (2004) .

[40] W. D. Goldberger, and M. B. Wise, Phenomenology of a stabilized modulus, Phys. Lett. B 475 (2000) 275–279.

[41] W. D. Goldberger, and M. B. Wise, Modulus Stabilization with Bulk Fields, Phys. Rev. Lett 83 (1999) 4922–4925.

[42] The CMS Collaboration, Search for signatures of extra dimensions in the diphoton mass spectrum at the Large Hadron Collider, arXiv:1112.0688 (2011) .

[43] The CDF Collaboration, Search for New Dielectron Resonances and Randall-Sundrum Gravitons at the Collider Detector at Fermilab, Phys. Rev. Lett. 107 (2011) 051801.

[44] The D0 Collaboration, Search for Randall-Sundrum Gravitons in the Dielectron and Diphoton Final States with 5.4 fb^{-1} of Data from pp Collisions at $\sqrt{s}$ = 1.96 TeV, Phys. Rev. Lett. 104 (2010) 241802.

[45] M. Dittmar, A. S. Nicollerat, and A. Djouadi, Z' studies at the LHC: an update, ETHZ-IPP PR-2003-01, CERN TH/2003-145 (2003) .

[46] B. C. Allanach et al, Exploring Small Extra Dimensions at the Large Hadron Collider, JHEP 12 (2002) .

[47] The CMS Collaboration, Forward-Backward Asymmetry of di-Lepton Pairs and the Weak-mixing Angle, CMS-PAS-EWK-10-011 (2011) .

[48] B. C. Allanach, K. Odagiri, M. A. Parker, and B. R. Webber, Searching for Narrow Graviton Resonances with the ATLAS Detector at the Large Hadron Collider, JHEP 9 (2000) .

[49] The ALICE Collaboration et al, The ALICE Experiment at the CERN Large Hadron Collider, JINST 3 S08002 (2008) .

[50] The ATLAS Collaboration et al, The ATLAS Experiment at the CERN Large Hadron Collider, JINST 3 S08003 (2008) .

[51] The CMS Collaboration et al, The CMS Experiment at the CERN Large Hadron Collider, JINST 3 S08004 (2008) .

[52] The LHCb Collaboration et al, The LHCb Detector at the LHC, JINST 3 S08005 (2008) .

[53] O. Brüning et al, LHC Design Report v.1 : The LHC Main Ring (CERN-2004-003-V-1) (2004) Chapter 2.

[54] The TOTEM Collaboration et al, The TOTEM Experiment at the CERN Large Hadron Collider, JINST 3 S08007 (2008) .

[55] The LHCf Collaboration et al, The LHCf Detector at the CERN Large Hadron Collider, JINST 3 S08006 (2008) .

[56] AC Team, The four main LHC experiments (CERN-AC-9906026) (1999) .

[57] M.Benedikt et al, LHC Design Report v.3 : The LHC Injector Chain (CERN-2004-003-V-3) (2004) .

[58] Christiane Lefèvre, Complexe des accélérateurs du CERN (CERN-DI-0812015) (2008) .

[59] CERN/AT/PhL, Interim Summary Report on the Analysis of the 19th September 2008 incident at the LHC (15th October).

[60] The ATLAS Collaboration, ATLAS Total Integrated Luminosity 2010, `https://atlas.web.cern.ch/Atlas/GROUPS/DATAPREPARATION/DataSummary/2010/daily-summary.html`.

[61] The ATLAS Collaboration, ATLAS Total Integrated Luminosity 2011, `https://atlas.web.cern.ch/Atlas/GROUPS/DATAPREPARATION/DataSummary/2011/daily-summary.html`.

[62] The ATLAS Collaboration, The ATLAS Experiment at the CERN Large Hadron Collider, JINST 3 S08003 (2008) Chapter 1.

[63] The ATLAS Collaboration, The ATLAS Experiment at the CERN Large Hadron Collider, JINST 3 S08003 (2008) Chapter 2.

[64] A Yamamoto et al, Progress in ATLAS central solenoid magnet, IEEE T. Appl. Supercond. 10 (2000) 353.

[65] The ATLAS Collaboration, The ATLAS Experiment at the CERN Large Hadron Collider, JINST 3 S08003 (2008) Chapter 4.

[66] M.S. Alam et al, The ATLAS silicon pixel sensors, Nucl. Instrum. Meth. A 456 (2001) 217.

[67] The ATLAS Collaboration, The ATLAS Experiment at the CERN Large Hadron Collider, JINST 3 S08003 (2008) Chapter 5.

[68] The ATLAS Collaboration, Liquid Argon Calorimeter Technical Design Report, CERN-LHCC-96-041 (1996) Chapter 1.

[69] The ATLAS Collaboration, The ATLAS Experiment at the CERN Large Hadron Collider, JINST 3 S08003 (2008) Chapter 8.

[70] The ATLAS Collaboration, The ATLAS Simulation Infrastructure, Eur. Phys. J C70 (2010) 823–874.

[71] M. Dobbs and J.B. Hansen, The HepMC C++ Monte Carlo event record for High Energy Physics, Comput. Phys. Commun 134 (2001) 41.

[72] The GEANT4 Collaboration, The HepMC C++ Monte Carlo event record for High Energy Physics, Nucl. Instrum. Meth. A 506 (2003) 250–303.

[73] A. Sherstnev, and R. S. Thorne, Parton Distributions for LO Generators, Eur. Phys. J. C 55 (2008) 553–575.

[74] T. Sjöstrand, S.Mrenn, and P.Skands, PYTHIA 6.4 physics and manual, JHEP 05 (2006) 26.

[75] M. L. Mangano, M. Moretti, F. Piccinini, R. Pittau, and A. D. Polosa, ALPGEN, a generator for hard multiparton processes in hadronic collisions, JHEP 001.

[76] CompHEP Collaboration, CompHEP 4.4: Automatic computations from Lagrangians to events, Nucl. Instrum. Meth. A534 (2004) 250–259.

[77] S.Frixione and B.Webber, Matching NLO QCD computations and parton shower simulations, JHEP 0206 (2002) 29.

[78] J.M.Butterworth, J.R.Forshaw, and M.H.Seymour, Multiparton interactions in photoproduction at HERA, Z, Phys C72 (1996) 637–646.

[79] G.Corcella et al, HERWIG 6: an event generator for hadron emmision reactions with interfering gluons (including supersymmetric processes), JHEP 01 (2001) 10.

[80] G.Corcella et al, HERWIG 6.5 Release Note, arXiv:hep-ph/0210213 .

[81] R. Hamberg, W.L. van Neerven, and T. Matsuura, A complete calculation of the order α_s^2 correction to the Drell-Yan K-factor, Nucl. Phys. B359 (1991) 342–405.

[82] C. M. Carloni Calame, G. Montagna, O. Nicrosini, and A. Vicini, Precision electroweak calculation of the charged current Drell-Yan process, JHEP 0612 (2006) 016.

[83] The ATLAS Collaboration, Search for high-mass dilepton resonances in pp collisions at $\sqrt{s} = 7$ TeV (Support Note), ATL-COM-PHYS-2011-770 (2011) .

[84] The ATLAS Collaboration, Search for high-mass dielectron resonances at $\sqrt{s} = 7$ TeV, ATLAS-COM-PHYS-2011-083 (2011) .

[85] The ATLAS Collaboration, Athena Release 16.6.5, `http://alxr.usatlas.bnl.gov/lxr-stb5/source/atlas/?v=release_16_6_5` (August 2011) .

[86] Rene Brun and Fons Rademakers, ROOT - An Object Oriented Data Analysis Framework, Nucl. Instrum. Meth.

[87] The ATLAS Collaboration, Athena Analysis Package, Release 16.6.5, `http://alxr.usatlas.bnl.gov/lxr-stb5/source/atlas/PhysicsAnalysis/AnalysisCommon/AnalysisExamples/?v=release_16_6_5` (August 2011) .

[88] The ATLAS Collaboration, Athena Pileup Reweighting Package, Release 16.6.5, `http://alxr.usatlas.bnl.gov/lxr-stb5/source/atlas/PhysicsAnalysis/AnalysisCommon/PileupReweighting/?v=release_16_6_5` (August 2011) .

[89] The ATLAS Collaboration, Athena Good Runs Lists Package, Release 16.6.5, `http://alxr.usatlas.bnl.gov/lxr-stb5/source/atlas/DataQuality/GoodRunsLists/?v=release_16_6_5` (August 2011) .

[90] The ATLAS Collaboration, The ATLAS Experiment at the CERN Large Hadron Collider, JINST 3 S08003 (2008) Chapter 10.

[91] M. Aharrouche et al, Response Uniformity of the ATLAS liquid Argon Electromagnetic Calorimeter, Nucl. Instrum. Meth. A 582 (2007) 429–455.

[92] The ATLAS Collaboration, Electron performance measurements with the ATLAS detector using the 2010 LHC proton-proton collision data, arXiv:1110.3174v1 [hep-ex] Submitted to Eur. Phys. J. C (2011) .

[93] The ATLAS Collaboration, Trigger ID definition, `http://alxr.usatlas.bnl.gov/lxr/source/atlas/Trigger/TrigHypothesis/TrigEgammaHypo/python/TrigEGammaPIDdefs.py` (December 2011) .

[94] The ATLAS Collaboration, Expected electron performance in the ATLAS experiment, ATL-PHYS-PUB-2011-016 (2011) 6–20.

[95] The ATLAS Collaboration, Search for high-mass dilepton resonances in pp collisions at $\sqrt{s} = 7$ TeV with the ATLAS detector, ATLAS-CONF-2011-083 (2011) .

[96] The ATLAS Collaboration, Search for New Particles in Two-Jet Final States in 7 TeV Proton-Proton Collisions with the ATLAS Detector at the LHC, Phys. Rev. Lett 105 (2010) .

[97] The ATLAS Collaboration, Atlantis event visualisation software, `http://www.hep.ucl.ac.uk/atlas/atlantis/` (November 2011) .

[98] M. C. Kumar, P. Mathews, V. Ravindran, and A. Tripathi, Direct photon pair production at the LHC to $O(\alpha_s)$ in TeV scale gravity models, Nucl. Phys B818 (2009) 28.

[99] M. C. Kumar, P. Mathews, and V. Ravindran, PDF and scale uncertainties of various DY distributions in ADD and RS models at hadron colliders, Eur. Phys. J C49 (2007) 599.

[100] The ATLAS Collaboration, J. M. Butterworth et al, Single and Diboson Production Cross Sections in pp collisions at $\sqrt{s} = 7$ TeV, ATL-COM-PHYS-2010-695 (2010) .

[101] ATLAS Electromagnetic Barrel Calorimeter Collaboration, M. Aharrouche et al, Energy linearity and resolution of the ATLAS electromagnetic barrel calorimeter in an electron test-beam, Nucl. Instrum. Meth. A568 (2006) 601–623.

[102] A Caldwell, D. Kollar, K. Kröninger, BAT - The Bayesian Analysis Toolkit, Computer Physics Communication 180 (2009) 2197.

[103] A. L. Read, Modified Frequentist Analysis of Seach Results (the CL_s Method), CERN-OPEN-2000-205 (2000) .

[104] V. F. Obraztsov, Confidence limits for processes with small statistics in several subchannels and with measurement errors, Nucl. Instrum. Meth. A277 (1988) 608.

[105] Glen Cowan, Statistical Data Analysis, first edition Edition, Oxford University Press, Clarendon Press, Oxford, 1998.

[106] E. J. Eichten, K. D. Lane, and M. E. Peskin, New Tests for Quark and Lepton Substructure, Phys. Rev. Lett 50 (1983) 811–814.

[107] J. Neyman and E. Pearson, On the Problem of the Most Efficient Tests of Statistical Hypotheses, Philosophical Transactions of the Royal Society of London 231 (1933) 289–337.

[108] R. Blair et al, ATLAS Standard Model Cross Section recommendations for 7 TeV LHC running, `https://svnweb.cern.ch/trac/atlasgrp/export/50132/Physics/StandardModel/xsectf/note/xsectf.pdf`.

[109] P. Golonka and Z. Wąs, PHOTOS Monte Carlo: a precision tool for QED corrections in Z and W decays, Eur. Phys. J. C 45 (2006) 97–107.

[110] C. M. Carloni Calame, G. Montagna, O. Nicrosini, and A. Vicini, Precision electroweak calculation of the production of high transverse-momentum lepton pairs at hadron colliders, JHEP 10 (2007) 109.

[111] TeV4LHC-Top and Electroweak Working Group Collaboration, C.E. Gerber et al, Tevatron-for-LHC Report: Top and Electroweak Physics, arXiv:0705.3251 [hep-ph] (2007) .

[112] C. Gwenlan and P. Loch, Recommendations for systematic error contributions from PDF to theoretical predictions, `https://indico.cern.ch/getFile.py/access?contribId=1&resId=0&materialId=slides&confId=137359`(2011) .

[113] A. Martin, W. Stirling, R. Thorne, and G. Watt, Parton Distributions for the LHC, Eur. Phys. J. C 63 (2009) 189.